

# Interacting Photons in Waveguide-QED and Applications in Quantum Information Processing

by

Huaixiu Zheng

Department of Physics  
Duke University

Date: \_\_\_\_\_

Approved:

---

Harold U. Baranger, Supervisor

---

Daniel J. Gauthier

---

Gleb Finkelstein

---

Shailesh Chandrasekharan

---

Jian-Guo Liu

Dissertation submitted in partial fulfillment of the requirements for the degree  
of  
Doctor of Philosophy in the Department of Physics  
in the Graduate School of Duke University  
2013

ABSTRACT

Interacting Photons in Waveguide-QED and  
Applications in Quantum Information  
Processing

by

Huaixiu Zheng

Department of Physics  
Duke University

Date: \_\_\_\_\_  
Approved:

---

Harold U. Baranger, Supervisor

---

Daniel J. Gauthier

---

Gleb Finkelstein

---

Shailesh Chandrasekharan

---

Jian-Guo Liu

An abstract of a dissertation submitted in partial fulfillment of the requirements  
for the degree of Doctor of Philosophy in the Department of Physics  
in the Graduate School of Duke University  
2013

Copyright © 2013 by Huaixiu Zheng  
All rights reserved except the rights granted by the  
Creative Commons Attribution-Noncommercial Licence

# Abstract

Strong coupling between light and matter has been demonstrated both in classical cavity quantum electrodynamics (QED) systems and in more recent circuit-QED experiments. This enables the generation of strong nonlinear photon-photon interactions at the single-photon level, which is of great interest for the observation of quantum nonlinear optical phenomena, the control of light quanta in quantum information protocols such as quantum networking, as well as the study of strongly correlated quantum many-body systems using light. Recently, strong coupling has also been realized in a variety of one-dimensional (1D) waveguide-QED experimental systems, which in turn makes them promising candidates for quantum information processing. Compared to cavity-QED systems, there are two new features in waveguide-QED: the existence of a continuum of states and the restricted 1D phase space, which together bring in new physical effects. This thesis consists of two parts: 1) understanding the fundamental interaction between local quantum objects, such as two-level systems and four-level systems, and photons confined in the waveguide; 2) exploring its implications in quantum information processing, in particular photonic quantum computation and quantum key distribution.

First, I demonstrate that by coupling a two-level system (TLS) or three/four-level system to a 1D continuum, strongly-correlated photons can be generated inside the waveguide. Photon-photon bound states, which decay exponentially

as a function of the relative coordinates of photons, appear in multiphoton scattering processes. As a result, photon bunching and antibunching can be observed in the photon-photon correlation function, and nonclassical light source can be generated on demand. In the case of an  $N$ -type four-level system, I show that the effective photon-photon interaction mediated by the four-level system, gives rise to a variety of nonlinear optical phenomena, including photon blockade, photon-induced tunneling, and creation of single-photon states and photon pairs with a high degree of spectral entanglement, all in the absence of a cavity. However, to enable greater quantum networking potential using waveguide-QED, it is important to study systems having more than just one TLS/qubit. I develop a numerical Green function method to study cooperative effects in a system of two qubits coupled to a 1D waveguide. Quantum beats emerge in photon-photon correlations, and persist to much longer time scales because of non-Markovian processes. In addition, this system can be used to generate a high-degree of long-distance entanglement when one of the two qubits is driven by an on-resonance laser, further paving the way toward waveguide-QED-based quantum networks.

Furthermore, based on our study of light-matter interactions in waveguide-QED, I investigate its implications in quantum information processing. First, I study quantum key distribution using the sub-Poissonian single photon source obtained by scattering a coherent state off a two-level system. The rate for key generation is found to be twice as large as for other sources. Second, I propose a new scheme for quantum computation using flying qubits—propagating photons in a one-dimensional waveguide—interacting with matter qubits. Photon-photon interactions are mediated by the coupling to a three- or four-level system, based on which photon-photon  $\pi$ -phase gates (Controlled-NOT) can be implemented for universal quantum computation. It is shown that high gate fidelity is possible

given recent dramatic experimental progress in superconducting circuits and photonic-crystal waveguides. The proposed system can be an important building block for future on-chip quantum networks.

To my wife Zhenhua Wang and my family in China

# Contents

<b>Abstract</b>	<b>iv</b>
<b>List of Tables</b>	<b>xiii</b>
<b>List of Figures</b>	<b>xiv</b>
<b>Acknowledgements</b>	<b>xxii</b>
<b>1 Introduction to Waveguide-QED</b>	<b>1</b>
1.1 Light-Matter Interaction in Open Space . . . . .	2
1.1.1 Field Quantization . . . . .	2
1.1.2 Hamiltonian of Dipole Interaction . . . . .	3
1.2 Fundamentals of Cavity-QED . . . . .	5
1.2.1 Field Quantization . . . . .	5
1.2.2 Jaynes-Cummings Model . . . . .	7
1.3 Fundamentals of Waveguide-QED . . . . .	8
1.3.1 Field Quantization . . . . .	8
1.3.2 Hamiltonian in Waveguide . . . . .	11
1.3.3 Loss . . . . .	15
1.4 Survey of Experimental Systems . . . . .	15
1.4.1 Cavity-QED Experiments . . . . .	16
1.4.2 Waveguide-QED Experiments . . . . .	17

<b>2 Photon-Photon Bound States in Waveguide-QED and Scattering of Fock and Coherent States off a Two-Level System</b>	<b>20</b>
2.1 Introduction . . . . .	21
2.2 Model Hamiltonian . . . . .	23
2.3 Analytical Solution of Scattering Eigenstates . . . . .	25
2.4 Scattering of Fock State Wavepackets . . . . .	34
2.4.1 Single-Photon Fock State Scattering . . . . .	37
2.4.2 Two-Photon Fock State Scattering . . . . .	37
2.4.3 Three-Photon Fock State Scattering . . . . .	40
2.5 Spectral Entanglement . . . . .	42
2.6 Scattering of Coherent State Wavepackets . . . . .	45
2.6.1 Second-Order Correlation Function . . . . .	46
2.6.2 Number Statistics . . . . .	48
2.7 Conclusion . . . . .	50
<b>3 Cavity-free Photon Blockade and Photon-induced Tunneling</b>	<b>52</b>
3.1 Introduction . . . . .	53
3.2 Model Hamiltonian . . . . .	54
3.3 Scattering Eigenstates . . . . .	57
3.4 Output States of Fock State Scattering . . . . .	61
3.5 Photonic Transport: Photon Blockade and Photon-induced Tunneling	64
3.5.1 Single-Photon . . . . .	65
3.5.2 Two-Photon . . . . .	65
3.5.3 Photon Blockade and Photon-induced Tunneling . . . . .	69
3.6 Spectral Entanglement . . . . .	70
3.7 Photon-Photon Correlation . . . . .	74

3.7.1	Non-Classical Light Source . . . . .	74
3.7.2	Second-Order Correlation Function . . . . .	76
3.8	Conclusion . . . . .	79
<b>4</b>	<b>Two-Qubit System: Persistent Quantum Beats and Long-Distance Entanglement</b>	<b>81</b>
4.1	Introduction . . . . .	82
4.2	Hamiltonian . . . . .	83
4.3	Single-Photon: Phase Gate . . . . .	84
4.3.1	Single-Photon Scattering Eigenstates . . . . .	84
4.3.2	Results . . . . .	86
4.4	Quantum Beats in Photon-Photon Correlation . . . . .	87
4.4.1	Mapping to a Bosonic Model . . . . .	87
4.4.2	Numerical Green Function Method . . . . .	88
4.4.3	Markovian Regime . . . . .	90
4.4.4	Non-Markovian Regime: Persistent Quantum Beats . . . . .	91
4.4.5	Two-Pole Approximation . . . . .	96
4.5	Qubit-Qubit Entanglement . . . . .	98
4.6	Loss and Possible Experimental Systems . . . . .	99
4.6.1	(a) Hybrid Fiber-Plasmonic Waveguide-QED System . . . . .	100
4.6.2	(b) Integrated Nanofiber-Trapped Atomic Ensemble System	101
4.6.3	(c) Slow-light Superconducting Waveguide-QED System . . . . .	102
4.7	Conclusion . . . . .	102
<b>5</b>	<b>Decoy-state Quantum Key Distribution with Nonclassical Light</b>	<b>104</b>
5.1	Introduction . . . . .	105
5.2	Nonclassical Light Source . . . . .	107

5.2.1	Model System . . . . .	107
5.2.2	Corrections of Loss . . . . .	109
5.2.3	Number Statistics of the Reflected Field . . . . .	112
5.3	Model for Decoy-State Quantum Key Distribution . . . . .	113
5.4	Key Generation Rate . . . . .	115
5.5	Conclusion . . . . .	117
<b>6</b>	<b>Waveguide-QED-Based Photonic Quantum Computation</b>	<b>119</b>
6.1	Introduction . . . . .	120
6.2	$\pi$ -Phase Gate: 4LS Scheme . . . . .	121
6.2.1	Photonic Qubits . . . . .	121
6.2.2	Model Hamiltonian . . . . .	122
6.2.3	Gate Operation . . . . .	123
6.2.4	Fidelity and Loss . . . . .	128
6.3	$\pi$ -Phase Gate: 3LS Scheme . . . . .	130
6.3.1	Model Hamiltonian . . . . .	131
6.3.2	Photon-Atom and Photon-Photon $\pi$ -Phase Gates . . . . .	132
6.3.3	Fidelity and Loss . . . . .	133
6.4	Photon-Qubit Quantum Memory . . . . .	135
6.5	Conclusion . . . . .	137
<b>7</b>	<b>Conclusions and Outlook</b>	<b>138</b>
7.1	Conclusions . . . . .	138
7.2	Outlook . . . . .	141
<b>A</b>	<b>Expressions for <math>\gamma_{1,2}</math>, <math>C_{1,2}</math> and <math>D_{1,2,3,4}</math></b>	<b>146</b>
<b>B</b>	<b>Three-photon asymptotic output state from 3LS and 4LS scattering</b>	<b>149</b>

<b>C Phase Analysis of Photon Blockade and Photon-Induced Tunneling</b>	<b>151</b>
<b>D Second-Order Correlation Function in the Schrödinger Picture</b>	<b>154</b>
<b>E Derivation of the Output States in the 4LS Scheme of Photonic <math>\pi</math>-phase Gate</b>	<b>156</b>
<b>Bibliography</b>	<b>161</b>
<b>Biography</b>	<b>176</b>

# List of Tables

1.1	Cavity-QED experiments which have achieved the strong coupling regime. $g$ : Rabi frequency. $\kappa$ : cavity photon loss rate. $\Gamma'$ : atom decay rate. $\kappa$ and $\Gamma'$ are in the same unit as $g$ . $Q$ : cavity quality factor. SC: superconducting; QD: quantum dot; PC: photonic crystal; TL: transmission line. . . . .	16
1.2	Waveguide-QED Experiments. Purcell factor $P$ is defined as $P = \frac{\Gamma_{wg}}{\Gamma_e}$ , where $\Gamma_{wg}$ and $\Gamma_e$ are the atomic decay rates into the waveguide modes and other modes, respectively. NV: nitrogen vacancy. QD: quantum dot. PCF: photonic-crystal fiber. PC: photonic crystal. SC: superconducting. . . . .	18

# List of Figures

1.1	One-dimensional optical cavity of length $L$ [1]. . . . .	6
1.2	Dynamics of an initially excited two-level system coupled to a on-resonance cavity [1] for (a) strong coupling regime, and (b) weak coupling regime. Solid lines: probability of the atom to be in the excited state; Dashed lines: probability for the cavity to contain a single photon. Time is measured in units of $\Gamma'^{-1}$ . . . . .	8
1.3	1D waveguide with length $L$ . The field is confined within $R$ to the center in the transverse direction. . . . .	9
1.4	Linearized dispersion relation in a 1D waveguide. Only the states close to $\omega_{eg}$ (within a width $\Gamma_{wg}$ ) are important for the dynamics of the system. Both the left-moving (blue solid line) and the right-moving (red solid line) fields are extended to negative energy range (blue dash and red dash lines). . . . .	12
1.5	Vacuum Rabi splitting in circuit-QED from Ref. [2, 3]. There are clearly two resolved peaks in the cavity transmission spectrum. The inset shows the Jaynes-Cummings ladder of the eigenspectrum.	17
2.1	Sketch of the structure considered: a 1D continuum of bosons coupled to a two-level-system with ground state $ g\rangle$ and excited state $ e\rangle$ . . . . .	23
2.2	Schematic of different processes in four-photon scattering by a two-level system. The plane waves are represented by wiggly lines, while the many-body bound states are represented by the ovals. .	31
2.3	Single-photon transmission ( $P_T^{(1)}$ ) and reflection ( $P_R^{(1)}$ ) probabilities as a function of the ratio between coupling strength $\Gamma$ and $\sigma$ . The incident photon is on resonance with the two level system ( $k_0 = \epsilon$ ) and we have considered the lossless case $\Gamma' = 0$ . . . . .	36

2.4 Two-photon transmission and reflection probabilities as a function of $\Gamma/\sigma$ . (a) Probability that both photons are transmitted (and hence are right-going, $P_{TT}^{(2)}$ ). (b) Probability that one photon is transmitted and one reflected (right-left, $P_{TR}^{(2)}$ ). (c) Probability that both photons are reflected (both left-going, $P_{RR}^{(2)}$ ). (d) The three processes on a single plot. The label PW refers to the contribution from the plane-wave term only, while BS refers to all the other contributions involving bound-state terms. The incident photons are on resonance with the two-level system ( $k_0 = \epsilon$ ), we consider the lossless case $\Gamma' = 0$ . Notice the large effect of the bound state on these quantities. . . . .	40
2.5 Three-photon transmission and reflection probabilities as a function of $\Gamma/\sigma$ . (a) Probability of all three photons transmitted ( $P_{TTT}^{(3)}$ ). (b) Probability of two photons transmitted and one reflected ( $P_{TTR}^{(3)}$ ). (c) Probability of one photon transmitted and two photons reflected ( $P_{TRR}^{(3)}$ ). (d) Probability of all three photons reflected ( $P_{RRR}^{(3)}$ ). (e) $P^3$ all together. The label PW refers to the contribution from only the plane wave term, while BS refers to all the other contributions, involving bound state terms. The incident photons are on resonance with the two level system ( $k_0 = \epsilon$ ), we consider the lossless case $\Gamma' = 0$ . . . . .	41
2.6 Two-photon joint spectrum of the output states after scattering off a 2LS in the case of a spectrally narrow incident wavepacket. Panels (a), (c), (e) show the uncorrelated spectra $G_{TT}(k_1, k_2)$ , $G_{TR}(k_1, k_2)$ , and $G_{RR}(k_1, k_2)$ , respectively. Panels (b), (d), (f) show the joint spectra of the two transmitted photons, one transmitted and one reflected, and two reflected photons, respectively. Panel (g) shows $F_{TT}$ along the line $k_1 + k_2 = 2k_0$ [dash line in panel (b)] as a function $k_2 - k_1$ . System parameters: $\Gamma = 9\Gamma'$ , $\sigma = 0.1\Gamma'$ , and $k_0 = \epsilon$ . The frequencies are in units of $\Gamma'$ . . . . .	44
2.7 Second-order correlation of the transmitted field given an incident coherent state with $\bar{n} \leq 1$ at various coupling strengths $\Gamma$ to the 1D continuum. (a) $\Gamma = 0.5\sigma$ , (b) $\Gamma = 1.4\sigma$ , (c) $\Gamma = 2.3\sigma$ , (d) $\Gamma = 2.9\sigma$ , (e) $\Gamma = 3.2\sigma$ , (f) $\Gamma = 4\sigma$ . The spontaneous emission rate to channels other than the 1D continuum is set to $\Gamma' = \sigma$ . Notice that the correlation behavior is very sensitive to the coupling strength to 1D continuum, showing both bunching and antibunching. . . . .	47

2.8	Photon number distribution of the transmitted field compared with a coherent state. We considered the lossless case $\Gamma' = 0$ . The statistics is non-Poissonian with the 2 and 3 photon content enhanced. . . . .	50
3.1	Sketch of the atom-waveguide system: (a) a $\Lambda$ -type three-level system, (b) an $N$ -type four-level system, (c) photons (yellow) in a 1D waveguide coupled to an atom (blue), which can be either the 3LS in (a) or the 4LS in (b). The transitions $ 1\rangle \leftrightarrow  2\rangle$ and $ 3\rangle \leftrightarrow  4\rangle$ are coupled to the waveguide modes with strength $V$ . The transition $ 2\rangle \leftrightarrow  3\rangle$ is driven by a semiclassical control field with Rabi frequency $\Omega$ and detuning $\Delta$ . Here, $\omega_c$ is the frequency of the control field. . . . .	55
3.2	Single-photon transmission $T$ (solid), reflection $R$ (dashed) and loss (dotted) as a function of incident photon detuning, for the values of $\sigma$ (the wavepacket width) and $\Omega$ (the strength of the control field) shown. Here, the effective Purcell factor is $P = 9$ . Note the sharp EIT window, particularly in the narrow wavepacket case. . . . .	64
3.3	Two-photon transmission and reflection probabilities for the 3LS and 4LS cases. (a)-(c) As a function of incident photon detuning $\delta_\omega$ with $P = 9$ and $\sigma = 0.2$ . (a) Probability that both photons are transmitted (and hence are right-going, $P_{TT}^{(2)}$ ). (b) Probability that one photon is transmitted and one reflected (right-left, $P_{TR}^{(2)}$ ). (c) Probability that both photons are reflected (both left-going, $P_{RR}^{(2)}$ ). (d)-(f) As a function of $P$ with $\delta_\omega = 0$ and $\sigma = 0.2$ . (g)-(i) As a function of $\sigma$ with $P = 9$ and $\delta_\omega = 0$ . The label PW refers to the contribution from the plane-wave term only, while BS refers to all the other contributions involving bound-state terms [Eq. (3.19)]. Here, we set $\Omega = 1.6$ . The bound state effect enhances transparency in the 3LS case but blocks two-photon transmission past a 4LS. Note that a non-zero $\sigma$ is crucial to observe these effects. . . . .	67
3.4	Photon blockade and photon-induced tunneling in transmission. Photon blockade strengths $P_{21}$ (solid line) and $P_{31}$ (dashed line) as a function of incident photon detuning $\delta_\omega$ , $P$ and $\sigma$ for (a)-(c) the 3LS case, and (d)-(f) the 4LS case. Here, $\Omega = 1.6$ . The 3LS causes photon-induced tunneling while the 4LS causes photon blockade. . . . .	69



3.8 Bunching and anti-bunching. Second-order correlation function $g^{(2)}(\tau)$ of the transmitted field for a weak incident coherent state ( $\bar{n} \ll 1$ ) of width $\sigma = 0.2$ , resonant with the atom ( $\delta_\omega = 0$ ). (a) Color map plot of $\log_{10}[g^{(2)}(0)]$ as a function of the strength of the classical control field, $\Omega$ , and the effective Purcell factor $P$ . The dashed line marks the border between bunching ( $g^{(2)}(0) > 1$ ) and anti-bunching ( $g^{(2)}(0) < 1$ ) behavior. (b) $g^{(2)}$ as a function of time delay $\tau$ in four cases (using $\Omega = 1.6$ ). Inset: zoom at short time scales. . . . .	78
4.1 Schematic diagram of the waveguide system and single-photon transmission. (a) Two qubits (separated by $L$ ) interacting with the waveguide continuum. Panels (b) and (c) show colormaps of the single-photon transmission probability $T$ and the phase shift $\theta$ , respectively, as a function of detuning $\delta = ck - \omega_0$ and $2kL$ . Here, we consider the lossless case $\Gamma' = 0$ . . . . .	84
4.2 Quantum beats in the Markovian regime. The second-order photon-photon correlation function of both the transmitted (top) and reflected (bottom) fields as a function of $t$ for $k_0L = 0$ (solid line) and $k_0L = \pi/2$ (dashed line). The incident weak coherent state is on resonance with the qubits: $k = k_0 = \omega_0/c$ . (Parameters: $\omega_0 = 100\Gamma$ and $\Gamma' = 0.1\Gamma$ ). . . . .	91
4.3 Persistent quantum beats in the non-Markovian regime. The second-order correlation function of both the transmitted (top) and reflected (bottom) fields is plotted as a function of $t$ for $k_0L = 25.5\pi$ (solid line) and $100.5\pi$ (dashed line). We set the incident coherent state on resonance with the qubits ( $k = k_0$ ), $\omega_0 = 100\Gamma$ and $\Gamma' = 0.1\Gamma$ . . . . .	93
4.4 Renormalized transition frequencies and decay rates of the symmetric (S) and antisymmetric (A) states. Panels (a)-(c) show the transition frequencies $\omega_S$ (thin solid line) and $\omega_A$ (thick solid line) obtained numerically from Eq. (4.20) together with $\omega_S$ (thin dashed line) and $\omega_A$ (thick dashed line) given by the Markov approximation. Panels (d)-(f) similarly show the decay rates $\Gamma_S$ and $\Gamma_A$ obtained both numerically and in the Markov approximation. ( $\omega_0 = 100\Gamma$ and $\Gamma' = 0.1\Gamma$ ). . . . .	95

4.5	The poles of the Green functions for (a) $k_0L = 0$ , (b) $k_0L = \frac{\pi}{2}$ , (c) $k_0L = 25.5\pi$ , and (d) $k_0L = 100.5\pi$ . Both the real and imaginary parts of the poles are in units of $\Gamma$ . We show all the poles with real part within $[\omega_0 - 4\Gamma, \omega_0 + 4\Gamma]$ . The poles corresponding to the $ S\rangle$ and $ A\rangle$ states are labeled as $S$ and $A$ , respectively. In case (d), there are four additional poles ( $C1-C4$ ) within the plotted range. . . . .	97
4.6	Long-distance qubit-qubit entanglement. (a) Schematic of setup: the first qubit is driven by a on resonance laser with Rabi frequency $\Omega_1$ . The steady state concurrence is plotted as a function of $k_0L$ for (b) $0 \leq k_0L \leq 5\pi$ , and (c) $95\pi \leq k_0L \leq 100\pi$ . The Rabi frequencies are $\Omega_1 = 0.1\Gamma$ , $\Omega_2 = 0$ . The driving laser is on resonance with the qubits. ( $\omega_0 = 100\Gamma$ and $\Gamma' = 0.1\Gamma$ ). . . . .	98
4.7	Three possible setups for long-distance entanglement in waveguide-QED. (a) Hybrid plasmonic system. The dielectric waveguide (light blue) is phase-matched with the plasmonic nanowires (yellow) so that efficient plasmon transfer between them can be realized. The nanowires are strongly coupled to the quantum dots (blue) in the tapered regions. Note that the length of the dielectric waveguide between the nanowires can be very long (indicated by breaks). (b) Tapered nanofiber system. An optical fiber (green) is tapered into narrow nanofibers in two regions. Two atomic ensembles (red) are trapped by and strongly coupled to the nanofibers. (c) Slow-light superconducting system. Two superconducting qubits (blue) couple strongly to the slow-light superconducting waveguide (red dashed box). . . . .	101
5.1	Schematic of QKD [4]: Alice sends quantum states ( $\Psi$ ) to Bob through a quantum channel. Eve can tap into the quantum channel without any restriction except the laws of quantum physics. Alice and Bob can also communicate via the classical channel (labeled $C$ ), into which Eve can only listen. . . . .	106
5.2	Schematic of the model system. The incoming coherent state pulse has a spectral width $\sigma$ . The excited state of the 2LS decays into waveguide modes and free space modes with rate $\Gamma$ and $\Gamma'$ , respectively. Here, we focus on the number statistics of the reflected field. . . . .	108

5.3 Nonclassical light source. The number statistics $P_n$ of the 2LS source (2LSS, solid), and a coherent state (CS, dashed) of the same mean photon number as a function of $\Gamma/\sigma$ . Inset: $P_n$ at $\sigma = \Gamma/2$ . Here, we set $P = \Gamma/\Gamma' = 20$ . For comparison, 2LSS without loss is shown in gray lines. . . . .	113
5.4 Key generation rate with different light sources: weak coherent state (WCS), heralded single-photon source (HSPS), and 2LS source (2LSS) with $\sigma = \Gamma/2$ and $P = 20$ . . . . .	116
5.5 Key generation rate of 2LS sources with parameter variation and loss: (a) $\sigma = 5\Gamma, 2\Gamma, \Gamma, 0.5\Gamma$ . Inset: maximal transmission distance ( $\ell_{\max}$ ) as a function $\Gamma/\sigma$ . $P = \Gamma/\Gamma' = 20$ ; (b) $P = 2, 5, 10, 20$ . Inset: $\ell_{\max}$ as a function of $P$ . $\sigma = \Gamma/2$ . . . . .	117
6.1 Gate operation: 1) trapping; 2) $\pi$ -phase; 3) retrieval. The gate sequences here illustrate the case of both photons $A$ and $B$ being in state $ \omega_1\rangle$ . For this case, step 4) does not cause any change and hence is not shown here. The left and right sides show the initial and final states, respectively. Inactive transitions in each step are gray-colored. . . . .	124
6.2 Fidelity and leakage error of the photon-photon $\pi$ -phase gate. (a) Fidelity $F$ as a function of the pulse width $\Delta T$ (in units of $\Gamma^{-1}$ ) for $P = 10, 20, 40, \infty$ . (b) The leakage probability $P_\ell$ as a function $P$ with $\Delta T = 10\Gamma^{-1}$ . . . . .	130
6.3 Schematic diagram of the operation sequence of the $\pi$ -phase gate between two photons $A$ and $B$ . The three-level system (3LS) is located a distance $a$ from the end of the semi-infinite waveguide and is initialized in an equal superposition of the $g$ and $s$ states. $A$ and $B$ are reflected successively from the semi-infinite waveguide coupled to the 3LS. Between the reflections, single-qubit rotation pulses (green rectangles) are applied to the atomic qubit made of states $ g\rangle$ and $ s\rangle$ . . . . .	132
6.4 Fidelity and leakage error of the photon-atom gate in the 3LS scheme. (a) Fidelity $F$ as a function of the pulse width $\Delta T$ (in units of $\Gamma^{-1}$ ) for four different cases. (b) The leakage probability $P_\ell$ as a function of the effective Purcell factor $P$ with a pulse width $\Delta T = 10\Gamma^{-1}$ . . . . .	135

6.5 Schematic diagram of an <i>M</i> -type five-level system as a quantum memory of qubit photons. The top and bottom panels show the initial and final states of mapping a qubit-photon state to a matter-qubit state. An arbitrary superposition of $\omega_0$ -photon (green pulse) and $\omega_1$ -photon (yellow pulse) is stored in the matter-qubit states $ s_0\rangle$ and $ s_1\rangle$ . Meanwhile, an auxiliary photon- <i>C</i> (blue pulse) is emitted after the mapping. . . . .	136
C.1 The integrand function $TB(k_1, k_2)$ of the interference term as a function of $k_1$ and $k_2$ . (a) $\delta = 0.0$ . (b) $\delta = 2.0$ . Here, $\Gamma = 6$ , $\Omega = 1.6$ . . . . .	152

# Acknowledgements

It would have been impossible for me to complete this thesis without the help from many people. I would like to thank them from the bottom of my heart.

First of all, I feel truly blessed to have Prof. Harold Baranger as my advisor. I have benefited so much from his guidance, his constant encouragements, his deep knowledge, and his enthusiasm on physics. In particular, I thank him for the availability for scientific discussions in spite of his busy schedule and many other commitments. Those discussions help me to develop deeper understanding of condensed matter physics and quantum science. Also, I feel very thankful for the unlimited freedom he gave me to explore several different research directions, at the same time providing his expert opinions on the feasibility of each idea we have. I feel extremely grateful for every effort he made to build me up on many aspects, including shaping research ideas together with me, bringing to my attention technical tricks, teaching me how to write scientific articles, encouraging me to attend conferences, involving me in collaborations and so on.

I would like to thank Prof. Daniel Gauthier for the fruitful collaboration and help on the waveguide-QED projects. He is the first person to talk to whenever we have some experimental issues related to our theoretical proposals. His expertise on quantum optics gives me a guidance in terms of where our theory results can possibly lead to. His inquiry on experimental relevance motivates me to have a good understanding of the connection between current experimental

status and theoretical findings, which is extremely important for theorists.

I would like to thank Prof. Gleb Finkelstein for the fruitful collaboration on the project of quantum phase transition in a dissipative environment. I learnt a lot about low-temperature transport measurement techniques in nanostructures from extensive discussions with him. His physical intuition and scientific enthusiasm always inspires me to think more deeply about the underlying physics behind the experimental phenomena.

I would like to express my appreciation to Dr. Serge Florens for the collaboration on the dissipation project and the hospitality during my stay in Grenoble in summer 2012. His thorough knowledge on Matsubara Green functions and outstanding physical intuition makes it possible for me to complete the key steps of the calculations in a very speedy manner. The companion on the trip to Provence makes my stay in France an unforgettable memory.

I thank Prof. Shailesh Chandrasekharan and Prof. Jian-Guo Liu for having interest in my research and serving as my Ph.D. committee. Their comments are very valuable to me. I also would like to thank Prof. Richard Palmer for giving helpful guidance as the Director of Graduate Studies when I first entered Duke, and Donna Ruger for taking care of all the documentary work.

I would like to thank some of the past and current members in the Baranger group and Finkelstein group: Dong Liu, Abhijit Mehta, Soumya Bera, Henok Mebrahtu, Yao-Lung Fang, Gu Zhang, Ivan Borzenets, Yuriy Bomze and Mauricio Pilo-Pais. In particular, I enjoyed working together with Dong Liu on the dissipation project. I benefited a lot from discussing and talking with him. I thank Abhijit Mehta for all the interesting discussions inside and outside of physics. I am grateful to Soumya Bera for sharing with me the polaron-antipolaron technique and the help during my stay in Grenoble. I thank Henok Mebrahtu for the

collaboration and the helpful discussions on low-temperature measurements. I would also like to thank several of my fellow graduate students for their friendship and encouragement, especially Ben Cerio, Georgios Laskaris, Yuan Lin, Abe Clark, Chris Coleman-Smith, Taritree Wongjirad and Qiujuan Ye.

I am grateful to the financial support I received from the GPNano Fellowship of the Nanoscience Program, and the John T. Chambers Scholars Fellowship of the Fitzpatrick Institute for Photonics. I also appreciate the funding I received from the Duke Graduate School and National Science Foundation to attend APS Marching Meetings, EP2DS, and Gordon Conference in Quantum Science.

Finally, I am indebted to my family in China for being constantly supportive of all of my endeavors along the way. My special thanks go to my wife, Zhenhua, for her endless love, support, patience and encouragement in the past five years.

# 1

## Introduction to Waveguide-QED

Understanding light-matter interaction is fundamental to quantum optics. Strong interactions can be achieved by placing atoms inside confined optical cavities. Cavity-based systems for quantum electrodynamics (QED) achieved the so-called strong-coupling regime by having a small mode volume of photons [1, 2, 5, 6, 7, 8, 9, 10, 11, 12, 13]. This enables the generation of strong nonlinear photon-photon interactions at the single-photon level, which is of great interest for the observation of quantum nonlinear optical phenomena [11, 14, 15, 16, 17], the control of light quanta in quantum information protocols such as quantum networking [18, 19], as well as the study of strongly correlated quantum many-body systems using light [20, 21, 22, 23, 24, 25, 26, 27, 28, 29, 30]. For example, electromagnetically induced transparency (EIT) [16] and photon blockade [14, 31, 32] have been observed in recent experiments with trapped atoms in an optical cavity [33, 34, 35] and with superconducting qubits in a microwave resonator [36]. Coherent transfer of quantum states between light and stationary qubits has been demonstrated in both cavity-QED [37] and circuit-QED [38, 39] systems.

Recently, an alternative waveguide-based QED system has emerged as a promising candidate for achieving strong coupling between photons and atoms, motivated by tremendous experimental progress [17, 40, 41, 42, 43, 44, 45, 46, 47, 48]. Waveguide-QED systems benefit from the strong confinement of light field inside the one-dimensional (1D) waveguide, which couples to nearby atoms. Compared to cavity-QED systems, the key physical element introduced in the waveguide QED geometry is that the atom couples to a continuum of modes. This relaxes the restriction of working with a narrow cavity bandwidth and avoids the complex tuning to match the cavity and the atom resonances.

In this Chapter, I start by reviewing the fundamental light-matter interaction in three-dimensional open space and then in cavity-QED systems, followed by an introduction to waveguide-QED systems. Next, I cover a survey of the current status of experimental progress in both cavity-QED and waveguide-QED systems.

## 1.1 Light-Matter Interaction in Open Space

### 1.1.1 *Field Quantization*

We start with field quantization of quantum electrodynamics in 3D free space. We assume an electromagnetic field confined inside a box of linear dimension  $L$ . We can quantize the field in open space by imposing periodic boundary conditions on the cubic of linear dimension  $L$ . The resulting vector potential and the electric and magnetic fields under Coulomb gauge can be expressed in

terms of the creation and annihilation operators in  $k$ -space  $a_{k\lambda}^\dagger$  and  $a_{k\lambda}$  as [1]

$$\begin{aligned}\mathbf{A}(\mathbf{r}, t) &= \sum_{k\lambda} \hat{\mathbf{e}}_{k\lambda} \sqrt{\frac{\hbar}{2\epsilon_0 V \omega_k}} [a_{k\lambda} e^{i(\mathbf{k}\cdot\mathbf{r}-\omega_k t)} + a_{k\lambda}^\dagger e^{-i(\mathbf{k}\cdot\mathbf{r}-\omega_k t)}], \\ \mathbf{E}(\mathbf{r}, t) = -\frac{\partial \mathbf{A}(\mathbf{r}, t)}{\partial t} &= i \sum_{k\lambda} \hat{\mathbf{e}}_{k\lambda} \sqrt{\frac{\hbar\omega_k}{2\epsilon_0 V}} [a_{k\lambda} e^{i(\mathbf{k}\cdot\mathbf{r}-\omega_k t)} - a_{k\lambda}^\dagger e^{-i(\mathbf{k}\cdot\mathbf{r}-\omega_k t)}], \\ \mathbf{B}(\mathbf{r}, t) = \nabla \times \mathbf{A}(\mathbf{r}, t) &= i \sum_{k\lambda} \frac{\hat{\mathbf{k}} \times \hat{\mathbf{e}}_{k\lambda}}{c} \sqrt{\frac{\hbar\omega_k}{2\epsilon_0 V}} [a_{k\lambda} e^{i(\mathbf{k}\cdot\mathbf{r}-\omega_k t)} - a_{k\lambda}^\dagger e^{-i(\mathbf{k}\cdot\mathbf{r}-\omega_k t)}].\end{aligned}\quad (1.1)$$

where  $\hat{\mathbf{k}} = \mathbf{k}/k$  is the unit vector,  $\omega_k$  is the photon frequency with wave-vector  $k$ , and  $\hat{\mathbf{e}}_{k\lambda}$  is the unit polarization vector with  $\lambda = 1, 2$ .  $V = L^3$  is the volume of the 3D box.

Because  $\hat{\mathbf{e}}_{k\lambda} \cdot \hat{\mathbf{e}}_{k\lambda'} = \delta_{\lambda\lambda'}$  and  $[a_{k\lambda}, a_{k'\lambda'}^\dagger] = \delta_{\lambda\lambda'} \delta_{kk'}$ , the energy of the field can be written as

$$\begin{aligned}H &= \frac{1}{2} \int_V d^3r (\epsilon_0 \mathbf{E}^2 + \mu_0^{-1} \mathbf{B}^2) \\ &= \sum_{k\lambda} \hbar\omega_k \left( a_{k\lambda}^\dagger a_{k\lambda} + \frac{1}{2} \right).\end{aligned}\quad (1.2)$$

### 1.1.2 Hamiltonian of Dipole Interaction

We assume a simple two level system with ground state  $|g\rangle$  and excited state  $|e\rangle$ . When the size of the two level system is much smaller than the wavelength corresponding to the transition frequency, we can apply the electric dipole approximation. Under the dipole approximation, the interaction between the two

level system and a static electric field (at  $\mathbf{r} = t = 0$ ) is given by

$$V^{AF} = -\mathbf{p} \cdot \mathbf{E} = -i \sum_{k\lambda} (\mathbf{p} \cdot \hat{\mathbf{e}}_{k\lambda}) \epsilon_k [a_{k\lambda} - a_{k\lambda}^\dagger], \quad (1.3)$$

where  $\mathbf{p}$  is the atomic dipole moment and  $\epsilon_k = \sqrt{\hbar\omega_k/2\epsilon_0 V}$  is the field strength per photon of frequency  $\omega_k$ .

Now, let us quantize the interaction Hamiltonian of  $V_{AF}$  in Eq. (1.3),

$$\begin{aligned} V_{AF} &= \{|g\rangle\langle g| + |e\rangle\langle e|\} \left\{ -i \sum_{k\lambda} (\mathbf{p} \cdot \hat{\mathbf{e}}_{k\lambda}) \epsilon_k [a_{k\lambda} - a_{k\lambda}^\dagger] \right\} \{|g\rangle\langle g| + |e\rangle\langle e|\} \\ &= -i \sum_{k\lambda} [\langle g|\mathbf{p} \cdot \hat{\mathbf{e}}_{k\lambda}|e\rangle|g\rangle\langle e| + \langle e|\mathbf{p} \cdot \hat{\mathbf{e}}_{k\lambda}|g\rangle|e\rangle\langle g|] \left[ \epsilon_k (a_{k\lambda} - a_{k\lambda}^\dagger) \right]. \end{aligned} \quad (1.4)$$

We can perform a rotation on  $a_{k\lambda}$  and  $a_{k\lambda}^\dagger$  to absorb  $-i$ , and define the raising and lowering atomic operators  $\sigma_+ = |e\rangle\langle g|$ ,  $\sigma_- = |g\rangle\langle e|$ . Without loss of generality, we assume the dipole matrix element  $d = \langle g|\mathbf{p} \cdot \hat{\mathbf{e}}_{k\lambda}|e\rangle = \langle e|\mathbf{p} \cdot \hat{\mathbf{e}}_{k\lambda}|g\rangle$  to be real. Then the dipole interaction Hamiltonian can be rewritten as

$$H_{AF} = \sum_{k\lambda} \epsilon_k d (\sigma_- + \sigma_+) (a_{k\lambda} + a_{k\lambda}^\dagger). \quad (1.5)$$

Applying the rotating wave approximation<sup>1</sup> and dropping the nonresonant terms which do not conserve the energy, we end up with the dipole interaction Hamiltonian as

$$H_{AF} = \sum_{k\lambda} \hbar g(k) (\sigma_+ a_{k\lambda} + \sigma_- a_{k\lambda}^\dagger), \quad (1.6)$$

---

<sup>1</sup> It is valid when the decay rate of the two level system is much smaller than the energy splitting  $\omega_{eg}$ , and is satisfied in most of current experiments.

with the wave-vector dependent Rabi frequency  $g(k)$  defined as

$$g(k) = d \sqrt{\frac{\omega_k}{2\epsilon_0 \hbar V}} \quad (1.7)$$

With the quantized dipole interaction Hamiltonian, we can calculate the spontaneous decay rate in free space using Fermi's golden rule,

$$\begin{aligned} \Gamma_e &= \frac{2\pi}{\hbar} \sum_{k\lambda} |\langle i | H^{AF} | f_{k\lambda} \rangle|^2 \delta(E_f - E_i) \\ &= \frac{2\pi}{\hbar^2} \sum_{k\lambda} |\hbar g(k)|^2 \delta(\omega_f - \omega_i) \\ &= 2\pi \rho(\omega_{eg}) |g(k_{eg})|^2 \\ &= \frac{d^2 \omega_{eg}^3}{\pi \epsilon_0 \hbar^2 c^3}. \end{aligned} \quad (1.8)$$

where  $\rho(\omega) = \frac{V\omega_k^2}{\pi^2 c^3}$  is the density of states,  $|i\rangle$  and  $|f_{k\lambda}\rangle$  are the initial and final states, respectively. Note that there are at least two conditions which have to be satisfied to validate the above calculation. First, the decay rate must be much smaller than the energy difference between the two states of the transition,  $\Gamma_e \ll \omega_{eg}$ . This makes sure the initial and final states are well defined. Second, the dependence of the matrix element and the density of states on frequency has to smooth and slowly varying, at least in the vicinity of the resonance frequency  $\omega_{eg}$ .

## 1.2 Fundamentals of Cavity-QED

### 1.2.1 Field Quantization

It is straightforward to apply the same technique as in the open space case to quantize the electromagnetic field confined within a finite volume cavity. Specif-

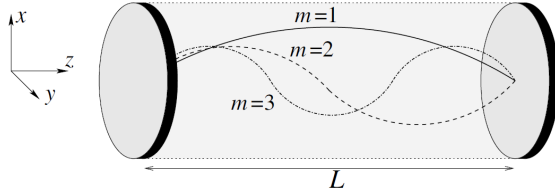


FIGURE 1.1: One-dimensional optical cavity of length  $L$  [1].

ically, let us consider a one-dimensional optical cavity with length  $L$ , as shown in Fig. 1.1. We assume the cavity has perfectly reflecting walls. Hence, the boundary condition is to require the electric field vanish on the walls. This will give a discrete spectrum as the solution of Maxwell equations. Now we have standing instead of running waves. The expressions for the fields now simplify to  $\mathbf{E}(\mathbf{r}, t) = \hat{\mathbf{e}} E(z, t) = \hat{x} E(z, t)$ , and  $\mathbf{B}(\mathbf{r}, t) = \hat{\mathbf{k}} \times \hat{\mathbf{e}} B(z, t) = \hat{y} B(z, t)$ . Imposing the boundary condition  $E(z = 0, t) = E(z = L, t) = 0$ , we find that the spatial eigenmodes take the form of  $\sin(k_m z)$ , where  $k_m = \pi m / L$ ,  $m = 1, 2, 3, \dots$ , with the frequencies  $\omega_m = ck_m$ . Now the quantized field in the  $k_m$  mode can be written as

$$\begin{aligned} E_m(z, t) &= \sqrt{\frac{\hbar\omega_m}{\epsilon_0 V}} [a_m e^{-i\omega_m t} + a_m^\dagger e^{i\omega_m t}] \sin(k_m z), \\ B_m(z, t) &= \frac{-i}{c} \sqrt{\frac{\hbar\omega_m}{\epsilon_0 V}} [a_m e^{-i\omega_m t} - a_m^\dagger e^{i\omega_m t}] \cos(k_m z), \end{aligned} \quad (1.9)$$

where  $V = SL$  is the mode volume with  $S$  being the transverse area. Again, the energy stored in the cavity field can be calculated as:

$$H = \sum_m \int_V dS dz \frac{1}{2} (\epsilon_0 \mathbf{E}_m^2 + \mu_0^{-1} \mathbf{B}_m^2) = \sum_m \hbar\omega_m (a_m^\dagger a_m + 1/2). \quad (1.10)$$

The integral  $\int dS \int_0^L \sin^2(k_m z) dz = S \cdot \frac{L}{2} = \frac{V}{2}$  is applied here.

### 1.2.2 Jaynes-Cummings Model

Now, let us consider the dipole interaction between an atom and the quantized field of a cavity. In particular, we assume that mode  $\omega_c$  is near resonant with the frequency  $\omega_{eg}$  of the atomic transition. Typically, the level space of the cavity modes is much larger than the width of the atomic level. Hence, the atom effectively interacts only with  $\omega_c$  mode, while all the other modes are decoupled from the atomic transition and can be safely neglected. With the dipole and rotating wave approximations, the total Hamiltonian of the system is described by the well-known Jaynes-Cummings model

$$\begin{aligned} H_{JC} &= H^A + H^F + H^{AF} \\ H^A &= \frac{1}{2}\hbar\omega_{eg}\sigma_z \\ H^F &= \hbar\omega_c a^\dagger a \\ H^{AF} &= \hbar g(\sigma_+ a + a^\dagger \sigma_-), \end{aligned} \tag{1.11a}$$

where  $g$  is the Rabi frequency defined in Eq.(1.7), and in this case is given by

$$g = d\sqrt{\omega/\hbar\epsilon_0 V} \sin(kz_0), \tag{1.12}$$

where  $d$  is the dipole matrix element, and  $z_0$  is the coordinate of the atom. From Eq. (1.12), we can see that the Rabi frequency can be very large if we make the cavity small enough or have a large dipole moment of the atom [2, 5].

With the losses taken into account, the system can be modeled by the following effective non-Hermitian Hamiltonian [1],

$$H_{eff} = H_{JC} - i\hbar\frac{1}{2}\Gamma' \sigma_+ \sigma_- - i\hbar\frac{1}{2}\kappa a^\dagger a, \tag{1.13}$$

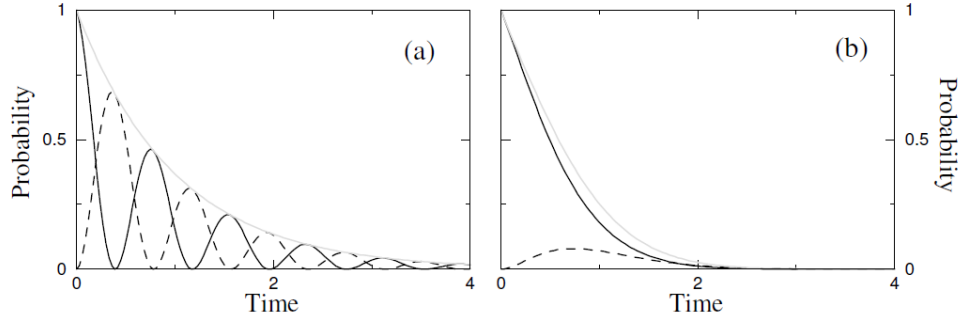


FIGURE 1.2: Dynamics of an initially excited two-level system coupled to a on-resonance cavity [1] for (a) strong coupling regime, and (b) weak coupling regime. Solid lines: probability of the atom to be in the excited state; Dashed lines: probability for the cavity to contain a single photon. Time is measured in units of  $\Gamma'^{-1}$

where the first term is defined in Eq. (1.11a), while the second and third terms describe the atomic and photonic relaxation, respectively. If we assume that initially the atom is excited and the cavity is in vacuum, as shown in Fig. 1.2(a) in the so-called strong coupling regime  $g > \Gamma', \kappa$ , the system undergoes damped coherent Rabi oscillations between the states  $|e, 0\rangle$  and  $|g, 1\rangle$ , both of which decay to the state  $|g, 0\rangle$  with rates  $\Gamma'$  and  $\kappa$ , respectively. The total population of the atom and the photon decays with the rate of  $\frac{1}{2}(\Gamma' + \kappa)$ . On the other hand, in the weak coupling regime as shown in Fig. 1.2(b),  $g \ll \Gamma', \kappa$ , the system is in the overdamped regime and simply decays exponentially into  $|g, 0\rangle$  without Rabi oscillations.

### 1.3 Fundamentals of Waveguide-QED

#### 1.3.1 Field Quantization

Now, let us consider a one-dimensional waveguide (for example, nanowire), which supports quantized travelling modes along the waveguide, as shown in Fig. 1.3. The transverse wave-vectors are discrete due to the boundary condition.



FIGURE 1.3: 1D waveguide with length  $L$ . The field is confined within  $R$  to the center in the transverse direction.

We choose one particular transverse mode  $k_{\perp}$ . The travelling mode  $k_{\parallel}$  can be written as  $\frac{2\pi n}{L}$ ,  $n = 1, 2, 3, \dots$ , where  $L$  is the length of the waveguide. For simplicity, we assume cylindrical geometry and the mode  $k_{\perp}$  is confined within the radius of  $R$  from the center.

Therefore, the electric field strength of the mode can be estimated from

$$\frac{\hbar\omega_k}{4} = \frac{1}{2}\epsilon_0 E^2 \cdot V_{\text{eff}}. \quad (1.14)$$

where  $V_{\text{eff}} = \pi R^2 L$  is the effective mode volume of  $k_{\perp}$ . This gives rise to the field strength as  $E = \sqrt{\hbar\omega_k / 2\epsilon_0 V_{\text{eff}}}$ . Therefore, the Rabi frequency can be estimated as

$$g(k) = \frac{d \cdot E}{\hbar} = d \sqrt{\frac{\omega_k}{2\hbar\epsilon_0 V_{\text{eff}}}}. \quad (1.15)$$

Notice that this formula takes essentially the same form as the cavity case in Eq. (1.12). However, in the cavity case, there is only one mode available; while in the waveguide case, there is in principle an infinite number of modes  $k_{\parallel} = \frac{2\pi n}{L}$ , in the limit of infinitely long waveguide,  $L \rightarrow \infty$ . Because of the existence of a continuum in the waveguide case, we can apply Fermi's golden rule to estimate

the decay rate into waveguide modes.

$$\begin{aligned}
\Gamma_{wg} &= \frac{2\pi}{\hbar} |\hbar g(\omega_{eg})|^2 \rho(E_{eg}) \\
&= \frac{2\pi}{\hbar^2} |\hbar g(\omega_{eg})|^2 \rho(\omega_{eg}) \\
&= 2\pi |g(\omega_{eg})|^2 \rho(\omega_{eg}) \\
&= 2\pi |g(\omega_{eg})|^2 (2L/2\pi) \frac{dk}{d\omega_k} \Big|_{\omega_{eg}} \\
&= \frac{d^2 \omega_{eg}}{\pi \epsilon_0 \hbar v_g R^2} \tag{1.16}
\end{aligned}$$

Here,  $v_g$  is the group velocity of the travelling mode.

We can define the effective Purcell factor by comparing the decay rate into the waveguide modes [Eq. (1.16)] and the decay rate into free space [Eq. (1.8)],

$$P \equiv \frac{\Gamma_{wg}}{\Gamma_e} = \frac{c^3}{\omega_{eg}^2 R^2 v_g}. \tag{1.17}$$

This Purcell factor  $P$  quantifies how the atomic excitation decays: in the limit  $P \rightarrow \infty$ , all the excitation will decay into the waveguide modes. Replacing  $\omega_{eg}$  by the corresponding wavelength,  $\omega_{eg} = \frac{2\pi c}{\lambda}$ , we obtain the following

$$P = \frac{1}{4\pi^2} \frac{\lambda^2 c}{R^2 v_g} \tag{1.18}$$

It is evident that a large Purcell factor is achievable via either subwavelength confinement of waveguide modes, i.e.  $R \leq \lambda$ , or a small group velocity, i.e.  $v_g \ll c$ .

### 1.3.2 Hamiltonian in Waveguide

With the 3D open space modes replaced by the 1D waveguide modes, we can write down the Hamiltonian corresponding to a two-level system dipole-coupled to a 1D waveguide

$$H_{wg} = \hbar\omega_{eg}\sigma_{ee} + \sum_k \hbar\omega_k a_k^\dagger a_k + \sum_k \hbar g(k) (\sigma_- a_k^\dagger + \sigma_+ a_k), \quad (1.19)$$

where  $\sigma_{ee} = |e\rangle\langle e|$ ,  $\sigma_- = |g\rangle\langle e|$ ,  $\sigma_+ = |e\rangle\langle g|$ , and we have set the ground state energy as the reference energy, i.e.  $E_g = 0$ .  $g(k)$  is the Rabi frequency defined in Eq. (1.15).

Next, we want to rewrite the above Hamiltonian in terms of integration in  $k$ -space. The conversion from summation to integration can be done via the following transformations

$$\begin{aligned} \sum_k &\rightarrow \frac{L}{2\pi} \int_{-\infty}^{\infty} dk, \\ a_k^\dagger &\rightarrow \sqrt{\frac{2\pi}{L}} a^\dagger(k), \\ \delta_{kk'} &\rightarrow \frac{2\pi}{L} \delta(k - k'). \end{aligned} \quad (1.20)$$

Using Eq. (1.20), we may rewrite the Hamiltonian in Eq. (1.19) in the following form

$$H_{wg} = \hbar\omega_{eg}\sigma_{ee} + \int dk \hbar\omega_k a^\dagger(k) a(k) + \int dk \hbar g(k) \sqrt{\frac{L}{2\pi}} [\sigma_- a^\dagger(k) + \sigma_+ a(k)]. \quad (1.21)$$

For the problem of a two-level system interacting with a continuum of waveguide modes, only the states near the resonant energy  $\hbar\omega_{eg}$  are essential for the

dynamics of the system, as shown in Fig. 1.4. In particular, the vacuum fluctuation in the waveguide will give a radiative correction to the energy-level of the excited state of the atom known as the *Lamb shift* [12]. That is the only allowed renormalization process under the rotating wave approximation, which is valid when the level width  $\Gamma_{wg} \ll \omega_{eg}$ . We absorb this frequency shift into  $\omega_{eg}$  in all the following calculations. Therefore, we may use the following approximations to simplify the above Hamiltonian:

- Linearize the spectrum over the relevant frequency range:  $\omega_k \approx v_g|k|$  (similar to what has been done in 1D Tomonaga-Luttinger model [49]);
- Assume a frequency-independent coupling matrix element:  $g(k) \equiv g$ ;
- Completely separate left- and right-moving photon fields with vanishing commutators;

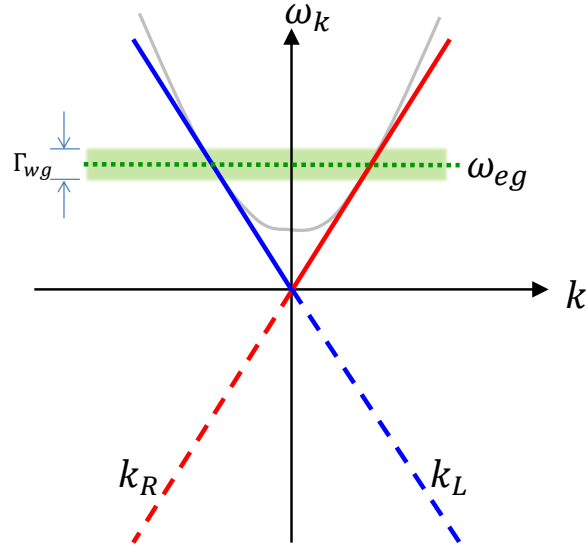


FIGURE 1.4: Linearized dispersion relation in a 1D waveguide. Only the states close to  $\omega_{eg}$  (within a width  $\Gamma_{wg}$ ) are important for the dynamics of the system. Both the left-moving (blue solid line) and the right-moving (red solid line) fields are extended to negative energy range (blue dash and red dash lines).

- Extend the range of the wave vector of left (right)-moving field  $k_L$  ( $k_R$ ) from  $[-\infty, 0]$  ( $[0, \infty]$ ) to  $[-\infty, \infty]$ . In principle, this allows for the existence of negative-energy modes, seeming to make the system ill-defined. However, it is not important because we consider only the dynamics near-resonant with the two-level system. It only affects the cutoff in the integral of the *Lamb shift*, which is already absorbed into  $\omega_{eg}$ .

Under these approximations, the relevant terms in Eq. (1.21) are transformed as

$$\begin{aligned}
\int_{-\infty}^{\infty} dk \hbar \omega_k a^\dagger(k) a(k) &\rightarrow \int_{-\infty}^{\infty} dk \hbar v_g |k| a^\dagger(k) a(k) \\
&\rightarrow \int_0^{\infty} dk \hbar v_g k \left( a_R^\dagger(k) a_R(k) + a_L^\dagger(-k) a_L(-k) \right) \\
&\rightarrow \int_{-\infty}^{\infty} dk \hbar v_g k \left( a_R^\dagger(k) a_R(k) + a_L^\dagger(-k) a_L(-k) \right) \\
&\rightarrow \int_{-\infty}^{\infty} dk \hbar v_g k \left( a_R^\dagger(k) a_R(k) - a_L^\dagger(k) a_L(k) \right), \tag{1.22}
\end{aligned}$$

$$\begin{aligned}
\int_{-\infty}^{\infty} dk \hbar g(k) \sqrt{\frac{L}{2\pi}} (\sigma_- a^\dagger(k) + \sigma_+ a(k)) \\
&\rightarrow \int_0^{\infty} dk \hbar g \sqrt{\frac{L}{2\pi}} \left( \sigma_- [a_R^\dagger(k) + a_L^\dagger(-k)] + \sigma_+ [a_R(k) + a_L(-k)] \right) \\
&\rightarrow \int_{-\infty}^{\infty} dk \hbar g \sqrt{\frac{L}{2\pi}} \left( \sigma_- [a_R^\dagger(k) + a_L^\dagger(-k)] + \sigma_+ [a_R(k) + a_L(-k)] \right) \\
&\rightarrow \int_{-\infty}^{\infty} dk \hbar g \sqrt{\frac{L}{2\pi}} \left( \sigma_- [a_R^\dagger(k) + a_L^\dagger(k)] + \sigma_+ [a_R(k) + a_L(k)] \right). \tag{1.23}
\end{aligned}$$

Collecting all the pieces together, we have the following approximate Hamiltonian:

nian for the 1D waveguide-QED system,

$$\begin{aligned}
H_{wg} &= \hbar\omega_{eg}\sigma_{ee} + \int dk \hbar v_g |k| a^\dagger(k) a(k) + \hbar g \sqrt{\frac{L}{2\pi}} \int dk (\sigma_- a^\dagger(k) + \sigma_+ a(k)) \\
&= \hbar\omega_{eg}\sigma_{ee} + \int_{-\infty}^{\infty} dk \hbar v_g k (a_R^\dagger(k) a_R(k) - a_L^\dagger(k) a_L(k)) \\
&\quad + \hbar g_{\text{eff}} \int dk \left( \sigma_- [a_R^\dagger(k) + a_L^\dagger(k)] + h.c. \right), \tag{1.24}
\end{aligned}$$

where  $g_{\text{eff}}$  is given by,

$$\begin{aligned}
g_{\text{eff}} &= g \sqrt{\frac{L}{2\pi}} = \sqrt{\frac{L}{2\pi} d} \sqrt{\frac{\omega_{eg}}{2\hbar\epsilon_0 V_{\text{eff}}}} \\
&= d \sqrt{\frac{\omega_{eg}}{4\pi^2\epsilon_0\hbar R^2}}. \tag{1.25}
\end{aligned}$$

Next, we want to transform the continuous model in  $k$ -space to real space via Fourier transformation,

$$\begin{aligned}
a_{L/R}(x) &= \frac{1}{\sqrt{2\pi}} \int dk e^{ikx} a_{L/R}(k), \\
a_{L/R}(k) &= \frac{1}{\sqrt{2\pi}} \int dx e^{-ikx} a_{L/R}(x). \tag{1.26}
\end{aligned}$$

Using the above transformation, we end up with the real-space Hamiltonian

$$\begin{aligned}
H_{wg} &= \hbar\omega_{eg}\sigma_{ee} + \int dx \hbar v_g \left[ a_R^\dagger(x) \left( -i \frac{d}{dx} \right) a_R(x) - a_L^\dagger(x) \left( -i \frac{d}{dx} \right) a_L(x) \right] \\
&\quad + \hbar V_{\text{eff}} \int dx \delta(x) \left( \sigma_- [a_R^\dagger(x) + a_L^\dagger(x)] + h.c. \right), \tag{1.27}
\end{aligned}$$

where  $V_{\text{eff}} = \sqrt{2\pi} g_{\text{eff}}$  is the coupling strength.

### 1.3.3 Loss

Finally, we want to introduce loss into our Hamiltonian. A non-Hermitian term  $(-i\hbar\Gamma'/2)\sigma_{ee}$  can be included to describe the decay of the excited state  $|e\rangle$  at a rate  $\Gamma'$  into other channels. This was first introduced in a “quantum jump” description of an open system [50].

$$\begin{aligned} H_{wg} = & \hbar \left( \omega_{eg} - \frac{i\Gamma'}{2} \right) \sigma_{ee} + \int dx \hbar v_g(-i) \left[ a_R^\dagger(x) \frac{da_R(x)}{dx} - a_L^\dagger(x) \frac{da_L(x)}{dx} \right] \\ & + \hbar V_{\text{eff}} \int dx \delta(x) \left( \sigma_- \left[ a_R^\dagger(x) + a_L^\dagger(x) \right] + h.c. \right). \end{aligned} \quad (1.28)$$

This Hamiltonian is a basis for all of our subsequent studies. In quantum optics, the  $\Gamma'$  term is called diagonal relaxation because it determines how fast the diagonal term  $\rho_{ee}$  of the atomic density operator decays. There is another term  $\Gamma_{\text{phase}}$  not included here, which accounts for all other possible mechanisms (other than  $\Gamma'$ ) of coherent relaxation of the atom which do not affect the populations. Together, the coherence relaxation rate can be expressed as  $\gamma_{eg} = \frac{\Gamma'}{2} + \Gamma_{\text{phase}}$ , which is also called off-diagonal relaxation because it determines the decay of the off-diagonal term  $\rho_{eg}$  of the atomic density operator. Often  $\Gamma'$  is denoted by  $1/T_1$  and  $\gamma_{eg}$  by  $1/T_2$ , where  $T_1$  and  $T_2$  are the corresponding relaxation times [1]. In principle, one could also include a non-Hermitian term  $-i\hbar\kappa a^\dagger(k)a(k)$  to describe the loss of photons. Here, for simplicity, we assume that we have a low-loss waveguide such that photonic loss can be neglected.

## 1.4 Survey of Experimental Systems

Recently, there has been tremendous experimental progress in both cavity-QED (circuit-QED in particular) and waveguide-QED systems.

Table 1.1: Cavity-QED experiments which have achieved the strong coupling regime.  $g$  : Rabi frequency.  $\kappa$  : cavity photon loss rate.  $\Gamma'$  : atom decay rate.  $\kappa$  and  $\Gamma'$  are in the same unit as  $g$ .  $Q$  : cavity quality factor. SC: superconducting; QD: quantum dot; PC: photonic crystal; TL: transmission line.

Expt. (year)	Cavity	Atom	$\frac{g}{2\pi}$	$\frac{\kappa}{2\pi}$	$\frac{\gamma}{2\pi}$	$Q$
[5] ('92)	optical cavity	Cs atom	3.2 MHz	2.5	0.9	$8 \times 10^4$
[53] ('96)	SC cavity	Rydberg atom	25 kHz	NA	NA	$7 \times 10^7$
[6] ('04)	microcavity	QD	$140 \mu eV$	100	1-10	8800
[54] ('04)	optical cavity	Cs atom	34 MHz	4.1	2.6	$9 \times 10^7$
[55] ('07)	PC nanocavity	QD	3 GHz	3.8	1.4	13300
[7] ('09)	optical cavity	Trapped ions	0.53 MHz	2.15	11.15	3000
[51] ('04)	SC TL	Cooper pair box	6 MHz	0.8	0.7	7500
[3] ('09)	SC TL	Transmon qubit	173 MHz	0.3	$\sim 0.8$	23000

#### 1.4.1 Cavity-QED Experiments

As mentioned above, the interesting “strong coupling regime” of cavity QED is achieved when the rate of absorption or emission of a single photon by the atom is larger than any of the rates of loss, i.e.,  $g > \kappa, \gamma$ . In this case, an excited atom in an initially empty cavity will emit one photon, which will then be trapped and reabsorbed again at rate  $2g$ . This is known as vacuum Rabi oscillations. As shown in Table 1.1, strong coupling has been demonstrated in a number of cavity-QED experimental systems including natural atoms trapped in an optical cavity [5], semiconductor quantum dots trapped in a microcavity [6], trapped ions [7], and superconducting qubits coupled to a coplanar transmission line [2, 51, 52].

The signal of “strong coupling regime” is the emergence of vacuum Rabi splitting in the transmission spectrum, as shown in Fig. 1.5. This is a circuit-QED experiment with microwave photons in a superconducting transmission line resonator, interacting with a superconducting transmon qubit [3]. In this experiment, they achieved  $g/\kappa \approx 576$ , and  $g/\gamma \approx 216$ , deep into the strong coupling regime. As a result, the transmission peaks from Rabi splitting can be

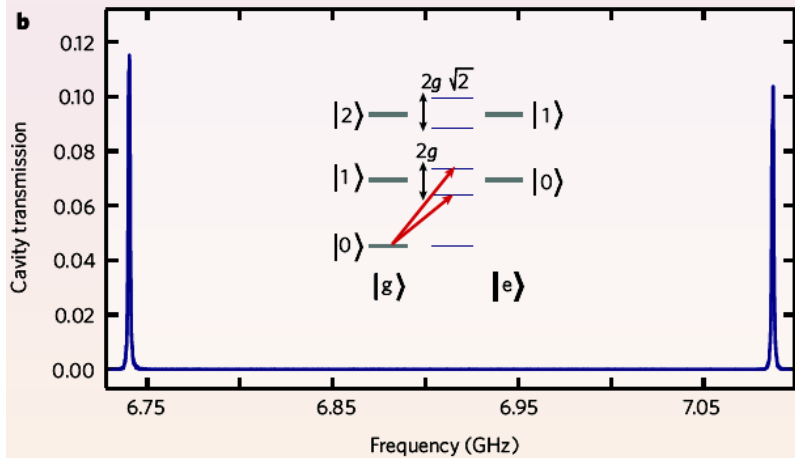


FIGURE 1.5: Vacuum Rabi splitting in circuit-QED from Ref.[2, 3]. There are clearly two resolved peaks in the cavity transmission spectrum. The inset shows the Jaynes-Cummings ladder of the eigenspectrum.

clearly identified in the cavity transmission spectrum. This spectacular achievement of circuit-QED originates from two underlying reasons. First, the cavity is a 1D transmission line with tight confinement of fields in the transverse direction, dramatically reducing the mode volume. Second, the transmon qubit is a macroscopic object with orders of magnitude higher dipole moment than real atoms.

#### 1.4.2 Waveguide-QED Experiments

Recently, there has been great effort to reach the strong coupling regime in 1D waveguide systems, which means the effective Purcell factor  $P$  defined in Eq.(1.17) is much larger than 1. Promising candidate systems include photonic crystal waveguides [47], plasmonic nanowires [17], hollow core fibres [41], tapered nanofibres [56], semiconductor or diamond nanowires [43, 45], and 1D open superconducting transmission lines [44, 46, 48, 57, 58]. The pioneering work was done in a plasmonic nanowire system [17]. Due to the subwavelength confinement of the plasmonic field inside the wire, the decay rate into

Table 1.2: Waveguide-QED Experiments. Purcell factor  $P$  is defined as  $P = \frac{\Gamma_{wg}}{\Gamma_e}$ , where  $\Gamma_{wg}$  and  $\Gamma_e$  are the atomic decay rates into the waveguide modes and other modes, respectively. NV: nitrogen vacancy. QD: quantum dot. PCF: photonic-crystal fiber. PC: photonic crystal. SC: superconducting.

Expt. (year)	Waveguide	Atom	$P$
[17] ('07)	silver nanowire	CdSe QD	$\frac{60\%}{40\%} = 1.5$
[42] ('10)	diamond nanowire	NV center	$\geq \frac{40\%}{60\%} \approx 0.67$
[41] ('09)	hollow-core PCF	Rb atoms	1%~10%
[43] ('10)	GaAs nanowire	InAs QD	$\frac{90\%}{10\%} = 9$
[44] ('10)	transmission line	SC flux qubit	3
[47] ('12)	PC waveguide	QD	5.7 ~ 24
[46] ('11)	SC transmission line	SC transmon qubit	$\geq 15$

the nanowire is strongly enhanced. However, plasmonic wires are very lossy due to the Ohmic loss during the plasmon propagation and this severely limits the potential of plasmonic systems. Later on, Claudon et al. [43] used a low loss photonic nanowire with the quantum dot embedded inside the wire. As a result, most of the spontaneous emission from the quantum dot is collected inside the nanowire. They are able to achieve a Purcell factor of 9. Recently, exciting progress has been made in photonic crystal waveguides [47] and 1D open superconducting transmission line [46, 48]. A Purcell factor larger than 15 has been realized. As a summary, Table 1.2 is a non-exhaustive list of recent waveguide-QED experiments.

The tremendous progress in waveguide-QED experiments makes the observations of several nonlinear quantum optical effects possible, as we will show in the first part of this thesis. In Chapter 2, we study a two-level system (TLS) coupled to a one-dimensional waveguide. Photon-photon bound states appear in multi-photon scattering due to the coupling between TLS and the waveguide. Such bound states cause several interesting effects: enhanced multiphoton transmission, spectral entanglement, photon bunching and antibunching and

generation of nonclassical light. In Chapter 3, we study the coupling of the waveguide to a three-level or four-level system. Effective repulsive or attractive interaction between photons can be produced, giving rise to either suppressed multiphoton transmission—photon blockade—or enhanced multiphoton transmission—photon-induced tunneling. As a result, a sub-Poissonian single-photon source can be generated on demand. In Chapter 4, we study the system of a one-dimensional waveguide coupled to two qubits with an arbitrary separation. This system is important because it is the minimal system toward scalable quantum networks using waveguide-QED. We demonstrate that non-Markovian processes give rise persistent quantum beats in photon correlation, and long-distance entanglement between the two qubits, increasing the potential of waveguide-QED systems for scalable quantum networks.

The second part of this thesis includes two applications of waveguide-QED in quantum information processing. In Chapter 5, we investigate a decoy-state quantum key distribution (QKD) scheme with a sub-Poissonian single-photon source generated by scattering a coherent state off a two-level system in a one-dimensional waveguide. We find that there is a substantial increase in the key generation rate compared to both weak coherent state and heralded single-photon decoy-state QKD. Furthermore, the performance is robust against either parameter variation or loss in the system, making it a promising candidate for future QKD systems. In Chapter 6, we propose a new scheme for photonic quantum computation using flying qubits—propagating photons in a one-dimensional waveguide interacting with matter qubits. We show that high gate fidelity is possible given recent dramatic experimental progress in superconducting circuits and photonic-crystal waveguides. The proposed system can be an important building block for future on-chip quantum networks.

## 2

# Photon-Photon Bound States in Waveguide-QED and Scattering of Fock and Coherent States off a Two-Level System

*Summary:* <sup>1</sup>Strong coupling between a two-level system (TLS) and bosonic modes produces dramatic quantum optics effects. We consider a one-dimensional continuum of bosons coupled to a single localized TLS, a system which may be realized in a variety of plasmonic, photonic, or electronic contexts. We present the exact many-body scattering eigenstate obtained by imposing open boundary conditions. Photon-photon bound states appear in the scattering of two or more photons due to the coupling between the photons and the TLS. Here, the terminology “photon-photon bound states” was introduced for multi-photon correlated states that can not be described by plane waves: their amplitudes decay exponentially as a function of relative coordinates of photons. They are different

---

<sup>1</sup> Part of the text of this chapter has been adapted from the following previously published article: Huaixiu Zheng, Daniel J. Gauthier, and Harold U. Baranger, “Waveguide QED: Many-body bound-state effects in coherent and Fock-state scattering from a two-level system”, *Phys. Rev. A* **82**, 063816 (2010).

from the “bound states” of a discrete energy spectrum, states in which particles are localized in a finite region and can not escape to infinity [59]. Such photon-photon bound states are shown to have a large effect on scattering of both Fock- and coherent-state wave packets. We compare the statistics of the transmitted light with a coherent state having the same mean photon number: as the interaction strength increases, the one-photon probability is suppressed rapidly, and the two- and three-photon probabilities are greatly enhanced due to the many-body bound states. This results in non-Poissonian light.

## 2.1 Introduction

Recently, there has been increasing interest in designing quantum optical elements based on the strong coupling between light and matter in waveguide-QED [38, 46, 60, 61, 62, 63, 64, 65, 66, 67, 68, 69, 70, 71, 72]. Several experimental systems have been proposed for realizing devices such as a single-photon transistor [62, 66] or a quantum switch [64, 65, 73], including surface plasmons coupled to a single two-level emitter [62], a superconducting transmission line resonator coupled to a local superconducting charge qubit [64, 65], and propagating photons in a 1D waveguide coupled to a two-level system [74, 75]. Most of the theoretical work in waveguide-QED focuses on a single-photon coupled to a local quantum system modeled as a two-level system (TLS). The key property used in the device proposals is that, if the energy of the incident photon is tuned to be on resonance with the TLS, the system will block the transmission of photons due to destructive interference between the directly transmitted photon and the photon reemitted by the impurity [62, 64].

A more challenging task is to study the two or more photon scattering problem in such systems. The two or more photon problem has been addressed

by using a generalized Bethe-ansatz [74, 75], an auxiliary-state method [76, 77], an input-output formalism [78], Fock-state master equation [79], and a Green-function approach [80, 81]. They showed that photon-photon bound states emerge as the photons interact with the two-level system. It is worth to mention that they are different from the “bound states” with a discrete energy spectrum, states in which particles are localized in a finite region and can not escape to infinity [59]. Effective attractive and repulsive interactions can be induced depending on the energy of the photons [74]. Such effective interactions between photons may provide new avenues for controlling photon entanglement [82]. However, the scattering eigenstates were not constructed explicitly in Ref. [75]: the bound states were found by first constructing Bethe-type scattering eigenstates and then deducing the bound states via the completeness of the basis. It is difficult to generalize the method in Ref. [75] to solve the three-photon (or more) scattering problem or scattering off systems with more complicated level structure in which we expect more complicated and interesting photon correlations.

We present a method to explicitly construct exact  $n$ -photon scattering eigenstates and then use the eigenstates to analyze the scattering of Fock- and coherent-state wavepackets. The system consists of a 1D bosonic continuum coupled to a local two-level-system as shown in Fig. 2.1. First, we explicitly construct the  $n$ -photon ( $n = 1$  to 4) scattering eigenstates by imposing open boundary conditions while requiring that the incoming wavefunctions consist entirely of plane waves [83, 84]. In addition to two-photon bound states, three-photon bound states appear in the three-photon scattering eigenstates, and likewise  $n$ -photon bound states appear in the  $n$ -photon scattering eigenstates. Second, to show the significance of these bound states in the scattering of practical light sources, we study the scattering of one-, two-, and three-photon Fock state wavepackets. It

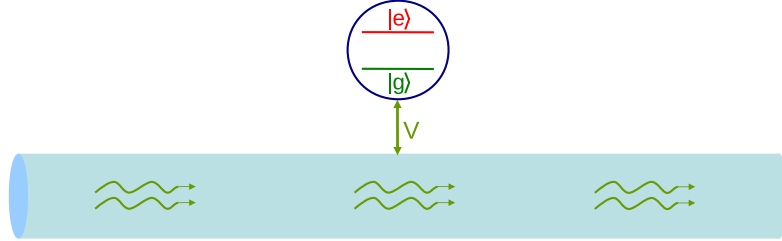


FIGURE 2.1: Sketch of the structure considered: a 1D continuum of bosons coupled to a two-level-system with ground state  $|g\rangle$  and excited state  $|e\rangle$ .

is shown that the two- and three-photon bound states dramatically enhance the transmission of two- and three-photon wavepackets, respectively. Thirdly, we compute the spectral entanglement in the two-photon scattering, and show that the photons in the transmitted field are spectrally entangled. Finally, we study the scattering of coherent states to determine the impact of the bound states on both the photon correlation and the statistics of the transmitted and reflected photons. Strong bunching and antibunching effects appear, and the statistics are non-Poissonian.

## 2.2 Model Hamiltonian

The system we study consists of a two-level system coupled to photons propagating in both directions in a one-dimensional waveguide [74, 75, 67]. The system is modeled by the Hamiltonian [74]

$$H = \int dx \frac{1}{i} \left[ a_R^\dagger(x) \frac{d}{dx} a_R(x) - a_L^\dagger(x) \frac{d}{dx} a_L(x) \right] + \left( \epsilon - \frac{i\Gamma'}{2} \right) |e\rangle \langle e| + \int dx V \delta(x) \left\{ [a_R^\dagger(x) + a_L^\dagger(x)] S^- + h.c. \right\}, \quad (2.1)$$

where  $a_R^\dagger(x)/a_L^\dagger(x)$  is the creation operator for a right-going/left-going photon at position  $x$ ,  $\epsilon$  is the level splitting between the ground state  $|g\rangle$  and the excited state  $|e\rangle$  of the two level system,  $\Gamma'$  is the decay rate into channels other than the 1D continuum,  $V$  is the frequency-independent coupling strength, and  $S^- = |g\rangle\langle e|$  is the atomic lowering operator. Throughout this chapter, we set the group velocity  $c$  and Plank's constant  $\hbar$  to 1 for simplicity.

It is natural to transform to modes which are either even or odd about the origin,  $a_{e/o}^\dagger(x) \equiv [a_R^\dagger(x) \pm a_L^\dagger(-x)]/\sqrt{2}$ . The Hamiltonian (2.1) is then decomposed into two decoupled modes:  $H = H_e + H_o$  with

$$\begin{aligned} H_e &= \int dx \frac{1}{i} a_e^\dagger(x) \frac{d}{dx} a_e(x) + (\epsilon - i\Gamma'/2) |e\rangle\langle e| + \int dx \bar{V} \delta(x) [a_e^\dagger(x) S^- + h.c.], \\ H_o &= \int dx \frac{1}{i} a_o^\dagger(x) \frac{d}{dx} a_o(x), \end{aligned} \quad (2.2)$$

where the effective coupling strength becomes  $\bar{V} = \sqrt{2}V$ . Note that the odd mode is free. The number operator for even bosons is  $n_e = \int dx a_e^\dagger(x) a_e(x)$ , that for the odd bosons is  $n_o = \int dx a_o^\dagger(x) a_o(x)$ , and the occupation number of the two-level system is  $n_{tls} = |e\rangle\langle e|$ . Because  $H$  commutes with certain number operators,  $[H, n_e + n_{tls}] = [H, n_o] = 0$ , the total number of excitations in both the even and odd spaces are separately conserved. We will now focus on finding the non-trivial even-mode solution and then transform back to the left/right representation.

## 2.3 Analytical Solution of Scattering Eigenstates

A  $n$ -excitation state ( $n = n_e + n_{tls}$ ) is given by

$$\begin{aligned} |\psi_n\rangle &= \int dx_1 \cdots dx_n g_n(x_1, \dots, x_n) a_e^\dagger(x_1) \cdots a_e^\dagger(x_n) |0, g\rangle \\ &+ \int dx_1 \cdots dx_{n-1} e_n(x_1, \dots, x_{n-1}) a_e^\dagger(x_1) \cdots a_e^\dagger(x_{n-1}) |0, e\rangle, \end{aligned} \quad (2.3)$$

where  $|0, g\rangle$  is the zero photon state with the atom in the ground state. From  $H_e|\psi_n\rangle = E_n|\psi_n\rangle$ , we obtain the Schrödinger equations

$$\begin{aligned} &\left[ \frac{1}{i}(\partial_1 + \cdots + \partial_n) - E_n \right] g_n(x_1, \dots, x_n) \\ &+ \frac{\bar{V}}{n} \left[ \delta(x_1) e_n(x_2, \dots, x_n) + \cdots + \delta(x_n) e_n(x_1, \dots, x_{n-1}) \right] = 0, \\ &\left[ \frac{1}{i}(\partial_1 + \cdots + \partial_{n-1}) - E_n + \epsilon - i\Gamma'/2 \right] e_n(x_1, \dots, x_{n-1}) + n\bar{V}g_n(0, x_1, \dots, x_{n-1}) = 0, \end{aligned} \quad (2.4)$$

where the eigenvalue  $E_n = k_1 + k_2 + \cdots + k_n$ , and  $g_n(x_1, \dots, x_n)$  is discontinuous at  $x_i = 0$ ,  $i = 1, \dots, n$ . In all the following calculations, we set  $g_n(0, x_1, \dots, x_{n-1}) = [g_n(0^+, x_1, \dots, x_{n-1}) + g_n(0^-, x_1, \dots, x_{n-1})]/2$  [83, 84]. The scattering eigenstates  $g_n(x_1, \dots, x_n)$  and  $e_n(x_1, \dots, x_{n-1})$  are constructed by imposing the boundary condition that, in the incident region,  $g_n(x_1, \dots, x_n)$  is free-bosonic plane wave. That is to say, for  $x_1, \dots, x_n < 0$ ,

$$g_n(x_1, \dots, x_n) = \frac{1}{n!} \sum_Q h_{k_1}(x_{Q_1}) \cdots h_{k_n}(x_{Q_n}), \quad (2.5a)$$

$$h_k(x) = \frac{1}{\sqrt{2\pi}} e^{ikx}. \quad (2.5b)$$

For  $n = 1$ , plane-wave solutions are sufficient to satisfy Eq. (2.4) with eigenenergy  $E = k$ :

$$g_1(x) = g_k(x) = h_k(x)[\theta(-x) + \bar{t}_k\theta(x)], \quad (2.6a)$$

$$e_1 = \frac{i}{2\sqrt{\pi}V}(\bar{t}_k - 1), \quad (2.6b)$$

$$\bar{t}_k = \frac{k - \epsilon + i\Gamma'/2 - i\Gamma/2}{k - \epsilon + i\Gamma'/2 + i\Gamma/2}, \quad (2.6c)$$

where  $\theta(x)$  is the step function and  $\Gamma = \bar{V}^2 = 2V^2$  is the spontaneous emission rate from the two-level-system to the 1D continuum. Note that  $\bar{t}_k$  is the transmission coefficient for the even problem; because the even mode is chiral,  $|\bar{t}_k| = 1$  when  $\Gamma' = 0$ .

For  $n = 2$ , plane-wave solutions are not sufficient to satisfy Eq. (2.4). As discussed by Shen and Fan [74, 75], a two-photon bound state<sup>2</sup> must be included to guarantee the completeness of the basis. Here, instead of extracting the bound state through a completeness check [74, 75], we construct the scattering eigenstate explicitly and find a two-photon bound state contribution to the solution, as has been done in the open interacting resonant-level model [83]. We require the two-photon solution to satisfy Eq. (2.5a) in the region  $x_1, x_2 < 0$  and solve for the solution in other regions using Eq. (2.4). This method of constructing scattering eigenstates can be generalized to three-, four-, and even more photon cases.

---

<sup>2</sup> They are *not* the conventional “bound states” with a discrete energy spectrum that is not degenerate with any continuum states. In traditional bound states, particles subjected to a potential are localized in a finite region and can not escape to infinity [59]. Here, our photon-photon bound states are scattering states extending to infinity and they decay exponentially only in the relative coordinate of the two photons.

The equations of motion for the two-photon case read

$$\left[ \frac{1}{i}(\partial_1 + \partial_2) - E_2 \right] g_2(x_1, x_2) + \frac{\bar{V}}{2} \left[ \delta(x_1)e_2(x_2) + \delta(x_2)e_2(x_1) \right] = 0, \quad (2.7a)$$

$$\left[ \frac{1}{i} \frac{d}{dx} - E_2 + \epsilon - i\Gamma'/2 \right] e_2(x) + 2\bar{V}g_2(0, x) = 0, \quad (2.7b)$$

which can be cast into the following set of equations

$$\left[ \frac{1}{i}(\partial_1 + \partial_2) - E_2 \right] g_2(x_1, x_2) = 0, \quad (2.8a)$$

$$e_2(x) = \frac{2i}{\bar{V}} [g_2(0^+, x) - g_2(0^-, x)], \quad (2.8b)$$

$$\left[ \frac{1}{i} \frac{d}{dx} - E_2 + \epsilon - i\Gamma'/2 \right] e_2(x) + \bar{V}[g_2(0^+, x) + g_2(0^-, x)] = 0, \quad (2.8c)$$

$$e_2(0^+) = e_2(0^-). \quad (2.8d)$$

Here,  $g_2(x_1, x_2)$  is discontinuous at  $x_1 = 0, x_2 = 0$  and we set  $g_2(x, 0) = [g_2(x, 0^+) + g_2(x, 0^-)]/2$ . We eliminate  $e_2(x)$  from the above equations and obtain

$$\left[ \frac{1}{i}(\partial_1 + \partial_2) - E_2 \right] g_2(x_1, x_2) = 0, \quad (2.9a)$$

$$\begin{aligned} & \left[ \frac{1}{i} \frac{d}{dx} - E_2 + \epsilon - i\Gamma'/2 - i\Gamma/2 \right] g_2(0^+, x) \\ &= \left[ \frac{1}{i} \frac{d}{dx} - E_2 + \epsilon - i\Gamma'/2 + i\Gamma/2 \right] g_2(0^-, x), \end{aligned} \quad (2.9b)$$

$$g_2(0^+, 0^+) - g_2(0^-, 0^+) = g_2(0^-, 0^+) - g_2(0^-, 0^-). \quad (2.9c)$$

Because of the bosonic symmetry, we can solve for  $g_2(x_1, x_2)$  by first considering the half space  $x_1 \leq x_2$  and then extending the result to the full sapce. In this case, there are three quadrants in real space: ①  $x_1 \leq x_2 < 0$ ; ②  $x_1 < 0 < x_2$ ; ③

$0 < x_1 \leq x_2$ . Eq. (2.9b) can be rewritten as two separate equations

$$\begin{aligned} \left[ \frac{1}{i} \frac{d}{dx} - E_2 + \epsilon - i\Gamma'/2 - i\Gamma/2 \right] g_2^{(2)}(x, 0^+) = \\ \left[ \frac{1}{i} \frac{d}{dx} - E_2 + \epsilon - i\Gamma'/2 + i\Gamma/2 \right] g_2^{(1)}(x, 0^-), \text{ for } x < 0, \end{aligned} \quad (2.10a)$$

$$\begin{aligned} \left[ \frac{1}{i} \frac{d}{dx} - E_2 + \epsilon - i\Gamma'/2 - i\Gamma/2 \right] g_2^{(3)}(0^+, x) = \\ \left[ \frac{1}{i} \frac{d}{dx} - E_2 + \epsilon - i\Gamma'/2 + i\Gamma/2 \right] g_2^{(2)}(0^-, x), \text{ for } x > 0. \end{aligned} \quad (2.10b)$$

Substituting  $g_2^{(1)}(x_1, 0^-)$  [Eq. (2.5)] into Eq. (2.10a), we solve to find

$$g_2^{(2)}(x, 0^+) = \frac{1}{2!} \left[ \bar{t}_{k_2} \frac{e^{ik_1 x}}{2\pi} + \bar{t}_{k_1} \frac{e^{ik_2 x}}{2\pi} \right] + A e^{[-(\Gamma+\Gamma')/2+i(k_1+k_2-\epsilon)]x}, \quad (2.11)$$

where  $A$  is a constant to be determined. Applying the constraint Eq. (2.9a) to  $g_2^{(2)}(x, 0^+)$ , we obtain

$$g_2^{(2)}(x_1, x_2) = \frac{1}{2!} \left[ \bar{t}_{k_2} \frac{e^{i(k_1 x_1 + k_2 x_2)}}{2\pi} + \bar{t}_{k_1} \frac{e^{i(k_2 x_1 + k_1 x_2)}}{2\pi} \right] + A e^{[\frac{\Gamma+\Gamma'}{2}+i\epsilon](x_2-x_1)} e^{i(k_1+k_2)x_1} \quad (2.12)$$

From Eq. (2.12), we can identify  $A$  to be zero: otherwise, the solution is not normalizable [ $e^{(\Gamma+\Gamma')(x_2-x_1)/2}$  is divergent when  $x_2 - x_1 \rightarrow \infty$ ]. Hence,  $g_2(x_1, x_2)$  in region ② is given by

$$g_2^{(2)}(x_1, x_2) = \frac{1}{2!} \left[ \bar{t}_{k_2} \frac{e^{i(k_1 x_1 + k_2 x_2)}}{2\pi} + \bar{t}_{k_1} \frac{e^{i(k_2 x_1 + k_1 x_2)}}{2\pi} \right]. \quad (2.13)$$

Substituting Eq. (2.13) into Eq. (2.10b) yields

$$g_2^{(3)}(0^+, x) = \frac{1}{2!} \bar{t}_{k_1} \bar{t}_{k_2} \left[ \frac{e^{ik_2 x}}{2\pi} + \frac{e^{ik_1 x}}{2\pi} \right] + B e^{[-(\Gamma+\Gamma')/2+i(k_1+k_2-\epsilon)]x}, \quad (2.14)$$

where  $B$  is a constant to be determined. Again, applying the constraint Eq. (2.9a)

to  $g_2^{(3)}(0^+, x)$ , we obtain

$$g_2^{(3)}(x_1, x_2) = \frac{\bar{t}_{k_1} \bar{t}_{k_2}}{2!} \left[ \frac{e^{i(k_1 x_1 + k_2 x_2)}}{2\pi} + \frac{e^{i(k_1 x_2 + k_2 x_1)}}{2\pi} \right] + B e^{(-\frac{\Gamma+\Gamma'}{2}-i\epsilon)(x_2-x_1)} e^{i(k_1+k_2)x_2} \quad (2.15)$$

Finally,  $B$  is found by substituting Eq.(2.5), Eq.(2.13), and Eq.(2.15) into the continuity condition Eq.(2.9c), yielding

$$B = -\frac{(\bar{t}_{k_1} - 1)(\bar{t}_{k_2} - 1)}{2\pi}. \quad (2.16)$$

Extending these solutions from the half space to the full space using the bosonic symmetry gives rise to the two-photon scattering eigenstate with eigenenergy  $E = k_1 + k_2$

$$\begin{aligned} g_2(x_1, x_2) &= g_{k_1, k_2}(x_1, x_2) = \frac{1}{2!} \left[ \sum_Q g_{k_1}(x_{Q_1}) g_{k_2}(x_{Q_2}) \right. \\ &\quad \left. + \sum_{PQ} B_{k_{P_1}, k_{P_2}}^{(2)}(x_{Q_1}, x_{Q_2}) \theta(x_{Q_1}) \right], \end{aligned} \quad (2.17a)$$

$$e_2(x) = \frac{\sqrt{2}i}{V} [g_2(0^+, x) - g_2(0^-, x)], \quad (2.17b)$$

$$\begin{aligned} B_{k_{P_1}, k_{P_2}}^{(2)}(x_{Q_1}, x_{Q_2}) &\equiv -(\bar{t}_{k_{P_1}} - 1)(\bar{t}_{k_{P_2}} - 1) h_{k_{P_1}}(x_{Q_2}) h_{k_{P_2}}(x_{Q_2}) \\ &\quad \times e^{[-(\Gamma+\Gamma')/2-i\epsilon]|x_{Q_2}-x_{Q_1}|} \theta(x_{Q_2} - x_{Q_1}). \end{aligned} \quad (2.17c)$$

Here,  $P = (P_1, P_2)$  and  $Q = (Q_1, Q_2)$  are permutations of  $(1, 2)$  needed to account for the bosonic symmetry of the wavefunction.  $B_{k_{P_1}, k_{P_2}}^{(2)}(x_{Q_1}, x_{Q_2}) \theta(x_{Q_1})$  is the two-body bound-state term. The binding strength of the two photons depends on the total spontaneous emission rate  $\Gamma + \Gamma'$ . Conceptually, two photons have two ways of going through the TLS. One way is to pass by the TLS independently as plane waves and gain a phase factor, which is described by the first term of  $g_2(x_1, x_2)$ .

The other way is to bind together and form a bound state, which is described by the second term. The formation of the bound state can be viewed as a result of stimulated emission: the first photon excites the TLS and the passing of the second photon stimulates emission of the first photon into the same right-going state, hence producing the bound state. Such bound states are a manifestation of the photon-photon correlation induced by having two or more photons interact with the same atom: the TLS can only absorb one photon within the lifetime  $(\Gamma + \Gamma')^{-1}$ .

For  $n = 3$ , a procedure similar to that used to solve the  $n = 2$  case yields

$$\begin{aligned} g_3(x_1, x_2, x_3) &= g_{k_1, k_2, k_3}(x_1, x_2, x_3) = \frac{1}{3!} \left[ \sum_Q g_{k_1}(x_{Q_1}) g_{k_2}(x_{Q_2}) g_{k_3}(x_{Q_3}) \right. \\ &\quad \left. + \sum_{PQ} g_{k_{P_1}}(x_{Q_1}) B_{k_{P_2}, k_{P_3}}^{(2)}(x_{Q_2}, x_{Q_3}) \theta(x_{Q_2}) + \sum_{PQ} B_{k_{P_1}, k_{P_2}, k_{P_3}}^{(3)}(x_{Q_1}, x_{Q_2}, x_{Q_3}) \theta(x_{Q_1}) \right], \\ e_3(x_1, x_2) &= \frac{3i}{\sqrt{2V}} [g_3(0^+, x_1, x_2) - g_3(0^-, x_1, x_2)], \\ B_{k_{P_1}, k_{P_2}, k_{P_3}}^{(3)}(x_{Q_1}, x_{Q_2}, x_{Q_3}) &\equiv 2(\bar{t}_{k_{P_1}} - 1)(\bar{t}_{k_{P_2}} - 1)(\bar{t}_{k_{P_3}} - 1) \\ &\quad \times h_{k_{P_1}}(x_{Q_2}) h_{k_{P_2}}(x_{Q_3}) h_{k_{P_3}}(x_{Q_3}) e^{[-(\Gamma + \Gamma')/2 - i\epsilon]|x_{Q_3} - x_{Q_1}|} \theta(x_{Q_{32}}) \theta(x_{Q_{21}}), \end{aligned} \quad (2.18)$$

where  $P = (P_1, P_2, P_3)$  and  $Q = (Q_1, Q_2, Q_3)$  are permutations of  $(1, 2, 3)$  and  $\theta(x_{Q_{ij}}) = \theta(x_{Q_i}) - \theta(x_{Q_j})$  for short. In addition to the two-photon bound state, there emerges a three-body bound state  $B_{k_{P_1}, k_{P_2}, k_{P_3}}^{(3)}(x_{Q_1}, x_{Q_2}, x_{Q_3}) \theta(x_{Q_1})$  in the region  $x_1, x_2, x_3 > 0$ . Conceptually, there are three ways for the three photons to pass by the atom: (i) all three photons propagate as independent plane waves; (ii) two photons form a two-body bound state, while the other one propagates independently as a plane wave; and (iii) all three photons bind together and form a three-body bound state. These three processes are described by the first,

second, and third terms of  $g_3(x_1, x_2, x_3)$ , respectively.

This simple picture can be applied to a general  $n$ -photon scattering process. For example, in the case of four-photon scattering, there are five ways for the four photons to pass by the atom as illustrated in Figure 2.2: (i) all four propagate as independent plane waves; (ii) two photons form a two-body bound state, while the other two propagate independently as plane waves; (iii) three photons form a three-body bound state, while the other one propagate independently as a plane wave; (iv) four photons form two independent two-body bound states; and (v) four photons form a four-body bound state. These five processes can be identified as the five terms of  $g_4(x_1, x_2, x_3, x_4)$  in the four-photon solution, which

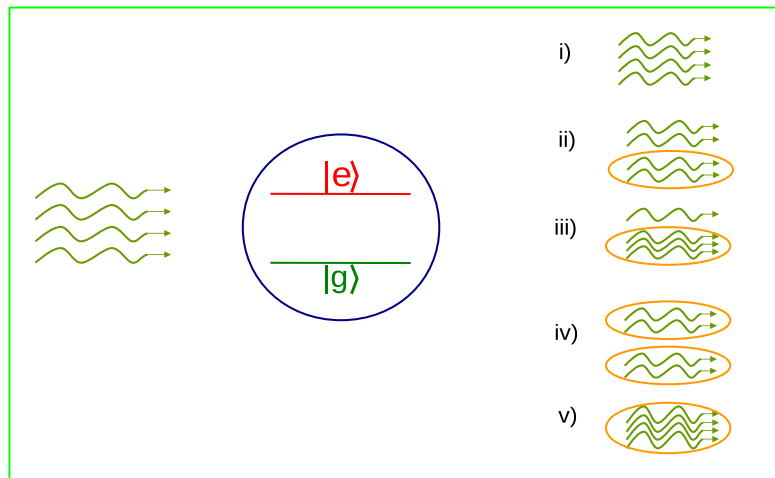


FIGURE 2.2: Schematic of different processes in four-photon scattering by a two-level system. The plane waves are represented by wiggly lines, while the many-body bound states are represented by the ovals.

is given by

$$\begin{aligned}
g_4(x_1, x_2, x_3, x_4) = & \frac{1}{4!} \left[ \sum_Q g_{k_1}(x_{Q1}) g_{k_2}(x_{Q2}) g_{k_3}(x_{Q3}) g_{k_4}(x_{Q4}) \right. \\
& + \sum_{PQ} g_{k_{P_1}}(x_{Q1}) g_{k_{P_2}}(x_{Q2}) B_{k_{P_3}, k_{P_4}}^{(2)}(x_{Q3}, x_{Q4}) \theta(x_{Q3}) \\
& + \sum_{PQ} g_{k_{P_1}}(x_{Q1}) B_{k_{P_2}, k_{P_3}, k_{P_4}}^{(3)}(x_{Q2}, x_{Q3}, x_{Q4}) \theta(x_{Q2}) \\
& + \sum_{PQ} B_{k_{P_1}, k_{P_2}}^{(2)}(x_{Q1}, x_{Q2}) B_{k_{P_3}, k_{P_4}}^{(2)}(x_{Q3}, x_{Q4}) \theta(x_{Q1}) \theta(x_{Q3}) \\
& \left. + \sum_{PQ} B_{k_{P_1}, k_{P_2}, k_{P_3}, k_{P_4}}^{(4)}(x_{Q1}, x_{Q2}, x_{Q3}, x_{Q4}) \theta(x_{Q1}) \right],
\end{aligned}$$

$$e_4(x_1, x_2, x_3) = \frac{4i}{\sqrt{2V}} [g_4(0^+, x_1, x_2, x_3) - g_4(0^-, x_1, x_2, x_3)],$$

$$\begin{aligned}
B_{k_{P_1}, k_{P_2}, k_{P_3}, k_{P_4}}^{(4)}(x_{Q1}, x_{Q2}, x_{Q3}, x_{Q4}) \equiv & -2^2 (\bar{t}_{k_{P_1}} - 1) (\bar{t}_{k_{P_2}} - 1) (\bar{t}_{k_{P_3}} - 1) (\bar{t}_{k_{P_4}} - 1) \\
& \times h_{k_{P_1}}(x_{Q2}) h_{k_{P_2}}(x_{Q3}) h_{k_{P_3}}(x_{Q4}) h_{k_{P_4}}(x_{Q4}) \\
& \times e^{[-(\Gamma + \Gamma')/2 - i\epsilon]|x_{Q4} - x_{Q1}|} \theta(x_{Q4} - x_{Q3}) \theta(x_{Q3} - x_{Q2}) \theta(x_{Q2} - x_{Q1}) \quad (2.19)
\end{aligned}$$

The scattering eigenstates of a general  $n$ -photon problem can be constructed recursively in a similar way: the only unknown term in  $g_n(x_1, \dots, x_n)$  is the  $n$ -photon bound state as all the other terms can be constructed from the solutions of the  $1, 2, \dots, (n-1)$ -photon problems. We extrapolate from the results of  $n = 2-4$  that, for general  $n$  ( $\geq 2$ ), the  $n$ -body bound state assumes the form

$$\begin{aligned}
B_{k_1, \dots, k_n}(x_1, \dots, x_n) = & -(-2)^{n-2} \prod_{i=1}^n (\bar{t}_{k_i} - 1) \prod_{i=1}^{n-1} \theta(x_{i+1} - x_i) \\
& \times h_{k_1}(x_n) h_{k_2}(x_2) \cdots h_{k_{n-1}}(x_{n-1}) h_{k_n}(x_n) e^{[-(\Gamma + \Gamma')/2 - i\epsilon]|x_n - x_1|}. \quad (2.20)
\end{aligned}$$

We have verified this expression for  $n = 5$ . Thus we have given explicit formulas for constructing the exact  $n$ -photon scattering eigenstates.

The exact scattering eigenstates can be used to construct the scattering matrix. According to the Lippmann-Schwinger formalism [85], one can read off the “in” state (before scattering) and the “out” state (after scattering) of a general  $n$ -photon S-matrix from  $g_n(x_1, \dots, x_n)$  in the input region ( $x_1 < 0, \dots, x_n < 0$ ) and in the output region ( $x_1 > 0, \dots, x_n > 0$ ), respectively. The “in” and “out” states of one and two photon scattering matrices are given by

$$|\phi_{in}^{(1)}\rangle_e = \int dx h_k(x) a_e^\dagger(x) |0\rangle, \quad (2.21a)$$

$$|\phi_{out}^{(1)}\rangle_e = \int dx \bar{t}_k h_k(x) a_e^\dagger(x) |0\rangle, \quad (2.21b)$$

and

$$\begin{aligned} |\phi_{in}^{(2)}\rangle_e &= \int dx_1 dx_2 \frac{1}{2!} \left[ \sum_Q h_{k_1}(x_{Q_1}) h_{k_2}(x_{Q_2}) \right] a_e^\dagger(x_1) a_e^\dagger(x_2) |0\rangle, \\ |\phi_{out}^{(2)}\rangle_e &= \int dx_1 dx_2 \frac{1}{2!} \left[ \sum_Q \bar{t}_{k_1} \bar{t}_{k_2} h_{k_1}(x_{Q_1}) h_{k_2}(x_{Q_2}) \right. \\ &\quad \left. + \sum_{PQ} B_{k_{P_1}, k_{P_2}}(x_{Q_1}, x_{Q_2}) \right] a_e^\dagger(x_1) a_e^\dagger(x_2) |0\rangle, \end{aligned} \quad (2.22)$$

and similarly for three and four photons. The corresponding S-matrices are

$$S_e^{(n)} = \int dk_1 \cdots dk_n \frac{1}{n!} |\phi_{out}^{(n)}\rangle_{ee} \langle \phi_{in}^{(n)}|. \quad (2.23)$$

Notice that the unitarity of the S-matrix is automatically satisfied since the incoming state  $|\phi_{in}^{(n)}\rangle_e$  is a complete basis set in the even space [75, 85].

The S-matrix in the odd space is just the identity operator because the odd

mode is free and decoupled from the impurity and the even mode,

$$S_o^{(n)} = \int dk_1 \cdots dk_n \frac{1}{n!} |\phi_{in}^{(n)}\rangle_o \langle \phi_{in}^{(n)}|, \quad (2.24a)$$

$$|\phi_{in}^{(n)}\rangle_o = \int dx_1 \cdots dx_n \frac{1}{n!} \sum_Q \prod_{i=1}^n h_{k_i}(x_{Q_i}) a_e^\dagger(x_i) |0\rangle. \quad (2.24b)$$

Finally, we wish to construct the scattering matrix in the right/left representation based on the S-matrices in the even/odd representation. For a general  $n$ -photon scattering problem, the possible scattering channels are that  $i$  photons undergo scattering in the even space and  $n - i$  photons undergo scattering in the odd space, with  $i$  running from 0 to  $n$ . In addition, the even and odd spaces are decoupled from each other. Therefore, the  $n$ -photon S-matrix is

$$S^{(n)} = \sum_{i=0}^n S_e^{(i)} \otimes S_o^{(n-i)}. \quad (2.25)$$

We will use this S-matrix to study the scattering of Fock states and coherent state wave packets in the right/left space in the subsequent sections.

## 2.4 Scattering of Fock State Wavepackets

In order to show the significance of the many-body bound states, we study the scattering of a Fock state off of a two-level system. We assume that the incident mode propagates to the right and the two level system is initially in the ground state. We use the S-matrices defined in Eq.(2.25) to evaluate the transmission and reflection coefficients. In practice, any state that contains a finite number of photons must have the form of a wave-packet. Thus, we start with the definition of the continuous-mode photon wave-packet creation operator in momentum

space [12]

$$a_\alpha^\dagger = \int dk \alpha(k) a^\dagger(k), \quad (2.26)$$

with the normalization condition  $\int dk |\alpha(k)|^2 = 1$ . The corresponding continuous-mode  $n$ -photon Fock state is

$$|n_\alpha\rangle = \frac{(a_\alpha^\dagger)^n}{\sqrt{n!}} |0\rangle, \quad (2.27)$$

and the output state after it scatters off the TLS is

$$|\text{out}_\alpha^{(n)}\rangle = S^{(n)} |n_\alpha\rangle. \quad (2.28)$$

To obtain the scattering probabilities of a Fock state from the S-matrix found in Section II, we follow the following general procedure. (i) First, we write an  $n$ -photon input Fock state traveling to the right in momentum space:  $|n_\alpha\rangle = (1/\sqrt{n!}) \int dk_1 \cdots dk_n \alpha(k_1) \cdots \alpha(k_n) |k_1, \dots, k_n\rangle$ ; (ii) Next, we apply the S-matrix on the input state and find the output state  $|\text{out}_\alpha^{(n)}\rangle = S^{(n)} |n_\alpha\rangle = (1/\sqrt{n!}) \int dk_1 \cdots dk_n \alpha(k_1) \cdots \alpha(k_n) S^{(n)} |k_1, \dots, k_n\rangle$  in the even/odd basis; (iii) We transform back to the right/left basis. Then we project the output state onto the  $n$ -photon (right/left-going) momentum basis and take the absolute value square to obtain the probabilities  $P(k_1, \dots, k_n)$  of finding the output state in  $|k_1, \dots, k_n\rangle$ ; (iv) Finally, we integrate  $P(k_1, \dots, k_n)$  over  $k_1, \dots, k_n$  to obtain the total transmission and reflection probabilities. Here, a right/left-going state is defined by a positive/negative momentum, i.e.,  $k_1 > 0, \dots, k_n > 0$  for  $|k_1, \dots, k_n\rangle_R$  and  $k_1 < 0, \dots, k_n < 0$  for  $|k_1, \dots, k_n\rangle_L$ .

For convenience, we choose Gaussian type wavepackets with the spectral

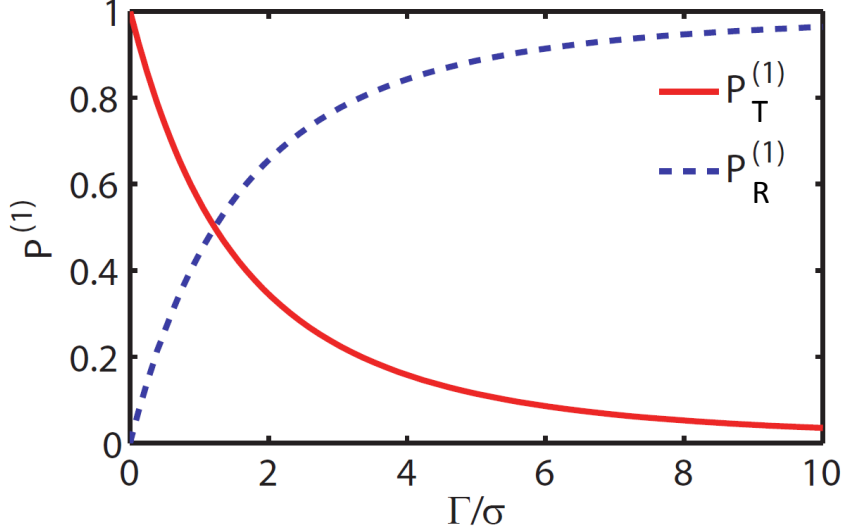


FIGURE 2.3: Single-photon transmission ( $P_T^{(1)}$ ) and reflection ( $P_R^{(1)}$ ) probabilities as a function of the ratio between coupling strength  $\Gamma$  and  $\sigma$ . The incident photon is on resonance with the two level system ( $k_0 = \epsilon$ ) and we have considered the lossless case  $\Gamma' = 0$ .

amplitude

$$\alpha(k) = (2\pi\sigma^2)^{-1/4} \exp\left(-\frac{(k - k_0)^2}{4\sigma^2}\right). \quad (2.29)$$

For all of the numerical examples in this chapter, we choose  $k_0 = \epsilon$ : the central frequency of the wavepacket is on resonance with the TLS, a condition which makes the interaction between the photons and the TLS strongest. We take the central momentum  $k_0 \gg \sigma$  so that the narrow-band condition is satisfied. We anticipate the effects of bound states are most prominent when  $\sigma \sim \Gamma$ , i.e., the pulse duration is on the order of the life time of the two level system.

### 2.4.1 Single-Photon Fock State Scattering

The probabilities of transmission ( $P_T^{(1)}$ ) and reflection ( $P_R^{(1)}$ ) for a single-photon Fock state are found as

$$P_T^{(1)} = \int_{k>0} dk |\langle k | \text{out}_\alpha^{(1)} \rangle|^2 = \int_{k>0} dk \alpha(k)^2 |t_k|^2, \quad (2.30a)$$

$$P_R^{(1)} = \int_{k<0} dk |\langle k | \text{out}_\alpha^{(1)} \rangle|^2 = \int_{k>0} dk \alpha(k)^2 |r_k|^2, \quad (2.30b)$$

where  $t_k = (\bar{t}_k + 1)/2$  and  $r_k = (\bar{t}_k - 1)/2$  and  $\bar{t}_k$  is the transmission coefficient defined above for the even mode [Eq. (2.6c)].

Note that the propagation of a single-photon is strongly modulated by the TLS as we turn on the coupling. In the strong-coupling limit, a single-photon is perfectly reflected and the two-level atom acts as a mirror. This perfect reflection is due to destructive interference between the directly transmitted state and the state re-emitted from the TLS. A single-photon transistor [62] and a quantum switch [64] have been proposed based on this perfect reflection.

### 2.4.2 Two-Photon Fock State Scattering

For two incident photons, following the general procedure above, we find that the transmission and reflection probabilities are

$$P_{TT}^{(2)} = \int_{k_1>0, k_2>0} dk_1 dk_2 \frac{1}{2!} |\langle k_1, k_2 | \text{out}_\alpha^{(2)} \rangle|^2, \quad (2.31a)$$

$$P_{TR}^{(2)} = \int_{k_1>0, k_2<0} dk_1 dk_2 |\langle k_1, k_2 | \text{out}_\alpha^{(2)} \rangle|^2, \quad (2.31b)$$

$$P_{RR}^{(2)} = \int_{k_1<0, k_2<0} dk_1 dk_2 \frac{1}{2!} |\langle k_1, k_2 | \text{out}_\alpha^{(2)} \rangle|^2, \quad (2.31c)$$

where  $P_{TT}^{(2)}$ ,  $P_{TR}^{(2)}$  and  $P_{RR}^{(2)}$  are, respectively, the probability for two photons to be transmitted (right-going), one transmitted and one reflected, and two photons reflected (left-going).

To show the significance of the bound state in the propagation of multi-photon Fock states, we separate each of the probabilities  $P_{TT}^{(2)}$ ,  $P_{TR}^{(2)}$  and  $P_{RR}^{(2)}$  into two parts. One part is the contribution from only the plane wave term (labeled PW), which is the direct transmission or reflection. The other is the contribution from all the other terms (labeled BS), including the bound state term as well as the interference term between the plane wave and bound state. Notice that the BS part vanishes in the absence of bound state, as in the case of single-photon scattering. Therefore, it is a manifestation of the nonlinear effect caused by the interaction between the TLS and two or more photons. As an example,  $P_{TT}^{(2)}$  split into PW and BS parts is

$$P_{TT}^{(2)} = \int_{k_1 > 0, k_2 > 0} dk_1 dk_2 |t(k_1, k_2) + B(k_1, k_2)|^2 = (P_{TT}^{(2)})_{\text{PW}} + (P_{TT}^{(2)})_{\text{BS}}, \quad (2.32\text{a})$$

$$(P_{TT}^{(2)})_{\text{PW}} = \int_{k_1 > 0, k_2 > 0} dk_1 dk_2 |t(k_1, k_2)|^2, \quad (2.32\text{b})$$

$$\begin{aligned} (P_{TT}^{(2)})_{\text{BS}} &= \int_{k_1 > 0, k_2 > 0} dk_1 dk_2 [t^*(k_1, k_2)B(k_1, k_2) \\ &\quad + t(k_1, k_2)B^*(k_1, k_2) + |B(k_1, k_2)|^2], \end{aligned} \quad (2.32\text{c})$$

$$t(k_1, k_2) = \alpha(k_1)\alpha(k_2)t_{k_1}t_{k_2}, \quad (2.32\text{d})$$

$$\begin{aligned} B(k_1, k_2) &= \left[ \frac{-i/2\pi}{k_1 - \epsilon + \frac{i(\Gamma + \Gamma')}{2}} + \frac{-i/2\pi}{k_2 - \epsilon + \frac{i(\Gamma + \Gamma')}{2}} \right] \\ &\times \int_{k' > 0} dk' \alpha(k')\alpha(k_1 + k_2 - k')r_{k'}r_{k_1+k_2-k'} . \end{aligned} \quad (2.32\text{e})$$

Figure 2.4 shows the three transmission probabilities  $P_{TT}^{(2)}$ ,  $P_{TR}^{(2)}$ , and  $P_{RR}^{(2)}$  for our standard parameters, with the contributions from the plane wave and bound state plotted separately in panels (a)-(c). Note that the presence of the bound state has a very substantial effect on these transmission probabilities. As shown in panels (a) and (b),  $P_{TT}^{(2)}$  and  $P_{TR}^{(2)}$  are enhanced by the formation of the bound state. This is mainly due to constructive interference between the plane wave and bound state. In contrast, panel (c) shows that  $P_{RR}^{(2)}$  is strongly reduced in the presence of the bound state because of destructive interference between the plane wave and bound state (change from  $\sim 0.8$  to  $\sim 0.4$  at  $\Gamma/\sigma = 2.5$ ). Therefore, the presence of the bound state tends to *increase* the one-photon and two-photon transmission, while *suppressing* the two-photon reflection.

A particularly interesting aspect of the results in Fig 2.4 is that the effect of the bound state is most prominent in the *intermediate* coupling regime, not at the strongest coupling. This is because, first, in the weak coupling limit, the interaction is too weak to produce a pronounced bound state for two-photon scattering, while, second, in the strong coupling limit, the TLS responds to the first photon too quickly (in a duration of order  $1/\Gamma$  with  $\Gamma = 2V^2$ ) for the second photon to produce a significant nonlinear effect. (The formation of the bound state requires the presence of both photons at the two-level system.) The optimal coupling strength  $\Gamma_m$  for producing nonlinear (bound state) effects lies at intermediate coupling, when the spontaneous emission rate  $\Gamma$  is on the order of the wavepacket width  $\sigma$ .

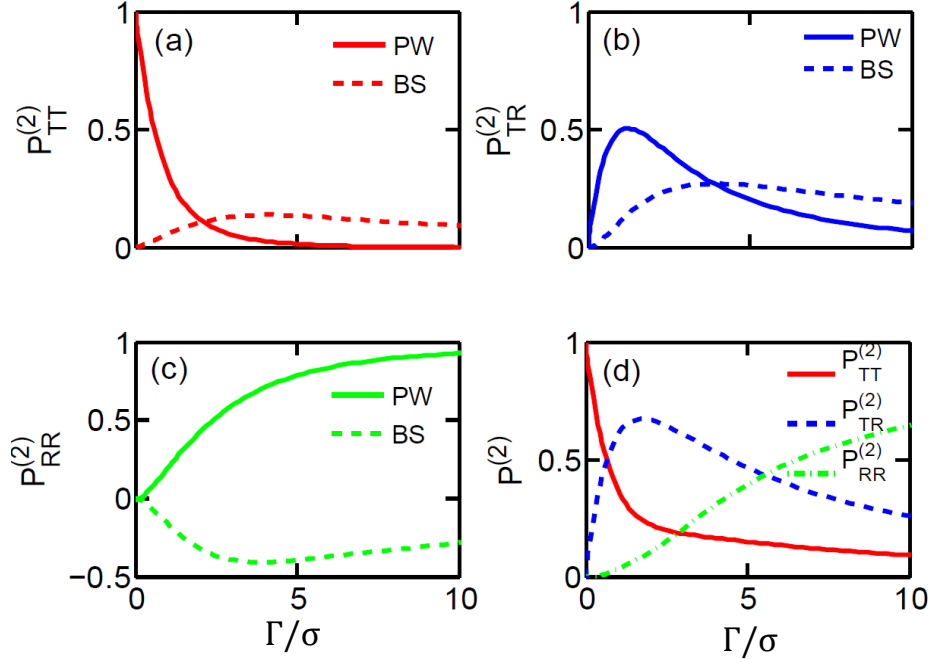


FIGURE 2.4: Two-photon transmission and reflection probabilities as a function of  $\Gamma/\sigma$ . (a) Probability that both photons are transmitted (and hence are right-going,  $P_{TT}^{(2)}$ ). (b) Probability that one photon is transmitted and one reflected (right-left,  $P_{TR}^{(2)}$ ). (c) Probability that both photons are reflected (both left-going,  $P_{RR}^{(2)}$ ). (d) The three processes on a single plot. The label PW refers to the contribution from the plane-wave term only, while BS refers to all the other contributions involving bound-state terms. The incident photons are on resonance with the two-level system ( $k_0 = \epsilon$ ), we consider the lossless case  $\Gamma' = 0$ . Notice the large effect of the bound state on these quantities.

#### 2.4.3 Three-Photon Fock State Scattering

Following the general procedure for obtaining scattering probabilities, the transmission and reflection probabilities for three-photon Fock state scattering are defined as

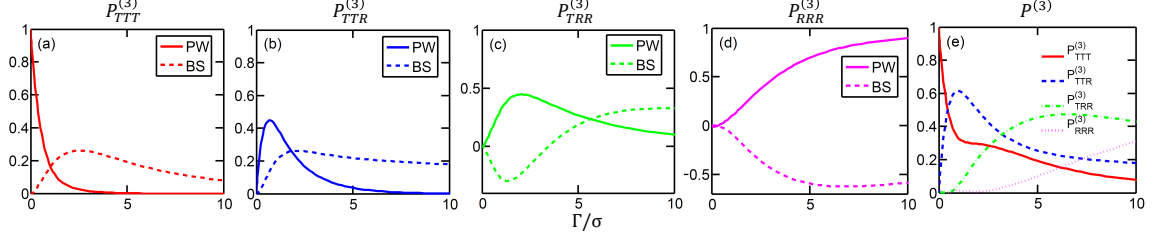


FIGURE 2.5: Three-photon transmission and reflection probabilities as a function of  $\Gamma/\sigma$ . (a) Probability of all three photons transmitted ( $P_{TTT}^{(3)}$ ). (b) Probability of two photons transmitted and one reflected ( $P_{TTR}^{(3)}$ ). (c) Probability of one photon transmitted and two photons reflected ( $P_{TRR}^{(3)}$ ). (d) Probability of all three photons reflected ( $P_{RRR}^{(3)}$ ). (e)  $P^3$  all together. The label PW refers to the contribution from only the plane wave term, while BS refers to all the other contributions, involving bound state terms. The incident photons are on resonance with the two level system ( $k_0 = \epsilon$ ), we consider the lossless case  $\Gamma' = 0$ .

$$\begin{aligned}
 P_{TTT}^{(3)} &= \int_{k_1 > 0, k_2 > 0, k_3 > 0} dk_1 dk_2 dk_3 \frac{1}{3!} |\langle k_1, k_2, k_3 | \text{out}_{\alpha}^{(3)} \rangle|^2, \\
 P_{TTR}^{(3)} &= \int_{k_1 > 0, k_2 > 0, k_3 < 0} dk_1 dk_2 dk_3 \frac{1}{2!} |\langle k_1, k_2, k_3 | \text{out}_{\alpha}^{(3)} \rangle|^2, \\
 P_{TRR}^{(3)} &= \int_{k_1 > 0, k_2 < 0, k_3 < 0} dk_1 dk_2 dk_3 \frac{1}{2!} |\langle k_1, k_2, k_3 | \text{out}_{\alpha}^{(3)} \rangle|^2, \\
 P_{RRR}^{(3)} &= \int_{k_1 < 0, k_2 < 0, k_3 < 0} dk_1 dk_2 dk_3 \frac{1}{3!} |\langle k_1, k_2, k_3 | \text{out}_{\alpha}^{(3)} \rangle|^2,
 \end{aligned} \tag{2.33}$$

where  $P_{TTT}^{(3)}$ ,  $P_{TTR}^{(3)}$ ,  $P_{TRR}^{(3)}$ , and  $P_{RRR}^{(3)}$  are the probabilities for three photons being transmitted (all right-going), two transmitted and one reflected, one transmitted and two reflected, and all three reflected (left-going), respectively. As in the two-photon scattering case, we separate each probability into two parts: the contribution of only the plane wave term (labeled PW) and the contribution from all the other terms (labeled BS), including the bound states as well as the interference between the plane wave and bound states. The probabilities and

the decomposition into PW and BS parts are plotted in Figure 2.5 for our usual parameters.

Figure 2.5 shows that the bound state contribution to the transmission probabilities is, as for two photons, very substantial. In panels (a) and (b), the BS parts of  $P_{TTT}^{(3)}$  and  $P_{TRR}^{(3)}$  are positive; thus, these probabilities are enhanced by the bound states. Panel (d) shows that  $P_{RRR}^{(3)}$  is suppressed by the bound state contribution for arbitrary coupling strength. In contrast, as we increase the coupling strength,  $P_{TRR}^{(3)}$  is first suppressed and then enhanced by the BS part as shown in Figure 2.5(c). Tuning the coupling strength changes the relative phase between the plane wave and bound state parts; for  $P_{TRR}^{(3)}$ , the interference between them happens to change from destructive to constructive as the coupling strength increases. Finally, as in the two-photon case, the most pronounced bound state effects occur in the intermediate coupling regime instead of the strong coupling limit.

## 2.5 Spectral Entanglement

It is evident the two-photon bound state in Eq. (2.32) is entangled in the momentum (or equivalently frequency) degree of freedom, i.e. it can not be separated into a product of single-photon states with definite momentum. To study the spectral aspect of the two-photon entanglement, we rewrite the two-photon output state [Eq. (2.31)] in momentum space as

$$\begin{aligned} |\psi^{(2)}\rangle = & \int dk_1 dk_2 \left[ f_{TT}(k_1, k_2) a_R^\dagger(k_1) a_R^\dagger(k_2) \right. \\ & + f_{TR}(k_1, k_2) a_R^\dagger(k_1) a_L^\dagger(k_2) \\ & \left. + f_{RR}(k_1, k_2) a_L^\dagger(k_1) a_L^\dagger(k_2) \right] |\emptyset\rangle, \end{aligned} \quad (2.34)$$

where  $f_{TT}(k_1, k_2)$ ,  $f_{TR}(k_1, k_2)$ , and  $f_{RR}(k_1, k_2)$  are the two-photon amplitudes for a transmitted pair, a pair of one transmitted and one reflected, and a reflected pair, respectively. Explicitly, they take the following form

$$f_{TT}(k_1, k_2) = t_2(k_1, k_2) + B(k_1, k_2), \quad (2.35a)$$

$$f_{TR}(k_1, k_2) = 2[rt(k_1, k_2) + B(k_1, k_2)], \quad (2.35b)$$

$$f_{RR}(k_1, k_2) = r_2(k_1, k_2) + B(k_1, k_2), \quad (2.35c)$$

$$t_2(k_1, k_2) = t_{k_1} t_{k_2} \alpha(k_1) \alpha(k_2), \quad (2.35d)$$

$$rt(k_1, k_2) = t_{k_1} r_{k_2} \alpha(k_1) \alpha(k_2), \quad (2.35e)$$

$$r_2(k_1, k_2) = r_{k_1} r_{k_2} \alpha(k_1) \alpha(k_2), \quad (2.35f)$$

where  $B(k_1, k_2)$  is given in Eq. (2.32). The first term in  $f(k_1, k_2)$  is the uncorrelated contribution, while the second term signals photon correlation. From Eq. (2.35), we define the joint spectral function of the two-photon states to be [86]

$$F_{\alpha\beta=TT, TR, RR}(k_1, k_2) = |f_{\alpha\beta}(k_1, k_2)|^2. \quad (2.36)$$

For the purpose of comparison, we also define the uncorrelated spectral function of the two-photon states,

$$G_{TT}(k_1, k_2) \equiv |t_2(k_1, k_2)|^2, \quad (2.37a)$$

$$G_{TR}(k_1, k_2) \equiv 4|rt(k_1, k_2)|^2, \quad (2.37b)$$

$$G_{RR}(k_1, k_2) \equiv |r_2(k_1, k_2)|^2. \quad (2.37c)$$

Figure 2.6 shows the two-photon joint spectrum in all the three scattering channels after sending the two-photon wavepacket with a narrow width ( $\sigma = 0.1\Gamma'$ ). As expected, the uncorrelated spectral shown in Fig. (2.6)(a), (2.6)(c) and (2.6)(e) have a circular shape in the 2D colormap of  $k_1$  and  $k_2$ . Similar circular

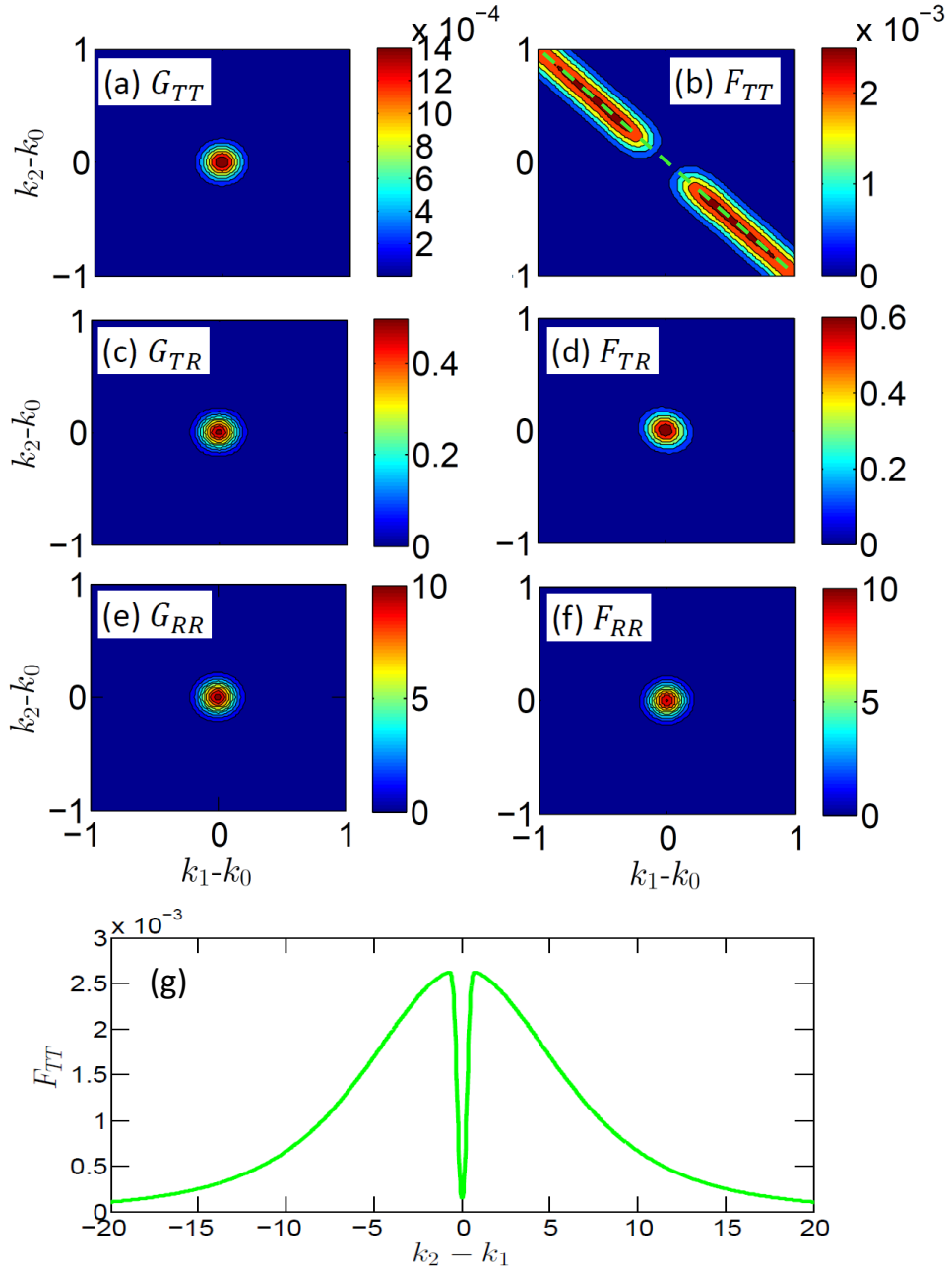


FIGURE 2.6: Two-photon joint spectrum of the output states after scattering off a 2LS in the case of a spectrally narrow incident wavepacket. Panels (a), (c), (e) show the uncorrelated spectra  $G_{TT}(k_1, k_2)$ ,  $G_{TR}(k_1, k_2)$ , and  $G_{RR}(k_1, k_2)$ , respectively. Panels (b), (d), (f) show the joint spectra of the two transmitted photons, one transmitted and one reflected, and two reflected photons, respectively. Panel (g) shows  $F_{TT}$  along the line  $k_1 + k_2 = 2k_0$  [dash line in panel (b)] as a function  $k_2 - k_1$ . System parameters:  $\Gamma = 9\Gamma'$ ,  $\sigma = 0.1\Gamma'$ , and  $k_0 = \epsilon$ . The frequencies are in units of  $\Gamma'$ .

shape is observed in the *TR* (one transmitted and one reflected) and *RR* (both reflected) channels, as shown in Fig.(2.6)(d) and (2.6)(f). This is simply because the bound-state term is too weak in these two cases compared to the plane wave term. Hence, the uncorrelated part still dominates the joint spectrum. However, in the *TT* (both transmitted) channel, Fig.(2.6)(b) shows a clear signature of correlation: the momentum of the photon pair is entangled along the line  $k_1 + k_2 = 2k_0$  with an uncertainty given by the wavepacket width  $\sigma$ . In particular, as shown in Fig.(2.6)(g), we notice that the joint spectrum in fact vanishes around  $k_1 = k_2 = k_0$ , which is due to the cancellation between the plane wave and bound state terms in Eq.(2.35b). The width of  $F_{TT}$  as a function of  $k_2 - k_1$  along the line  $k_1 + k_2 = 2k_0$  is given by  $\Gamma$ , which determines the bandwidth of spectral entanglement.

## 2.6 Scattering of Coherent State Wavepackets

We now turn to studying the scattering of coherent states in order to show, first, the strong photon-photon correlation induced by the the two-level system and, second, the change in photon number statistics. The incident coherent state wavepacket is defined by [12]

$$|\alpha\rangle = e^{a_\alpha^\dagger - \bar{n}/2} |0\rangle, \quad (2.38)$$

with  $a_\alpha^\dagger = \int dk \alpha(k) a^\dagger(k)$ , and mean photon number  $\bar{n} = \int dk |\alpha(k)|^2$ . A Gaussian type wavepacket is chosen

$$\alpha(k) = \frac{\sqrt{\bar{n}}}{(2\pi\sigma^2)^{1/4}} \exp\left(-\frac{(k - k_0)^2}{4\sigma^2}\right); \quad (2.39)$$

for numerical evaluations, we set, as before  $k_0 = \epsilon \gg \sigma$ . The output state  $|\text{out}_\alpha\rangle$  is then

$$|\text{out}_\alpha\rangle = \sum_n S^{(n)} |\alpha\rangle \quad (2.40)$$

We assume the incident coherent state is right-going and the two-level system is in the ground state initially. We present the analysis of second-order correlation and photon number statistics in the transmitted field.

### 2.6.1 Second-Order Correlation Function

The second-order correlation function of the transmitted field is defined as [12]

$$g^{(2)}(x_2 - x_1) = \frac{\langle \text{out}_\alpha | a_R^\dagger(x_1) a_R^\dagger(x_2) a_R(x_2) a_R(x_1) | \text{out}_\alpha \rangle}{\langle \text{out}_\alpha | a_R^\dagger(x_1) a_R(x_1) | \text{out}_\alpha \rangle^2}. \quad (2.41)$$

We consider the mean photon number  $\bar{n} \leq 1.0$ . In this case, the probability to find  $n \geq 3$  number states is much smaller than that of  $n = 2$  number states. Therefore, we neglect the contributions from  $n \geq 3$  number states. The second-order correlation function simplifies to

$$g^{(2)}(x_2 - x_1) = \frac{\left| \int dk_1 dk_2 \alpha(k_1) \alpha(k_2) (t_{k_1} t_{k_2} - r_{k_1} r_{k_2} e^{-\frac{(\Gamma + \Gamma')(x_2 - x_1)}{2}}) \right|^2}{\left| \int dk_1 dk_2 \alpha(k_1) \alpha(k_2) t_{k_1} t_{k_2} \right|^2}. \quad (2.42)$$

The contributions from the directly transmitted state and the bound state can be identified as the first term and second term in the numerator of  $g^{(2)}(x_2 - x_1)$  in Eq. (2.42). In the absence of the bound state,  $g^{(2)}(x_2 - x_1)$  is always equal to unity. As we turn on the interaction, the interference between the directly transmitted state and the bound state will give rise to interesting correlation behavior. Figure 2.7 shows the second-order correlation as a function of  $\Gamma(x_2 - x_1)$  at various coupling strengths,  $\Gamma$ , to the 1D mode with  $\Gamma' = \sigma$ . In the weak

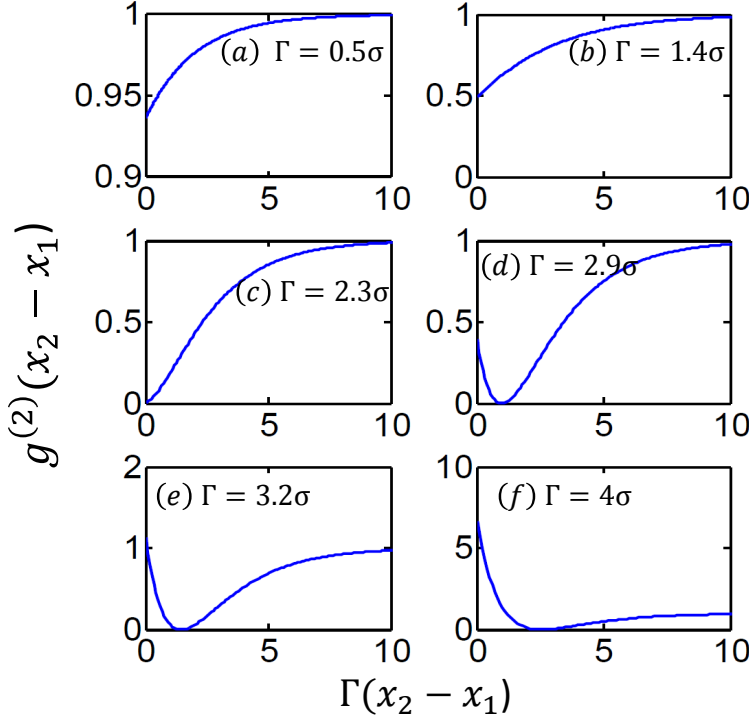


FIGURE 2.7: Second-order correlation of the transmitted field given an incident coherent state with  $\bar{n} \leq 1$  at various coupling strengths  $\Gamma$  to the 1D continuum. (a)  $\Gamma = 0.5\sigma$ , (b)  $\Gamma = 1.4\sigma$ , (c)  $\Gamma = 2.3\sigma$ , (d)  $\Gamma = 2.9\sigma$ , (e)  $\Gamma = 3.2\sigma$ , (f)  $\Gamma = 4\sigma$ . The spontaneous emission rate to channels other than the 1D continuum is set to  $\Gamma' = \sigma$ . Notice that the correlation behavior is very sensitive to the coupling strength to 1D continuum, showing both bunching and antibunching.

coupling limit ( $\Gamma = 0.5\sigma$ ) as shown in Figure 2.7(a), the directly transmitted state dominates and  $g^{(2)}(0)$  is slightly smaller than 1. We observe a slight initial antibunching. As  $\Gamma$  increases [Figure 2.7(b)-(c)],  $g^{(2)}(0)$  further decreases and the initial antibunching gets stronger and becomes strongest at  $\Gamma = 2.3\sigma$  when  $g^{(2)}(0) = 0$ . Notice that the antibunching is getting weaker as one moves away from the origin for  $\Gamma \leq 2.3\sigma$ . Further increase of  $\Gamma$  starts to change the initial antibunching [ $\Gamma = 2.9\sigma$ ,  $g^{(2)}(0) < 1$ ] to bunching [ $\Gamma = 3.2\sigma$ ,  $g^{(2)}(0) > 1$ ] as shown in Figure 2.7(d)-(f). In this case, the bound state starts to dominate the correlation behavior. It is remarkable that, for  $\Gamma > 2.3\sigma$ , the initial antibunching ( $\Gamma < 3.2\sigma$ ) or bunching ( $\Gamma > 3.2\sigma$ ) is followed by a later antibunching  $g^{(2)}(0) = 0$ , which is

caused by the cancellation of the directly transmitted state and the bound state. The formation of the bound state gives rise to a rich phenomenon of photon-photon correlation, which is very sensitive to the coupling strength  $\Gamma$  to the 1D mode. *Effective attractive or repulsive interaction between photons is induced by the presence of a single two-level system* [74].

Our results agree with the theoretical findings obtained by Chang *et al.* [62] using a very different approach. Recently, the experimental observations by Hoi *et al.* [48] confirmed our findings of photon bunching shown in Fig. 2.7. In the lossless  $\Gamma' = 0$  case, as we increase the coupling strength, the transmission for individual photons is reduced rapidly [see, for example, Figure 2.3 and Figure 2.4(a)]. But the two-photon bound state can strongly enhance the transmission. Therefore, we will observe a strong initial bunching followed by a later antibunching, similar to Figure 2.7(f).

### 2.6.2 Number Statistics

Given the output state  $|\text{out}_\alpha\rangle$ , we measure the photon number distribution in the transmitted field following the general procedure described in Sec. 2.4. The total density matrix of the output field reads

$$\rho = |\text{out}_\alpha\rangle\langle\text{out}_\alpha|. \quad (2.43)$$

The reduced density matrix of the transmitted field can be obtained by tracing out the reflected photons

$$\rho_T = \text{Tr}_R[\rho] =_R \langle 0|\rho|0\rangle_R + \int dk \, {}_R\langle k|\rho|k\rangle_R + \frac{1}{2!} \int dk_1 dk_2 \, {}_{RR}\langle k_1 k_2|\rho|k_1 k_2\rangle_{RR} + \dots, \quad (2.44)$$

where  $|k\rangle_R = a_L^\dagger(k)|0\rangle$  and  $|k_1 k_2\rangle_{RR} = a_L^\dagger(k_1)a_L^\dagger(k_2)|0\rangle$ . Then, we can measure the number statistics of the transmitted field by projecting the reduced density matrix onto various number states

$$\begin{aligned} P_0 &= {}_T\langle 0|\rho_T|0\rangle_T, \\ P_1 &= \int dk {}_T\langle k|\rho_T|k\rangle_T, \\ P_2 &= \frac{1}{2!} \int dk_1 dk_2 {}_{TT}\langle k_1 k_2|\rho_T|k_1 k_2\rangle_{TT}, \\ P_3 &= \frac{1}{3!} \int dk_1 dk_2 dk_3 {}_{TTT}\langle k_1 k_2 k_3|\rho_T|k_1 k_2 k_3\rangle_{TTT}, \end{aligned} \quad (2.45)$$

where  $|k\rangle_T = a_R^\dagger(k)|0\rangle$  and  $|k_1 k_2\rangle_{TT} = a_R^\dagger(k_1)a_R^\dagger(k_2)|0\rangle$ .

We consider a mean photon number  $\bar{n} \leq 1.0$  in the incident coherent state. In this case, the probability to find the four photon state is negligible ( $\leq 1.6\%$ ). Hence, we truncate all the calculations in Eqs.(2.44) and (2.45) up to three-photon. We compare the photon number distribution  $P_n$  of the output state with  $(P_n)_{\text{Poisson}}$  of a coherent state having the same mean photon number.

Figure 2.8 shows the ratio between  $(P_n)_{\text{Poisson}}$  and  $P_n$  as a function of the coupling strength  $\Gamma$  and the mean photon number  $\bar{n}$  of the incident coherent state. The zero-photon probability does not deviate from that of a coherent state much in the whole parameter region we considered. The one-photon probability is smaller than the corresponding probability in a coherent state. In contrast, the two- and three-photon probabilities are much larger than the ones in a coherent state, especially in the strong coupling regime. This is to say, the interaction between photons and the two-level system redistributes the probabilities among different photon numbers. *The one-photon probability is reduced and is redistributed to the two- and three-photon probabilities.* This is mainly because the bound states

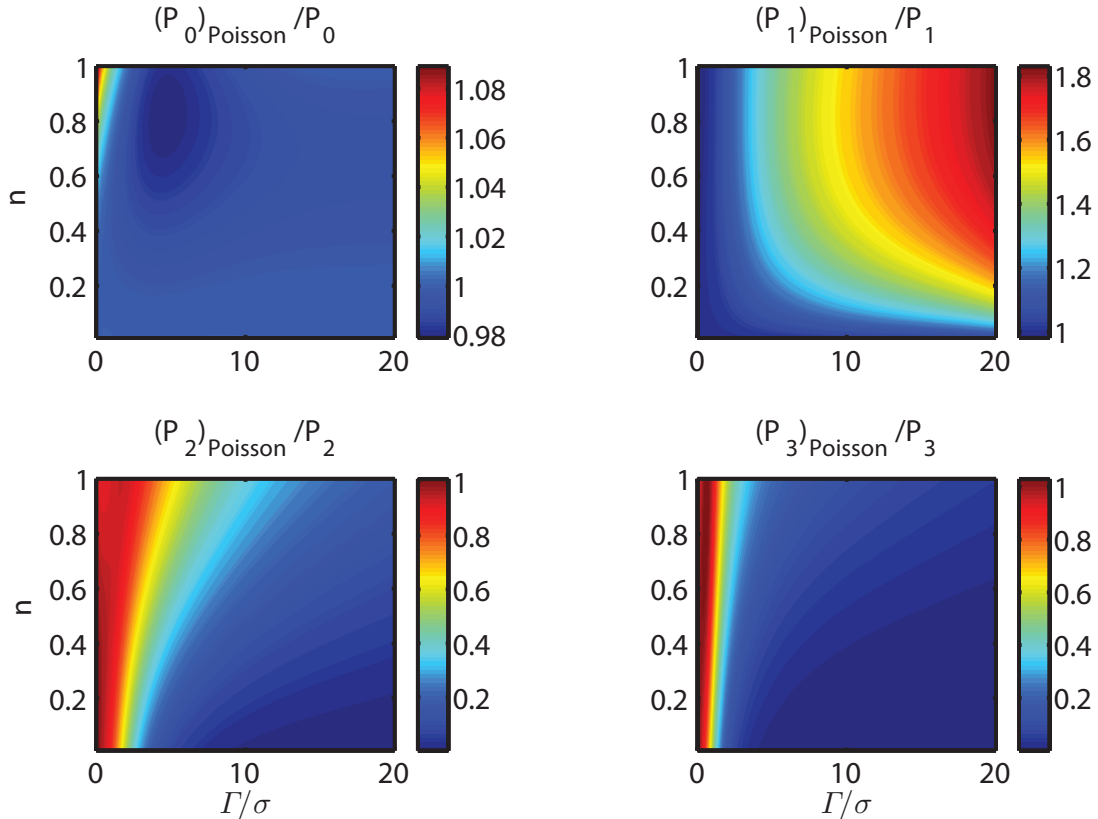


FIGURE 2.8: Photon number distribution of the transmitted field compared with a coherent state. We considered the lossless case  $\Gamma' = 0$ . The statistics is non-Poissonian with the 2 and 3 photon content enhanced.

enhance the transmission of multi-photon states as we have shown in Sec. 2.4. In conclusion, we obtain a non-Poissonian light source after the scattering. It is perhaps possible to use this strongly-correlated light source to perform decoy-state quantum key distribution in order to raise the key generation rate [87, 88, 89, 90], as discussed later in Chapter 5.

## 2.7 Conclusion

In this chapter, we present a general method to construct the exact scattering eigenstates for the problem of  $n$ -photons interacting with a two-level system. Many-body bound states appear in the presence of the coupling between pho-

tons and the two-level system. Furthermore, the scattering matrices are extracted using the Lippmann-Schwinger formalism. We emphasize that the completeness of the S-matrices is guaranteed by imposing open boundary conditions and requiring the incident field to be free plane waves. Based on the S-matrices, we study the scattering of the Fock states and coherent states. The bound states are shown to enhance the transmission of multi-photon states and suppress the transmission of single-photon states. We compute the spectral entanglement in the two-photon scattering, and find that photons are entangled in frequency due to the nonlinear interaction with the 2LS. In the transmitted field of coherent state scattering, photons exhibit strong bunching or antibunching effects depending on the coupling strength. This is a manifestation of the many-body bound states. We determine the photon number distribution and find that the one-photon state is transferred to two- and three-photon states. This results in a non-Poissonian light source which have important applications in quantum information.

# 3

## Cavity-free Photon Blockade and Photon-induced Tunneling

*Summary:* <sup>1</sup>We study the generation of strongly-correlated photons and observation of cavity-free photon blockade and photon-induced tunneling by coupling an atom to photonic quantum fields in a one-dimensional waveguide. Specifically, we consider a three-level or four-level system for the atom. Photon-photon bound-states emerge as a manifestation of the strong photon-photon correlation mediated by the atom. Effective repulsive or attractive interaction between photons can be produced, causing either suppressed multiphoton transmission (photon blockade) or enhanced multiphoton transmission (photon-induced tunneling). As a result, nonclassical light sources can be generated on demand by sending coherent states into the proposed system. We calculate the second-order correlation function of the transmitted field and observe bunching and

---

<sup>1</sup> Part of the text of this chapter has been adapted from the following previously published articles: [a] Huaixiu Zheng, Daniel J. Gauthier, and Harold U. Baranger, “Cavity-Free Photon Blockade Induced by Many-Body Bound States”, *Phys. Rev. Lett.* **107**, 223601 (2011); [b] Huaixiu Zheng, Daniel J. Gauthier, and Harold U. Baranger, “Strongly-correlated photons generated by coupling a three- or four-level system to a waveguide”, *Phys. Rev. A* **85**, 043832 (2012).

anti-bunching caused by the bound-states. Furthermore, we demonstrate that the proposed system can produce photon pairs with a high degree of spectral entanglement, which have a large capacity for carrying information and are important for large-alphabet quantum communication.

### 3.1 Introduction

In this Chapter, we consider using a waveguide-QED system to generate strongly-correlated photons through coupling to a three-level or four-level system (3LS or 4LS). Such strongly-correlated photons can be used to study quantum optical phenomena, such as photon blockade and photon-induced tunneling, and many-body physics [24] as well as to implement large-alphabet quantum communication protocols [91, 92]. Specifically, to probe the strong photon-photon correlation mediated by the 3LS or 4LS, we study photonic transport, second-order correlation, and spectral entanglement of the correlated photon states. As done previously in Chapter 2, we explicitly construct the scattering eigenstates by imposing an open boundary condition and setting the incident state to be a free plane wave. In the multiphoton solutions, photon-photon bound-states emerge, which have significant impact on the transport, spectral entanglement, and second-order correlation function. While single-photon transport exhibits EIT, multiphoton transport shows photon-induced tunneling and photon blockade. A highly entangled photon pair in frequency is obtained by scattering a two-photon state off the 4LS. Finally, we study the scattering of a coherent state wavepacket, whose number statistics become non-Poissonian. Strong bunching and anti-bunching appear in the second-order correlation function.

This Chapter is organized as follows. In Sec. 3.2, we introduce the model Hamiltonian, identify relevant experimental systems, and solve for the scatter-

ing eigenstates for one-, two- and three-photon states. With the scattering eigenstates, the asymptotic output states from scattering Fock states off the 3LS or 4LS are obtained in Sec. 3.3. In Sec. 3.5, we study the photonic transport of Fock states and analyze the effect caused by the photon-photon bound-states. In Sec. 3.6, we calculate the spectral entanglement for the two-photon case and demonstrate that highly entangled photon pairs are obtained. In Sec. 3.7, the signatures of photon correlation are revealed in the number statistics and second-order correlation function after scattering a coherent state wavepacket. Finally, we conclude in Sec. 3.8.

### 3.2 Model Hamiltonian

We consider the scattering problem of photons in a one-dimensional waveguide side-coupled to a single atom, as shown in Figure 3.1. By “*atom*” we mean a local emitter with discrete levels, which could be formed from natural atoms, quantum dots, trapped ions, or superconducting qubits.

Here, two types of local emitter are considered: a driven  $\Lambda$ -type 3LS and an  $N$ -type 4LS. The single-photon dynamics for the 3LS was previously studied in Ref. [66] and a two-photon solution was found in Ref. [69] in the limit of weak control field. Here, without assuming a weak control field, we solve the scattering problem for both the 3LS and 4LS in the general case. We mainly focus on the photon-photon correlation induced by the atom: physically, the interesting physics originates from the interplay of quantum interference in the 1D waveguide and interaction effects induced by the atom. Such interaction can be understood by treating the atom as a bosonic site and the ground and excited states as zero and one boson states, respectively. Unphysical multiple occupation is removed by adding an infinitely large repulsive on-site interaction term [67],

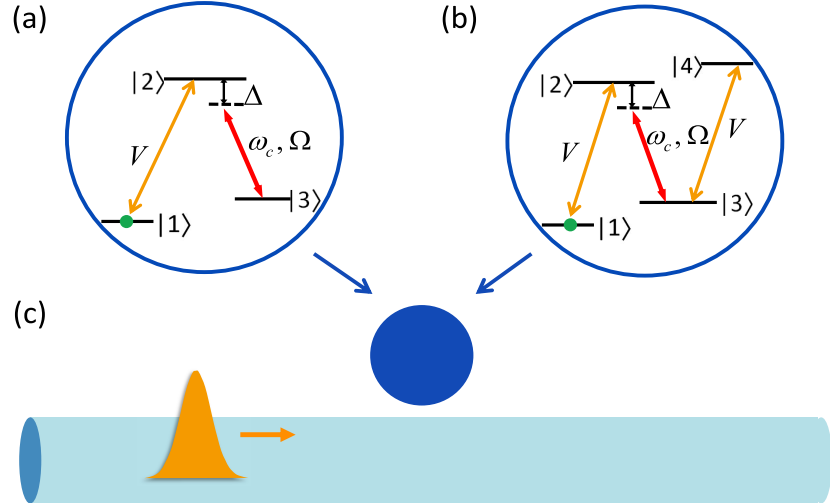


FIGURE 3.1: Sketch of the atom-waveguide system: (a) a  $\Lambda$ -type three-level system, (b) an  $N$ -type four-level system, (c) photons (yellow) in a 1D waveguide coupled to an atom (blue), which can be either the 3LS in (a) or the 4LS in (b). The transitions  $|1\rangle \leftrightarrow |2\rangle$  and  $|3\rangle \leftrightarrow |4\rangle$  are coupled to the waveguide modes with strength  $V$ . The transition  $|2\rangle \leftrightarrow |3\rangle$  is driven by a semiclassical control field with Rabi frequency  $\Omega$  and detuning  $\Delta$ . Here,  $\omega_c$  is the frequency of the control field.

which is the underlying mechanism responsible for the formation of photon-photon bound states [69, 70, 74, 75, 93]. The proposed system could be realized either in optical systems [17, 43, 45, 94, 95] or in microwave superconducting (SC) circuits [40, 44, 96, 57, 97]. For the optical systems, the driven 3LS and 4LS have been studied in both the trapped ion [98] and cavity systems [34, 35, 99, 100]. For the microwave SC systems, the 3LS and 4LS have already been realized using SC qubits [40, 46, 96, 97, 101, 102, 103, 104].

We start with the Hamiltonian in the rotating wave approximation, describing a continuum photonic field in a 1D waveguide coupled to a single atom [66, 69,

70, 74, 93]

$$H = H_{\text{wg}} + H_{\text{atom}} + H_c,$$

$$H_{\text{wg}} = \int dx (-i) \hbar c \left[ a_R^\dagger(x) \frac{d}{dx} a_R(x) - a_L^\dagger(x) \frac{d}{dx} a_L(x) \right], \quad (3.1)$$

where  $a_{R,L}^\dagger(x)$  is the creation operator for a right- or left-going photon at position  $x$  and  $c$  is the group velocity of photons. For the driven  $\Lambda$ -type 3LS,

$$\begin{aligned} H_{\text{atom}}^{(\Lambda)} &= \sum_{j=2,3} \hbar \left( \epsilon_j - \frac{i\Gamma_j}{2} \right) |j\rangle\langle j| + \frac{\hbar\Omega}{2} \left( |2\rangle\langle 3| + \text{h.c.} \right), \\ H_c^{(\Lambda)} &= \int dx \hbar V \delta(x) \left\{ [a_R^\dagger(x) + a_L^\dagger(x)] |1\rangle\langle 2| + \text{h.c.} \right\}. \end{aligned} \quad (3.2)$$

For the  $N$ -type 4LS,

$$\begin{aligned} H_{\text{atom}}^{(N)} &= \sum_{j=2}^4 \hbar \left( \epsilon_j - \frac{i\Gamma_j}{2} \right) |j\rangle\langle j| + \frac{\hbar\Omega}{2} \left( |2\rangle\langle 3| + \text{h.c.} \right), \\ H_c^{(N)} &= \int dx \hbar V \delta(x) \left\{ [a_R^\dagger(x) + a_L^\dagger(x)] (|1\rangle\langle 2| + |3\rangle\langle 4|) + \text{h.c.} \right\}. \end{aligned} \quad (3.3)$$

Here, the energy reference is the energy of the ground state  $|1\rangle$ , and  $\epsilon_2 = \omega_{21}$ ,  $\epsilon_3 = \epsilon_2 - \Delta$ , and  $\epsilon_4 = \epsilon_3 + \omega_{43}$ , where  $\omega_{21}$  and  $\omega_{43}$  are the  $|1\rangle \leftrightarrow |2\rangle$ , and  $|3\rangle \leftrightarrow |4\rangle$  transition frequencies, respectively. In the spirit of the quantum jump picture [50], we include an imaginary term in the energy level to model the spontaneous emission of the excited states at rate  $\Gamma_j$  to modes other than the waveguide continuum. The spontaneous emission rate to the 1D waveguide continuum is given by  $\Gamma = 2V^2/c$  (from Fermi's golden rule). Notice that the use of the rotating wave approximation is justified by the fact that  $\hbar\Gamma \ll \hbar\omega_{21}$ , which is the case in current experiments [40, 43, 44, 45, 46].

It is convenient to transform the right/left modes to even/odd modes:  $a_e^\dagger(x) = a_R^\dagger(x) + a_L^\dagger(-x)/\sqrt{2}$  and  $a_o^\dagger(x) = a_R^\dagger(x) - a_L^\dagger(-x)/\sqrt{2}$ . This decomposes the Hamiltonian into two decoupled modes. The even mode couples to the atom and the odd mode is free:  $H = H_e + H_o$  with

$$H_e = \int dx (-i)\hbar c a_e^\dagger(x) \frac{d}{dx} a_e(x) + H_{\text{atom}} + H_c, \quad (3.4a)$$

$$H_o = \int dx (-i)\hbar c a_o^\dagger(x) \frac{d}{dx} a_o(x). \quad (3.4b)$$

The coupling Hamiltonian  $H_c$  is now

$$H_c^{(\Lambda)} = \int dx \hbar \overline{V} \delta(x) \{ a_e^\dagger(x) |1\rangle\langle 2| + \text{h.c.} \}, \quad (3.5a)$$

$$H_c^{(N)} = \int dx \hbar \overline{V} \delta(x) \{ a_e^\dagger(x) (|1\rangle\langle 2| + |3\rangle\langle 4|) + \text{h.c.} \}, \quad (3.5b)$$

where  $\overline{V} = \sqrt{2}V$ .

### 3.3 Scattering Eigenstates

Hereafter, we will concentrate on solving for the scattering eigenstates in the even space. Because  $[H, \hat{n}_e + \hat{n}_{\text{atom}}] = [H, \hat{n}_o] = 0$  for the number operators  $\hat{n}_{e/o} \equiv \int dx \hat{a}_{e/o}^\dagger(x) \hat{a}_{e/o}(x)$  and the atomic excitation  $\hat{n}_{\text{atom}}$ , the total number of excitations in both the even and odd spaces are separately conserved. Therefore,

a general  $n$ -excitation state in the even space ( $n = n_e + n_{\text{atom}}$ ) is given by

$$\begin{aligned} |\Psi_n^{(\Lambda)}\rangle_e &= \left[ \int dx^n g^{(n)}(x) \hat{a}_e^\dagger(x_1) \cdots \hat{a}_e^\dagger(x_n) \right. \\ &\quad \left. + \int dx^{n-1} \sum_{j=2,3} f_j^{(n)}(x) S_{1j}^+ \hat{a}_e^\dagger(x_1) \cdots \hat{a}_e^\dagger(x_{n-1}) \right] |\emptyset, 1\rangle, \end{aligned} \quad (3.6a)$$

$$\begin{aligned} |\Psi_n^{(N)}\rangle_e &= \left[ \int dx^n g^{(n)}(x) \hat{a}_e^\dagger(x_1) \cdots \hat{a}_e^\dagger(x_n) \right. \\ &\quad \left. + \int dx^{n-1} \sum_{j=2,3} f_j^{(n)}(x) S_{1j}^+ \hat{a}_e^\dagger(x_1) \cdots \hat{a}_e^\dagger(x_{n-1}) \right. \\ &\quad \left. + \int dx^{n-2} f_4^{(n)}(x) S_{14}^+ \hat{a}_e^\dagger(x_1) \cdots \hat{a}_e^\dagger(x_{n-2}) \right] |\emptyset, 1\rangle, \end{aligned} \quad (3.6b)$$

where  $|\emptyset, 1\rangle$  is the zero-photon state with the atom in the ground state  $|1\rangle$  and  $S_{ij}^+ = |j\rangle\langle i|$ .

The scattering eigenstates are constructed by imposing the open boundary condition that  $g^{(n)}(x)$  is a free-bosonic plane wave in the incident region [83, 93, 70]. That is, for  $x_1, \dots, x_n < 0$ ,

$$g^{(n)}(x) = \frac{1}{n!} \sum_Q h_{k_1}(x_{Q_1}) \cdots h_{k_n}(x_{Q_n}), \quad h_k(x) = \frac{e^{ikx}}{\sqrt{2\pi}}, \quad (3.7)$$

where  $Q = (Q_1, \dots, Q_n)$  is a permutation of  $(1, \dots, n)$ . Solving the Schrödinger equation with this open boundary condition, we find the scattering eigenstates for the systems we consider here (for a detailed derivation for a two-level system, see Chapter 2 Sec. 2.3). Below, we present the one-, two-, and three-photon scattering eigenstates, which have the same form for the 3LS and 4LS cases. In the even space, the one-photon scattering eigenstate with eigenenergy  $E = \hbar ck$

is given by

$$g^{(1)}(x) \equiv g_k(x) = h_k(x) [\theta(-x) + \bar{t}_k \theta(x)], \quad (3.8a)$$

$$\bar{t}_k = \frac{[ck - \epsilon_2 + \Delta + i\Gamma_3/2][ck - \epsilon_2 + (i\Gamma_2 - i\Gamma)/2] - \Omega^2/4}{[ck - \epsilon_2 + \Delta + i\Gamma_3/2][ck - \epsilon_2 + (i\Gamma_2 + i\Gamma)/2] - \Omega^2/4}, \quad (3.8b)$$

where  $\theta(x)$  is the step function. The one-photon scattering eigenstate is exactly the same for both the 3LS and 4LS because it takes at least two quanta to excite level  $|4\rangle$ : for single-photon processes, the 3LS and 4LS cases are equivalent.

For two-photon scattering, we start with a free plane wave in the region  $x_1, x_2 < 0$ , and use the Schrödinger equation to find the wave function first in the region  $x_1 < 0 < x_2$  and then for  $0 < x_1, x_2$  [93]. We arrive at the following two-photon scattering eigenstate with eigenenergy  $E = \hbar c(k_1 + k_2)$ :

$$g^{(2)}(x_1, x_2) = \frac{1}{2!} \left[ \sum_Q g_{k_1}(x_{Q_1}) g_{k_2}(x_{Q_2}) + \sum_{PQ} B_{k_{P_1}, k_{P_2}}^{(2)}(x_{Q_1}, x_{Q_2}) \theta(x_{Q_1}) \right], \quad (3.9a)$$

$$B_{k_{P_1}, k_{P_2}}^{(2)}(x_{Q_1}, x_{Q_2}) = e^{iEx_{Q_2}} \sum_{j=1,2} C_j e^{-\gamma_j |x_2 - x_1|} \theta(x_{Q_{2j}}), \quad (3.9b)$$

where  $P = (P_1, P_2)$  and  $Q = (Q_1, Q_2)$  are permutations of  $(1, 2)$ ,  $\theta(x_{Q_{ij}}) = \theta(x_{Q_i} - x_{Q_j})$ , and  $B^{(2)}$  is a two-photon bound state<sup>2</sup>— $\text{Re}[\gamma_{1,2}] > 0$ . Our solution applies for the general case of arbitrary strength of the control field. Taking the weak control field limit for the 3LS case, we checked that one recovers the two-photon solution found in Ref. [69].

Following the same procedure, we obtain the three-photon scattering eigen-

---

<sup>2</sup> They are *not* the “bound states” with a discrete energy spectrum, states in which particles are localized in a finite region and can not escape to infinity [59].

state with eigenenergy  $E = \hbar c(k_1 + k_2 + k_3)$ :

$$\begin{aligned}
g^{(3)}(x_1, x_2, x_3) &= \frac{1}{3!} \left\{ \sum_Q g_{k_1}(x_{Q_1}) g_{k_2}(x_{Q_2}) g_{k_3}(x_{Q_3}) \right. \\
&\quad + \sum_{PQ} \left[ g_{k_{P_1}}(x_{Q_1}) B_{k_{P_2}, k_{P_3}}^{(2)}(x_{Q_2}, x_{Q_3}) \theta(x_{Q_2}) \right. \\
&\quad \left. \left. + B_{k_{P_1}, k_{P_2}, k_{P_3}}^{(3)}(x_{Q_1}, x_{Q_2}, x_{Q_3}) \theta(x_{Q_1}) \right] \right\}, \\
B_{k_{P_1}, k_{P_2}, k_{P_3}}^{(3)}(x_{Q_1}, x_{Q_2}, x_{Q_3}) &= e^{i[k_{P_1}x_{Q_2} + (k_{P_2} + k_{P_3})x_{Q_3}]} \left[ \sum_{j=1,2} D_j e^{-\gamma_j |x_{Q_3} - x_{Q_1}|} \right. \\
&\quad \left. + D_3 e^{-\gamma_1 |x_{Q_3} - x_{Q_2}| - \gamma_2 |x_{Q_2} - x_{Q_1}|} \right. \\
&\quad \left. + D_4 e^{-\gamma_2 |x_{Q_3} - x_{Q_2}| - \gamma_1 |x_{Q_2} - x_{Q_1}|} \right] \theta(x_{Q_{32}}) \theta(x_{Q_{21}}), \quad (3.10)
\end{aligned}$$

where  $B^{(3)}$  is a three-photon bound state,  $P = (P_1, P_2, P_3)$  and  $Q = (Q_1, Q_2, Q_3)$  are permutations of  $(1, 2, 3)$ . The coefficients  $C_{1,2}$  and  $D_{1,2,3,4}$  in the bound states depend on the system parameters and have different functional forms for the 3LS and 4LS. Expressions for  $\gamma_{1,2}$ ,  $C_{1,2}$ , and  $D_{1,2,3,4}$  are given in Appendix A. Notice that the bound states here have more structure than in the two-level case [74, 75, 93]; for example, the two-photon bound state has *two* characteristic binding strengths instead of one. This is due to the internal atomic structure: for the 3LS or 4LS, the photonic field couples to the transitions from the ground state to both of the eigenstates in the dressed state picture of levels  $|2\rangle$  and  $|3\rangle$ , giving rise to two binding strengths. Such bound states are a manifestation of the photon-photon correlation induced by having more than two photons interact with the same atom. For the 4LS case, this leads to strikingly different multiphoton transport behavior compared to the single-photon transport [70].

From the scattering eigenstates, we construct  $n$ -photon ( $n = 1$  to 3) scattering

matrices ( $S$  matrices) using the Lippmann-Schwinger formalism [75, 85, 93]. The output states are then obtained by applying the  $S$  matrices on the incident states [93].

### 3.4 Output States of Fock State Scattering

In this section, we present the output states from scattering one-, two-, and three-photon number states off of a 3LS or 4LS. We assume that the incident state propagates to the right and the atom is initially in the ground state. Specifically, we consider incident states in the form of a wavepacket for two reasons: (i) in practice, any state that contains a finite number of photons is a wavepacket; (ii) as we will show, sending in wavepackets with a finite width is crucial in order to observe the bound state effects in the measurements. The continuous-mode photon-wavepacket creation operator is given by [12]

$$a_{\alpha, R/L}^\dagger = \int dk \alpha(k) a_{R/L}^\dagger(k), \quad (3.11)$$

where  $a_{R/L}^\dagger(k) = (1/\sqrt{2\pi}) \int dx e^{ikx} a_{R/L}^\dagger(x)$  and the amplitude  $\alpha(k)$  satisfies the normalization condition  $\int dk |\alpha(k)|^2 = 1$ . An incident right-going  $n$ -photon Fock state is defined as

$$|n_\alpha\rangle_R = \frac{(a_{\alpha, R}^\dagger)^n}{\sqrt{n!}} |\emptyset\rangle. \quad (3.12)$$

With the  $n$ -photon  $S$  matrices  $S^{(n)}$ , we are able to find the asymptotic output state long after the scattering ( $t \rightarrow +\infty$ ) [93]. Specifically, the single-photon output

state is given by

$$|\psi^{(1)}\rangle = \int dk \alpha(k) |\phi^{(1)}(k)\rangle, \quad |\phi^{(1)}(k)\rangle = t_k |k\rangle_R + r_k |k\rangle_L, \quad (3.13a)$$

$$|k\rangle_{R/L} = a_{R/L}^\dagger(k) |\emptyset\rangle, \quad t_k \equiv (\bar{t}_k + 1)/2, \quad r_k \equiv (\bar{t}_k - 1)/2. \quad (3.13b)$$

The two-photon output state reads

$$|\psi^{(2)}\rangle = \int dk_1 dk_2 \frac{1}{\sqrt{2}} \alpha(k_1) \alpha(k_2) |\phi^{(2)}(k_1, k_2)\rangle, \quad (3.14a)$$

$$\begin{aligned} |\phi^{(2)}(k_1, k_2)\rangle &= \int dx_1 dx_2 \left[ \frac{1}{2} t_{k_1, k_2}(x_1, x_2) a_R^\dagger(x_1) a_R^\dagger(x_2) \right. \\ &\quad \left. + r t_{k_1, k_2}(x_1, -x_2) a_R^\dagger(x_1) a_L^\dagger(x_2) \right. \\ &\quad \left. + \frac{1}{2} r_{k_1, k_2}(-x_1, -x_2) a_L^\dagger(x_1) a_L^\dagger(x_2) \right] |\emptyset\rangle, \end{aligned} \quad (3.14b)$$

where

$$\begin{aligned} t_{k_1, k_2} &\equiv t_{k_1} t_{k_2} h_{k_1}(x_1) h_{k_2}(x_2) + \frac{1}{4} B_{k_1, k_2}^{(2)}(x_1, x_2) + k_1 \leftrightarrow k_2, \\ r t_{k_1, k_2} &\equiv t_{k_1} r_{k_2} h_{k_1}(x_1) h_{k_2}(x_2) + \frac{1}{4} B_{k_1, k_2}^{(2)}(x_1, x_2) + k_1 \leftrightarrow k_2, \\ r_{k_1, k_2} &\equiv r_{k_1} r_{k_2} h_{k_1}(x_1) h_{k_2}(x_2) + \frac{1}{4} B_{k_1, k_2}^{(2)}(x_1, x_2) + k_1 \leftrightarrow k_2, \\ B_{k_1, k_2}^{(2)}(x_1, x_2) &\equiv e^{i(k_1+k_2)x_2} \sum_{j=1,2} C_j e^{-\gamma_j |x_2-x_1|} \theta(x_{21}) + (x_1 \leftrightarrow x_2). \end{aligned} \quad (3.15)$$

In Eq.(3.14), the output state has three components  $t_{k_1, k_2}$ ,  $r t_{k_1, k_2}$  (which is not a product), and  $r_{k_1, k_2}$ , corresponding to two-photon transmission, one-photon transmitted and one-photon reflected, and two-photon reflection, respectively. The first term in each of these functions is the plane-wave term. The second term is the bound-state term associated with the momentum-nonconserved (for

individual photons) processes. The three-photon output state takes a similar form and is shown in Appendix B.

With the output states, we can study induced photon-photon correlation by applying various measurements on them. We present results for transport, spectral entanglement, number statistics, and second-order correlation in the following three sections. Throughout this chapter, we choose incident Gaussian wavepackets with the spectral amplitude

$$\alpha(\omega) = \frac{1}{(2\pi\sigma^2)^{1/4}} \exp \left[ -\frac{(\omega - \omega_0)^2}{4\sigma^2} \right], \quad (3.16)$$

where  $\sigma$  is the width and  $\omega_0$  is the central frequency. We assume that level  $|3\rangle$  is metastable ( $\Gamma_3=0$ ) and levels  $|2\rangle$  and  $|4\rangle$  have the same loss rate:  $\Gamma_2 = \Gamma_4$ . In addition, we assume that the transitions  $|1\rangle \leftrightarrow |2\rangle$  and  $|3\rangle \leftrightarrow |4\rangle$  are at the same frequency,  $\omega_{21} = \omega_{43}$ , and the detuning of the control field is zero,  $\Delta = 0$ . We set the loss rate as our reference frequency unit:  $\Gamma_2 = \Gamma_4 = 1$ . The coupling strength to the waveguide is characterized by the effective Purcell factor  $P = \Gamma/\Gamma_2 = \Gamma$ . Plasmonic waveguide systems have been predicted to have a large Purcell factor [62] and a value of  $P = 1.5$  has been demonstrated experimentally [17]. Slot waveguides have been theoretically shown to have large values of  $P$  reaching 16. Recently, by carefully tailoring the ends of photonic nanowires, J. Claudon *et al.* achieved a value of  $P \geq 9$  in the experiment [43, 45]. Furthermore,  $5.7 < P < 24$  was demonstrated in a photonic crystal waveguide coupled to a quantum dot [47]. In superconducting circuits with 1D open superconducting transmission lines [40, 44, 46], even larger values of  $P$  have been achieved, exceeding 15 [46].

### 3.5 Photonic Transport: Photon Blockade and Photon-induced Tunneling

In this section, we study single-photon and two-photon transport in the presence of photon-photon bound states. Previously, cavity-QED systems have been used to study various nonlinear quantum optical phenomena such as photon blockade [33], which means photons tend to block each other during transmission, and photon induced-tunneling [105], which means photons enhance the transmission of each other. Here, we show that both photon blockade and photon-induced tunneling emerge in the waveguide-QED system without the need of a cavity.

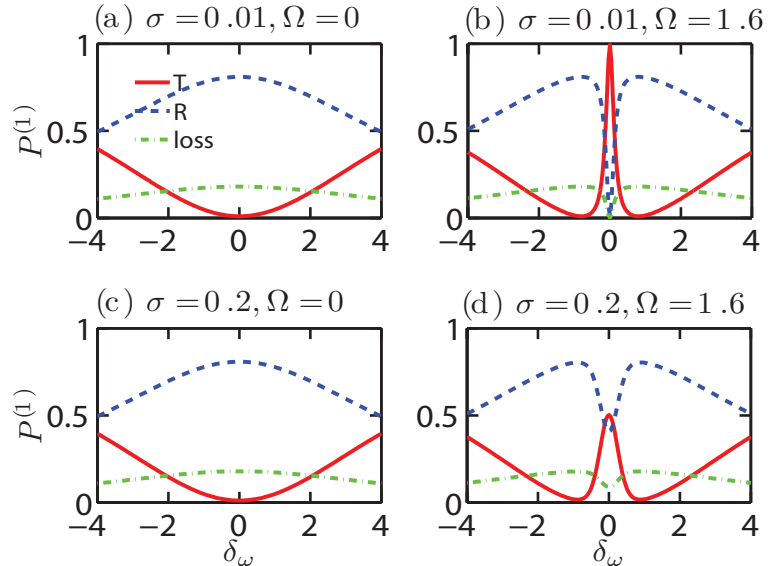


FIGURE 3.2: Single-photon transmission  $T$  (solid), reflection  $R$  (dashed) and loss (dotted) as a function of incident photon detuning, for the values of  $\sigma$  (the wavepacket width) and  $\Omega$  (the strength of the control field) shown. Here, the effective Purcell factor is  $P = 9$ . Note the sharp EIT window, particularly in the narrow wavepacket case.

### 3.5.1 Single-Photon

With the output state in Eq. (3.13), the transmission ( $T$ ), and reflection ( $R$ ) probabilities for a single-photon are

$$T = \int dk |_R \langle k | \psi^{(1)} \rangle|^2 = \int dk \alpha^2(k) |t_k|^2, \quad (3.17a)$$

$$R = \int dk |_L \langle k | \psi^{(1)} \rangle|^2 = \int dk \alpha^2(k) |r_k|^2, \quad (3.17b)$$

which are the same for both the 3LS and 4LS cases. Figure 3.2 shows  $T$ ,  $R$ , and the loss ( $1 - T - R$ ) as a function of the detuning  $\delta_\omega \equiv \omega_0 - \omega_{21}$  at  $P = 9$ . Clearly, EIT appears in Fig. 3.2(b), when the control field is on. As one increases the width of the wavepacket, as shown in Fig. 3.2(d), the EIT peak is suppressed as  $\sigma$  becomes comparable with the width of EIT window ( $\sim \Omega^2/2\Gamma$ ), see Eqs. (3.8) and (3.13). In Fig. 3.2(a), and (c), we set  $\Omega = 0$ , which means the control field is off and the 3LS (4LS) becomes a reflective two-level system [62, 93, 70]. Notice that the width of the reflective peak in the  $\Omega = 0$  case is  $\sim \Gamma$  and hence is insensitive to the increase of  $\sigma$  from 0.01 to 0.2.

### 3.5.2 Two-Photon

The two-photon transmission and reflection probabilities are given by

$$P_{TT}^{(2)} = \int dk_1 dk_2 \frac{1}{2} |_{TT} \langle k_1, k_2 | \psi^{(2)} \rangle|^2, \quad (3.18a)$$

$$P_{TR}^{(2)} = \int dk_1 dk_2 |_{TR} \langle k_1, k_2 | \psi^{(2)} \rangle|^2, \quad (3.18b)$$

$$P_{RR}^{(2)} = \int dk_1 dk_2 \frac{1}{2} |_{RR} \langle k_1, k_2 | \psi^{(2)} \rangle|^2, \quad (3.18c)$$

where  $P_{TT}^{(2)}$ ,  $P_{TR}^{(2)}$ , and  $P_{RR}^{(2)}$  are the probabilities to observe two transmitted photons, one transmitted and one reflected photons, and two reflected photons, respectively. We separate the two-photon transmission and reflection probabilities into two parts:  $(P^{(2)})_{\text{PW}}$  is the contribution from independent single-particle transmission (denoted PW for “plane wave”), and  $(P^{(2)})_{\text{BS}}$  is the contribution from both the bound-state term in Eq.(3.14) and the interference between the plane wave and bound-state terms. As an example,  $P_{TT}^{(2)}$  is split as follows

$$P_{TT}^{(2)} = \int dk_1 dk_2 |\tilde{t}_2(k_1, k_2) + \tilde{B}(k_1, k_2)|^2 = (P_{TT}^{(2)})_{\text{PW}} + (P_{TT}^{(2)})_{\text{BS}}, \quad (3.19a)$$

$$(P_{TT}^{(2)})_{\text{PW}} = \int dk_1 dk_2 |\tilde{t}_2(k_1, k_2)|^2, \quad (3.19b)$$

$$(P_{TT}^{(2)})_{\text{BS}} = \int dk_1 dk_2 [\tilde{t}_2^*(k_1, k_2) \tilde{B}(k_1, k_2) + c.c. + |\tilde{B}(k_1, k_2)|^2], \quad (3.19c)$$

where

$$\begin{aligned} \tilde{t}_2(k_1, k_2) &= \alpha(k_1)\alpha(k_2)t_{k_1}t_{k_2}, \\ \tilde{B}(k_1, k_2) &= \frac{i}{4c} \sum_{j=1,2} \left( \frac{1}{k_1 + i\gamma_j} + \frac{1}{k_2 + i\gamma_j} \right) \\ &\times \int dk \alpha(k) \alpha(k_1 + k_2 - k) C_j(k, k_1 + k_2 - k). \end{aligned} \quad (3.20)$$

Figure 3.3 shows the two-photon transmission and reflection probabilities for both the 3LS and 4LS cases, decomposed in this way. Because the PW term is from the single-particle solution, it is the same for both the 3LS and 4LS. However,  $(P^{(2)})_{\text{BS}}$  is quite different for the 3LS and 4LS. Figure 3.3(a)-(c) shows  $P^{(2)}$  as a function of incident photon detuning. Close to resonance, in the 3LS case  $(P^{(2)})_{\text{BS}}$  enhances the two-photon transmission  $P_{TT}^{(2)}$  while suppressing  $P_{TR}^{(2)}$ .

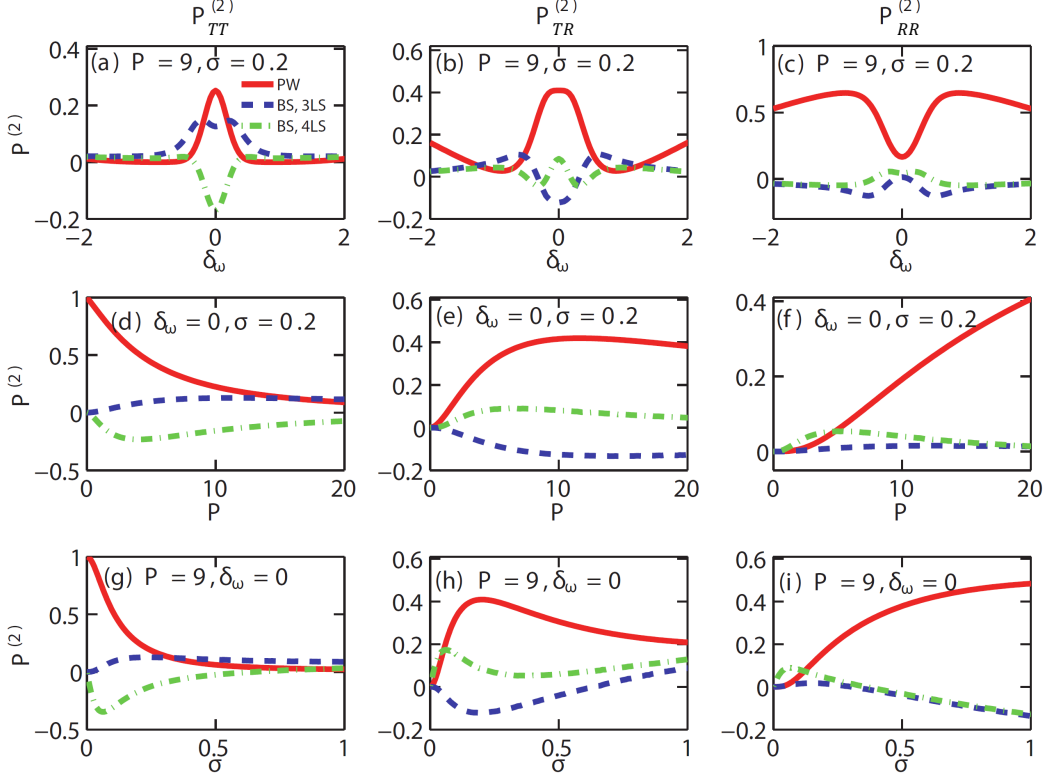


FIGURE 3.3: Two-photon transmission and reflection probabilities for the 3LS and 4LS cases. (a)-(c) As a function of incident photon detuning  $\delta_\omega$  with  $P = 9$  and  $\sigma = 0.2$ . (a) Probability that both photons are transmitted (and hence are right-going,  $P_{TT}^{(2)}$ ). (b) Probability that one photon is transmitted and one reflected (right-left,  $P_{TR}^{(2)}$ ). (c) Probability that both photons are reflected (both left-going,  $P_{RR}^{(2)}$ ). (d)-(f) As a function of  $P$  with  $\delta_\omega = 0$  and  $\sigma = 0.2$ . (g)-(i) As a function of  $\sigma$  with  $P = 9$  and  $\delta_\omega = 0$ . The label PW refers to the contribution from the plane-wave term only, while BS refers to all the other contributions involving bound-state terms [Eq. (3.19)]. Here, we set  $\Omega = 1.6$ . The bound state effect enhances transparency in the 3LS case but blocks two-photon transmission past a 4LS. Note that a non-zero  $\sigma$  is crucial to observe these effects.

In contrast, in the 4LS case  $(P^{(2)})_{\text{BS}}$  has exactly the opposite effect. This leads to enhanced multiphoton EIT for the 3LS [69] and photon blockade for the 4LS [70]. Such enhanced EIT and photon blockade are caused by the interference between the two multiphoton scattering pathways: passing by the atom as independent particles or a composite particle in the form of bound states (for a detailed analysis, see Appendix C).

In Fig. 3.3(d)-(f), we plot  $P^{(2)}$  as a function the effective Purcell factor  $P$  for the on-resonance case,  $\delta_\omega = 0$ . It is remarkable that, for  $P_{TT}^{(2)}$  and  $P_{TR}^{(2)}$ ,  $(P^{(2)})_{\text{BS}}$  becomes comparable to  $(P^{(2)})_{\text{PW}}$  in the strong coupling regime. An important implication is that the bound-state effect can be observed in photonic transport experiments, given recent rapid experimental advances [40, 43, 44, 45, 46].

Fig. 3.3(g)-(i) shows  $P^{(2)}$  as a function of the wavepacket width  $\sigma$  with  $P = 9$  and the photons on resonance with the atom. There are several notable features. First, as  $\sigma$  approaches zero,  $(P^{(2)})_{\text{BS}}$  shrinks to zero for both the 3LS and 4LS cases. This further highlights that sending in a wavepacket with a finite width is crucial to observe the bound state effect in photonic transport. Physically, this occurs because, in the  $\sigma = 0$  limit under EIT conditions, the atom is fully transparent ( $T = 1$ ) to the incoming photons and hence the atom-mediated photon-photon interaction is absent, inhibiting any bound state effect. For the general case without EIT conditions, the above conclusion still holds: as  $\sigma \rightarrow 0$ , the bound state effect vanishes in multiphoton transport. This is because the bound-state term in Eq. (3.20) originates from the coincident photons at the atomic site: as  $\sigma \rightarrow 0$ , the wavepacket becomes infinitely long and the probability of coincidence vanishes. Second, notice that while  $(P^{(2)})_{\text{BS}}$  approaches zero for  $P_{TT}^{(2)}$  as  $\sigma$  increases, its magnitude for  $P_{TR}^{(2)}$  and  $P_{RR}^{(2)}$  increases after an initial decrease. This is due to the enhanced interference between the plane-wave and bound-state terms [Eq. (3.14)] for  $P_{TR}^{(2)}$  and  $P_{RR}^{(2)}$ .

The result for three photon scattering shows behavior similar to the two-photon case. To avoid duplication, we do not present it here.

### 3.5.3 Photon Blockade and Photon-induced Tunneling

To quantify the observed enhancement of EIT and photon blockade in Fig. 3.3, we define the strength of photon blockade  $P_{21}$  for the two-photon case by the conditional probability for transmitting a second photon given that the first photon has already been transmitted, normalized by the single-photon transmission probability. For independent photons, there is no photon blockade and  $P_{21} = 1$ . In the opposite limit of strong photon blockade,  $P_{21}$  is suppressed towards zero.

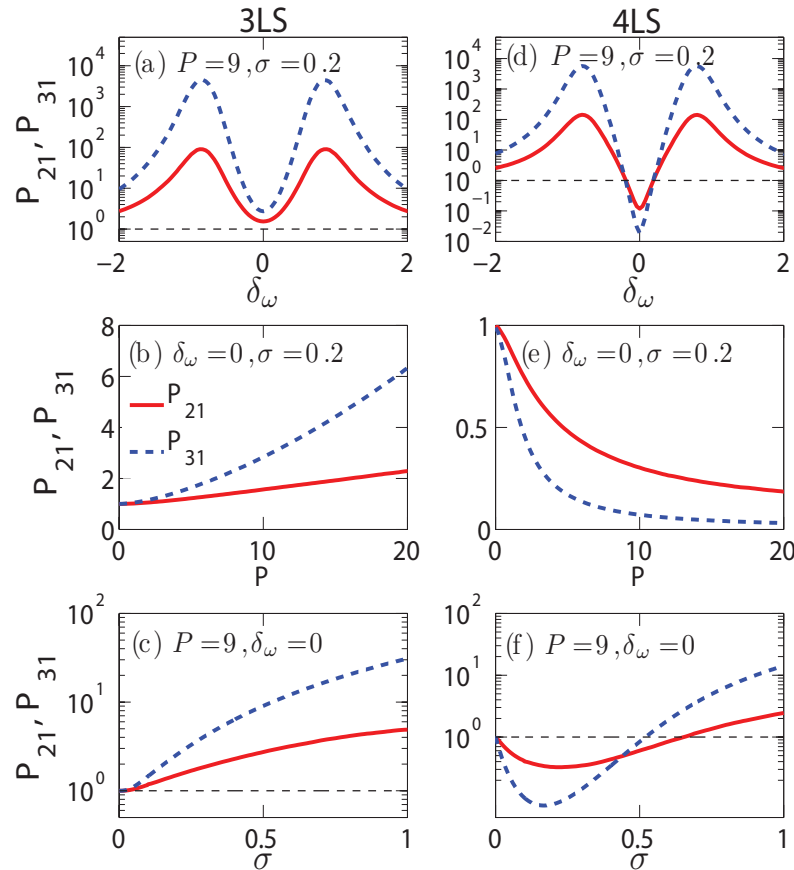


FIGURE 3.4: Photon blockade and photon-induced tunneling in transmission. Photon blockade strengths  $P_{21}$  (solid line) and  $P_{31}$  (dashed line) as a function of incident photon detuning  $\delta_\omega$ ,  $P$  and  $\sigma$  for (a)-(c) the 3LS case, and (d)-(f) the 4LS case. Here,  $\Omega = 1.6$ . The 3LS causes photon-induced tunneling while the 4LS causes photon blockade.

Similarly, we can define  $P_{31}$  for the three-photon case. We thus have

$$P_{21} \equiv \frac{P_{TT}^{(2)}}{T^2}, \quad P_{31} \equiv \frac{P_{TTT}^{(3)}}{T^3}. \quad (3.21)$$

As shown in Fig. 3.4(a)-(c), for the 3LS case, the single-photon EIT is enhanced in two-photon and three-photon transmission by interaction with the 3LS. Pronounced photon-induced tunneling [105] due to the strong correlations between transmitted photons occurs in this case:  $P_{21}, P_{31} > 1$ . In contrast, as shown in Fig. 3.4(d) and (e), scattering from a 4LS exhibits a different behavior within the EIT window, namely, photon blockade [70]:  $P_{21}, P_{31} < 1$ . However, away from the EIT window,  $P_{21}$  and  $P_{31}$  become larger than 1, signaling a new regime of multi-photon transmission—photon-induced tunneling [105]. For increasing coupling strength [Fig. 3.4(e)],  $P_{21}$  and  $P_{31}$  approach zero asymptotically when the incident photons are on resonance with the 4LS. In addition, from Fig. 3.4(c) and (f), we confirm that both photon blockade and photon-induced tunneling go away in the zero-width limit ( $\sigma \rightarrow 0$ ).

### 3.6 Spectral Entanglement

It is clear that the two-photon bound state in Eq. (3.14) is entangled in the momentum (or equivalently frequency) degree of freedom. To probe this spectral aspect of the two-photon entanglement, we rewrite the two-photon output state [Eq. (3.14)] in frequency space as

$$\begin{aligned} |\psi^{(2)}\rangle = & \int d\omega_1 d\omega_2 \left[ f_{TT}(\omega_1, \omega_2) a_R^\dagger(\omega_1) a_R^\dagger(\omega_2) \right. \\ & + f_{TR}(\omega_1, \omega_2) a_R^\dagger(\omega_1) a_L^\dagger(\omega_2) \\ & \left. + f_{RR}(\omega_1, \omega_2) a_L^\dagger(\omega_1) a_L^\dagger(\omega_2) \right] |\emptyset\rangle, \end{aligned} \quad (3.22)$$

where  $f_{TT}(\omega_1, \omega_2)$ ,  $f_{TR}(\omega_1, \omega_2)$ , and  $f_{RR}(\omega_1, \omega_2)$  are the two-photon amplitudes for a transmitted pair, a pair of one transmitted and one reflected, and a reflected pair, respectively. Explicitly, they take the following form

$$f_{TT}(\omega_1, \omega_2) = \tilde{t}_2(\omega_1, \omega_2) + \tilde{B}(\omega_1, \omega_2), \quad (3.23a)$$

$$f_{TR}(\omega_1, \omega_2) = 2[\tilde{r}t(\omega_1, \omega_2) + \tilde{B}(\omega_1, \omega_2)], \quad (3.23b)$$

$$f_{RR}(\omega_1, \omega_2) = \tilde{r}_2(\omega_1, \omega_2) + \tilde{B}(\omega_1, \omega_2), \quad (3.23c)$$

$$\tilde{t}_2(\omega_1, \omega_2) = t_{\omega_1} t_{\omega_2} \alpha(\omega_1) \alpha(\omega_2), \quad (3.23d)$$

$$\tilde{r}t(\omega_1, \omega_2) = t_{\omega_1} r_{\omega_2} \alpha(\omega_1) \alpha(\omega_2), \quad (3.23e)$$

$$\tilde{r}_2(\omega_1, \omega_2) = r_{\omega_1} r_{\omega_2} \alpha(\omega_1) \alpha(\omega_2), \quad (3.23f)$$

where  $\tilde{B}(\omega_1, \omega_2)$  is given in Eq.(3.20). The first term in  $f(\omega_1, \omega_2)$  is the uncorrelated contribution, while the second term signals photon correlation. From Eq.(3.23), we define the joint spectral function of the two-photon states to be [86]

$$F_{\alpha\beta=TT, TR, RR}(\omega_1, \omega_2) = |f_{\alpha\beta}(\omega_1, \omega_2)|^2. \quad (3.24)$$

For the purpose of comparison, we also define the uncorrelated spectral function of the two-photon states,

$$G_{TT}(\omega_1, \omega_2) \equiv |\tilde{t}_2(\omega_1, \omega_2)|^2, \quad (3.25a)$$

$$G_{TR}(\omega_1, \omega_2) \equiv 4|\tilde{r}t(\omega_1, \omega_2)|^2, \quad (3.25b)$$

$$G_{RR}(\omega_1, \omega_2) \equiv |\tilde{r}_2(\omega_1, \omega_2)|^2. \quad (3.25c)$$

Figure 3.5 shows the two-photon uncorrelated and joint spectra in the case of on-resonance photons ( $\delta_\omega = 0$ ) and for a spectrally narrow wavepacket ( $\sigma = 0.01$ ). With the chosen parameters, the EIT peak width is much larger than

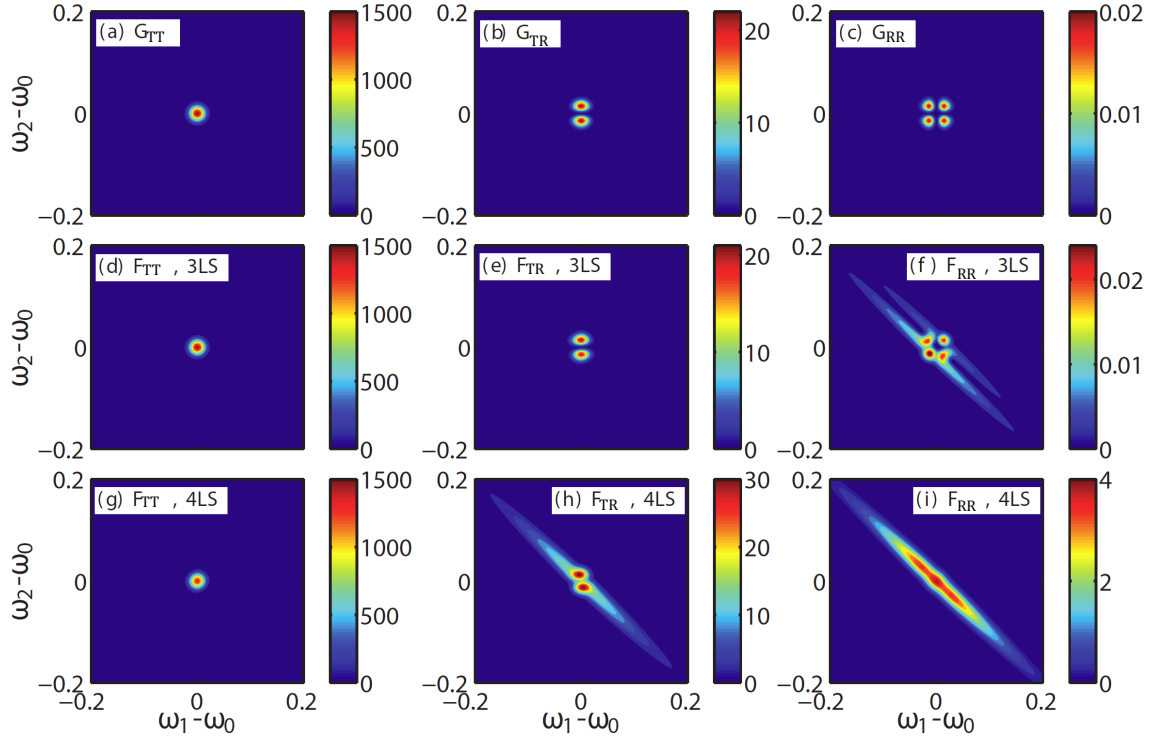


FIGURE 3.5: Two-photon joint spectrum of the output states after scattering off a 3LS and 4LS in the case of a spectrally narrow incident wavepacket. Panels (a)-(c) show the uncorrelated spectra  $G_{TT}(\omega_1, \omega_2)$ ,  $G_{TR}(\omega_1, \omega_2)$ , and  $G_{RR}(\omega_1, \omega_2)$ , respectively. Panels (d)-(f) show the joint spectra of the field after scattering off a 3LS for two transmitted photons, for one transmitted and one reflected, and for two reflected photons, respectively. Panels (g)-(i) show the joint spectra of the fields after scattering off a 4LS. Strong spectral entanglement is indicated in panel (i); this reflected field is essentially a pure two-photon bound state. System parameters:  $P = 9$ ,  $\Omega = 1.6$ ,  $\delta_\omega = 0$ ,  $\sigma = 0.01$ . We set the loss rate of level 2 as our frequency unit:  $\Gamma_2 = 1$ .

the wavepacket,  $\sim \Omega^2/2\Gamma \cong 0.14 \gg \sigma$ . Therefore, for the uncorrelated pair of transmitted photons [ $G_{TT}$ , Fig. 3.5(a)], there is only a sharp peak at  $\omega_1 = \omega_2 = \omega_0$  caused by the Gaussian spectrum of the incident photons. For the uncorrelated pair of one transmitted and one reflected photons ( $G_{TR}$ ), there are two peaks resulting from the interplay of the spectrum of the incident photons and the rapid increase of the reflection probability away from the EIT peak (see Fig. 3.2). Accordingly, there are four peaks for the case of two reflected photons, as shown

in Fig. 3.5(c).

Figure 3.5(d)-(f) shows the joint spectra for the case of 3LS scattering. It is evident that the joint spectra of the pair of two transmitted photons ( $F_{TT}$ ), and the pair of one transmitted and one reflected photons ( $F_{TR}$ ), are dominated by the uncorrelated transmission. The joint spectrum of the pair of two reflected photons [Fig. 3.5(f)] is slightly modified from the uncorrelated spectrum along the diagonal line. This is caused by the correlated bound state term  $\tilde{B}(\omega_1, \omega_2)$ . For the 3LS case with the chosen parameters, the correlation term  $\tilde{B}(\omega_1, \omega_2)$  is of order  $10^{-1}$  and hence is too weak to affect  $F_{TT}$  and  $F_{TR}$ .

In contrast, for the 4LS case [Fig. 3.5(g)-(i)],  $F_{TR}$  and  $F_{RR}$  are greatly modified by the correlation term, while  $F_{TT}$  is still dominated by the uncorrelated transmission. In particular, as shown in Fig. 3.5 (i), the joint spectrum of the reflected pair is dominated by  $\tilde{B}(\omega_1, \omega_2)$ . *This pair is primarily made up of a pure two-photon bound state:* the frequencies of the photon pair are correlated along the line  $\omega_1 + \omega_2 = 2\omega_0$  with uncertainty  $\sigma$ . A similar correlated photon pair was demonstrated in a two-level system shown in Fig. 2.6 as well as in a waveguide-cavity system [106]. Notice that the bandwidth (along the line  $\omega_1 + \omega_2 = 2\omega_0$ ) of spectral entanglement is much narrower than that shown in Fig. 2.6. This is because the bandwidth is given by  $\Gamma$  in the 2LS case (Fig. 2.6), while in the 4LS case it is determined by the EIT peak width  $\Omega^2/2\Gamma$ .

The two-photon bound state is a composite object of photons with effective *attractive* interaction; it displays strong bunching behavior in photon-photon correlation measurements. Such a photon pair is highly entangled in frequency because measurement of the frequency of one photon unambiguously determines that of the other. This strong spectral correlation provides more information per photon pair and could be used to implement large-alphabet quantum commu-

nication [92].

### 3.7 Photon-Photon Correlation

In this section, we study the scattering of a coherent state off a 3LS or 4LS. We probe the strong photon-photon correlation in the transmitted field by studying first the number statistics and then the second-order correlation function.

#### 3.7.1 Non-Classical Light Source

We consider the case that the 3LS or 4LS is in its ground state initially and there is an incident continuous-mode coherent state of mean photon number

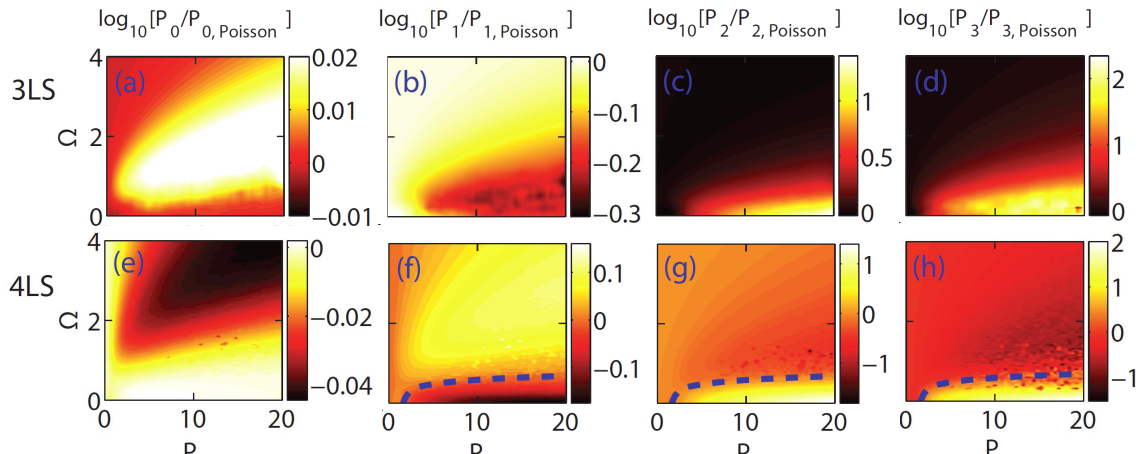


FIGURE 3.6: Nonclassical light source. Photon number statistics quantified by  $\log_{10}(P_n/P_{n,\text{Poisson}})$ , where  $P_n$  and  $P_{n,\text{Poisson}}$  are the  $n$ -photon probability in the transmitted field and in a coherent state with the same mean photon number, respectively. Panels (a)-(d) show the results of the transmitted field after scattering off the 3LS for  $n = 0, 1, 2, 3$ , respectively. Panels (e)-(h) show the results of the transmitted field after scattering off the 4LS for  $n = 0, 1, 2, 3$ , respectively. The dashed line is a guide to the eye for equal probabilities,  $P_n/P_{n,\text{Poisson}} = 1$ . The speckle in the plots is numerical noise, coming from numerical evaluation of high-dimensional integrals in computing the transmission and reflection probabilities. System parameters:  $\delta_\omega = 0$ ,  $\sigma = 0.2$ , and  $\bar{n} = 1$  in the incident coherent state. Scattering off a 3LS enhances the multiphoton content of the pulse because of multi-photon EIT; in contrast, the photon blockade in the 4LS case suppresses essentially all multi-photon content, thus realizing a single-photon source.

$\bar{n} = 1$ , spectral width  $\sigma = 0.2$ , and central frequency on resonance with the atom,  $\omega_0 = \omega_{21}$ . In this case, the contribution from the four-photon state can be neglected ( $\sim 1.6\%$ ). The photon-number statistics in the transmitted field is obtained by first applying the  $S$  matrices to the incident state and then measuring the transmitted field, as described in Ref. [93].

We present the results for both the 3LS and 4LS cases in Fig. 3.6 by taking the ratio of the photon-number distribution in the transmitted field  $P_n$  ( $n = 0, 1, 2, 3$ ) to that of a coherent state  $P_{n,\text{Poisson}}$  having the same mean photon number as the transmitted field. From Fig. 3.6(a)-(d), it is clear that when the EIT condition is satisfied, the 3LS induces strong photon-photon interactions, which in turn reduce the one-photon probability and redistributes the weight to the two- and three-photon probabilities. This comes about because the bound state in the 3LS case enhances multiphoton EIT, as we have shown in Sec. 3.5.

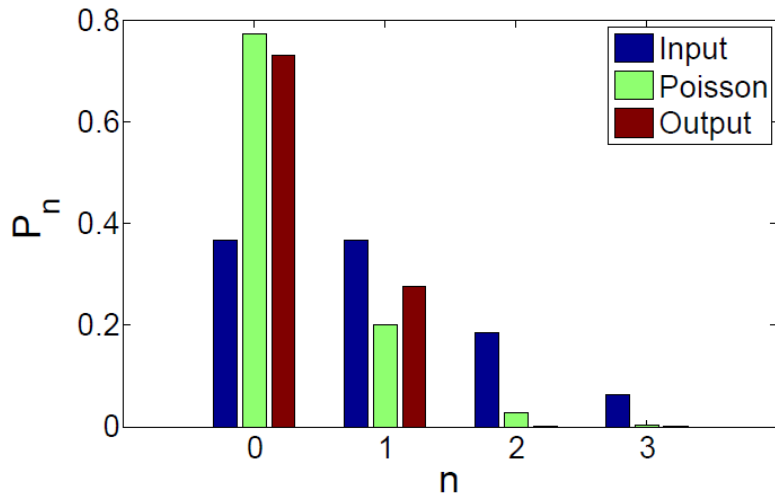


FIGURE 3.7: Photon number statistics of the transmitted field compared to a Poissonian field with the same mean photon number. Blue bar: input coherent state; red bar: output from scattering off 4LS; green bar: Poissonian distribution. System parameters:  $P = 11$ ,  $\Omega = 1.4$ ,  $\delta_\omega = 0$ ,  $\sigma = 0.2$ , and  $\bar{n} = 1$  in the incident coherent state.

In contrast, for the 4LS case shown in Fig. 3.6(e)-(h), in most of the parameter space, we have enhanced single-photon probability while suppressed multiphoton content:  $P_1 > P_{1,\text{Poisson}}$  and  $P_{2(3)} < P_{2(3),\text{Poisson}}$ . For instance, in Fig. 3.7, we show the specific case of  $P = 11$  and  $\Omega = 1.4$ . Clearly, the nonlinear interaction between photons and 4LS leads to the photon number redistribution among different sectors: multiphoton contents are transferred to single photon sector. This gives rise to a sub-Poissonian single-photon source [70], which comes about because, while EIT occurs in the single-photon transmission, multiphoton states experience photon blockade, as shown in Sec. 3.5. Therefore, we demonstrate that the waveguide-atom system is capable of generating nonclassical light, which may find applications distributed quantum networking [18, 19] or in quantum cryptography [88, 89, 107, 108] as shown in Chapter 5.

### 3.7.2 Second-Order Correlation Function

To further probe the nonclassical character of the transmitted field, we calculate the second-order correlation function  $g^{(2)}(\tau)$ , which is often measured experimentally. For a steady state,  $g^{(2)}$  of the transmitted field is defined as

$$g^{(2)}(\tau) = \lim_{t \rightarrow \infty} \frac{\langle a_R^\dagger(x, t) a_R^\dagger(x, t + \tau) a_R(x, t + \tau) a_R(x, t) \rangle}{\langle a_R^\dagger(x, t) a_R(x, t) \rangle \langle a_R^\dagger(x, t + \tau) a_R(x, t + \tau) \rangle}. \quad (3.26)$$

As shown in Appendix D, for our system, this definition is equivalent to following expression in the Schrödinger picture,

$$g^{(2)}(\tau) = \frac{\langle \psi | a_R^\dagger(x) a_R^\dagger(x + c\tau) a_R(x + c\tau) a_R(x) | \psi \rangle}{\langle \psi | a_R^\dagger(x) a_R(x) | \psi \rangle \langle \psi | a_R^\dagger(x + c\tau) a_R(x + c\tau) | \psi \rangle}, \quad (3.27)$$

where  $|\psi\rangle$  is the asymptotic output state. With a weak incident coherent state (mean photon number  $\bar{n} \ll 1$ ), we consider only the contribution of the two-

photon and one-photon states in the numerator and denominator in Eq.(3.27), respectively. Substitution of the single-photon and two-photon transmission wavefunctions from Eqs.(3.13) and (3.14) into Eq.(3.27) yields the explicit expression

$$g^{(2)}(\tau) = \frac{|\int dk_1 dk_2 \alpha(k_1) \alpha(k_2) [t_{k_1} t_{k_2} (e^{-ik_1\tau} + e^{-ik_2\tau}) + B(\tau)]|^2}{|\int dk_1 dk_2 \alpha(k_1) \alpha(k_2) t_{k_1} t_{k_2} (e^{-ik_1\tau} + e^{-ik_2\tau})|^2},$$

$$B(\tau) = \pi(C_1 e^{-\gamma_1 c\tau} + C_2 e^{-\gamma_2 c\tau}). \quad (3.28)$$

In the numerator, the first term and the second term  $B(\tau)$  come from the plane wave and bound state pieces, respectively, in Eq.(3.14).

Figure 3.8(a) shows  $g^{(2)}(0)$ , which is the same for the 3LS and 4LS cases. The presence of level  $|4\rangle$  does not contribute to  $g^{(2)}(0)$ : it takes two quanta to excite  $|4\rangle$ , which then deexcites in the form of cascade emission with zero probability to emit two photons at the same time. In Fig.3.8(a), there is rich bunching and anti-bunching behavior, caused by the two-body bound state. At  $\tau=0$ , the amplitude of the bound state term in Eq.(3.28) is  $B(0) = -2r_{k_1} r_{k_2}$ , where  $r_{k_1(2)}$  is the single-photon reflection coefficient. Hence, in the numerator of  $g^{(2)}(0)$ , the amplitudes of the plane-wave and bound-state terms are out of phase. When  $P = 0$ , the bound state term is zero and  $g^{(2)}(0) = 1$ . As  $P$  increases, the strength of the bound state increases, causing  $g^{(2)}(0)$  to decrease until the bound state term cancels the plane wave term exactly, producing complete anti-bunching. Further increase of  $P$  leads to a rise of  $g^{(2)}(0)$  and eventually photon bunching.

By comparing Fig. 3.4(c)-(d) and Fig. 3.8(a), we find that photon anti-bunching and photon blockade, and photon bunching and photon-induced tunneling do *not* have a one-to-one correspondence. For example, in the whole parameter regime of Fig. 3.4(d), photon blockade is present; while in Fig. 3.8, there is a

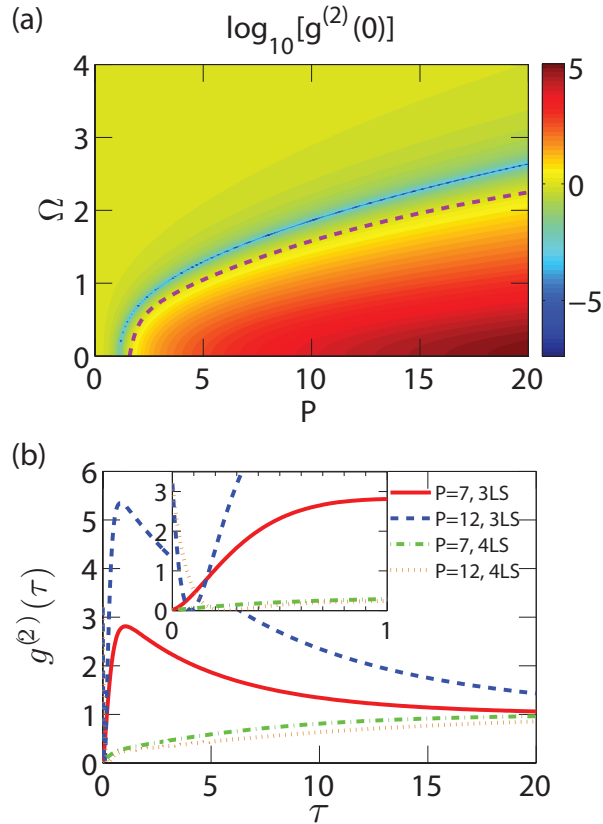


FIGURE 3.8: Bunching and anti-bunching. Second-order correlation function  $g^{(2)}(\tau)$  of the transmitted field for a weak incident coherent state ( $\bar{n} \ll 1$ ) of width  $\sigma = 0.2$ , resonant with the atom ( $\delta_\omega = 0$ ). (a) Color map plot of  $\log_{10}[g^{(2)}(0)]$  as a function of the strength of the classical control field,  $\Omega$ , and the effective Purcell factor  $P$ . The dashed line marks the border between bunching ( $g^{(2)}(0) > 1$ ) and anti-bunching ( $g^{(2)}(0) < 1$ ) behavior. (b)  $g^{(2)}$  as a function of time delay  $\tau$  in four cases (using  $\Omega = 1.6$ ). Inset: zoom at short time scales.

large region of parameter space where photon bunching [ $g^{(2)}(0) > 1$ ] instead of photon anti-bunching [ $g^{(2)}(0) < 1$ ] is observed. This is because we are studying a state of continuous modes and performing instantaneous measurements at two space-time points  $(x, t)$  and  $(x, t + \tau)$ . If one integrates over the time  $t$  in the measurement [12], as done in many experiments in which the detector integration time is much longer than the wavepacket duration, one finds a one-to-one correspondence between photon anti-bunching and photon blockade, and

photon bunching and photon-induced tunneling.

The time dependence of  $g^{(2)}(\tau)$  is shown in Fig. 3.8(b). There are two characteristic time scales:  $\tau_1 = 1/\text{Re}[c\gamma_1]$  and  $\tau_2 = 1/\text{Re}[c\gamma_2]$ . Within the short time scale,  $g^{(2)}$  can display either bunching or anti-bunching for both the 3LS and 4LS cases, depending on the system parameters, as shown in the inset of Fig. 3.8. On the long time scale, for the 3LS case,  $g^{(2)}$  shows bunching— $g^{(2)}(\tau) > 1$ —corresponding to the enhanced multiphoton transmission already apparent from both the photon-induced tunneling [Fig. 3.4(c)] and the enhanced multiphoton content in the number statistics [Fig. 3.6]. For the 4LS case, anti-bunching [ $g^{(2)}(\tau) < 1$ ] dominates at long times, corresponding to the photon blockade observed in Fig. 3.4(d) and the enhanced single-photon content in Fig. 3.6. *Hence, for our pulsed output state,  $g^{(2)}(\tau = 0)$  displays rich physics due to the induced photon-photon correlation, but is not necessarily a good guide to the photon statistics.*

### 3.8 Conclusion

In summary, we present a waveguide-QED-based scheme to generate strongly-correlated photons, of interest for both many-body physics and quantum information science. Photon bound-states appear in the scattering eigenstates as a manifestation of the photon-photon correlation. As a result, while single photons experience EIT in the proposed waveguide-atom system, multiphoton states can display either photon blockade or photon-induced tunneling, depending on the detailed structure of the “atom”. From either the photon blockade or photon-induced tunneling that occurs, nonclassical light sources can be generated by sending coherent states into the system. In the most interesting case, a 4LS removes the multiphoton content from the coherent state, leaving a pulse with

only zero or single photon content.

In addition, we find that the system can be used to produce highly entangled photon pair states in frequency space, potentially of use for large alphabet quantum communication. Finally, we show that rich bunching or anti-bunching behavior is present in the second-order correlation function as a signature of the strong photon-photon correlation mediated by the “atom”. Given the recent rapid experimental advances in several realizations, the proposed waveguide-QED system is emerging as a promising route to *cavity-free open quantum networks*, which are crucial for both large-scale quantum computation and long-distance quantum communication.

# 4

## Two-Qubit System: Persistent Quantum Beats and Long-Distance Entanglement

*Summary:* <sup>1</sup>We study photon-photon correlations and entanglement generation in a one-dimensional waveguide coupled to two qubits with an arbitrary spatial separation. To treat the combination of nonlinear elements and 1D continuum, we develop a novel Green function method. The vacuum-mediated qubit-qubit interactions cause quantum beats to appear in the second-order correlation function. We go beyond the Markovian regime and observe that such quantum beats persist much longer than the qubit life time. A high degree of long-distance entanglement can be generated, increasing the potential of waveguide-QED systems for scalable quantum networking.

---

<sup>1</sup> Part of the text of this chapter has been adapted from the following previously published article: Huaixiu Zheng, and Harold U. Baranger, "Persistent Quantum Beats and Long-Distance Entanglement from Waveguide-Mediated Interactions", *Phys. Rev. Lett.* **110**, 113601 (2013).

## 4.1 Introduction

One-dimensional (1D) waveguide-QED systems are emerging as promising candidates for quantum information processing [18, 61, 62, 64, 66, 67, 68, 69, 70, 74, 75, 93, 109, 110, 111], motivated by tremendous experimental progress in a wide variety of systems [17, 41, 42, 43, 44, 45, 46, 47, 48, 71]. Over the past few years, a *single* emitter strongly coupled to a 1D waveguide has been studied extensively [61, 62, 64, 66, 67, 68, 69, 70, 72, 74, 75, 93, 111]. Photon-photon bound states [69, 70, 74] emerge as a result of nonlinear interactions between the emitter and the 1D bosonic continuum, and single-photon switches [62, 66, 68] have been proposed based on a single three-level emitter. Experimentally, a quantum amplifier [71] and a single-photon router [46] have been demonstrated using superconducting qubits coupled to open transmission lines. To enable greater quantum networking potential using waveguide-QED [18], it is important to study systems having more than just one qubit.

In this Chapter, we study cooperative effects of *two* qubits strongly coupled to a 1D waveguide, finding the photon-photon correlations and qubit entanglement beyond the well-studied Markovian regime [112, 113, 114, 115]. A key feature is the combination of these two highly nonlinear quantum elements with the 1D continuum of states. In comparison to either linear elements coupled to a waveguide [116, 117, 118, 119] or two qubits coupled to a single mode serving as a bus [120], both of which have been studied previously, new physical effects appear. To study these effects, we develop a numerical Green function method to compute the photon correlation function for an arbitrary interqubit separation.

The strong quantum interference in 1D, in contrast to the three-dimensional case [121], makes the vacuum-mediated qubit-qubit interaction [122] long-ranged.

We find that quantum beats emerge in the photon-photon correlations, and persist to much longer time scales in the non-Markovian regime. We show that such persistent quantum beats arise from quantum interference between emission from two subradiant states. Furthermore, we demonstrate that a high-degree of long-distance entanglement can be generated, thus supporting waveguide-QED-based open quantum networks.

## 4.2 Hamiltonian

As shown in Fig. 4.1(a), we consider two qubits with transition frequencies  $\omega_1$  and  $\omega_2$ , separation  $L = \ell_2 - \ell_1$ , and dipole couplings to a 1D waveguide. The Hamiltonian of the system is <sup>2</sup>

$$\begin{aligned} H &= \sum_{j=1,2} \hbar(\omega_j - i\Gamma'_j/2)\sigma_j^+ \sigma_j^- + H_{wg} \\ &+ \sum_{j=1,2} \sum_{\alpha=R,L} \int dx \hbar V_j \delta(x - \ell_j) [a_\alpha^\dagger(x) \sigma_j^- + \text{h.c.}], \\ H_{wg} &= \int dx \frac{\hbar c}{i} \left[ a_R^\dagger(x) \frac{d}{dx} a_R(x) - a_L^\dagger(x) \frac{d}{dx} a_L(x) \right], \end{aligned} \quad (4.1)$$

where  $a_{R,L}^\dagger(x)$  is the creation operator for a right- or left-going photon at position  $x$  and  $c$  is the group velocity of photons.  $\sigma_j^+$  and  $\sigma_j^-$  are the qubit raising and lowering operators, respectively. An imaginary term in the energy level is included to model the spontaneous emission of the excited states at rate  $\Gamma'_{1,2}$  to modes other than the waveguide continuum [50]. The decay rate to the waveguide continuum is given by  $\Gamma_j = 2V_j^2/c$ .

---

<sup>2</sup> Note that we adopt the rotating wave approximation (RWA) at the level of Hamiltonian. As pointed out in [123], within the RWA causality in photon propagation is preserved by extending the frequency integrals to minus infinity. We carry out this scheme in all of our numerical calculations.

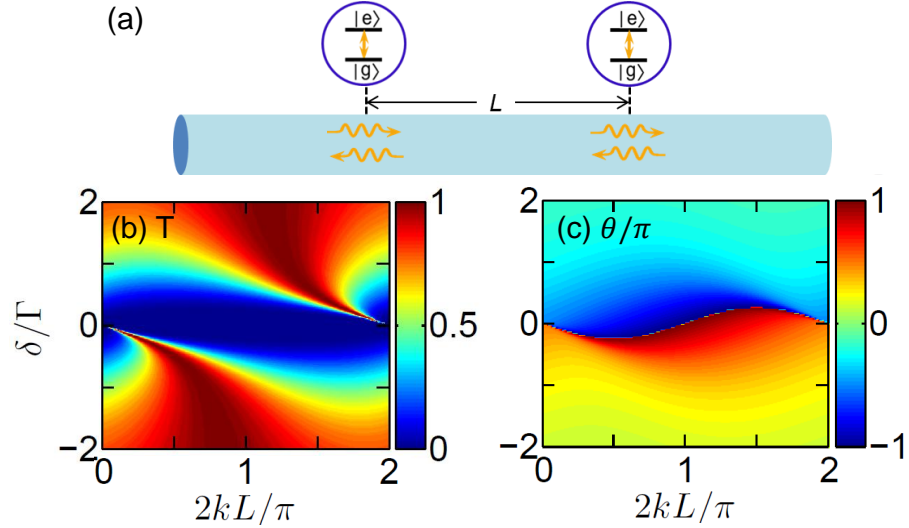


FIGURE 4.1: Schematic diagram of the waveguide system and single-photon transmission. (a) Two qubits (separated by  $L$ ) interacting with the waveguide continuum. Panels (b) and (c) show colormaps of the single-photon transmission probability  $T$  and the phase shift  $\theta$ , respectively, as a function of detuning  $\delta = ck - \omega_0$  and  $2kL$ . Here, we consider the lossless case  $\Gamma' = 0$ .

We first solve for the single-photon scattering eigenstates, and then tackle the problem of multi-photon scattering using a numerical Green function method. In particular, we map the model to a bosonic model and develop a numerical approach to solve the interacting problem in the bosonic model.

### 4.3 Single-Photon: Phase Gate

#### 4.3.1 Single-Photon Scattering Eigenstates

A general single-photon scattering eigenstate of the system described by Eq. (4.1) reads

$$|\phi_1\rangle = \int dx \left[ \phi_R(x)a_R^\dagger(x) + \phi_L(x)a_L^\dagger(x) + e_1\sigma_1^+ + e_2\sigma_2^+ \right] |0, g_1g_2\rangle, \quad (4.2)$$

where  $|0, g_1g_2\rangle$  is the zero photon state with both qubits in the ground state. The Schrödinger equation  $H|\phi_1\rangle = E|\phi_1\rangle$  gives

$$\begin{aligned} \left[ -i\hbar c \frac{d}{dx} - E \right] \phi_R(x) + \hbar V_1 \delta(x - \ell_1) e_1 + \hbar V_2 \delta(x - \ell_2) e_2 &= 0, \\ \left[ i\hbar c \frac{d}{dx} - E \right] \phi_L(x) + \hbar V_1 \delta(x - \ell_1) e_1 + \hbar V_2 \delta(x - \ell_2) e_2 &= 0, \\ (\hbar\omega_1 - i\Gamma'_1/2 - E) e_1 + \hbar V_1 [\phi_R(\ell_1) + \phi_L(\ell_1)] &= 0, \\ (\hbar\omega_2 - i\Gamma'_2/2 - E) e_2 + \hbar V_2 [\phi_R(\ell_2) + \phi_L(\ell_2)] &= 0. \end{aligned} \quad (4.3)$$

Assuming an incident right-going photon of wave vector  $k = E/c$ , the wavefunction takes the following form

$$\begin{aligned} \phi_R(x) &= \frac{e^{ikx}}{\sqrt{2\pi}} [\theta(\ell_1 - x) + t_{12}\theta(x - \ell_1)\theta(\ell_2 - x) + t_k\theta(x - \ell_2)], \\ \phi_L(x) &= \frac{e^{-ikx}}{\sqrt{2\pi}} [r_k\theta(\ell_1 - x) + r_{12}\theta(x - \ell_1)\theta(\ell_2 - x)], \end{aligned} \quad (4.4)$$

where  $\theta(x)$  is the step function. Setting  $\phi_{R,L}(\ell_{1,2}) = [\phi_{R,L}(\ell_{1,2}^+) + \phi_{R,L}(\ell_{1,2}^-)]/2$  and plugging Eq. (4.4) into Eq. (4.3), we obtain the following solution

$$\begin{aligned} t_{12} &= \frac{(ck - \omega_1 + i\Gamma'_1/2)(ck - \omega_2 + i\Gamma'_2/2 + i\Gamma_2/2)}{(ck - \omega_1 + i\Gamma'_1/2 + i\Gamma_1/2)(ck - \omega_2 + i\Gamma'_2/2 + i\Gamma_2/2) + \Gamma_1\Gamma_2 e^{2ikL}/4}, \\ r_{12} &= \frac{-i\Gamma_2(ck - \omega_1 + i\Gamma'_1/2)e^{2ik\ell_2}/2}{(ck - \omega_1 + i\Gamma'_1/2 + i\Gamma_1/2)(ck - \omega_2 + i\Gamma'_2/2 + i\Gamma_2/2) + \Gamma_1\Gamma_2 e^{2ikL}/4}, \\ t_k &= \frac{(ck - \omega_1 + i\Gamma'_1/2)(ck - \omega_2 + i\Gamma'_2/2)}{(ck - \omega_1 + i\Gamma'_1/2 + i\Gamma_1/2)(ck - \omega_2 + i\Gamma'_2/2 + i\Gamma_2/2) + \Gamma_1\Gamma_2 e^{2ikL}/4}, \\ r_k &= \frac{-i\Gamma_2(ck - \omega_1 + i\Gamma'_1/2 - i\Gamma_1/2)e^{2ik\ell_2}/2 - i\Gamma_1(ck - \omega_2 + i\Gamma'_2/2 + i\Gamma_2/2)e^{2ik\ell_1}/2}{(ck - \omega_1 + i\Gamma'_1/2 + i\Gamma_1/2)(ck - \omega_2 + i\Gamma'_2/2 + i\Gamma_2/2) + \Gamma_1\Gamma_2 e^{2ikL}/4}, \\ e_1 &= \left( ic\sqrt{\frac{2}{\Gamma_1}} \right) \frac{e^{ik\ell_1}}{\sqrt{2\pi}} (t_{12} - 1), & e_2 &= \left( ic\sqrt{\frac{2}{\Gamma_2}} \right) \frac{e^{ik\ell_2}}{\sqrt{2\pi}} (t_k - t_{12}). \end{aligned} \quad (4.5)$$

Throughout this Chapter, we assume two identical qubits:  $\Gamma_1 = \Gamma_2 \equiv \Gamma$ ,  $\omega_1 = \omega_2 \equiv \omega_0 \gg \Gamma$ , and  $\Gamma'_1 = \Gamma'_2 \equiv \Gamma'$ . In this case,  $t_k$  reduces to the following expression.

$$t_k \equiv \sqrt{T}e^{i\theta} = \frac{(ck - \omega_0 + \frac{i\Gamma'}{2})^2}{(ck - \omega_0 + \frac{i\Gamma+i\Gamma'}{2})^2 + \frac{\Gamma^2}{4}e^{2ikL}}. \quad (4.6)$$

Similarly, we can solve for the single-photon scattering eigenstate for an incident right-going photon of wave vector  $k = E/c$ . We represent the wavefunction with an incident right-going and left-going photon by  $|\phi_1(k)\rangle_R$  and  $|\phi_1(k)\rangle_L$ , respectively.

#### 4.3.2 Results

As shown in Fig. 4.1(b), there is a large window of perfect transmission:  $T \approx 1$ , even when the detuning ( $\delta = ck - \omega_0$ ) of the single photon is within the resonance line width ( $\sim \Gamma$ ). This is in sharp contrast to the single-qubit case, where perfect transmission is only possible for far off-resonance photons [62]. Such perfect transmission occurs when the reflections from the two qubits interfere destructively and cancel each other completely. Furthermore, Fig. 4.1(c) shows that within the resonance line width, there is a considerable phase shift  $\theta$ . This feature of single-photon transmission can be used to implement a photon-atom phase gate. For example, in the case of  $\delta = -0.5\Gamma$  and  $kL = \pi/4$ , the single photon passes through the system with unit probability and a  $\pi/2$  phase shift. Two successive passes will give rise to a photon-atom  $\pi$ -phase gate, which can be further used to realize a photon-photon phase gate [124].

## 4.4 Quantum Beats in Photon-Photon Correlation

To study the interaction effects, we develop a novel Green function method to calculate the full interacting scattering eigenstates and so photon-photon correlations.

### 4.4.1 Mapping to a Bosonic Model

We start with a reformulated Hamiltonian [67]

$$\begin{aligned}
 H &= H_0 + V, \quad V = \sum_{j=1,2} \frac{U}{2} d_j^\dagger d_j (d_j^\dagger d_j - 1), \\
 H_0 &= \sum_{j=1,2} \hbar(\omega_j - i\Gamma'_j/2) d_j^\dagger d_j + H_{wg} \\
 &\quad + \sum_{j=1,2} \sum_{\alpha=R,L} \int dx \hbar V_j \delta(x - a_j) [a_\alpha^\dagger(x) d_j + \text{h.c.}], \tag{4.7}
 \end{aligned}$$

where  $d_j^\dagger$  and  $d_j$  are bosonic creation and annihilation operators on the qubit sites. The qubit ground and excited states correspond to zero- and one-boson states, respectively. Unphysical multiple occupation is removed by including a large repulsive on-site interaction term  $U$ ; the Hamiltonians in Eqs. (4.1) and (4.7) become equivalent in the limit  $U \rightarrow \infty$ . The non-interacting scattering eigenstates can be obtained easily from  $H_0|\phi\rangle = E|\phi\rangle$ . The full interacting scattering eigenstates  $|\psi\rangle$  are connected to  $|\phi\rangle$  through the Lippmann-Schwinger equation [85, 110, 125]

$$|\psi\rangle = |\phi\rangle + G^R(E)V|\psi\rangle, \quad G^R(E) = \frac{1}{E - H_0 + i0^+}. \tag{4.8}$$

#### 4.4.2 Numerical Green Function Method

With the Lippmann-Schwinger equation (4.8), we can solve for the full interacting solution. The non-interacting eigenstates are simply products of single-photon states.

$$\begin{aligned} |\phi_n(k_1, \dots, k_n)\rangle_{\alpha_1, \dots, \alpha_n} &= |\phi_1(k_1)\rangle_{\alpha_1} |\phi_1(k_2)\rangle_{\alpha_2} \cdots |\phi_1(k_n)\rangle_{\alpha_n}, \quad \alpha_j = R, L, j = 1-n, \\ H_0 |\phi_n(k_1, \dots, k_n)\rangle_{\alpha_1, \dots, \alpha_n} &= c(k_1 + \dots + k_n) |\phi_n(k_1, \dots, k_n)\rangle_{\alpha_1, \dots, \alpha_n}. \end{aligned} \quad (4.9)$$

For simplicity, we will focus on the two-particle solution from now on. Extending the formalism to the many-particle solution is straightforward. The two-particle identity in real-space can be written as

$$\begin{aligned} I_2 &= I_2^x \otimes |\emptyset\rangle\langle\emptyset| + I_1^x \otimes \sum_{i=1,2} |d_i\rangle\langle d_i| + I_0^x \otimes \sum_{i \leq j} |d_i d_j\rangle\langle d_i d_j|, \\ I_n^x &= \sum_{\alpha_1 \dots \alpha_n = R, L} \int dx_1 \cdots dx_n |x_1 \cdots x_n\rangle_{\alpha_1 \dots \alpha_n} \langle x_1 \cdots x_n|, \end{aligned} \quad (4.10)$$

where  $|\emptyset\rangle$  is the ground state of the two qubits (bosonic sites),  $|d_i\rangle = d_i^\dagger |\emptyset\rangle$ ,  $|d_i d_i\rangle = \frac{(d_i^\dagger)^2}{\sqrt{2}} |\emptyset\rangle$  and  $|d_1 d_2\rangle = d_1^\dagger d_2^\dagger |\emptyset\rangle$ . Inserting the above identity into Eq. (4.8), we obtain

$$\begin{aligned} |\psi_2(k_1, k_2)\rangle_{\alpha_1, \alpha_2} &= |\phi_2(k_1, k_2)\rangle_{\alpha_1, \alpha_2} + G^R(E) V I_2 |\psi_2(k_1, k_2)\rangle_{\alpha_1, \alpha_2} \\ &= |\phi_2(k_1, k_2)\rangle_{\alpha_1, \alpha_2} + U G^R(E) \sum_{i=1,2} |d_i d_i\rangle\langle d_i d_i| |\psi_2(k_1, k_2)\rangle_{\alpha_1, \alpha_2} \end{aligned} \quad (4.11)$$

Projecting Eq. (E.6) onto  $\langle d_i d_i |$  yields

$$\begin{pmatrix} \langle d_1 d_1 | \psi_2(k_1, k_2) \rangle_{\alpha_1, \alpha_2} \\ \langle d_2 d_2 | \psi_2(k_1, k_2) \rangle_{\alpha_1, \alpha_2} \end{pmatrix} = \begin{pmatrix} \langle d_1 d_1 | \phi_2(k_1, k_2) \rangle_{\alpha_1, \alpha_2} \\ \langle d_2 d_2 | \phi_2(k_1, k_2) \rangle_{\alpha_1, \alpha_2} \end{pmatrix} + U \begin{bmatrix} G_{11} & G_{12} \\ G_{21} & G_{22} \end{bmatrix} \begin{pmatrix} \langle d_1 d_1 | \psi_2(k_1, k_2) \rangle_{\alpha_1, \alpha_2} \\ \langle d_2 d_2 | \psi_2(k_1, k_2) \rangle_{\alpha_1, \alpha_2} \end{pmatrix}, \quad (4.12)$$

where we introduce the short-hand notation  $G_{ij} = \langle d_i d_i | G^R(E) | d_j d_j \rangle$ . Solving Eq. (4.12) gives rise to

$$\begin{pmatrix} \langle d_1 d_1 | \psi_2(k_1, k_2) \rangle_{\alpha_1, \alpha_2} \\ \langle d_2 d_2 | \psi_2(k_1, k_2) \rangle_{\alpha_1, \alpha_2} \end{pmatrix} = \left( I - U \begin{bmatrix} G_{11} & G_{12} \\ G_{21} & G_{22} \end{bmatrix} \right)^{-1} \begin{pmatrix} \langle d_1 d_1 | \phi_2(k_1, k_2) \rangle_{\alpha_1, \alpha_2} \\ \langle d_2 d_2 | \phi_2(k_1, k_2) \rangle_{\alpha_1, \alpha_2} \end{pmatrix}. \quad (4.13)$$

Projecting Eq. (E.6) onto a two-photon basis state  $\langle x_1 x_2 |$  and taking the  $U \rightarrow \infty$  limit, we obtain the full interacting two-photon solution

$$\begin{aligned} \langle x_1 x_2 | \psi_2(k_1, k_2) \rangle_{\alpha_1, \alpha_2} &= \langle x_1 x_2 | \phi_2(k_1, k_2) \rangle_{\alpha_1, \alpha_2} \\ &+ U \begin{pmatrix} G_1(x_1, x_2) & G_2(x_1, x_2) \end{pmatrix} \begin{pmatrix} \langle d_1 d_1 | \psi_2(k_1, k_2) \rangle_{\alpha_1, \alpha_2} \\ \langle d_2 d_2 | \psi_2(k_1, k_2) \rangle_{\alpha_1, \alpha_2} \end{pmatrix} \\ &= \langle x_1 x_2 | \phi_2(k_1, k_2) \rangle_{\alpha_1, \alpha_2} - G_{xd} G_{dd}^{-1} \begin{pmatrix} \langle d_1 d_1 | \phi_2(k_1, k_2) \rangle_{\alpha_1, \alpha_2} \\ \langle d_2 d_2 | \phi_2(k_1, k_2) \rangle_{\alpha_1, \alpha_2} \end{pmatrix}, \end{aligned} \quad (4.14)$$

where  $G_i(x_1, x_2) = \langle x_1 x_2 | G^R(E) | d_i d_i \rangle$  and

$$\begin{aligned} G_{xd} &\equiv \begin{pmatrix} G_1(x_1, x_2) & G_2(x_1, x_2) \end{pmatrix}, \\ G_{dd} &\equiv \begin{bmatrix} G_{11} & G_{12} \\ G_{21} & G_{22} \end{bmatrix}. \end{aligned} \quad (4.15)$$

Hence, the remaining task is to calculate all the Green functions in Eq. (4.14). This can be done using the two-photon non-interacting scattering eigenstates,

from which we can construct a two-particle identity in momentum space

$$I'_2 = \sum_{\alpha_1, \alpha_2=R,L} \int dk_1 dk_2 |\phi_2(k_1, k_2)\rangle_{\alpha_1, \alpha_2} \langle \phi_2(k_1, k_2)|. \quad (4.16)$$

Using Eq. (4.9), the Green functions can be evaluated as

$$\begin{aligned} G_{ij} &= \langle d_i d_i | G^R(E) I'_2 | d_j d_j \rangle \\ &= \sum_{\alpha_1, \alpha_2=R,L} \int dk_1 dk_2 \frac{\langle d_i d_i | \phi_2(k_1, k_2) \rangle_{\alpha_1, \alpha_2} \langle \phi_2(k_1, k_2) | d_j d_j \rangle}{E - ck_1 - ck_2 + i0^+}, \\ G_i(x_1, x_2) &= \langle x_1 x_2 | G^R(E) I'_2 | d_i d_i \rangle \\ &= \sum_{\alpha_1, \alpha_2=R,L} \int dk_1 dk_2 \frac{\langle x_1 x_2 | \phi_2(k_1, k_2) \rangle_{\alpha_1, \alpha_2} \langle \phi_2(k_1, k_2) | d_i d_i \rangle}{E - ck_1 - ck_2 + i0^+}. \end{aligned} \quad (4.17)$$

Doing the integrals numerically gives the full interacting two-particle solution. Assuming a weak continuous wave incident laser, with the interacting solution in Eq. (4.14) we can calculate the second-order correlation function  $g_2(t)$  [12] for an arbitrary interqubit separation.

#### 4.4.3 Markovian Regime

Figure 4.2 shows  $g_2(t)$  for both the transmitted and reflected fields when the probe laser is on resonance with the qubit:  $k = k_0$  ( $k_0 \equiv \omega_0/c$ ). When the two qubits are colocated [109] ( $L = 0$ ),  $g_2(t)$  of the transmitted field shows strong initial bunching followed by antibunching, while  $g_2(t)$  of the reflected field shows perfect antibunching at  $t = 0$ ,  $g_2(0) = 0$ . This behavior is similar to that in the single qubit case [62, 93]. When the two qubits are spatially separated by  $L = \pi/2k_0$ , we observe in both the transmitted and reflected fields the development of quantum beats (oscillations). Since these beats occur in  $g_2(t)$ , they necessarily

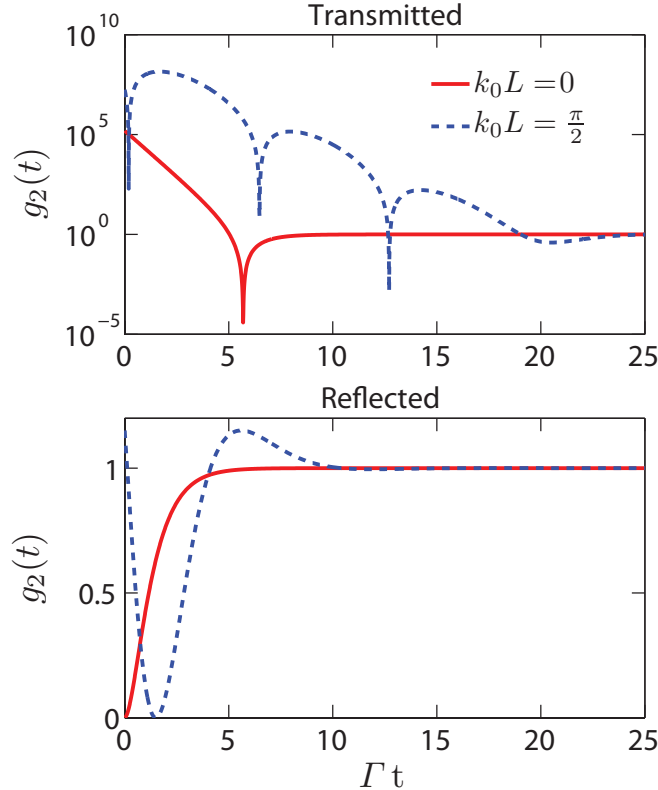


FIGURE 4.2: Quantum beats in the Markovian regime. The second-order photon-photon correlation function of both the transmitted (top) and reflected (bottom) fields as a function of  $t$  for  $k_0 L = 0$  (solid line) and  $k_0 L = \pi/2$  (dashed line). The incident weak coherent state is on resonance with the qubits:  $k = k_0 = \omega_0/c$ . (Parameters:  $\omega_0 = 100\Gamma$  and  $\Gamma' = 0.1\Gamma$ .)

involve the nonlinearity of the qubits and do not occur for, *e.g.*, waveguide-coupled oscillators.

#### 4.4.4 Non-Markovian Regime: Persistent Quantum Beats

As one increases the separation  $L$ , one may expect from the well-known 3D result that the quantum beats disappear [126]. However, in our 1D system they do not: Figure 4.3 shows  $g_2(t)$  for two cases,  $k_0 L = 25.5\pi$  and  $100.5\pi$ , from which it is clear that the beats persist to long time. The 1D nature is key in producing strong quantum interference effects and so long-range qubit-qubit interactions.

To interpret these exact numerical results, we compare them with the solution under the well-known Markov approximation. For small separations ( $k_0L \leq \pi$ ), the system is Markovian [126]: the causal propagation time of photons between the two qubits can be neglected and so the qubits interact instantaneously. To understand quantum beats in this limit, we use a master equation for the density matrix  $\rho$  of the qubits in the Markov approximation. Integrating out the 1D bosonic degrees of freedom yields [121]

$$\begin{aligned}\frac{\partial\rho}{\partial t} &= \frac{i}{\hbar}[\rho, H_c] - \sum_{i,j=1,2} \frac{\Gamma_{ij}}{2}(\rho\sigma_i^+\sigma_j^- + \sigma_i^+\sigma_j^-\rho - 2\sigma_i^-\rho\sigma_j^+), \\ H_c &= \hbar\omega_0 \sum_{i=1,2} \sigma_i^+\sigma_i^- + \hbar\Omega_{12}(\sigma_1^+\sigma_2^- + \sigma_2^+\sigma_1^-),\end{aligned}\tag{4.18}$$

where  $\Gamma_{ii} \equiv \Gamma + \Gamma'$  while  $\Gamma_{12} \equiv \Gamma\cos(\omega_0L/c)$  and  $\Omega_{12} \equiv (\Gamma/2)\sin(\omega_0L/c)$  are the vacuum-mediated spontaneous and coherent couplings, respectively. Transforming to symmetric and antisymmetric states  $|S, A\rangle = (|g_1e_2\rangle \pm |e_1g_2\rangle)/\sqrt{2}$  gives a more transparent form:

$$\begin{aligned}\frac{\partial\rho}{\partial t} &= \frac{i}{\hbar}[\rho, H_c] - \sum_{\beta=S,A} \frac{\Gamma_\beta}{2}(\rho\sigma_\beta^+\sigma_\beta^- + \sigma_\beta^+\sigma_\beta^-\rho - 2\sigma_\beta^-\rho\sigma_\beta^+), \\ H_c &= \sum_{\beta=S,A} \hbar\omega_\beta\sigma_\beta^+\sigma_\beta^-, \end{aligned}\tag{4.19}$$

where  $\sigma_{S,A}^+ \equiv (\sigma_1^+ \pm \sigma_2^+)/\sqrt{2}$ ,  $\Gamma_{S,A} \equiv \Gamma + \Gamma' \pm \Gamma_{12}$ , and  $\omega_{S,A} \equiv \omega_0 \pm \Omega_{12}$ . Note that  $|S\rangle$  and  $|A\rangle$  are decoupled from each other and have transition frequencies  $\omega_{S,A}$  and decay rates  $\Gamma_{S,A}$  which oscillate as a function of  $L$ . When  $L = 0$ ,  $\Gamma_S = 2\Gamma + \Gamma'$  and  $\Gamma_A = \Gamma'$ .  $|S\rangle$  is in the superradiant state, while  $|A\rangle$  is subradiant. The waveguide couples only to the superradiant state and so the photon-photon correlation mimics that for a single-qubit. However, when  $k_0L = \pi/2$ ,  $\Gamma_S = \Gamma_A = \Gamma + \Gamma'$ ,

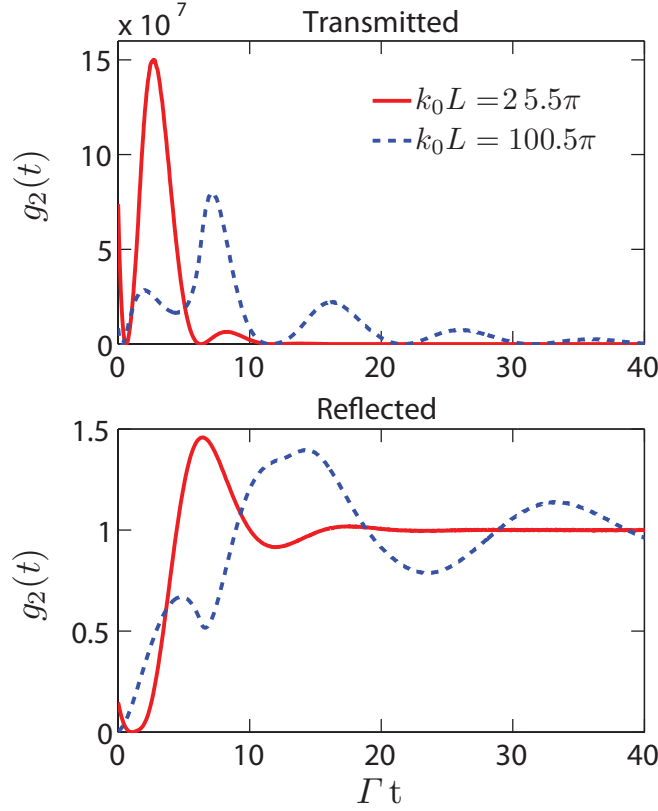


FIGURE 4.3: Persistent quantum beats in the non-Markovian regime. The second-order correlation function of both the transmitted (top) and reflected (bottom) fields is plotted as a function of  $t$  for  $k_0 L = 25.5\pi$  (solid line) and  $100.5\pi$  (dashed line). We set the incident coherent state on resonance with the qubits ( $k = k_0$ ),  $\omega_0 = 100\Gamma$  and  $\Gamma' = 0.1\Gamma$ .

$\omega_{S,A} = \omega_0 \pm \Gamma/2$ , and the waveguide couples to both  $|S\rangle$  and  $|A\rangle$ . The quantum interference between the transitions  $|S\rangle \rightarrow |g_1g_2\rangle$  and  $|A\rangle \rightarrow |g_1g_2\rangle$  gives rise to quantum beats at frequency  $\omega_S - \omega_A = \Gamma$ , as shown in Fig. 4.2.

As one increases the separation  $L$  and goes beyond the Markovian regime, Eq. (4.18) is not a valid description of the system because the causal propagation time of photons (or retardation effect) has to be included. Comparing the results in Figs. 4.2 and 4.3, we see that quantum beats are *more* visible in the non-Markovian regime in both the transmitted and reflected fields and persist to a much longer time scale, especially for the case  $k_0 L = 100.5\pi$ . This is surprising

because while the characteristic time scale in the system is  $\Gamma^{-1} \sim L/c$ , there are still quantum beats for  $t > 40\Gamma^{-1}$  in Fig. 4.3. This means the photon-photon correlation survives after even 40 round trips between the two qubits.

To better understand the persistent quantum beats, we extract the transition frequencies and decay rates of the two qubit system beyond the Markovian regime. This is achieved by analyzing the poles of the Green function defined in Eq. (4.8); they are given by

$$F(\omega) = \left[ \omega - \omega_0 + \frac{i(\Gamma + \Gamma')}{2} \right]^2 + \frac{\Gamma^2}{4} e^{2i\omega L/c} = 0. \quad (4.20)$$

In the Markovian regime, one can safely replace  $\omega$  by  $\omega_0$  in the exponent, given that  $\omega_0 \gg \Gamma$  and  $L \ll c\Gamma^{-1}$ . Eq. (4.20) then yields  $\omega_{\pm} = \omega_0 - i(\Gamma + \Gamma')/2 \pm i\Gamma e^{i\omega_0 L/c}/2$ . The real and imaginary parts of  $\omega_{\pm}$  correspond to the transition frequencies and decay rates, which are nothing but  $\omega_{S,A}$  and  $-\Gamma_{S,A}/2$  obtained using the Markov approximation [Eq. (4.19)]. Beyond this Markovian regime, we solve Eq. (4.20) iteratively by gradually increasing  $L$ .

Figure 4.4 shows that both  $\omega_{S,A}$  and  $\Gamma_{S,A}$  deviate significantly from their Markovian values as  $k_0 L$  becomes large [Figs. 4.4(c) and 4.4(d)]. The expanded detail plots, Figs. 4.4(a) and 4.4(e), show that the Markov approximation works well for  $k_0 L \in [0, 5\pi]$ . At large  $k_0 L$ , however, *both* the symmetric and antisymmetric states become subradiant [ $\Gamma_{S,A} \ll \Gamma$ , Fig. 4.4(f)]. This suppression of decay comes about in the following way: after the initial excitation of and emission from the first qubit, it can be reexcited by the pulse reflected from the second qubit. From the excitation probability of the first qubit through many emission-reexcitation cycles, an effective qubit life time can be defined: it is greatly lengthened by the causal propagation of photons between the two qubits.  $\Gamma_{S,A}$  charac-

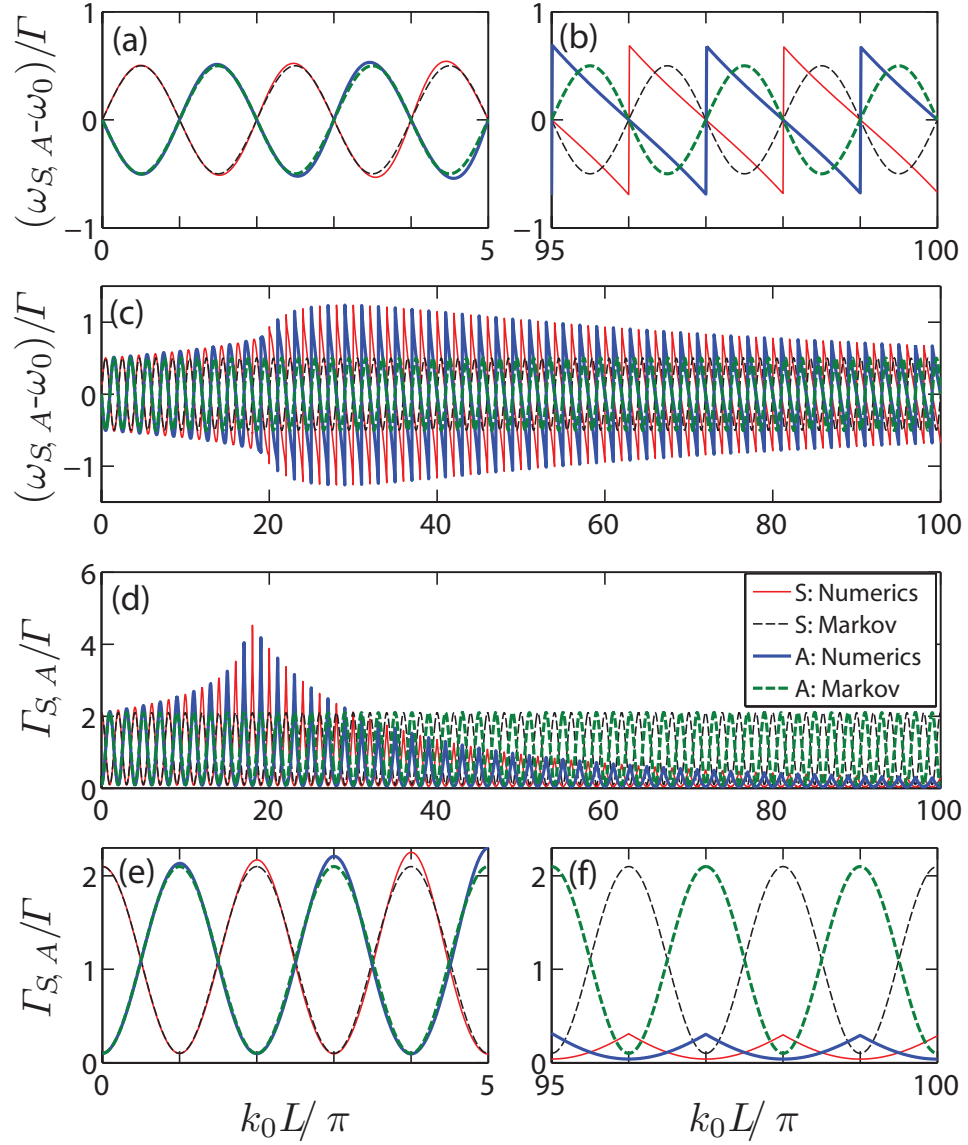


FIGURE 4.4: Renormalized transition frequencies and decay rates of the symmetric (S) and antisymmetric (A) states. Panels (a)-(c) show the transition frequencies  $\omega_S$  (thin solid line) and  $\omega_A$  (thick solid line) obtained numerically from Eq. (4.20) together with  $\omega_S$  (thin dashed line) and  $\omega_A$  (thick dashed line) given by the Markov approximation. Panels (d)-(f) similarly show the decay rates  $\Gamma_S$  and  $\Gamma_A$  obtained both numerically and in the Markov approximation. ( $\omega_0 = 100\Gamma$  and  $\Gamma' = 0.1\Gamma$ .)

terize the average long time decay quantitatively.

#### 4.4.5 Two-Pole Approximation

The nonlinear equation Eq. (4.20) gives rise, of course, to infinitely many poles for  $L > 0$ . These poles represent collective states of two spatially separated qubits with vacuum-mediated interactions. They are eigenmodes of the density matrix of the two qubits. The “two-pole” approximation of retaining only the symmetric and antisymmetric states is a good approximation because  $(\omega_{S,A} - \omega_0, \Gamma_{S,A})$  are the two poles closest to the origin  $(0, 0)$ . As we will show below,  $|S\rangle$  and  $|A\rangle$  have much smaller decay rates than all the other collective states. Therefore, these two slowly decaying states dominate the long-time dynamics and quantum interference between their spontaneous emissions is the physical origin of the persistent quantum beats observed in Fig. 4.3.

Figure 4.5 plots the poles computed numerically in four different cases. For small  $L$ , Figs. 4.5(a) and 4.5(b) show that there are only two poles corresponding to  $|S\rangle$  and  $|A\rangle$  states within a large range of frequency. At large  $L$ , however, both the symmetric and antisymmetric states become subradiant [ $\Gamma_{S,A} \ll \Gamma$ ]. Furthermore, as  $L$  increases, there are additional poles as shown in Figs. 4.5(c) and 4.5(d), corresponding to collective states generated in non-Markovian processes. For  $L \gg c\Gamma^{-1}$ , the two-pole approximation breaks down as the additional poles of collective states become close enough to  $|S\rangle$  and  $|A\rangle$  states.

Here, we want to analyze the case  $k_0 L = 100.5\pi$  [Fig. 4.5(d)], where  $L \sim c\Gamma^{-1}$  and the two-pole approximation is still valid as we will show below. With a driving laser on resonance with the qubits and a Rabi frequency  $\Omega$ , the probability to excite a state  $|y\rangle$  ( $\omega_y, \Gamma_y$ ) is

$$P_y = \frac{1}{2 + \left(\frac{\omega_y - \omega_0}{\Omega}\right)^2 + \left(\frac{\Gamma_y}{2\Omega}\right)^2}. \quad (4.21)$$

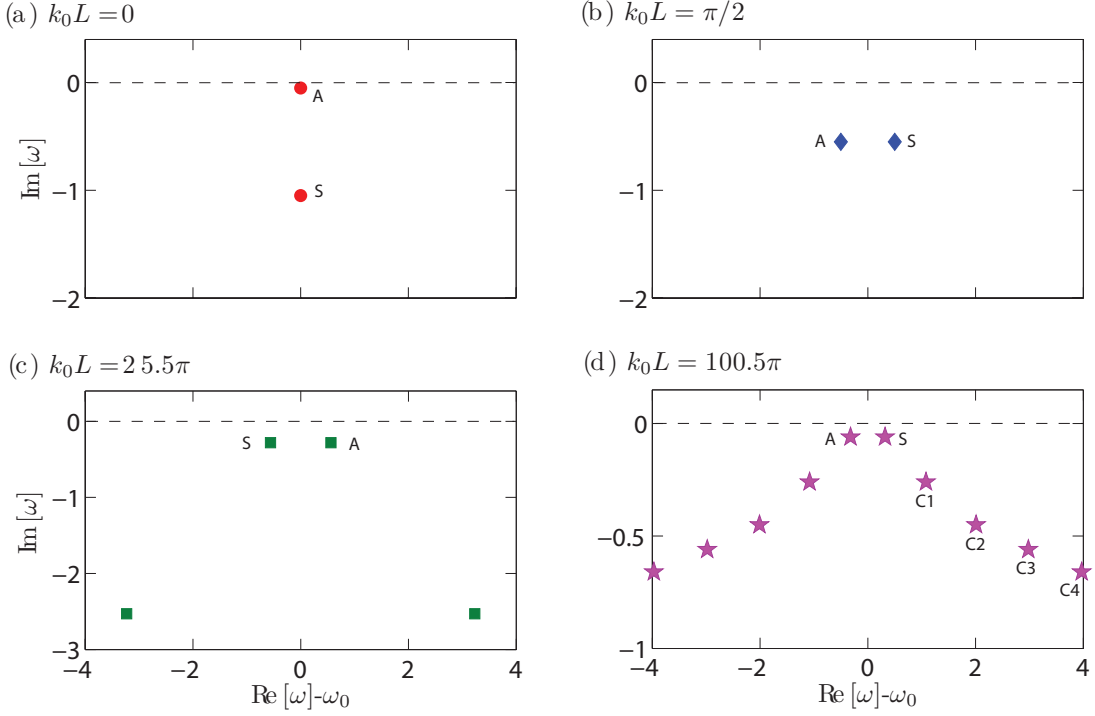


FIGURE 4.5: The poles of the Green functions for (a)  $k_0L = 0$ , (b)  $k_0L = \frac{\pi}{2}$ , (c)  $k_0L = 25.5\pi$ , and (d)  $k_0L = 100.5\pi$ . Both the real and imaginary parts of the poles are in units of  $\Gamma$ . We show all the poles with real part within  $[\omega_0 - 4\Gamma, \omega_0 + 4\Gamma]$ . The poles corresponding to the  $|S\rangle$  and  $|A\rangle$  states are labeled as  $S$  and  $A$ , respectively. In case (d), there are four additional poles ( $C1-C4$ ) within the plotted range.

Using this formula, we can calculate the probability of exciting the states corresponding to  $S(\omega_0 + 0.32\Gamma, 0.12\Gamma)$ ,  $A(\omega_0 - 0.32\Gamma, 0.12\Gamma)$ ,  $C1(\omega_0 + 1.08\Gamma, 0.52\Gamma)$ ,  $C2(\omega_0 + 2.01\Gamma, 0.90\Gamma)$ ,  $C3(\omega_0 + 2.98\Gamma, 1.12\Gamma)$  and  $C4(\omega_0 + 3.97\Gamma, 1.32\Gamma)$ . In the limit of weak driving laser,  $\Omega \rightarrow 0$ , we have

$$\begin{aligned} P_{C1} &= 8.6\%P_S, P_{C2} = 2.5\%P_S, \\ P_{C3} &= 1.1\%P_S, P_{C4} = 0.7\%P_S. \end{aligned} \quad (4.22)$$

Hence, compared to states  $C1-C4$ ,  $S$  and  $A$  states are well populated and dominate the qubit-qubit interactions for the parameter regime considered.

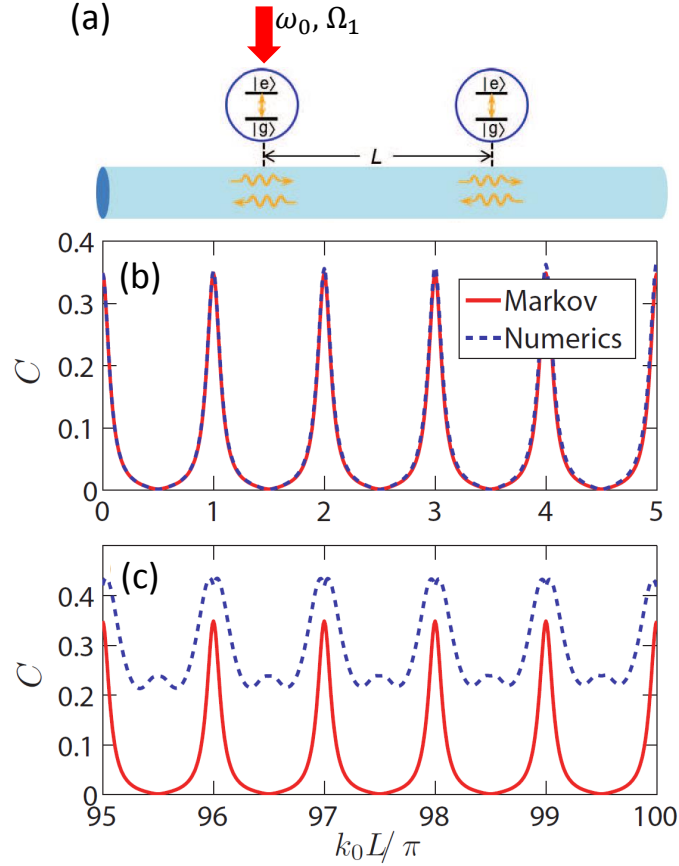


FIGURE 4.6: Long-distance qubit-qubit entanglement. (a) Schematic of setup: the first qubit is driven by a on resonance laser with Rabi frequency  $\Omega_1$ . The steady state concurrence is plotted as a function of  $k_0 L$  for (b)  $0 \leq k_0 L \leq 5\pi$ , and (c)  $95\pi \leq k_0 L \leq 100\pi$ . The Rabi frequencies are  $\Omega_1 = 0.1\Gamma$ ,  $\Omega_2 = 0$ . The driving laser is on resonance with the qubits. ( $\omega_0 = 100\Gamma$  and  $\Gamma' = 0.1\Gamma$ .)

## 4.5 Qubit-Qubit Entanglement

With the “two-pole” approximation, we study qubit-qubit entanglement using the master equation Eq.(4.19) with  $\omega_{S,A}$  and  $\Gamma_{S,A}$  replaced by the renormalized values obtained from Eq.(4.20). We focus on the steady state case by including a continuous weak driving laser on resonance with the first qubit as shown in Fig. 4.6(a):  $H_L = \hbar\Omega_1(\sigma_1^+ + \sigma_1^-)$  [114, 115]. The entanglement is characterized by the concurrence [127]; Figure 4.6 shows its steady state value for the Rabi

frequency  $\Omega_1 = 0.1\Gamma$ . It is worth mentioning that the maximum concurrence we obtained is  $\leq 0.5$  rather than 1. This is because when the first qubit decays, half of the excitation will propagate to the left, and hence only the other half excitation will propagate to the second qubit to entangle them. For small separation [Fig. 4.6(b)], the concurrence agrees with that obtained using the Markov approximation [114]:  $C$  reaches its maximum when the maximally-entangled two-qubit subradiant state (either  $|S\rangle$  or  $|A\rangle$ ) has a minimal decay rate and is well populated [115]. Between two peaks,  $C$  vanishes because the symmetric and antisymmetric states are now barely populated and the usual decay rate,  $\Gamma + \Gamma' \gg \Omega_1$ , holds<sup>3</sup>.

In contrast, Fig. 4.6(c) shows that the Markovian predictions break down: we observe enhanced entanglement for an arbitrary interqubit separation. Such enhancement is due to non-Markovian processes: both  $|S\rangle$  and  $|A\rangle$  become subradiant (Fig. 4.4) with decay rates much smaller than  $\Gamma$  and hence are well populated. Thus, long-range entanglement is possible due to non-Markovian processes, making 1D waveguide-QED systems promising candidates for scalable quantum networking.

## 4.6 Loss and Possible Experimental Systems

Accessing the non-Markovian regime requires a large (effective) distance between the qubits and hence low loss in the waveguide. Here, we have included the loss of the qubit by using an effective Purcell factor of 10 (*i.e.*  $\sim 10\%$  loss). Because waveguide loss has the same effect on system performance as qubit loss (both lead to photon leakage), we expect that the observed persistent quantum beats

---

<sup>3</sup> The population of an excited state with detuning  $\Delta$ , decay rate  $\Gamma$ , and Rabi frequency  $\Omega$  is given by  $1/[2 + (\Delta/\Omega)^2 + (\Gamma/2\Omega)^2]$ .

and long-distance entanglement are robust against waveguide loss on this same level, namely  $\sim 10\%$ . While some waveguides in current experimental systems are very lossy (such as plasmonic nanowires [17]), we can circumvent this difficulty by using either a hybrid optical fiber systems or slow-light superconducting systems. In the first case, low-loss optical fibers are used to transmit light over a long distance. The transmission length we are considering is of order 100 wavelengths, thus of order 100 microns for typical quantum dots or atoms. Loss over such a distance in state of the art fiber is very small: taking a 4dB/km fiber, the loss will be on the order of 1 ppm. In the second case, the actual transmission length is very short, but due to the reduced speed of light one can still reach the non-Markovian regime. Below are three plausible experimental settings: (a) and (b) belong to the first case and (c) illustrates the second case.

#### 4.6.1 (a) Hybrid Fiber-Plasmonic Waveguide-QED System

Figure 4.7(a) shows an integrated fiber-plasmonic waveguide-QED system. The idea of hybrid plasmonic systems was first proposed by Chang et al. [62]. Since then, there has been extensive experimental [128, 129], and theoretical [130, 131, 132] work along this line. In the schematic, the optical fiber is coupled to two tapered plasmonic nanowires. Due to the subwavelength confinement [62], the plasmonic field in the nanowires couples strongly to the local qubits, e.g. quantum dots [17]. Coupling the nanowires to a dielectric waveguide ensures that the quantum state can be transmitted over long distance without being dissipated in the nanowires.

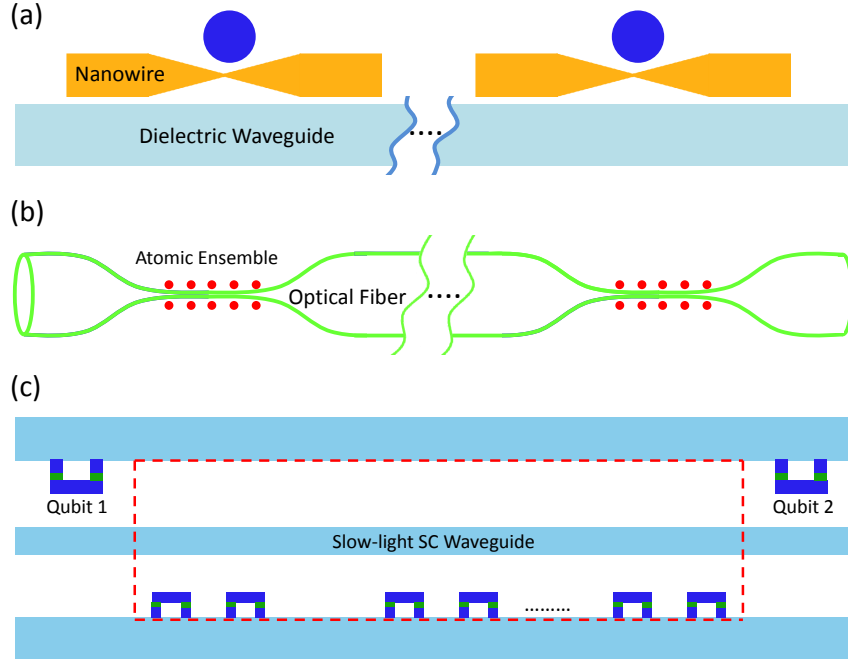


FIGURE 4.7: Three possible setups for long-distance entanglement in waveguide-QED. (a) Hybrid plasmonic system. The dielectric waveguide (light blue) is phase-matched with the plasmonic nanowires (yellow) so that efficient plasmon transfer between them can be realized. The nanowires are strongly coupled to the quantum dots (blue) in the tapered regions. Note that the length of the dielectric waveguide between the nanowires can be very long (indicated by breaks). (b) Tapered nanofiber system. An optical fiber (green) is tapered into narrow nanofibers in two regions. Two atomic ensembles (red) are trapped by and strongly coupled to the nanofibers. (c) Slow-light superconducting system. Two superconducting qubits (blue) couple strongly to the slow-light superconducting waveguide (red dashed box).

#### 4.6.2 (b) Integrated Nanofiber-Trapped Atomic Ensemble System

In the second example, a long optical fiber is tapered into a narrow nanofiber in two regions. Then, two atomic ensembles are trapped by the evanescent field surrounding the nanofibers. Strong coupling is achieved between the propagating photons in the nanofiber and the atomic ensembles [133]. Such a setting is a clear extension of the experimental systems demonstrated by several groups [56, 133].

#### 4.6.3 (c) Slow-light Superconducting Waveguide-QED System

In the third example, a 1D open superconducting transmission line is coupled to two superconducting qubits. It has been experimentally demonstrated that this system is deep in the strong coupling regime [46]. However, the typical length of the transmission line is on the order of the wavelength of propagating microwave photons. Hence, the separation of the two qubits is limited to the photon wavelength. To reach the non-Markovian regime, we can make the effective distance between the two qubits large by the slow-light scheme first proposed by Shen and Fan [134]. The idea is to couple the transmission line to an additional periodic array of unit cells made of two qubits. Flat photonic bands can be generated to slow down the microwave photons. While not true long-distance propagation, this could be an effective way to experimentally probe non-Markovian effects. In addition to the slow-light superconducting circuit system, very recently experimentalists in Sweden have demonstrated strong coupling of quantum circuits to surface acoustic wave (SAW) [135] in the quantum regime with a group velocity 3 orders of magnitude lower than the speed of light. The coupled SAW-double-qubit system should be able to access the non-Markovian physics in the near future.

## 4.7 Conclusion

In summary, we develop a novel Green function method to study cooperative effects of two qubits coupled to a 1D waveguide. Both the nonlinear effects of the qubits and the continuum of modes in the waveguide are included. We find that long-range qubit-qubit interactions are generated by non-Markovian processes, which in turn give rise to persistent quantum beats in the photon correlations

and a high degree of long-distance entanglement. Several potential experimental setups are identified to realize the proposed system.

# 5

## Decoy-state Quantum Key Distribution with Nonclassical Light

*Summary:* <sup>1</sup>Based on our understanding of light-matter interactions in waveguide-QED, we study the applications in quantum information processing, in particular quantum key distribution. We investigate a decoy-state quantum key distribution (QKD) scheme with a sub-Poissonian single-photon source, which is generated on demand by scattering a coherent state off a two-level system in a one-dimensional waveguide. We show that, compared to coherent state decoy-state QKD, there is a two-fold increase of the key generation rate. Furthermore, the performance is shown to be robust against various imperfections of the system.

---

<sup>1</sup> Part of the text of this chapter has been adapted from the following previously published article: Huaixiu Zheng, Daniel J. Gauthier, and Harold U. Baranger, "Decoy-state quantum key distribution with nonclassical light generated in a one-dimensional waveguide", *Opt. Lett.* **38**, 622 (2013).

## 5.1 Introduction

Quantum physics has brought revolutionary changes to the way we think about the world and has led to the birth of a new field: quantum communication. Quantum communication is the art of transferring information encoded in quantum states from one place to another. The best known example is quantum key distribution (QKD) [4], which is the first commercially available application of quantum information science. The general settings of QKD are shown in Fig. 5.1. Quantum key distribution allows two distant users, *Alice* and *Bob*, to share a secret key with unconditional security (independent of the power of the eavesdropper *Eve*) guaranteed by principles of quantum physics: any action by which Eve tries to extract information from the transferred quantum state is a generic form of quantum measurement, which unavoidably will modify the quantum state and hence will be caught by Alice and Bob. The first QKD protocol was proposed by Bennett and Brassard in 1984 and hence was called BB84 later on [136]. It assumes the use of an ideal single-photon source: Alice holds a source of single photons and encodes information in the polarization degree of freedom. In particular, the bits are coded in either the horizontal or vertical (+) basis, or the complimentary basis, i.e.  $+45^\circ / -45^\circ (\times)$ :  $|H\rangle$  for  $0_+$ ;  $|V\rangle$  for  $1_+$ ;  $|+45^\circ\rangle$  for  $0_\times$ ;  $| -45^\circ\rangle$  for  $1_\times$ .

Given the coding scheme, the BB84 protocol works in the following way [4]:

1. Alice prepares a single photon in one of the four basis states and sends it to Bob via the quantum channel. Bob measures it in either the + or the  $\times$  basis. This procedure is repeated  $N$  times, giving both Alice and Bob a list of  $N$  bits.
2. Alice and Bob communicate through the classical channel, compare the basis of each photon and discard the cases in which they have chosen different bases.

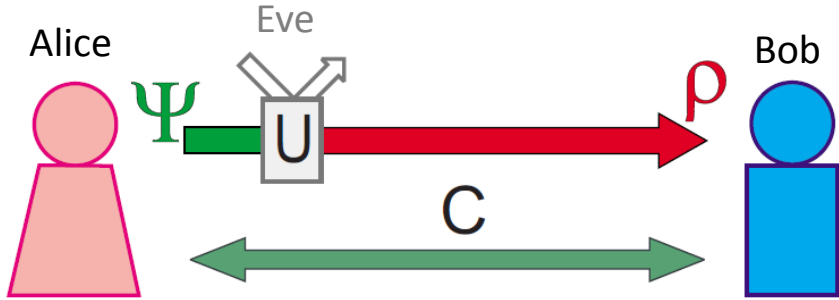


FIGURE 5.1: Schematic of QKD [4]: Alice sends quantum states ( $\Psi$ ) to Bob through a quantum channel. Eve can tap into the quantum channel without any restriction except the laws of quantum physics. Alice and Bob can also communicate via the classical channel (labeled  $C$ ), into which Eve can only listen.

At the end, they have a list of about  $N/2$  bits, which is the so-called raw key.

3. Alice and Bob reveal a random sample of some bits of the raw key, and estimate the error rate and hence the information about eavesdropping by Eve. In the absence of errors, the raw key is the same for Alice and Bob and then it is already the secret key. However, if there are errors, Alice and Bob have to correct them and get rid of the information Eve has obtained.

In reality, however, a single-photon source is still beyond the current technology despite tremendous experimental effort worldwide. Hence, most QKD experiments use weak coherent states (WCS) from attenuated lasers as a photon source [4, 137]. Two drawbacks come with the WCS: the multiphoton and the vacuum components. The vacuum content limits Bob's detection rate, and hence leads to a shorter maximal distance. The multiphoton component makes QKD vulnerable to the photon number splitting attack, where the eavesdropper (Eve) can suppress single-photon signals and split multiphoton signals, keeping one copy and sending one copy to Bob. This way, Eve obtains the full information without being detected, and the unconditional security breaks down. The decoy state method was proposed to beat such attacks [87, 88, 89]. Alice prepares a

set of additional states—decoy states—in addition to the standard BB84 signal states. The decoy states are used only for the purpose of detecting eavesdropping, while the BB84 signal states are used only to generate secret keys between Alice and Bob. The only difference between the decoy states and the signal states is their photon number statistics. Hence, there is no way for Eve to distinguish a decoy state from a signal state. This way, Alice and Bob will have a better idea of the attack situation in the quantum channel, and hence can dramatically improve the performance of key generation.

In this Chapter, we combine the decoy-state method with a sub-Poissonian single-photon source generated on demand by scattering in a waveguide. We find that there is a substantial increase in the key generation rate and maximal transmission distance compared to both WCS and heralded single-photon decoy-state QKD. Furthermore, the performance is robust against either parameter variation or loss in the system, making it a promising candidate for future QKD systems.

## 5.2 Nonclassical Light Source

### 5.2.1 *Model System*

As shown in Chapter 2, it is possible to generate nonclassical light [48, 93] by sending a coherent state into a 1D waveguide which is side-coupled to a quantum nonlinear element, such as a two-level system (2LS) [62, 74]. Figure 5.2 shows the schematic of the system we use to generate nonclassical light for QKD in this Chapter. The nonlinearity of the quantum element (2LS) leads to a distinct difference between multiphoton and single-photon scattering. For example, when two photons interact with a 2LS simultaneously, the 2LS will only be able to absorb one photon and hence the pair will have a high transmission probability, leading

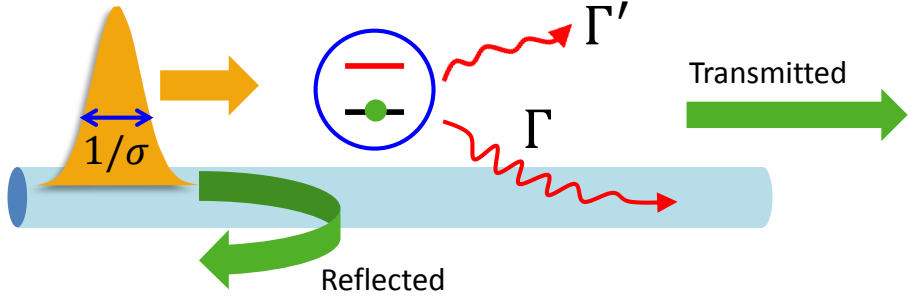


FIGURE 5.2: Schematic of the model system. The incoming coherent state pulse has a spectral width  $\sigma$ . The excited state of the 2LS decays into waveguide modes and free space modes with rate  $\Gamma$  and  $\Gamma'$ , respectively. Here, we focus on the number statistics of the reflected field.

to photon bunching and super-Poissonian photon statistics [48, 93]. The model we use is presented in detail in Chapter 2 (and Ref. [93]). It includes absorption of photons by the 2LS and subsequent spontaneous emission into the waveguide mode at rate  $\Gamma$ . In addition, a loss rate  $\Gamma'$  models subsequent emission into modes other than the waveguide mode (as well as possible non-radiative processes) [62, 93]. The input coherent state has mean photon number  $\bar{n} = 1$ . We take a Gaussian wave-packet with central frequency on resonance with the 2LS and root-mean-square spectral width  $\sigma$ . The loss rate  $\Gamma'$  decreases the number of photons in the waveguide, thus changing the number statistics. When  $\Gamma'$  is small compared to  $\sigma$  and  $\Gamma$ , multi-photon loss is negligible: the loss from an  $n$ -photon pulse appears as an  $n - 1$  photon pulse, for which we then naturally use the  $n - 1$  photon transmission and reflection to distribute the probability between the transmitted and reflected fields. Now we show the details of correcting the contribution of loss to the number statistics in the reflected field on which we mainly focus in this Chapter.

### 5.2.2 Corrections of Loss

After including a non-zero loss rate  $\Gamma'$  of the 2LS, the total probabilities of all photon sectors ( $P_n$ ) do not sum up to 1. That is because photons can leak out through the excited 2LS with rate  $\Gamma'$ . Here, we present an analysis of the loss contribution to the number statistics and correct the corresponding  $P_n$  so that they do sum up to 1 at the end. However, it is worth mentioning that the corrected number statistics is very close to the one without correcting for loss.

As shown in Chapter 2 (and Ref. [93]), there are three different scattering channels after sending an incoming photon state into the coupled waveguide-2LS system: 1) transmission channel in the waveguide in which the photon-state gets transmitted; 2) reflection channel in the waveguide in which the photon-state gets reflected; 3) loss channel out of the waveguide in which the photon-state was first absorbed by the 2LS and then decays into free-space modes. Notice that the loss channel is present once a non-zero loss rate  $\Gamma'$  is used. In our calculation, we are able to compute the properties of the transmission and reflection channels, from which we can infer the property of loss channel. Below, we present analysis for  $n = 1, 2, 3$  Fock state scattering.

#### 1-photon Fock-State Scattering

Injecting an incoming 1-photon state from the left, we know there are three possible outcomes (channels): this single-photon can get transmitted to the right of the 2LS, or get reflected back to the left of the 2LS, or get lost during the period the 2LS is excited. We define the 1-photon transmission, reflection and loss probabilities as  $P_{1T}$ ,  $P_{1R}$  and  $P_{1\text{loss}}$ , respectively ( $T$  denotes transmission and  $R$  denotes reflection.) We calculated  $P_{1T}$  and  $P_{1R}$  from the scattering solution [93], and then from the conservation of probability, we know that  $P_{1\text{loss}} = 1 - P_{1T} - P_{1R}$ .

The loss probability  $P_{\text{loss}}$  contributes to the  $n = 0$  (vacuum) sector. If we measure the number statistics in the reflected field,  $P_{1T}$  and  $P_{1R}$  contribute to the  $n = 0$  and  $n = 1$  sectors, respectively.

### 2-photon Fock-State Scattering

Injecting an incoming 2-photon state from the left, we know there are six possible outcomes (channels): both photons get transmitted, one transmitted and one reflected, both reflected, one transmitted and one lost, one reflected and one lost, and both lost. We define the corresponding probabilities as  $P_{2TT}$ ,  $P_{2TR}$ ,  $P_{2RR}$ ,  $P_{1T+1\text{loss}}$ ,  $P_{1R+1\text{loss}}$ , and  $P_{2\text{loss}}$ . Because the 2LS can only absorb one photon at a time, the events in which two photons are lost are very rare for the low-loss case. The condition for low loss is  $P \gg 1$ ; if one has only  $P \gtrsim 1$ , then we require in addition  $\sigma \gtrsim \Gamma'$  so that the 2LS is not re-excited after a loss event. Therefore, we neglect the two photon loss probability  $P_{2\text{loss}} \rightarrow 0$ .

What we actually calculated from our scattering solution are  $P_{2TT}$ ,  $P_{2TR}$  and  $P_{2RR}$ , and again from the conservation of probability, we know that  $P_{1T+1\text{loss}} + P_{1R+1\text{loss}} = 1 - P_{2TT} - P_{2TR} - P_{2RR}$ . Furthermore, we make the assumption that that after one of the two photons is lost, the other one scatters as if it was the only photon. According to this argument, we can separate  $P_{1T+1\text{loss}}$  from  $P_{1R+1\text{loss}}$  using our knowledge of single-photon scattering:

$$\begin{aligned} P_{1T+1\text{loss}} &= [1 - P_{2TT} - P_{2TR} - P_{2RR}] \frac{P_{1T}}{P_{1T} + P_{1T}}, \\ P_{1R+1\text{loss}} &= [1 - P_{2TT} - P_{2TR} - P_{2RR}] \frac{P_{1R}}{P_{1T} + P_{1T}}. \end{aligned} \quad (5.1)$$

Regarding the number statistics in the reflected field,  $P_{2TT}$ ,  $P_{2TR}$  and  $P_{2RR}$  will contribute to  $n = 0$ ,  $n = 1$  and  $n = 2$  sectors, respectively.  $P_{1T+1\text{loss}}$  and  $P_{1R+1\text{loss}}$  will contribute to  $n = 0$  and  $n = 1$  sectors, respectively.

### 3-photon Fock-State Scattering

Now, we consider injecting an incoming 3-photon state from the left. Again, we neglect events of two or more photons getting lost. There are seven possible outcomes (channels): three photons all get transmitted, two transmitted and one reflected, one transmitted and two reflected, all three get reflected, two transmitted and one lost, one transmitted and one reflected and one lost, and two reflected and one lost. The corresponding probabilities are  $P_{3TTT}$ ,  $P_{3TTR}$ ,  $P_{3TRR}$ ,  $P_{3RRR}$ ,  $P_{2TT+1\text{loss}}$ ,  $P_{2TR+1\text{loss}}$  and  $P_{2RR+1\text{loss}}$ . From the calculated  $P_{3TTT}$ ,  $P_{3TTR}$ ,  $P_{3TRR}$ ,  $P_{3RRR}$  and the conservation of probability, we know that  $P_{2TT+1\text{loss}} + P_{2TR+1\text{loss}} + P_{2RR+1\text{loss}} = 1 - P_{3TTT} - P_{3TTR} - P_{3TRR} - P_{3RRR}$ . Furthermore, we assume that after one of the three photons is lost, the other two scatter as if there were only two photons. Based on this argument and our knowledge of two-photon scattering, we can separate  $P_{2TT+1\text{loss}}$ ,  $P_{2TR+1\text{loss}}$  and  $P_{2RR+1\text{loss}}$ :

$$\begin{aligned} P_{2TT+1\text{loss}} &= [1 - P_{3TTT} - P_{3TTR} - P_{3TRR} - P_{3RRR}] \frac{P_{2TT}}{P_{2TT} + P_{2TR} + P_{2RR}}, \\ P_{2TR+1\text{loss}} &= [1 - P_{3TTT} - P_{3TTR} - P_{3TRR} - P_{3RRR}] \frac{P_{2TR}}{P_{2TT} + P_{2TR} + P_{2RR}}, \\ P_{2RR+1\text{loss}} &= [1 - P_{3TTT} - P_{3TTR} - P_{3TRR} - P_{3RRR}] \frac{P_{2RR}}{P_{2TT} + P_{2TR} + P_{2RR}}. \end{aligned} \quad (5.2)$$

For the number statistics in the reflected field,  $P_{3TTT}$  and  $P_{2TT+1\text{loss}}$ ,  $P_{3TTR}$  and  $P_{2TR+1\text{loss}}$ ,  $P_{3TRR}$  and  $P_{2RR+1\text{loss}}$ , and  $P_{3RRR}$  will contribute to  $n = 0$ ,  $n = 1$ ,  $n = 2$  and  $n = 3$  sectors, respectively.

### Coherent-State Scattering

Given an incoming coherent state with probability  $p_i$  of  $i$ -photon state, we can calculate the number statistics in the reflected field from the above discussion of Fock-state scattering. Choosing a mean photon number  $\bar{n} = 1$ , we consider up

to 3–photon scattering. With the contribution from the loss included, we obtain the probability  $P_i$  of having an  $i$ –photon state in the reflected field as follows:

$$\begin{aligned} P_0 &= p_0 + p_1 [P_{1T} + P_{1\text{loss}}] + p_2 [P_{2TT} + P_{1T+1\text{loss}}] + p_3 [P_{3TTT} + P_{2TT+1\text{loss}}] + \dots, \\ P_1 &= p_1 P_{1R} + p_2 [P_{2TR} + P_{1R+1\text{loss}}] + p_3 [P_{3TTR} + P_{2TR+1\text{loss}}] + \dots, \\ P_2 &= p_2 P_{2RR} + p_3 [P_{3TRR} + P_{2RR+1\text{loss}}] + \dots, \\ P_3 &= p_3 P_{3RRR} + \dots. \end{aligned} \tag{5.3}$$

This is the final result with the loss contribution corrected.  $P_{i=0-3}$  gives rise to the number statistics of the reflected field.

### 5.2.3 Number Statistics of the Reflected Field

Here, we show that the reflected field has sub-Poissonian statistics after correcting for the contribution of loss as shown in Sec. 5.2.2. Figure 5.3 shows the probabilities  $P_n$  to measure  $n$ -photon states in the reflected field after scattering a coherent state off the 2LS. We will call such a photon source the “2LS source”. We set the effective Purcell factor  $P = \Gamma/\Gamma' = 20$  [47] for now, and return to the effect of loss later. For comparison, we also show  $P_n$  (dashed line) of a coherent state with the same mean photon number as the reflected field. It is remarkable that, for the full parameter range, the reflected field has higher single-photon and lower vacuum and multiphoton content than the coherent state. In the insert of Fig. 5.3, we show that the multiphoton content is strongly suppressed at  $\sigma = \Gamma/2$ . This is in agreement with the observed antibunching behavior of microwave photons [48], and is the key to increasing the key generation rate.

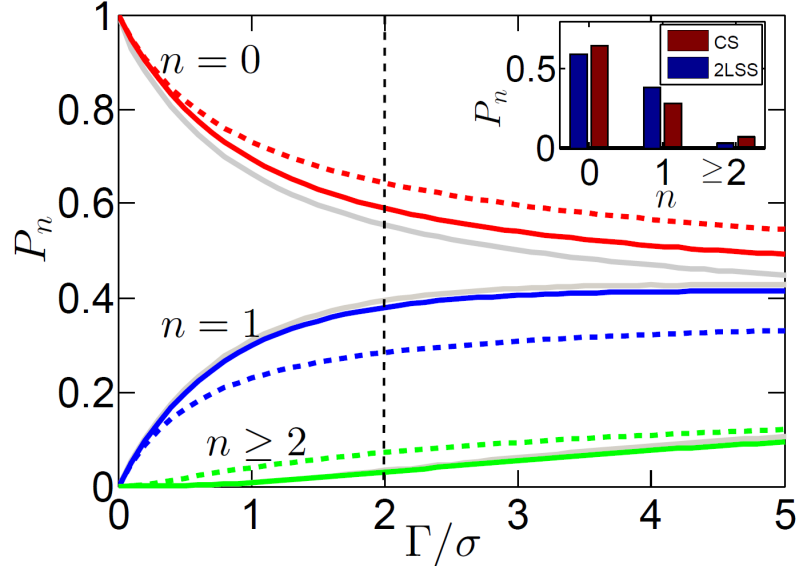


FIGURE 5.3: Nonclassical light source. The number statistics  $P_n$  of the 2LS source (2LSS, solid), and a coherent state (CS, dashed) of the same mean photon number as a function of  $\Gamma/\sigma$ . Inset:  $P_n$  at  $\sigma = \Gamma/2$ . Here, we set  $P = \Gamma/\Gamma' = 20$ . For comparison, 2LSS without loss is shown in gray lines.

### 5.3 Model for Decoy-State Quantum Key Distribution

Now, we discuss the decoy-state method with light sources, including weak coherent states, a heralded single-photon source (HSPS), and the 2LS source (2LSS). The secure key generation rate (per signal pulse emitted by Alice) is given by [138]

$$R \geq q\{-Q_s f(E_s)H_2(E_s) + Q_1[1 - H_2(e_1)]\}, \quad (5.4)$$

where the efficiency  $q$  is 1/2 for the Bennett-Brassard 1984 (BB84) protocol,  $f(E_s)$  is the error correction efficiency (we use  $f = 1.22$  [139]),  $Q_s$  and  $E_s$  are the overall gain and error rate of signal states, respectively,  $Q_1$  and  $e_1$  are the gain and error rate of single-photon states, respectively, and  $H_2(x)$  is the binary Shannon information function:  $H_2(x) = -x\log_2(x) - (1-x)\log_2(1-x)$ .

In Eq.(5.4), while  $Q_s$  and  $E_s$  are measurable quantities in experiments,  $Q_1$

and  $e_1$  are unknown variables.  $Q_s$  and  $E_s$  are given by

$$Q_s = \sum_{n=0}^{\infty} p_n^s Y_n, \quad E_s = \frac{1}{Q_s} \sum_{n=0}^{\infty} p_n^s Y_n e_n, \quad (5.5)$$

where  $p_n^s$  is the  $n$ -photon probability of signal states,  $e_n$  is the error rate of an  $n$ -photon state, and  $Y_n$  is the  $n$ -photon yield, i.e., the conditional probability of a click on Bob's side given that Alice has sent an  $n$ -photon state.

To generate a lower bound on the key generation rate, we have to estimate a lower bound of  $Q_1$  (or equivalently  $Y_1$  as  $Q_1 = p_1^s Y_1$ ) and an upper bound of  $e_1$ . Estimating the lower bound  $Y_1^l$  and the upper bound  $e_1^u$  based solely on Eq.(5.5) unavoidably underestimates the secure key generation rate due to the lack of enough information about the transmission channel. The decoy-state idea [87, 88, 89] is a clever way to obtain additional channel information by sending in additional decoy states. The decoy states are used to detect eavesdropping, but not for key generation. By measuring the transmission of the decoy states, Alice and Bob have another set of constraints

$$Q_d = \sum_{n=0}^{\infty} p_n^d Y_n, \quad E_d = \frac{1}{Q_d} \sum_{n=0}^{\infty} p_n^d Y_n e_n, \quad (5.6)$$

where  $Q_d$  and  $E_d$  are the measured overall gain and error rate of decoy states, respectively. Because Eve has no way to distinguish an  $n$ -photon decoy state from an  $n$ -photon signal state, the yield  $Y_n$  and the error rate  $e_n$  are the same for both the decoy and signal states.

For our numerical simulation, we use the channel model in Ref.[140] to calculate the experimental parameters  $Q_s$ ,  $E_s$ ,  $Q_d$ , and  $E_d$ . In this model, the yield is  $Y_n = 1 - (1 - Y_0)(1 - \eta)^n$ , where  $Y_0$  is the background rate and  $\eta$  is the over-

all transmittance given by  $\eta = t_{AB}\eta_{Bob}$ , where  $t_{AB} = 10^{-\alpha\ell/10}$  is the channel transmittance and  $\eta_{Bob}$  is the detection efficiency on Bob's side. Here,  $\alpha$  is the loss coefficient and  $\ell$  is the transmission distance. The error rate is given by  $e_n = [e_0Y_0 + e_d(Y_n - Y_0)]/Y_n$ , where  $e_d$  is the probability that a photon hits the wrong detector and  $e_0$  is the error rate of the background. We use the experimental parameters in Ref.[141]:  $\alpha = 0.21\text{dB/km}$ ,  $e_d = 3.3\%$ ,  $Y_0 = 1.7 \times 10^{-6}$ ,  $e_0 = 0.5$ , and  $\eta_{Bob} = 0.045$ .

We apply the linear programming method [142] to estimate  $Y_1^l$  and  $e_1^u$  from Eqs.(5.5) and (5.6). This method is applicable to light sources with general number statistics. We use two decoy states—the vacuum and a weak decoy state. For the weak coherent states, the key generation rate is optimized in terms of the mean photon number in both the signal and decoy states [140]. For the heralded single-photons, we use the number statistics from Ref.[143]. For the 2LS source, the signal and decoy states are generated by scattering coherent states of  $\bar{n} = 1$  and  $\bar{n} = 0.02$ , respectively. We choose  $\sigma = \Gamma/2$ .

## 5.4 Key Generation Rate

Figure 5.4 shows the resulting decoy-state scheme key generation rate as a function of the transmission distance. The key generation rate is cut off when it falls below the error rate in the channel. The cut-off distance sets the maximal transmission distance  $\ell_{max}$ . With the same experimental parameters and estimation technique, our scheme using the 2LS source obtains a two-fold increasing of key generation rate compared to the case of using a weak coherent state instead. The maximal transmission distance  $\ell_{max}$  is increased as well. In addition, our scheme also outperforms the heralded single-photon source scheme [143]. Such a performance enhancement is due to the reduced vacuum and multiphoton contents,

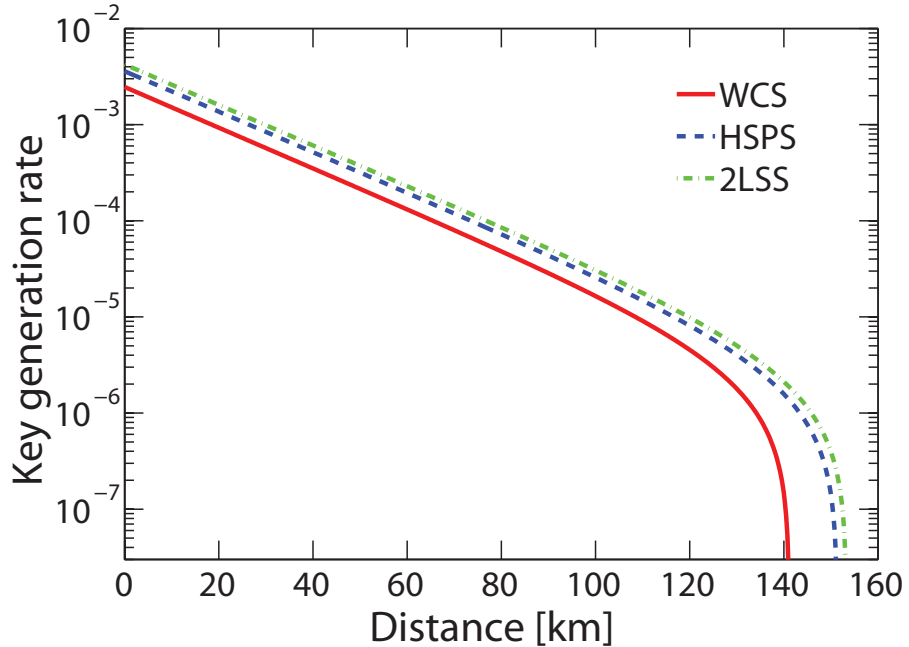


FIGURE 5.4: Key generation rate with different light sources: weak coherent state (WCS), heralded single-photon source (HSPS), and 2LS source (2LSS) with  $\sigma = \Gamma/2$  and  $P = 20$ .

as shown in Fig. 5.3.

Next, we investigate the robustness of our scheme with respect to the variation of system parameter  $\Gamma/\sigma$ . As shown in Fig. 5.5(a), the key generation rate gradually converges as  $\Gamma/\sigma$  increases. In particular, the insert shows that the maximal transmission distance ( $\ell_{\max}$ ) has little change for  $\Gamma/\sigma \geq 1$ .

The effect of loss on the system performance is shown in Figure 5.5(b). We fix  $\sigma = \Gamma/2$  and choose different loss rates  $\Gamma'$  of the 2LS. In Fig. 5.5(b), we observe that, as  $P$  increases, the key generation rate increases and converges. It is evident that, for  $P \geq 10$ , the performance is very reliable against loss as shown in the insert. Given that values of  $P$  as large as 20 have already been achieved in recent experiments [47, 48], our scheme can be practically useful for quantum key distribution.

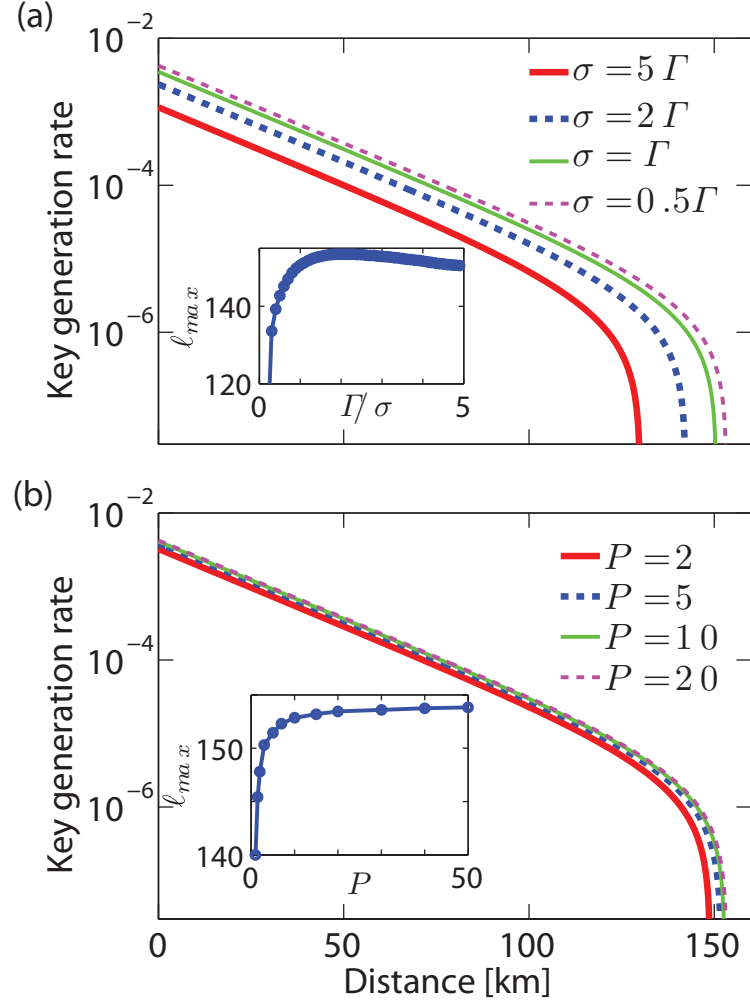


FIGURE 5.5: Key generation rate of 2LS sources with parameter variation and loss: (a)  $\sigma = 5\Gamma, 2\Gamma, \Gamma, 0.5\Gamma$ . Inset: maximal transmission distance ( $\ell_{max}$ ) as a function  $\Gamma/\sigma$ . (b)  $P = 2, 5, 10, 20$ . Inset:  $\ell_{max}$  as a function of  $P$ .  $\sigma = \Gamma/2$ .

## 5.5 Conclusion

We demonstrate a practical method for decoy-state QKD with a nonclassical light source generated using waveguide-QED. The nonlinear 2LS leads to distinct processes in single-photon and multiphoton scattering. As a result, the number statistics of the reflected field is sub-Poissonian with more single-photon content and less multi-photon content compared to Poissonian light sources.

The loss effect of the 2LS on the number statistics is taken into account in our channel model. We use a linear programming approach to estimate the lower bound of key generation rate. The resulting performance of our scheme outperforms decoy-state QKD with both weak coherent states and the heralded single-photons. Finally, we show that our scheme is reliable against various experimental imperfections such as variation of pulse width and loss due to the 2LS.

# 6

## Waveguide-QED-Based Photonic Quantum Computation

*Summary:* <sup>1</sup>We propose a new scheme for photonic quantum computation using flying qubits—propagating photons in a one-dimensional waveguide interacting with matter qubits. Photon-photon interactions are mediated by the coupling to a three-level or four-level system, based on which photon-photon  $\pi$ -phase gates (Controlled-NOT) can be implemented for universal quantum computation. We show that high gate fidelity is possible given recent dramatic experimental progress in superconducting circuits and photonic-crystal waveguides. The proposed system can be an important building block for future on-chip quantum networks.

---

<sup>1</sup> Part of the text of this chapter has been adapted from the following preprint submitted to Phys. Rev. Lett.: Huaixiu Zheng, Daniel J. Gauthier, and Harold U. Baranger, “Waveguide-QED-Based Photonic Quantum Computation”, arXiv:1211.1711 (2012).

## 6.1 Introduction

Quantum computers hold great promise for outperforming any classical computer in solving certain problems such as integer factorization [144], as well as in efficiently simulating quantum many-body systems [145, 146]. While quantum computation schemes often encode information in stationary qubits such as atoms, trapped ions, quantum dots and superconducting qubits [147], flying qubits—photons—have several appealing features as carriers of quantum information [147, 148]. Most importantly, photons have long coherence times because they rarely interact, and yet can be readily manipulated at the single photon level using linear optics. Furthermore, photonic quantum computation is potentially scalable [148] in view of the recent controlled generation of single-photon pulses [43, 47, 57, 149, 150] and demonstration of stable quantum memories [151, 152]. However, weak photon-photon interaction makes it very challenging to realize the two-qubit gates necessary for universal computation between single-photons. Several schemes have been proposed to circumvent this difficulty. The linear optics scheme [153] uses quantum interference between qubit photons and auxiliary photons to generate an effective nonlinear interaction between qubit photons. Other approaches include employing trapped atoms in a cavity [124, 154] or Rydberg atoms [155, 156] to realize two-qubit gates.

In this Chapter, we propose an alternative scheme for photonic quantum computation: using strong coupling between local emitters and photons in a one-dimensional (1D) waveguide. Because of recent tremendous experimental progress [17, 41, 42, 43, 44, 45, 46, 47, 57, 71], 1D waveguide systems are becoming promising candidates for quantum information processing. A variety of capabilities have been proposed [62, 64, 66, 67, 68, 69, 70, 74, 111], particularly at

the single photon level, yet protocols compatible with current waveguide setups for some important tasks, notably two-qubit gates, have rarely been investigated [157]. In our proposal, we construct photonic two-qubit gates solely based on scattering in a waveguide system that is accessible in current experiments. The photonic qubits are initialized by and returned to quantum memories [151, 152] in order to realize long-term storage. Compared with the cavity approach, our setup is simplified and avoids the complexity of stabilizing the resonance between the cavity modes and the atom. The gate has a wide bandwidth, and its operation time is determined solely by the coupling strength. Combining the simplicity of the system and the scalability of photons, our waveguide-QED-based scheme opens a new avenue towards scalable quantum computation and distributed quantum networks [18] in a cavity-free setting.

We present a  $\pi$ -phase gate scheme based on a four-level system (4LS) and a three-level system (3LS) in Sec. 6.2 and Sec. 6.3, respectively. In Sec. 6.4 we give an example of a photon-qubit quantum memory from an extension of the 4LS scheme. Finally, we conclude in Sec. 6.5.

## 6.2 $\pi$ -Phase Gate: 4LS Scheme

### 6.2.1 Photonic Qubits

The photonic qubits are encoded in the frequency degree of freedom,  $|\omega_0\rangle$  and  $|\omega_1\rangle$ , for simplicity. Single photons can be generated from the emission of quantum dots [43, 45, 47] or using circuit-QED systems [57], and single-qubit rotations can be realized using a Mach-Zehnder interferometer [158, 159]. Hence, we focus on two-qubit gates and, in particular, a  $\pi$ -phase (Controlled-NOT) gate. We consider a semi-infinite 1D waveguide side-coupled to a four-level system that is located a distance  $a$  from the end (Fig. 6.1). Such a setup can be realized in a va-

riety of experimental systems using superconducting transmission lines [44, 71], diamond nanowires coupled to NV centers [42], photonic-crystal waveguides coupled to quantum dots [47], hollow fibers with trapped cold atoms [41], or plasmonic nanowires [17]. We now show that a  $\pi$ -phase gate between two photons  $A$  and  $B$  can be realized by reflecting them from the end of the waveguide.

Generalization of our scheme to polarization-encoded qubits is straightforward. The key to this generalization is to choose a four-level system such that both the transitions  $1 \rightarrow 2$  and  $3 \rightarrow 4$  are polarization selective, i.e., they interact with, for example, only  $\pi$ -polarized photons but not  $\sigma$ -polarized photons. In this case, we can define our photonic polarization-qubit to be  $|0\rangle = |\omega_0\rangle_\sigma$  and  $|1\rangle = |\omega_1\rangle_\pi$ . Since information is stored in the polarization degree of freedom, single-qubit operations can be performed via polarization rotations. Then all the discussions of two-qubit gates follow easily with the newly defined polarization qubits.

### 6.2.2 Model Hamiltonian

The Hamiltonian of the system (Fig. 6.1) is given by

$$\begin{aligned}
H &= H_{\text{wg}} + \sum_{i=2}^4 \hbar(\Omega_i - i\Gamma'_i/2)\sigma_{ii} \\
&\quad + \sum_{\alpha=R,L} \int dx \hbar V \delta(x) [a_\alpha^\dagger(x)(\sigma_{12} + \sigma_{32} + \sigma_{34}) + \text{h.c.}], \\
H_{\text{wg}} &= \int dx \frac{\hbar c}{i} \left[ a_R^\dagger(x) \frac{d}{dx} a_R(x) - a_L^\dagger(x) \frac{d}{dx} a_L(x) \right], \tag{6.1}
\end{aligned}$$

where  $a_{R,L}(x)$  are the propagation modes along the  $x$  axis of the waveguide,  $\sigma_{ij} \equiv |i\rangle\langle j|$ , and we use the energy level of ground state  $|1\rangle$  as the energy reference. An imaginary term models the loss of the excited state at rate  $\Gamma'_i$ . The decay

rate to the waveguide continuum is  $\Gamma = 2V^2/c$ , where  $c$  is the group velocity of photons. For our gate operation, we require that the transitions  $1 \rightarrow 2$  and  $3 \rightarrow 4$  have the same frequency  $\Omega_{12} = \Omega_{34}$  (where  $\Omega_{ij} \equiv \Omega_j - \Omega_i$ ); in contrast, the frequency of the  $3 \rightarrow 2$  transition should be distinctly different, satisfying  $|\Omega_{32} - \Omega_{12}| \gg \Gamma$ . In addition, for simplicity, we assume that (i) transitions  $1 \rightarrow 2$ ,  $3 \rightarrow 2$ , and  $3 \rightarrow 4$  have the same coupling strength  $\Gamma$  to the waveguide modes, (ii) state 3 is metastable with loss rate  $\Gamma'_3 = 0$ , and (iii) states 2 and 4 have the same loss rate  $\Gamma' \equiv \Gamma'_2 = \Gamma'_4$ . None of these additional assumptions are essential. Here, we set  $\hbar = c = 1$ .

The photon qubit consists of two distinct frequencies. Frequency  $\omega_1$  is chosen to be on resonance with the transitions  $1 \rightarrow 2$  and  $3 \rightarrow 4$ , *i.e.*  $\omega_1 = \Omega_{12}$ . In contrast,  $\omega_0$  is far off resonance from all of the atomic transitions—an  $\omega_0$  photon does not interact with the four-level system (4LS). The 4LS is initialized in  $|1\rangle$ . Here, we assume that we have quantum memories [151, 152] available, one for qubit photon  $A$  and another for  $B$ , and we give an example in Sec. 6.4.

### 6.2.3 Gate Operation

As illustrated in Fig. 6.1, a  $\pi$ -phase gate between photon pulses  $A$  and  $B$  can be realized via the following steps. (1) Trapping: photon  $A$  (of frequency  $\omega_A$ ) is sent into the system. If  $A$  is in state  $|\omega_1\rangle$ , it is trapped, an auxiliary photon  $C$  of frequency  $\Omega_{32}$  is emitted, and the 4LS is put into  $|3\rangle$ . Otherwise,  $A$  will come out without interacting with the 4LS. We call the output the  $A'$  photon. (2)  $\pi$ -phase: a second qubit photon  $B$  (of frequency  $\omega_B$ ) is sent into the system; it gains a  $\pi$ -phase if both  $\omega_B = \omega_1$  and the 4LS is in state  $|3\rangle$ . Otherwise,  $B$  will either pass through without any change if  $\omega_B = \omega_0$ , or be trapped followed by the emission of a  $C'$ -photon of frequency  $\Omega_{32}$  if  $\omega_B = \omega_1$  and the 4LS is in

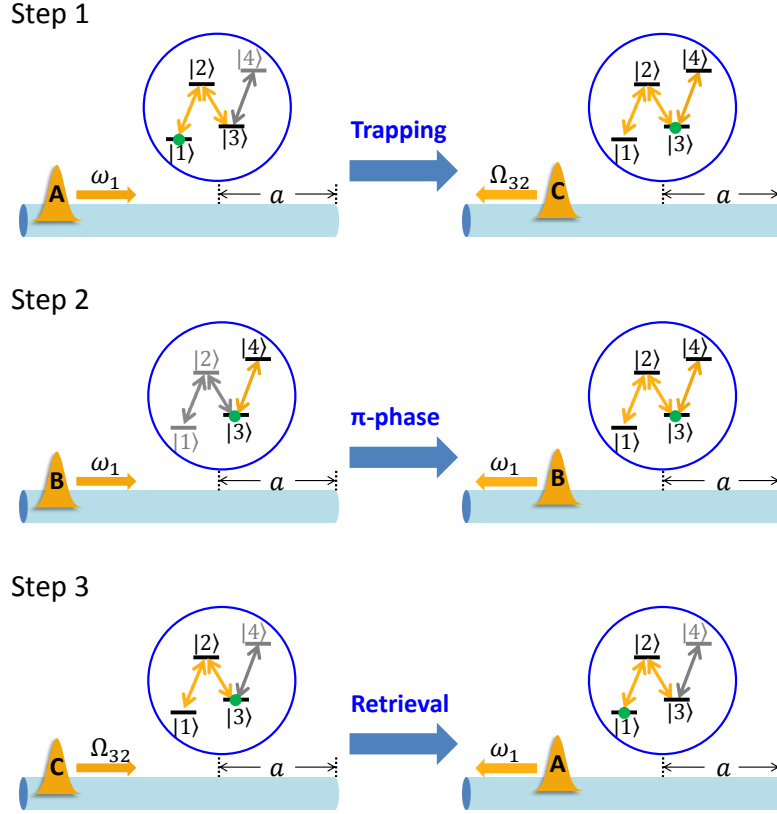


FIGURE 6.1: Gate operation: 1) trapping; 2)  $\pi$ -phase; 3) retrieval. The gate sequences here illustrate the case of both photons  $A$  and  $B$  being in state  $|\omega_1\rangle$ . For this case, step 4) does not cause any change and hence is not shown here. The left and right sides show the initial and final states, respectively. Inactive transitions in each step are gray-colored.

state  $|1\rangle$ . (3) Retrieval of A: by time reversal arguments, sending in the output photon  $A'$  retrieves photon  $A$ , which is further directed to and stored in quantum memory  $A$ . (4) Retrieval of B: in the case of  $\omega_A = \omega_0$  and  $\omega_B = \omega_1$ , photon  $B$  will be trapped by the 4LS in step 2—we retrieve it by simply sending in the auxiliary photon  $C$ . In all the other cases, photon  $C$  simply passes through the 4LS without any change. Photon  $B$  from either step 2 or 4 is directed to and stored in quantum memory  $B$ . Therefore, only when  $\omega_A = \omega_B = \omega_1$  is a  $\pi$ -phase generated by their interaction with the 4LS. We now analyze each of these steps.

*Step 1—Trapping.* For an incoming single photon  $A$  in mode  $|\omega_A\rangle$  and initial state  $|1\rangle$  of the 4LS, the output state of the system, obtained by imposing wavefunction matching [70, 111] and hard-wall boundary condition at the end of the waveguide [157], is

$$|\phi_1^{\text{out}}(\omega_A)\rangle = r_{11}(\omega_A)|\omega_A\rangle \otimes |1\rangle + r_{13}(\omega_A)|\tilde{\omega}_A\rangle \otimes |3\rangle, \quad (6.2)$$

where

$$\begin{aligned} \tilde{\omega} &= \omega - \Omega_{13}, \\ r_{11}(\omega) &= e^{2i\omega a} \frac{-\Omega_{12} + \frac{i\Gamma'}{2} + \omega - \frac{i\Gamma}{2}[e^{2i\tilde{\omega}a} - e^{-2i\omega a}]}{\Omega_{12} - \frac{i\Gamma'}{2} - \omega + \frac{i\Gamma}{2}[e^{2i\tilde{\omega}a} + e^{2i\omega a} - 2]}, \\ r_{13}(\omega) &= \frac{(i\Gamma/2)(e^{2i\omega a} - 1)[e^{2i\tilde{\omega}a} - 1]}{\Omega_{12} - \frac{i\Gamma'}{2} - \omega + \frac{i\Gamma}{2}[e^{2i\tilde{\omega}a} + e^{2i\omega a} - 2]}. \end{aligned} \quad (6.3)$$

The detailed derivation is given in Appendix E. We first illustrate the operation principle for the lossless case  $\Gamma' = 0$  and then later analyze the effect of loss in detail. We assume that the key condition  $2(\Omega_{12} + \Omega_{32})a = 2n_1\pi$  is satisfied; in addition, we can make the trivial choice  $2\omega_0a = (2n_0 + 1)\pi$  ( $n_0, n_1$  are integers). Then, if the incoming qubit photon- $A$  is in mode  $|\omega_0\rangle$ ,  $r_{11}(\omega_0) = 1$  and  $r_{13}(\omega_0) = 0$  because  $\omega_0$  is far off resonance from all the transitions. Hence, it will reflect from the system without change, leaving the 4LS in  $|1\rangle$ . On the other hand, if photon- $A$  is in mode  $|\omega_1\rangle$ , the on-resonance interaction with the  $1 \rightarrow 2$  transition gives  $r_{11}(\omega_1) = 0$  and  $r_{13}(\omega_1) = -1$ . As a result, it will be trapped and stored in level  $|3\rangle$  of the 4LS, emitting an auxiliary  $C$ -photon at frequency  $\omega_1 - \Omega_{13} = \Omega_{32}$ .

*Step 2— $\pi$ -phase.* Now send in the second qubit, photon- $B$  in mode  $|\omega_B\rangle$ . The

output state after scattering reads

$$\begin{aligned} |\phi_2^{\text{out}}(\omega_A, \omega_B)\rangle &= r_{11}(\omega_A)|\omega_A\rangle \otimes |\phi_1^{\text{out}}(\omega_B)\rangle \\ &+ r_{13}(\omega_A)R_3(\omega_B)|\tilde{\omega}_A\rangle|\omega_B\rangle \otimes |3\rangle, \end{aligned} \quad (6.4)$$

where

$$R_3(\omega) = \frac{-(\Omega_{12} - \frac{i\Gamma'}{2} - \omega)e^{2i\omega a} + \frac{i\Gamma}{2}(1 - e^{2i\omega a})}{\Omega_{12} - \frac{i\Gamma'}{2} - \omega - \frac{i\Gamma}{2}(1 - e^{2i\omega a})}. \quad (6.5)$$

Here, we neglect the transition  $3 \rightarrow 2$  because  $\omega_{0,1}$  is chosen to be far detuned from  $\Omega_{32}$ . If photon- $B$  is in mode  $|\omega_0\rangle$ , it is far off resonance from the transitions, and, using the same value of  $a$  as above,  $r_{11}(\omega_0) = R_3(\omega_0) = 1$  while  $r_{13}(\omega_0) = 0$ . Hence, the output state in this case is  $|\phi_1^{\text{out}}(\omega_A)\rangle \otimes |\omega_B\rangle$ —photon- $B$  is unaffected. However, if photon- $B$  is in  $|\omega_1\rangle$ , the state after scattering is

$$\begin{aligned} |\phi_2^{\text{out}}(\omega_A, \omega_B = \omega_1)\rangle &= r_{13}(\omega_A)R_3(\omega_B)|\tilde{\omega}_A\rangle|\omega_B\rangle|3\rangle \\ &+ r_{11}(\omega_A)r_{13}(\omega_B)|\omega_A\rangle|\tilde{\omega}_B\rangle|3\rangle. \end{aligned} \quad (6.6)$$

Two possible outcomes exist: (i) if the 4LS is in state  $|1\rangle$  after step 1, photon- $B$  will be trapped, but (ii) if the 4LS is in state  $|3\rangle$ , photon- $B$  is on resonance with transition  $3 \rightarrow 4$  and gains a  $\pi$ -phase [ $R_3(\omega_1) = e^{i\pi}$ ]. The 4LS being in state  $|3\rangle$  is, of course, conditioned upon photon- $A$  in step 1 being in  $|\omega_1\rangle$ . Notice that the  $\pi$ -phase shift is independent of coupling strength  $\Gamma$  which only determines the operation bandwidth of photon pulses (for details, see the following discussions on fidelity). Such a robust  $\pi$ -phase shift of the reflected photon is a result of Fano resonances [62, 160, 161]: complete destructive interference occurs in the transmission between the two paths—photons can either pass through the 4LS or skip it.

*Step 3—Retrieval of A.* By sending in the output photon from step 1, we retrieve photon-*A*. This process is the time-reversal of photon trapping. The full wavefunction that results is increasingly complicated; accordingly, we focus on the specific case needed—using the two conditions  $2(\Omega_{12} + \Omega_{32})a = 2n_1\pi$  and  $2\omega_0a = (2n_0 + 1)\pi$  introduced in step 1—and relegate the full wavefunction, useful for other cases, to Appendix E. The state after this step reads

$$\begin{aligned} |\phi_3^{\text{out}}(\omega_A, \omega_B)\rangle &= r_{11}(\omega_A)r_{11}(\omega_B)|\omega_B\rangle \otimes r_{11}(\omega_A)|\omega_A\rangle|1\rangle \\ &\quad + r_{11}(\omega_A)r_{13}(\omega_B)|\tilde{\omega}_B\rangle \otimes R_3(\omega_A)|\omega_A\rangle|3\rangle \\ &\quad + r_{13}(\omega_A)R_3(\omega_B)|\omega_B\rangle \otimes r_{31}(\omega_A)|\omega_A\rangle|1\rangle \end{aligned} \quad (6.7)$$

with

$$r_{31}(\omega) = \frac{(i\Gamma/2)(e^{2i\tilde{\omega}a} - 1)[e^{2i\omega a} - 1]}{\Omega_{32} - \frac{i\Gamma}{2} - \tilde{\omega} + \frac{i\Gamma}{2}[e^{2i\omega a} + e^{2i\tilde{\omega}a} - 2]}. \quad (6.8)$$

In our case, all of the factors  $r_{ij}$  and  $R_3$  are either 0 or  $\pm 1$ . The first line of Eq. (6.7) corresponds to input qubits in the 00 state, line two is for 01, and the last line covers both 10 and 11.

*Step 4—Retrieval of B.* In the case  $\omega_A = \omega_0$  and  $\omega_B = \omega_1$ , photon *B* is trapped in the 4LS in step 2. Time reversal arguments imply that sending in a *C* photon of frequency  $\Omega_{32}$  will release photon *B* in this case but will simply pass through the system without interacting in the other cases. The final state after all four steps is

$$\begin{aligned} |\phi_4^{\text{out}}\rangle &= f_1(\omega_A, \omega_B)|\omega_A\rangle|\omega_B\rangle|\omega_C\rangle|1\rangle \\ &\quad - f_2(\omega_A, \omega_B)|\omega_A\rangle|\tilde{\omega}_B\rangle|\omega'_C\rangle|1\rangle \end{aligned} \quad (6.9)$$

where

$$\begin{aligned} f_1(\omega_A, \omega_B) &= r_{11}^2(\omega_A) r_{11}(\omega_B) + r_{13}(\omega_A) r_{31}(\omega_A) R_3(\omega_B), \\ f_2(\omega_A, \omega_B) &= r_{11}(\omega_A) R_3(\omega_A) r_{13}(\omega_B). \end{aligned} \quad (6.10)$$

The second line in Eq. (6.9) corresponds to the case of the input  $\omega_A = \omega_0$  and  $\omega_B = \omega_1$ ; the state  $|\omega'_C\rangle$  signifies that the frequency of the  $C$  photon is now  $\omega_1$ —it is the retrieved  $B$  photon. By filtering out the frequency  $\Omega_{32}$  and relabeling  $|\omega'_C\rangle$  as  $|\omega_B\rangle$ , we obtain the final state  $|\phi_f(\omega_A = \omega_i, \omega_B = \omega_j)\rangle = (-1)^{ij} |\omega_i\rangle |\omega_j\rangle \otimes |1\rangle$ ,  $i, j = 0$  or  $1$ . Thus we see that the above steps give rise to the desired  $\pi$ -phase gate:

$$U_{AB} = \exp \{ i\pi |\omega_1\rangle_A \langle \omega_1| \otimes |\omega_1\rangle_B \langle \omega_1| \}. \quad (6.11)$$

Here, we assume the use of quantum memories and direct photon  $A$  from step 3 to quantum memory  $A$ . Photon  $B$  from either step 2 or 4 is directed to quantum memory  $B$  after filtering out frequency  $\omega_C$ .

#### 6.2.4 Fidelity and Loss

We now analyze the gate performance by considering photon pulses with a finite spectral width  $\sigma$  and including atomic loss ( $\Gamma' > 0$ ). In particular, we consider Gaussian input pulses  $A$ ,  $B$ , and  $C$  centered at frequencies  $\omega_1$ ,  $\omega_1$ , and  $\Omega_{32}$ , respectively:

$$\begin{aligned} |\phi_{A,B}\rangle &= \int d\omega_{A,B} g_\sigma(\omega_{A,B} - \omega_1) |\omega_{A,B}\rangle, \\ |\phi_C\rangle &= \int d\omega_C g_\sigma(\omega_C - \Omega_{32}) |\omega_C\rangle, \quad g_\sigma(\omega) \propto e^{-\frac{\omega^2}{2\sigma^2}}. \end{aligned} \quad (6.12)$$

The corresponding temporal width is  $\Delta T = 1/(2\sigma)$ . After the scattering, the final state of the system is  $|\phi_f\rangle = \int d\omega_A d\omega_B d\omega_C g_\sigma(\omega_A) g_\sigma(\omega_B) g_\sigma(\omega_C) |\phi_4^{\text{out}}(\omega_A, \omega_B, \omega_C)\rangle$ .

The fidelity of the photon-atom gate is given by

$$F \equiv |\langle \psi | \phi_f \rangle|^2, \quad (6.13)$$

where  $|\psi\rangle = -|\phi_A\rangle|\phi_B\rangle|\phi_C\rangle \otimes |1\rangle$  is the target state.

The atomic loss is characterized by introducing the effective Purcell factor  $P = \Gamma/\Gamma'$ . We note that large values of  $P$  ( $> 20$ ) have been demonstrated in recent experiments using either superconducting circuits [46], photonic-crystal waveguides [47], or semiconductor nanowires. To quantify the effect of loss, we define the probability of leakage,  $P_\ell$ , to be the probability of losing the photon during the operation through spontaneous emission

$$P_\ell \equiv 1 - |\langle \phi_f | \phi_f \rangle|^2. \quad (6.14)$$

Figure 6.2(a) shows the fidelity of our scheme as a function of the pulse width  $\Delta T$ . For a short pulse, the spectral width is large, and so the fidelity is limited by the large frequency variation. As  $\Delta T$  increases to  $10\Gamma^{-1}$ , the fidelity starts to saturate and is only limited by the atomic loss. A fidelity of 86% and 94% can be achieved for  $P = 20$  and  $P = 40$ , respectively. Figure 6.2(b) shows that the leakage error decays rapidly as  $P$  increases and can be as small as a few percent for  $P$  approaching 100, which is feasible in the near future given the rapid experimental advances in 1D waveguide systems. Such a leakage error is acceptable, especially since it can be efficiently corrected by concatenated coding [124, 144].

We now make a rough estimate of the gate operation time. Since the gate fidelity is insensitive to the pulse width variation once  $\Delta T$  is sufficiently large [Fig. 6.2(a)], we choose  $\Delta T = 10\Gamma^{-1}$  for practical estimation. Using a superconducting circuit as an example, we estimate the duration of our photon-

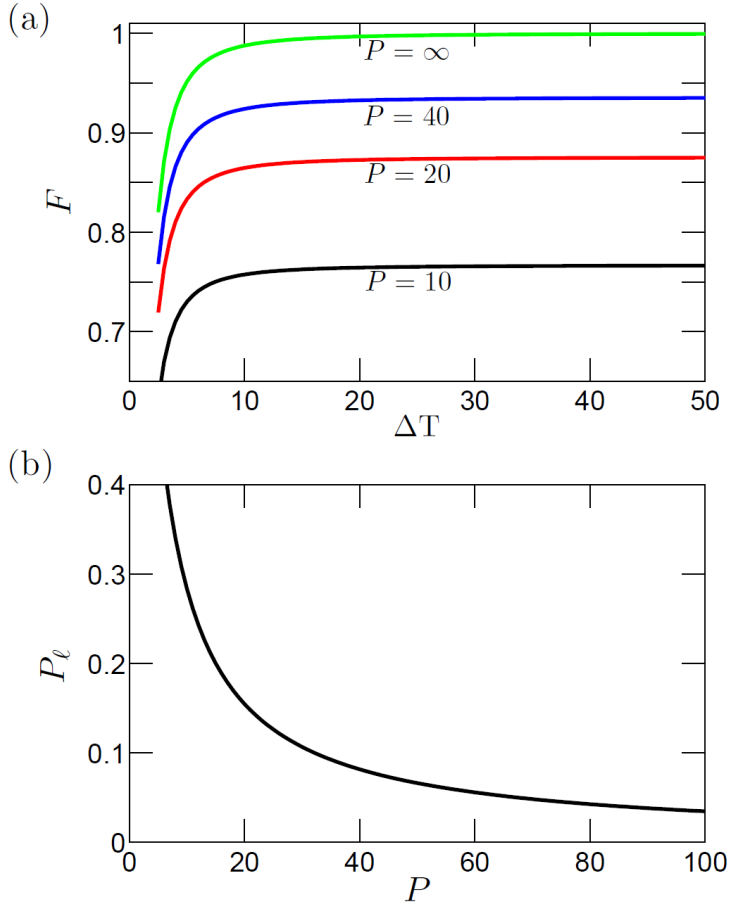


FIGURE 6.2: Fidelity and leakage error of the photon-photon  $\pi$ -phase gate. (a) Fidelity  $F$  as a function of the pulse width  $\Delta T$  (in units of  $\Gamma^{-1}$ ) for  $P = 10, 20, 40, \infty$ . (b) The leakage probability  $P_\ell$  as a function  $P$  with  $\Delta T = 10\Gamma^{-1}$ .

photon  $\pi$ -phase gate to be  $30\Gamma^{-1} \sim 300$  ns for a superconducting qubit with  $\Gamma = 2\pi \times 100$  MHz [46]. Such an operation time is compatible with current qubit coherence times, which are on the order of  $1\mu\text{s}$ <sup>2</sup>.

### 6.3 $\pi$ -Phase Gate: 3LS Scheme

An alternative  $\pi$ -phase gate using only a three level system (3LS) is possible by adapting the cavity-based proposal of Ref. [124]. First, one constructs a  $\pi$ -phase

---

<sup>2</sup> Recently, even higher coherence times ( $10\text{-}20\mu\text{s}$  [162] and  $\sim 0.1\text{ ms}$  [163]) have been achieved by placing the qubit in a 3D cavity.

gate between a photon qubit and the local qubit (3LS). Then, using the photon-atom  $\pi$ -phase gate as a building block, a  $\pi$ -phase gate between two photons  $A$  and  $B$  can be implemented by sending them into the system successively. This proposal has the additional advantage of naturally realizing a photon-atom  $\pi$ -phase gate, which can be used to entangle distant quantum nodes in a large quantum network [19].

### 6.3.1 Model Hamiltonian

In this realization (Fig. 6.3), we consider a semi-infinite 1D waveguide side-coupled to a 3LS, which is located a distance  $a$  from the end. Such a system could be realized in a variety of experimental systems [17, 41, 44, 47, 71]. A  $\pi$ -phase gate between two photons  $A$  and  $B$  is realized by reflecting them from the end of the waveguide.

The Hamiltonian of the system is given by

$$\begin{aligned} H_1 &= H_{\text{wg}} + H_{ee} + \sum_{\alpha=R,L} \int dx \hbar V \delta(x) [a_\alpha^\dagger(x) \sigma_{ge} + \text{h.c.}], \\ H_{\text{wg}} &= \int dx \frac{\hbar c}{i} \left[ a_R^\dagger(x) \frac{d}{dx} a_R(x) - a_L^\dagger(x) \frac{d}{dx} a_L(x) \right], \end{aligned} \quad (6.15)$$

where  $H_{ee} = \hbar(\Omega_{eg} - i\Gamma'/2)\sigma_{ee}$  and  $\sigma_{ij} \equiv |i\rangle\langle j|$ . The transition from the ground state  $|g\rangle$  to the excited state  $|e\rangle$  couples to the waveguide modes ( $a_{R,L}$ ); an imaginary term models the loss of the excited state at rate  $\Gamma'$ . The decay rate to the waveguide continuum is  $\Gamma = 2V^2/c$ , where  $c$  is the group velocity of photons. Note that the metastable state  $|s\rangle$  does not appear in the Hamiltonian as it is decoupled from the waveguide; however, its presence is essential since  $|g\rangle$  and  $|s\rangle$  form the atomic qubit. As in Sec. 6.2, we consider a photonic qubit coded in the frequency domain.

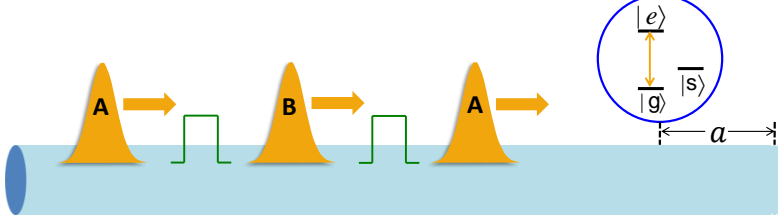


FIGURE 6.3: Schematic diagram of the operation sequence of the  $\pi$ -phase gate between two photons  $A$  and  $B$ . The three-level system (3LS) is located a distance  $a$  from the end of the semi-infinite waveguide and is initialized in an equal superposition of the  $g$  and  $s$  states.  $A$  and  $B$  are reflected successively from the semi-infinite waveguide coupled to the 3LS. Between the reflections, single-qubit rotation pulses (green rectangles) are applied to the atomic qubit made of states  $|g\rangle$  and  $|s\rangle$ .

### 6.3.2 Photon-Atom and Photon-Photon $\pi$ -Phase Gates

Our first step is to realize a photon-atom  $\pi$ -phase gate. Consider a single incoming photon with frequency  $\omega$ . In the case that the three-level system is in  $|g\rangle$ , we obtain the output state by imposing a hard-wall boundary condition at the end of the waveguide, thus giving

$$\begin{aligned} |\phi_g^{\text{out}}(\omega)\rangle &= r_g(\omega)|\omega\rangle_L, \\ r_g(\omega) &= \frac{-(\Delta - \frac{i\Gamma'}{2})e^{2i\omega a} + \frac{i\Gamma}{2}(1 - e^{2i\omega a})}{\Delta - \frac{i\Gamma'}{2} - \frac{i\Gamma}{2}(1 - e^{2i\omega a})}, \end{aligned} \quad (6.16)$$

where  $\Delta = \Omega_{eg} - \omega$  is the detuning. We first illustrate the operation principle for the lossless case  $\Gamma' = 0$  and then later analyze the effect of loss in detail. In the lossless case, we always have perfect reflection— $|r_g(\omega)|^2 = 1$ —because the waveguide is semi-infinite. Choosing two frequencies  $\omega_1 = \Omega_{eg}$  and  $|\omega_0 - \Omega_{eg}| \gg \Gamma$ , we have  $r_g(\omega_1) = -1$  and  $r_g(\omega_0) = -e^{2i\omega_0 a}$ . On the other hand, if the qubit is in  $|s\rangle$ , the photon gains a trivial phase shift  $r_s(\omega) = -e^{2i\omega a}$ . Therefore, under the conditions  $2\omega_0 a = (2n_0 + 1)\pi$  and  $2\Omega_{eg} a = (2n_1 + 1)\pi$  with  $n_0, n_1 \in \mathbb{Z}$ , we realize a  $\pi$ -phase gate between the photonic qubit ( $|\omega_0\rangle, |\omega_1\rangle$ ) and the atomic qubit ( $|g\rangle, |s\rangle$ ).

$|s\rangle\rangle$ :

$$r_g(\omega_0) = r_s(\omega_0) = r_s(\omega_1) = -r_g(\omega_1) = 1,$$

$$U_{\text{photon-atom}} = \exp \left\{ i\pi |\omega_1\rangle\langle\omega_1| \otimes |g\rangle\langle g| \right\}. \quad (6.17)$$

Using the photon-atom  $\pi$ -phase gate as a building block, we can implement a  $\pi$ -phase gate between two photons  $A$  and  $B$  as in the cavity-based proposal of Ref. [124]. First, initialize the atom in the state  $|\phi_a\rangle = (|g\rangle + |s\rangle)/\sqrt{2}$ . Next, send in photon- $A$  followed by a  $\pi/2$  rotation on the atom. Third, send in photon- $B$  followed by a  $-\pi/2$  rotation on the atom. Finally, send in photon- $A$  again. This procedure produces a  $\pi$ -phase gate

$$U_{AB} = \exp \left\{ i\pi |\omega_1\rangle_A\langle\omega_1| \otimes |\omega_1\rangle_B\langle\omega_1| \right\}. \quad (6.18)$$

Our scheme closely resembles the cavity-based proposal [124], but we rely on a different mechanism to generate the  $\pi$ -phase shift in a cavity-free setting. As for the 4LS scheme in Sec. 6.2, this phase gate requires fine tuning so that, as noted above,  $2\Omega_{eg}a = (2n_1 + 1)\pi$ ; this is possible using superconducting qubits, for instance, for which the transition frequencies can be easily tuned using external magnetic flux [164].

### 6.3.3 Fidelity and Loss

To analyze the gate performance in this scheme, we consider photon pulses with a finite spectral width  $\sigma$  and include atomic loss ( $\Gamma' > 0$ ). In particular, we consider a Gaussian input pulse centered at frequency  $\omega_1$ :

$$|\phi_i\rangle = \int d\omega g_\sigma(\omega) |\omega\rangle \otimes |\phi_a\rangle, \quad (6.19)$$

$$g_\sigma(\omega) \propto \exp\{-(\omega - \omega_1)^2/2\sigma^2\}. \quad (6.20)$$

The temporal width is  $\Delta T = 1/(2\sigma)$ . After the scattering, the final state of the system is

$$|\phi_f\rangle = \int d\omega g_\sigma(\omega) \times \{r_g(\omega)|\omega\rangle \otimes |g\rangle + r_s(\omega)|\omega\rangle \otimes |s\rangle\} / \sqrt{2}.$$

The fidelity of the photon-atom gate is given by

$$F \equiv |\langle\psi|\phi_f\rangle|^2 = \left| \frac{1}{2} \int d\omega g_\sigma^2(\omega) [r_g(\omega) - r_s(\omega)] \right|^2, \quad (6.21)$$

where  $|\psi\rangle = |\omega_1\rangle \otimes (-|g\rangle + |s\rangle)/\sqrt{2}$  is the target state. The atomic loss is characterized by introducing the effective Purcell factor  $P = \Gamma/\Gamma'$ . To measure the effect of loss quantitatively, we define the probability of leakage,  $P_\ell$ , as the probability of losing the photon during the operation through spontaneous emission:

$$P_\ell \equiv 1 - |\langle\phi_f|\phi_f\rangle|^2 = 1 - \left| \int d\omega g_\sigma^2(\omega) \frac{[|r_g(\omega)|^2 + 1]}{2} \right|^2. \quad (6.22)$$

Figure 6.4(a) shows the fidelity  $F$  as a function of pulse temporal width  $\Delta T$ . For a short pulse, the spectral width is large, and so the fidelity is limited by the large frequency variation of the conditional phase  $r_g(\omega)$ . As  $\Delta T$  increases to  $10\Gamma^{-1}$ , the fidelity starts to saturate and is only limited by the atomic loss. A high fidelity ( $\geq 95\%$ ) can be achieved for a practical value of  $P \geq 20$ . Figure 6.4(b) shows that the leakage probability decreases quickly as one increases  $P$  and is on the order of a few percent for  $P \geq 20$ . Further improvement in both fidelity and loss can be expected from the rapidly development of 1D waveguide technology and schemes using off-resonance mechanisms to reduce the loss.

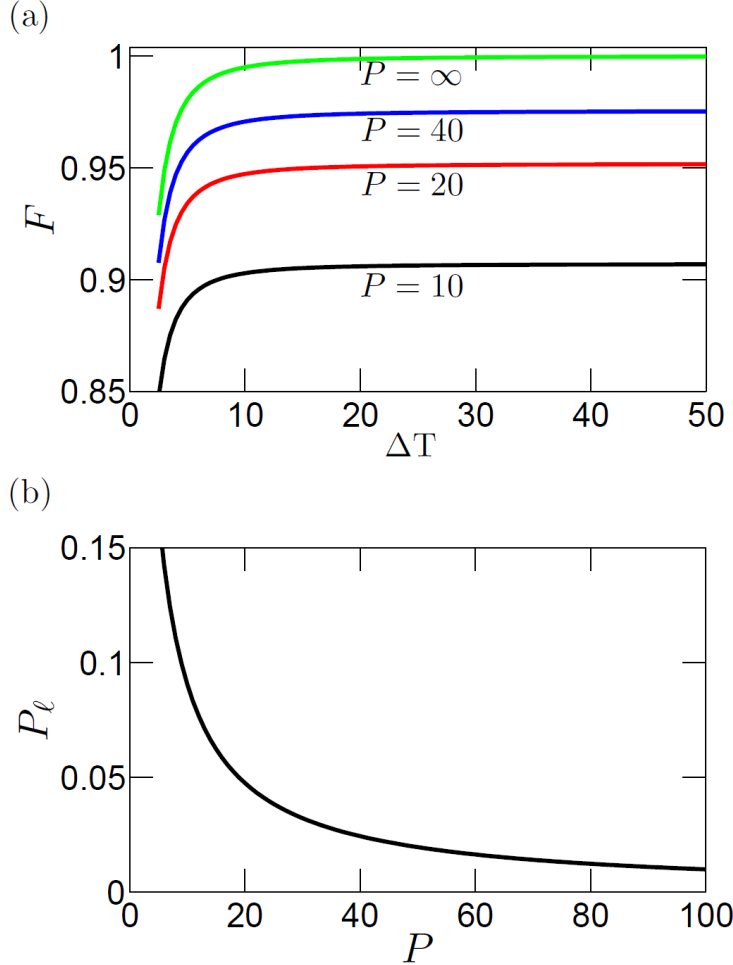


FIGURE 6.4: Fidelity and leakage error of the photon-atom gate in the 3LS scheme. (a) Fidelity  $F$  as a function of the pulse width  $\Delta T$  (in units of  $\Gamma^{-1}$ ) for four different cases. (b) The leakage probability  $P_\ell$  as a function of the effective Purcell factor  $P$  with a pulse width  $\Delta T = 10\Gamma^{-1}$ .

## 6.4 Photon-Qubit Quantum Memory

We extend the 4LS scheme presented in Sec. 6.2 to an M-type five-level system (5LS) to construct a quantum memory of the qubit photons, as shown in Fig. (6.5).

The 5LS is chosen so that the transition energies of the ground state  $|s\rangle$  to the two excited states  $|e_0\rangle$  and  $|e_1\rangle$  match the photon-qubit frequencies  $\omega_0$  and  $\omega_1$ , respectively. Because  $\omega_0$  and  $\omega_1$  are well separated in frequency ( $|\omega_0 - \omega_1| \gg \Gamma$ ), the  $|\omega_0\rangle$  ( $|\omega_1\rangle$ ) photon only interacts with the  $g \rightarrow e_0$  ( $g \rightarrow e_1$ ) transition. In

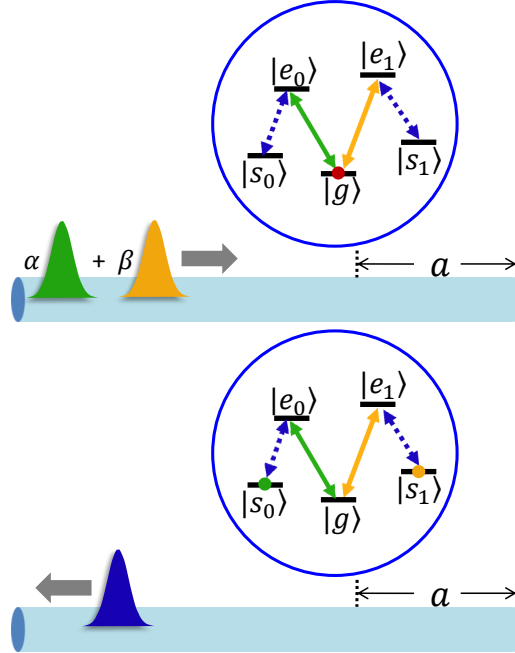


FIGURE 6.5: Schematic diagram of an  $M$ -type five-level system as a quantum memory of qubit photons. The top and bottom panels show the initial and final states of mapping a qubit-photon state to a matter-qubit state. An arbitrary superposition of  $\omega_0$ -photon (green pulse) and  $\omega_1$ -photon (yellow pulse) is stored in the matter-qubit states  $|s_0\rangle$  and  $|s_1\rangle$ . Meanwhile, an auxiliary photon- $C$  (blue pulse) is emitted after the mapping.

addition, the  $s_0 \rightarrow e_0$  and  $s_1 \rightarrow e_1$  transitions have the transition energy  $\omega_{es}$ . According to our calculations in the trapping step in Sec. 6.2, the output state of an incoming  $|\omega_0\rangle$  photon with the 5LS initialized in ground state  $|g\rangle$  reads

$$|\phi_0\rangle = |\omega_{es}\rangle \otimes |s_0\rangle. \quad (6.23)$$

Similarly, the output state of an incoming  $|\omega_1\rangle$  photon is

$$|\phi_1\rangle = |\omega_{es}\rangle \otimes |s_1\rangle. \quad (6.24)$$

Hence, the output state after scattering an arbitrary photon-qubit state  $\alpha|\omega_0\rangle + \beta|\omega_1\rangle$  reads

$$|\phi_{\text{out}}\rangle = (\alpha|s_0\rangle + \beta|s_1\rangle) \otimes |\omega_{es}\rangle. \quad (6.25)$$

Therefore, the photon-qubit is mapping into a matter-qubit made of two metastable states  $|s_0\rangle$  and  $|s_1\rangle$ ; at the same time, an auxiliary photon- $C$  of frequency  $\omega_{es}$  is emitted. Retrieval of the photon-qubit can be done simply by sending in the auxiliary photon- $C$ . Similarly, the generalization of this quantum memory to polarization-encoded photon qubits is straightforward: we choose the 5LS such that the transitions  $g \rightarrow e_0$  and  $g \rightarrow e_1$  only interact with  $\pi$ -polarized and  $\sigma$ -polarized photons respectively. Defining the  $\sigma$ -polarized ( $\pi$ -polarized) photons as the logic 0 (logic 1) qubit states, the above scheme will work as a quantum memory of the polarization-encoded photonic qubits.

## 6.5 Conclusion

In summary, we demonstrate that two-qubit gates for photonic quantum computation can be designed in 1D waveguide-QED systems. Our waveguide-based proposal has several potential advantages over quantum computation based on cavity photons or stationary qubits. The operation time here is limited only by the coupling strength, while in the cavity case the cavity line width is the bottleneck. Also, our scheme does not require fine tuning of the interaction time, which is often a significant source of error. Overall, the system proposed here can be an important building block for future on-chip quantum networks: taking superconducting circuits as an example, we can envision such a network with (i) single photons generated using microwave resonators [57], (ii) qubit photons stored in quantum memories formed from the  $M$ -level scheme, (iii) photon flow regulated by single-photon routers [46], and (iv) two-photon operations realized by our 4LS-waveguide system.

# Conclusions and Outlook

In this last Chapter, I summarize the main findings presented in this thesis. Then, I will discuss about open questions and possible future directions.

## 7.1 Conclusions

In the first part of this thesis (Chapters 2-4), we study light-matter interactions in one-dimensional (1D) waveguide-QED systems, which are becoming a promising platform for quantum information processing. This field is motivated by recent tremendous experimental progress in a variety of systems, including plasmonic wires [17], photonic wires [42, 43, 45], photonic crystal waveguides [47], tapered nanofibers [41, 56], superconducting transmission lines [40, 44, 46, 48] and so on. Compared to the conventional cavity-QED systems, waveguide-QED systems have a new feature: the existence of a continuum in the 1D phase space. As a result, a wide range of quantum optical phenomena such as photon-photon bound state appear in such systems. Based on our understanding of the fundamental interaction mechanism, in the second part of this thesis (Chapters 5-6),

we propose and investigate in detail potential applications of waveguide-QED in quantum science such as quantum key distribution and photonic quantum computation.

In Chapter 2, we study the simplest waveguide-QED system, i.e. a two-level system (TLS) coupled to a one-dimensional waveguide. This system has been studied experimentally in different contexts, including plasmonic system [17], photonic crystal waveguide [47] and superconducting circuits [40, 44, 46, 48] etc. We solve for the exact scattering eigenstates by using an open boundary condition. Photon-photon bound states appear in multi-photon scattering due to the coupling between TLS and the waveguide. Such bound states cause several interesting effects. For example, multi-photon transmission is enhanced when the photons are on resonance with the TLS. Pronounced spectral entanglement is generated among initially uncorrelated photons in the transmitted field. Rich bunching and antibunching behavior is observed in the second-order correlation function. In addition, non-Poissonian light can be generated by sending in coherent states.

In Chapter 3, we study the coupling of the waveguide to a three-level or four-level system. Effective repulsive or attractive interaction between photons can be produced, giving rise to either suppressed multiphoton transmission—photon blockade—or enhanced multiphoton transmission—photon-induced tunneling. As a result, a sub-Poissonian single-photon source can be generated on demand when the incoming coherent state is on resonance with the 4LS. This comes about because single photons experience electromagnetically-induced transparency (EIT), while multiphotons experience photon blockade. Furthermore, we show that the proposed system can produce photon pairs with a high degree of spectral entanglement, which have a large capacity for carrying information and are important

for large-alphabet quantum communication.

In Chapter 4, we study the system of a one-dimensional waveguide coupled to two qubits with an arbitrary separation. This system is important because it is the minimal system toward scalable quantum networks using waveguide-QED. On the other hand, it was rarely studied partially because no analytical solution exists for the general case of arbitrary inter-qubit separation. To overcome this difficulty, we develop a novel numerical Green function method, enabling us to treat the combination of nonlinear elements (TLS) and 1D continuum for the general case. We find that the vacuum-mediated qubit-qubit interactions cause quantum beats to appear in the second-order correlation function. For the first time, we go beyond the Markovian regime, i.e. small separation of two qubits, and observe that quantum beats persist much longer than the qubit life time when the two qubits are far apart. A quantitative picture of subradiance is developed to explain such persistent quantum beats. Finally, we demonstrate that a high-degree of long-distance entanglement between the two qubits can be generated, increasing the potential of waveguide-QED systems for scalable quantum networks.

The second part of this thesis includes two applications of waveguide-QED in quantum information processing. In Chapter 5, we investigate a decoy-state quantum key distribution (QKD) scheme with a sub-Poissonian single-photon source. As shown in Chapter 2, this light source is generated on demand by scattering a coherent state off a two-level system in a one-dimensional waveguide. We find that there is a substantial increase in the key generation rate and maximal transmission distance compared to both weak coherent state and heralded single-photon decoy-state QKD. Furthermore, the performance is robust against either parameter variation or loss in the system, making it a promising candidate for

future QKD systems.

In Chapter 6, we propose a new scheme for photonic quantum computation using flying qubits—propagating photons in a one-dimensional waveguide interacting with matter qubits. Photon-photon interactions are mediated by the coupling to a three-level or four-level system, based on which photon-photon  $\pi$ -phase gates (Controlled-NOT) can be implemented for universal quantum computation. We show that high gate fidelity is possible given recent dramatic experimental progress in superconducting circuits and photonic-crystal waveguides. Furthermore, our waveguide-based proposal has several potential advantages over quantum computation based on cavity photons or stationary qubits. The operation time is limited only by the coupling strength, while in the cavity case the cavity line width is the bottleneck. Also, our scheme does not require fine tuning of the interaction time, which is often a significant source of error. Overall, the proposed system can be an important building block for future on-chip quantum networks.

## 7.2 Outlook

The field of waveguide-QED is a young field starting to explode in the past few years, mainly because of a series of beautiful experiments reaching the strong-coupling regime. The rapid development of the field in turn also exposes us to a lot of open questions from the theoretical perspective. Current theoretical research in the field has been mostly focused on the problem of a single local quantum emitter coupled to a 1D waveguide within the rotating wave approximation (RWA) [62, 66, 67, 68, 69, 70, 72, 74, 75, 93, 111], which means the coupling strength is much smaller than the transition frequencies. However, it is crucial to study systems of more than one quantum emitter in order to transfer

quantum information and generate long-distance entanglement in a quantum network [18].

In addition, even though most current waveguide-QED experiments are well described by the rotating wave approximation, it has been shown both experimentally and theoretically that the ultrastrong coupling regime is within reach in the near future [165, 166]. Realizing ultrastrong coupling between light and matter would bring in a whole spectrum of new physics, such as Kondo effects in bosonic systems [167, 168], superradiant quantum phase transitions [169] and so on. Furthermore, in Chapter 4 we studied the two-qubit waveguide-QED system and uncovered rich physics due to non-Markovian processes in such a relatively simple system. We believe there is much more non-Markovian physics to discover in more complicated setups, such as systems having many-qubits or more than one waveguide.

In light of open questions mentioned above, I propose and outline the following possible future directions as extensions of this thesis:

1. Is it possible to generate more exotic and strongly-correlated photons or photonic phases in a dense system? Under the rotating wave approximation, the problem of scattering photons off a single quantum emitter has been extensively studied in the past, partially because there is an exact solution to the problem after performing the even/odd transformation of the photonic field with respect to the quantum emitter as shown in Chapter 2 and Chapter 3. However, once we introduce more than one quantum emitter, this analytical technique stops working and alternative methods are required.

As shown in Chapter 4, we developed a novel numerical Green function

method to study cooperative effects in a system of two qubits strongly coupled to a 1D waveguide. This numerical approach enables us to compute the second-order correlation function of photons and qubit-qubit entanglement in the steady state scenario, beyond the well-studied Markovian regime. A straightforward extension of our current Green function method should be able to tackle the problem of a dense system of multiple quantum emitters interacting with a finite density of photons in the waveguide. In particular, the correlation between photons is expected to be largely enhanced due to the frequent light-matter interactions. This would lead to a novel way of creating more exotic strongly-interacting photons, which potentially can reveal striking 1D many-body physics (such as power law decay) and even undergo fermionization under certain conditions [25]. On the other hand, better understanding of interactions in a large system would be beneficial for both designing waveguide-QED-based entanglement and computing schemes [68, 170] and evaluating the potential of waveguide systems to scale up in an open quantum network.

2. How can we simulate Kondo-type models using photons? Going beyond the rotating wave approximation is technically challenging, because the conservation of excitation number is broken after including the counter-rotating terms. To study the ground state properties, a renormalization group method can be developed to identify the fixed points and the phase diagram qualitatively. To probe the effects of counter-rotating terms on the photon scattering spectrum and second-order correlation function, a Keldysh Green function method is necessary for such non-equilibrium processes [168]. Physically, the counter-rotating terms closely resemble the

spin-flip operators, which are known to give rise to exotic correlation effects in Kondo and spin-boson models.

Indeed, previous study has shown that using the rapidly developing superconducting technology, one can engineer a device with two superconducting transmission lines and a double-island charge qubit so that the system is well described by the spin-boson model. Recently, Goldstein *et al.* shows that Kondo physics can be revealed in the inelastic scattering spectrum of microwave photons off a quantum impurity in Josephson-junction array [168]. This opens up a new avenue of studying Kondo effects with optical/microwave tools not available in traditional condensed matter physics. Further extension of the single-impurity model will lead to realizations of other Kondo-type models, such as the two-impurity Kondo model, two-channel Kondo model, Kondo-lattice, where qualitatively new and exotic physics is still not well studied in fermionic systems due to lack of effective ways to probe the underlying correlation effects. Therefore, a lot of research remains to be done to design such models using current waveguide-QED systems, and to develop appropriate theoretical tools such as renormalization group and Keldysh methods to investigate the strong-correlation physics.

### 3. What kind of non-Markovian effects can we expect in multi-qubit systems?

The non-Markovian effects discussed in Chapter 4 are probably only the tip of the iceberg to be uncovered. First, we can extend the Green function technique in a straightforward manner for multi-qubit systems. We should expect richer non-Markovian physics. For instance, what kind of correlation can be generated due to non-Markovian processes in a multi-qubit system?

And how does the correlation change as one changes the number of qubits, i.e., does it become stronger or weaker as the system becomes denser? From the perspective of qubits, will one be able to generate long-distance entanglement among qubits as we observed in Chapter 4? If yes, how does it depend on the separation of the two qubits or the position of the driven qubits (one can drive the qubit in the middle or on the edge of qubit chain)? Second, we can think of going beyond the Green function technique developed in Chapter 4, which is applicable for weak laser fields. It is a challenging but interesting task to develop new methods to include both non-Markovian behavior and strong driving fields. Physically, one could ask whether there is new non-Markovian physics beyond the weak-driving limit.

In a nutshell, there are a lot of exciting opportunities on the theory side of waveguide-QED research. New theoretical techniques are to be developed to tackle many of the interesting yet challenging open questions. New ideas are in need to utilize the current or near-future waveguide-QED systems to either study fundamental physics at the interface of quantum optics and condensed matter physics, or build a platform for novel applications in quantum information processing.

# Appendix A

## Expressions for $\gamma_{1,2}$ , $C_{1,2}$ and $D_{1,2,3,4}$

In this Appendix, we give explicit expressions for the constants  $\gamma_{1,2}$ ,  $C_{1,2}$ , and  $D_{1,2,3,4}$  that appear in Eqs. (3.9) and (3.10) in Chapter 3 for both the 3LS and 4LS scattering eigenstates.  $\gamma_{1,2}$  is the same for both cases and is given by

$$c\gamma_{1,2} = \frac{\Gamma + \Gamma_2 + \Gamma_3}{4} + \xi \pm i \left( \pm \frac{\Delta}{2} + \epsilon_2 + \eta \right), \quad (\text{A.1a})$$

$$\xi = \frac{\sqrt{2}}{4} \left( \sqrt{\chi^2 + 4\Delta^2\Gamma'^2} - \chi \right)^{1/2}, \quad \eta = \frac{\sqrt{2}}{4} \left( \sqrt{\chi^2 + 4\Delta^2\Gamma'^2} + \chi \right)^{1/2}, \quad (\text{A.1b})$$

$$\Gamma' = \frac{\Gamma + \Gamma_2 - \Gamma_3}{2}, \quad \chi = \Delta^2 + \Omega^2 - \Gamma'^2. \quad (\text{A.1c})$$

For the  $\Lambda$ -type 3LS and  $N$ -type 4LS cases,  $C_{1,2}$  and  $D_{1,2,3,4}$  take the same form

$$\begin{aligned}
C_{1,2}^{(\Lambda, N)}(k_1, k_2) &= \frac{\pm \beta^{(\Lambda, N)}(k_1, k_2) - \alpha(k_1, k_2)\lambda_{2,1}}{\lambda_1 - \lambda_2}, \\
D_1^{(\Lambda, N)}(k_1, k_2, k_3) &= \frac{\beta_{13}^{(\Lambda, N)}(k_1) - \alpha_{13}(k_1)\lambda_2}{\lambda_1 - \lambda_2} C_1^{(\Lambda, N)}(k_2, k_3), \\
D_2^{(\Lambda, N)}(k_1, k_2, k_3) &= \frac{-\beta_{24}^{(\Lambda, N)}(k_1) + \alpha_{24}(k_1)\lambda_1}{\lambda_1 - \lambda_2} C_2^{(\Lambda, N)}(k_2, k_3), \\
D_3^{(\Lambda, N)}(k_1, k_2, k_3) &= \frac{-\beta_{13}^{(\Lambda, N)}(k_1) + \alpha_{13}(k_1)\lambda_1}{\lambda_1 - \lambda_2} C_1^{(\Lambda, N)}(k_2, k_3), \\
D_4^{(\Lambda, N)}(k_1, k_2, k_3) &= \frac{\beta_{24}^{(\Lambda, N)}(k_1) - \alpha_{24}(k_1)\lambda_2}{\lambda_1 - \lambda_2} C_2^{(\Lambda, N)}(k_2, k_3), \\
\lambda_{1,2} &= \frac{\Gamma + \Gamma_2 - \Gamma_3}{4} \pm \xi + i\left(\frac{\Delta}{2} \pm \eta\right), \tag{A.2}
\end{aligned}$$

where the superscript  $\Lambda$  stands for the 3LS and  $N$  for the 4LS.  $\alpha$ 's and  $\beta$ 's in the above equation read

$$\alpha(k_1, k_2) = -\frac{(\bar{t}_{k_1} - 1)(\bar{t}_{k_2} - 1)}{2\pi}, \tag{A.3a}$$

$$\beta(k_1, k_2)^{(\Lambda)} = \frac{\Gamma\Omega^2}{16\pi} \left[ \frac{\bar{t}_{k_1} - 1}{\rho_{k_2}} + \frac{\bar{t}_{k_2} - 1}{\rho_{k_1}} \right], \tag{A.3b}$$

$$\beta(k_1, k_2)^{(N)} = \frac{\Gamma\Omega^2}{16\pi} \left[ \frac{\bar{t}_{k_1} - \nu(k_1, k_2)}{\rho_{k_2}} + \frac{\bar{t}_{k_2} - \nu(k_1, k_2)}{\rho_{k_1}} \right], \tag{A.3c}$$

$$\nu(k_1, k_2) = \frac{\epsilon_4 - E - (i\Gamma_4 - i\Gamma)/2}{\epsilon_4 - E - (i\Gamma_4 + i\Gamma)/2}, \tag{A.3d}$$

$$\rho_k = \left( ck - \epsilon_2 + \Delta + \frac{i\Gamma_3}{2} \right) \left( ck - \epsilon_2 + \frac{i\Gamma_2 + i\Gamma}{2} \right) - \frac{\Omega^2}{4}, \tag{A.3e}$$

where  $\bar{t}_k$  is given in Eq.(3.8b) in Chapter 3.  $\alpha_{13}$ ,  $\alpha_{24}$ ,  $\beta_{13}$  and  $\beta_{24}$  are given by

$$\begin{aligned}\alpha_{13}(k) &= \alpha_{24}(k) = -\frac{2(\bar{t}_k - 1)}{\sqrt{2\pi}}, \\ \beta_{13}(k)^{(\Lambda)} &= \frac{1}{\sqrt{2\pi}} \left[ \frac{\Gamma\Omega^2}{4\rho_k} - (\bar{t}_k - 1) \lambda_1 \right], \quad \beta_{13}(k)^{(N)} = \frac{1}{\sqrt{2\pi}} \left\{ \frac{\Gamma\Omega^2}{4\rho_k} - [\bar{t}_k - \mu_1(k)] \lambda_1 \right\}, \\ \beta_{24}(k)^{(\Lambda)} &= \frac{1}{\sqrt{2\pi}} \left[ \frac{\Gamma\Omega^2}{4\rho_k} - (\bar{t}_k - 1) \lambda_2 \right], \quad \beta_{24}(k)^{(N)} = \frac{1}{\sqrt{2\pi}} \left\{ \frac{\Gamma\Omega^2}{4\rho_k} - [\bar{t}_k - \mu_2(k)] \lambda_2 \right\}, \\ \mu_{1,2}(k) &= \frac{\epsilon_4 - i\Gamma_4/2 - ck + i\Gamma/2 + ic\gamma_{1,2}}{\epsilon_4 - i\Gamma_4/2 - ck - i\Gamma/2 + ic\gamma_{1,2}}.\end{aligned}\tag{A.4}$$

## Appendix B

### Three-photon asymptotic output state from 3LS and 4LS scattering

In this Appendix, we present the asymptotic output state after scattering a three-photon right-going Fock state off a 3LS or 4LS in Chapter 3. The form of the wave functions is

$$\begin{aligned}
|\psi^{(3)}\rangle &= \int dk_1 dk_2 dk_3 \frac{1}{\sqrt{3!}} \alpha(k_1) \alpha(k_2) \alpha(k_3) |\phi^{(3)}(k_1, k_2, k_3)\rangle, \\
|\phi^{(3)}(k_1, k_2, k_3)\rangle &= \int dx_1 dx_2 dx_3 \left[ \frac{1}{3!} ttt_{k_1, k_2, k_3}(x_1, x_2, x_3) a_R^\dagger(x_1) a_R^\dagger(x_2) a_R^\dagger(x_3) \right. \\
&\quad + \frac{1}{2!} ttr_{k_1, k_2, k_3}(x_1, x_2, -x_3) a_R^\dagger(x_1) a_R^\dagger(x_2) a_L^\dagger(x_3) \\
&\quad + \frac{1}{2!} trr_{k_1, k_2, k_3}(x_1, -x_2, -x_3) a_R^\dagger(x_1) a_L^\dagger(x_2) a_L^\dagger(x_3) \\
&\quad \left. + \frac{1}{3!} rrr_{k_1, k_2, k_3}(-x_1, -x_2, -x_3) a_L^\dagger(x_1) a_L^\dagger(x_2) a_L^\dagger(x_3) \right] |\emptyset\rangle. \quad (\text{B.1})
\end{aligned}$$

Here,  $ttt_{k_1, k_2, k_3}(x_1, x_2, x_3)$ ,  $ttr_{k_1, k_2, k_3}(x_1, x_2, x_3)$ ,  $trr_{k_1, k_2, k_3}(x_1, x_2, x_3)$ , and  $rrr_{k_1, k_2, k_3}(x_1, x_2, x_3)$  are the terms representing three-photons being transmitted,

two being transmitted and one reflected, one being transmitted and two reflected, and all three being reflected, respectively. They take the following general form ( $\alpha, \beta, \gamma = t$  or  $r$ )

$$\begin{aligned} \alpha\beta\gamma_{k_1,k_2,k_3}(x_1, x_2, x_3) &= \sum_Q \alpha_{k_{Q_1}}\beta_{k_{Q_2}}\gamma_{k_{Q_3}} h_{k_{Q_1}}(x_1)h_{k_{Q_2}}(x_2)h_{k_{Q_3}}(x_3) \\ &+ \frac{1}{4} \sum_Q \left[ \alpha_{k_{Q_1}} h_{k_{Q_1}}(x_1) B_{k_{Q_2}, k_{Q_3}}^{(2)}(x_2, x_3) + \beta_{k_{Q_1}} h_{k_{Q_1}}(x_2) B_{k_{Q_2}, k_{Q_3}}^{(2)}(x_1, x_3) \right. \\ &\quad \left. + \gamma_{k_{Q_1}} h_{k_{Q_1}}(x_3) B_{k_{Q_2}, k_{Q_3}}^{(2)}(x_1, x_2) \right] + \frac{1}{8} \sum_{PQ} B_{k_{P_1}, k_{P_2}, k_{P_3}}^{(3)}(x_{Q_1}, x_{Q_2}, x_{Q_3}). \quad (\text{B.2}) \end{aligned}$$

where  $t_k$  and  $r_k$  are the single-photon transmission and reflection probabilities given in Eq. (3.13c),  $B_{k_1, k_2}^{(2)}(x_1, x_2)$  is given in Eq. (3.15), and  $B_{k_1, k_2, k_3}^{(3)}(x_1, x_2, x_3)$  is given in Eq. (3.10). In Eq. (B.2), the first term comes from the process of three-photons passing by the atom as independent particles. The second term corresponds to the process of one-photon passing through as an independent particle while the other two photons form a composite particle in a two-photon bound-state (with three possible combinations). The third term originates from the three-photon bound-state process.

## Appendix C

### Phase Analysis of Photon Blockade and Photon-Induced Tunneling

In Fig. 3.3 of Chapter 3, we show that the observed photon blockade and photon-induced tunneling originate from destructive and constructive interference effects, respectively. In this section, we present a detailed analysis of the relative phase between the plane-wave and bound-state terms. The two-photon transmission probability  $T_2$  for the two-photon scattering is given by

$$T_2 = \int dk_1 dk_2 |T(k_1, k_2) + B(k_1, k_2)|^2, \quad (\text{C.1})$$

where  $k_1$  and  $k_2$  are the momenta of the two photons in the wavepacket. The plane-wave term  $T(k_1, k_2)$  and the bound-state term  $B(k_1, k_2)$  take the form

$$\begin{aligned} T(k_1, k_2) &= \alpha(k_1)\alpha(k_2)t_{k_1}t_{k_2}, \\ B(k_1, k_2) &= \sum_{i,j=1,2} \frac{\sqrt{\Gamma}/8}{k_i - i\gamma_j} \int dk' \alpha(k')\alpha(k_1 + k_2 - k')C_j(k', k_1 + k_2 - k'), \end{aligned} \quad (\text{C.2})$$

where  $\alpha(k)$  is the amplitude of a Gaussian wavepacket with central frequency  $\omega_0$  and width  $\sigma$ . In momentum space, the central momentum is  $k_0 = \omega_0/c$  and the width is  $\sigma/c$ , where  $c$  is the group velocity of photons in the waveguide. By defining the phase difference  $\theta(k_1, k_2)$  between  $T(k_1, k_2)$  and  $B(k_1, k_2)$ ,  $T_2$  can be written as

$$T_2 = \int dk_1 dk_2 |T(k_1, k_2)|^2 + \int dk_1 dk_2 |B(k_1, k_2)|^2 \\ + \int dk_1 dk_2 2|T(k_1, k_2)B(k_1, k_2)|\cos\theta(k_1, k_2), \quad (\text{C.3})$$

where the first term is the plane-wave term, the second term is the interference between the plane-wave and bound-state terms, and the third term is the contribution from the bound-state term. In the main text, the first term is denoted

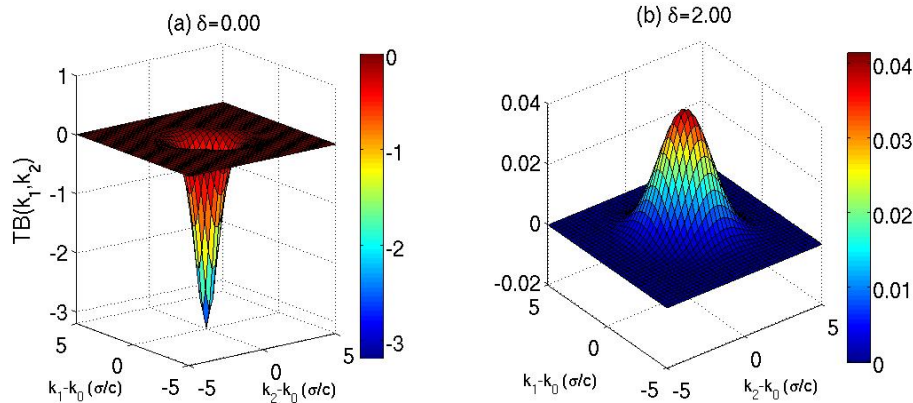


FIGURE C.1: The integrand function  $TB(k_1, k_2)$  of the interference term as a function of  $k_1$  and  $k_2$ . (a)  $\delta = 0.0$ . (b)  $\delta = 2.0$ . Here,  $\Gamma = 6$ ,  $\Omega = 1.6$ .

$(T_2)_{PW}$  and the second and third terms together are called  $(T_2)_{BS}$ . Denote the intergrand function of the interference term as,

$$TB(k_1, k_2) = 2|T(k_1, k_2)B(k_1, k_2)|\cos\theta(k_1, k_2). \quad (\text{C.4})$$

The phase  $\theta(k_1, k_2)$ , or specifically, the sign of  $\cos\theta(k_1, k_2)$ , determines whether the interference is constructive or destructive.

We numerically evaluate  $TB(k_1, k_2)$  in two cases:  $\delta = \omega_0 - \omega_{21} = 0.0$  and  $\delta = \omega_0 - \omega_{21} = 2.0$ . Here, the unit of detuning  $\delta$  is set by the loss rate  $\Gamma_2$ . Figure C.1 shows  $TB(k_1, k_2)$  as a function of  $k_1 - k_0$  and  $k_2 - k_0$ . As expected for a Gaussian packet, the value of  $TB(k_1, k_2)$  is centered at  $k_1 = k_2 = k_0$  in both cases. However, the sign of the peaks in the two cases differs. For  $\delta = 0.0$ , a negative peak indicates destructive interference, giving rise to photon blockade when the incident photons are on resonance with the 4LS. For  $\delta = 2.0$ , a positive peak indicates constructive interference, producing photon-induced tunneling when the photons are far off resonance.

# Appendix D

## Second-Order Correlation Function in the Schrödinger Picture

In this Appendix, we demonstrate the equivalence between Eq. (3.26) and Eq. (3.27) in Sec. 3.7. Typically, the second-order correlation function is defined in the Heisenberg picture as,

$$g^{(2)}(x_1, t_1; x_2, t_2) = \frac{\langle \psi_0 | \hat{a}^\dagger(x_1, t_1) \hat{a}^\dagger(x_2, t_2) \hat{a}(x_2, t_2) \hat{a}(x_1, t_1) | \psi_0 \rangle}{\langle \psi_0 | \hat{a}^\dagger(x_1, t_1) \hat{a}(x_1, t_1) | \psi_0 \rangle \langle \psi_0 | \hat{a}^\dagger(x_2, t_2) \hat{a}(x_2, t_2) | \psi_0 \rangle} \quad (\text{D.1})$$

where  $|\psi_0\rangle$  is the state in the Heisenberg picture, or equivalently, the initial state in the Schrödinger picture and  $\hat{a}^\dagger(x, t)$  is the operator in the Heisenberg picture.  $\hat{a}^\dagger(x, t)$  can be expressed in terms of the operator in the Schrödinger picture as

$$\hat{a}^\dagger(x, t) = e^{iHt/\hbar} \hat{a}^\dagger(x) e^{-iHt/\hbar}. \quad (\text{D.2})$$

Taking  $x_1 = x_2 = x$  in Eq. (D.1), we obtain the two-time correlation function

$$g^{(2)}(x, t_1; x, t_2) = \frac{\langle \psi_0 | \hat{a}^\dagger(x, t_1) \hat{a}^\dagger(x, t_2) \hat{a}(x, t_2) \hat{a}(x, t_1) | \psi_0 \rangle}{\langle \psi_0 | \hat{a}^\dagger(x, t_1) \hat{a}(x, t_1) | \psi_0 \rangle \langle \psi_0 | \hat{a}^\dagger(x, t_2) \hat{a}(x, t_2) | \psi_0 \rangle}. \quad (\text{D.3})$$

If the field operator satisfies the following relation

$$\hat{a}^\dagger(x, t) = \hat{a}^\dagger(x - ct), \quad (\text{D.4})$$

$g^{(2)}(x, t_1; x, t_2)$  is then the same as  $g^{(2)}(x, t_1; x', t_1)$  with  $x' = x - c(t_2 - t_1)$ . Using Eqs. (D.2) and (D.4), we can rewrite (D.3) in the Schrödinger picture as

$$g^{(2)}(x, t_1; x', t_1) = \frac{\langle \psi(t_1) | \hat{a}^\dagger(x) \hat{a}^\dagger(x') \hat{a}(x') \hat{a}(x) | \psi(t_1) \rangle}{\langle \psi(t_1) | \hat{a}^\dagger(x) \hat{a}(x) | \psi(t_1) \rangle \langle \psi(t_1) | \hat{a}^\dagger(x') \hat{a}(x') | \psi(t_1) \rangle}, \quad (\text{D.5})$$

where  $|\psi(t_1)\rangle$  is the state at  $t = t_1$  evolving from the initial state  $|\psi_0\rangle$  under the Hamiltonian  $H$ . Therefore, as long as Eq. (D.4) holds, the definition of  $g^{(2)}$  in the Heisenberg picture Eq. (D.3) is equivalent to Eq. (D.5) defined in the Schrödinger picture. Physically, this means that measuring the two-time correlation at the same spatial position is equivalent to measuring the spatial correlation at the same time for a non-dispersive field.

In our problem, it is straightforward to show that Eq. (D.4) is satisfied by the right-going field. With the Hamiltonian defined in Eq. (3.1) in the main text, the equation of motion for the right-going field in the 4LS case is

$$\left( \frac{\partial}{\partial x} + \frac{1}{c} \frac{\partial}{\partial t} \right) \hat{a}_R^\dagger(x, t) = \frac{iV}{c} [S_{12}^+(t) + S_{34}^+(t)] \delta(x). \quad (\text{D.6})$$

Formally, the above equation can be integrated to yield

$$\hat{a}_R^\dagger(x, t) = \hat{a}_{R, free}^\dagger(x - ct) + \frac{iV}{c} [S_{12}^+(t - x/c) + S_{34}^+(t - x/c)] \theta(x). \quad (\text{D.7})$$

A similar expression can be obtained in the 3LS case. Hence, Eq. (D.4) holds, and we use Eq. (D.5) to evaluate the second-order correlation function of the transmitted field with  $|\psi(t_1)\rangle$  being our final output state.

## Appendix E

### Derivation of the Output States in the 4LS Scheme of Photonic $\pi$ -phase Gate

Here, we present a detailed derivation of the output states in Eqs. (6.2)-(6.9) in Chapter 6 Sec. 6.2.3. For an incoming left-going photon of frequency  $\omega_A$  and initialized 4LS in state  $|1\rangle$ , the single-photon scattering eigenstate can be written as

$$\begin{aligned} |\psi_1\rangle &= \int dx [\phi_{1R}(x)a_R^\dagger(x) + \phi_{1L}(x)a_L^\dagger(x)]|1, \emptyset\rangle + e_2|2, \emptyset\rangle \\ &\quad + \int dx [\phi_{3R}(x)a_R^\dagger(x) + \phi_{3L}(x)a_L^\dagger(x)]|3, \emptyset\rangle, \end{aligned} \tag{E.1}$$

where  $|i, \emptyset\rangle$  is the vacuum state of photons with the 4LS in state  $|i\rangle$ . The Schrödinger equation  $H|\psi_1\rangle = \hbar\omega_A|\psi_1\rangle$  gives

$$(-i\frac{d}{dx} - \omega_A)\phi_{1R}(x) + V\delta(x)e_2 = 0, \quad (\text{E.2a})$$

$$(i\frac{d}{dx} - \omega_A)\phi_{1L}(x) + V\delta(x)e_2 = 0, \quad (\text{E.2b})$$

$$(-i\frac{d}{dx} + \Omega_3 - \omega_A)\phi_{3R}(x) + V\delta(x)e_2 = 0, \quad (\text{E.2c})$$

$$(i\frac{d}{dx} + \Omega_3 - \omega_A)\phi_{3L}(x) + V\delta(x)e_2 = 0, \quad (\text{E.2d})$$

$$(\Omega_2 - \frac{i\Gamma'}{2} - \omega_A)e_2 + V \sum_{i=1,3} [\phi_{iR}(0) + \phi_{iL}(0)] = 0. \quad (\text{E.2e})$$

We assume the following solution ansatz

$$\phi_{1R}(x) = e^{ik_1 x}[\theta(-x) + \beta_{1R}\theta(x)], \quad (\text{E.3a})$$

$$\phi_{1L}(x) = e^{-ik_1 x}[\alpha_{1L}\theta(-x) + \beta_{1L}\theta(x)], \quad (\text{E.3b})$$

$$\phi_{3R}(x) = e^{ik_3 x}\beta_{3R}\theta(x), \quad (\text{E.3c})$$

$$\phi_{3L}(x) = e^{-ik_3 x}[\alpha_{3L}\theta(-x) + \beta_{3L}\theta(x)], \quad (\text{E.3d})$$

where  $k_1 = \omega_A$  and  $k_3 = \omega_A - \Omega_3$  (we set  $c = 1$ ). Substituting Eq.(E.3) into Eq.(E.2), setting  $\phi_{iR/L}(0) = [\phi_{iR/L}(0^+) + \phi_{iR/L}(0^-)]/2$ , and imposing the hard-wall boundary condition at the end of the waveguide

$$\phi_{1R}(a) + \phi_{1L}(a) = \phi_{3R}(a) + \phi_{3L}(a) = 0, \quad (\text{E.4})$$

we obtain the following solution

$$\begin{aligned}\alpha_{1L} &= e^{2i\omega_A a} \frac{-\Omega_2 + \frac{i\Gamma'}{2} + \omega_A - \frac{i\Gamma}{2}[e^{2i\tilde{\omega}_A a} - e^{-2i\omega_A a}]}{\Omega_2 - \frac{i\Gamma'}{2} - \omega_A + \frac{i\Gamma}{2}[e^{2i\tilde{\omega}_A a} + e^{2i\omega_A a} - 2]}, \\ \alpha_{3L} &= \frac{(i\Gamma/2)(e^{2i\omega_A a} - 1)[e^{2i\tilde{\omega}_A a} - 1]}{\Omega_2 - \frac{i\Gamma'}{2} - \omega_A + \frac{i\Gamma}{2}[e^{2i\tilde{\omega}_A a} + e^{2i\omega_A a} - 2]},\end{aligned}\quad (\text{E.5})$$

where  $\tilde{\omega}_A = \omega_A - \Omega_3$ . According to the Lippmann-Schwinger formalism [85, 75, 93], we read off the “out” state after scattering from the scattering eigenstate in Eq.(E.1). The resulting asymptotic output state  $|\phi_1^{\text{out}}(\omega_A)\rangle$  of photon  $A$  is then given in Eq.(6.2) in Chapter 6 with  $r_{11}$  and  $r_{13}$  corresponding to  $\alpha_{1L}$  and  $\alpha_{3L}$ , respectively.

Next, in Step 2 we send in the second photon  $B$  of frequency  $\omega_B$ . If the 4LS is in state  $|1\rangle$ , then photon- $B$  will scatter in the same way as the first photon and the output state is  $|\phi_1^{\text{out}}(\omega_B)\rangle$ . If the 4LS is in state  $|3\rangle$  and we neglect the transition  $3 \rightarrow 2$  since photon- $B$  is far off resonance from it, then photon- $B$  will interact with the transition  $3 \rightarrow 4$  only. The single-photon scattering eigenstate takes the form

$$|\psi_2\rangle = \int dx [\phi_R(x)a_R^\dagger(x) + \phi_L(x)a_L^\dagger(x)]|3, \emptyset\rangle + e_4|4, \emptyset\rangle. \quad (\text{E.6})$$

From the Schrödinger equation  $H|\psi_2\rangle = \hbar\omega_B|\psi_2\rangle$ , we have

$$(-i\frac{d}{dx} - \omega_B)\phi_R(x) + V\delta(x)e_4 = 0, \quad (\text{E.7a})$$

$$(i\frac{d}{dx} - \omega_B)\phi_L(x) + V\delta(x)e_4 = 0, \quad (\text{E.7b})$$

$$(\Omega_{34} - \frac{i\Gamma'}{2} - \omega_B)e_4 + V[\phi_R(0) + \phi_L(0)] = 0. \quad (\text{E.7c})$$

Again, we assume the following ansatz

$$\phi_R(x) = e^{ik_4x}[\theta(-x) + \beta_R\theta(x)], \quad (\text{E.8a})$$

$$\phi_L(x) = e^{-ik_4x}[\alpha_L\theta(-x) + \beta_L\theta(x)], \quad (\text{E.8b})$$

where  $k_4 = \omega_B$ . Using the hard-wall boundary condition  $\phi_R(a) + \phi_L(a) = 0$ , it is straightforward to obtain the following solution

$$\begin{aligned} \beta_R &= -e^{-2i\omega_B a}\beta_L = \frac{\Omega_{34} - \frac{i\Gamma'}{2} - \omega_B}{\Omega_{34} - \frac{i\Gamma'}{2} - \omega_B - \frac{i\Gamma}{2}(1 - e^{2i\omega_B a})}, \\ \alpha_L &= \frac{-(\Omega_{34} - \frac{i\Gamma'}{2} - \omega_B)e^{2i\omega_B a} + \frac{i\Gamma}{2}(1 - e^{2i\omega_B a})}{\Omega_{34} - \frac{i\Gamma'}{2} - \omega_B - \frac{i\Gamma}{2}(1 - e^{2i\omega_B a})}. \end{aligned} \quad (\text{E.9})$$

Again, we read off the output state of photon-*B* for the case 4LS in state  $|3\rangle$  as  $R_3(\omega_B)|\omega_B\rangle \otimes |3\rangle$  with  $R_3$  corresponding to  $\alpha_L$ . Combining the output states from both cases 4LS in states  $|1\rangle$  and  $|3\rangle$ , we obtain the general output state after Step 2 in Eq. (6.4) in Chapter 6.

Finally, in steps 3 and 4 we send in the output *A'* photon from Step 1 and the auxiliary photon-*C* with frequency  $\omega_C = \Omega_{32}$ . By sending in the output photon-*A'* from step 1, we retrieve photon-*A*. This is the time-reversal process of photon trapping. The state after this step reads

$$\begin{aligned} |\phi_3^{\text{out}}(\omega_A, \omega_B)\rangle &= r_{11}(\omega_A)r_{11}(\omega_B)|\omega_B\rangle \otimes |\phi_1^{\text{out}}(\omega_A)\rangle \\ &+ r_{11}(\omega_A)r_{13}(\omega_B)|\tilde{\omega}_B\rangle \otimes [R_3(\omega_A)|\omega_A\rangle|3\rangle] \\ &+ r_{13}(\omega_A)R_3(\omega_B)|\omega_B\rangle \otimes |\phi_3(\tilde{\omega}_A)\rangle, \end{aligned} \quad (\text{E.10})$$

where  $|\phi_1^{\text{out}}(\omega_A)\rangle$  is given in Eq. (6.2) in Chapter 6 and

$$|\phi_3(\omega)\rangle = r_{33}(\omega)|\omega\rangle \otimes |3\rangle + r_{31}(\omega)|\bar{\omega}\rangle \otimes |1\rangle, \quad (\text{E.11})$$

with

$$\bar{\omega} = \omega + \Omega_{13},$$

$$r_{33}(\omega) = e^{2i\omega a} \frac{-\Omega_{32} + \frac{i\Gamma'}{2} + \omega - \frac{i\Gamma}{2}[e^{2i\bar{\omega}a} - e^{-2i\omega a}]}{\Omega_{32} - \frac{i\Gamma'}{2} - \omega + \frac{i\Gamma}{2}[e^{2i\bar{\omega}a} + e^{2i\omega a} - 2]},$$

$$r_{31}(\omega) = \frac{(i\Gamma/2)(e^{2i\omega a} - 1)[e^{2i\bar{\omega}a} - 1]}{\Omega_{32} - \frac{i\Gamma'}{2} - \omega + \frac{i\Gamma}{2}[e^{2i\bar{\omega}a} + e^{2i\omega a} - 2]}. \quad (\text{E.12})$$

In case of  $\omega_A = \omega_0$  and  $\omega_B = \omega_1$ , photon  $B$  will be trapped in the 4LS in step (2). To retrieve the trapped photon  $B$ , we send in photon of frequency  $\omega_C$  in step 4. According to time reversal argument, sending in a  $C$  photon of frequency  $\Omega_{32}$  will release photon  $B$ . The final state after all four steps reads

$$|\phi_4^{\text{out}}(\omega_A, \omega_B, \omega_C)\rangle = f_1(\omega_A, \omega_B)|\omega_A\rangle|\omega_B\rangle|\omega_C\rangle|1\rangle$$

$$+ [f_2(\omega_A, \omega_B)|\tilde{\omega}_A\rangle|\omega_B\rangle$$

$$+ f_3(\omega_A, \omega_B)|\omega_A\rangle|\tilde{\omega}_B\rangle]|f_3(\omega_C)\rangle. \quad (\text{E.13})$$

where

$$f_1(\omega_A, \omega_B) = r_{11}^2(\omega_A)r_{11}(\omega_B) + r_{13}(\omega_A)r_{31}(\tilde{\omega}_A)R_3(\omega_B),$$

$$f_2(\omega_A, \omega_B) = r_{11}(\omega_A)r_{13}(\omega_A)r_{11}(\omega_B)$$

$$+ r_{13}(\omega_A)r_{33}(\tilde{\omega}_A)R_3(\omega_B),$$

$$f_3(\omega_A, \omega_B) = r_{11}(\omega_A)R_3(\omega_A)r_{13}(\omega_B). \quad (\text{E.14})$$

# Bibliography

- [1] P. Lambropoulos and D. Petrosyan. *Fundamentals of Quantum Optics and Quantum Information*. Springer-Verlag Berlin, Heidelberg, 2007.
- [2] R. J. Schoelkopf and S. M. Girvin. Wiring up quantum systems. *Nature*, 451:664, 2008.
- [3] L. S. Bishop, J. M. Chow, J. Koch, A. A. Houck, M. H. Devoret, E. Thuneberg, S. M. Girvin, and R. J. Schoelkopf. Nonlinear response of the vacuum rabi resonance. *Nat. Phys.*, 5:105, 2009.
- [4] N. J. Cerf M. Dušek N. Lütkenhaus V. Scarani, H. Bechmann-Pasquinucci and M. Peev. The security of practical quantum key distribution. *Rev. Mod. Phys.*, 81:1301, 2009.
- [5] R. J. Thompson, G. Rempe, and H. J. Kimble. Observation of normal-mode splitting for an atom in an optical cavity. *Phys. Rev. Lett.*, 68(8):1132–1135, Feb 1992.
- [6] J. P. Reithmaier, G. Se ogonk, A. Löffler, C. Hofmann, S. Kuhn, S. Reitzenstein, L. V. Keldysh, V. D. Kulakovskii, T. L. Reinecke, and A. Forchel1. Strong coupling in a single quantum dot-semiconductor microcavity system. *Nature*, 432:197–200, 2004.
- [7] P. F. Herskind, A. Dantan, J. P. Marler, M. Albert, and M. Drewsen. Realization of collective strong coupling with ion coulomb crystals in an optical cavity. *Nat. Phys.*, 5:494, 2009.
- [8] H. Mabuchi and A. C. Doherty. Cavity Quantum Electrodynamics: Coherence in Context. *Science*, 298(5597):1372–1377, 2002.
- [9] Kerry J. Vahala. Optical microcavities. *Nature*, 424:839, 2003.
- [10] Herbert Walther, B.T.H. Varcoe, Berthold-Georg Englert, and Thomas Becker. Cavity quantum electrodynamics. *Rep. Prog. Phys.*, 69:1325–1382, 2006.

- [11] M. O. Scully and M. S. Zubairy. *Quantum Optics*. Cambridge University Express, Cambridge, 1997.
- [12] R. Loudon. *The Quantum Theory of Light*. Oxford University Press, New York, third edition, 2003.
- [13] P. Meystre and M. Sargent III. *Elements of Quantum Optics*. Springer, New York, third edition, 1999.
- [14] A. Imamoğlu, H. Schmidt, G. Woods, and M. Deutsch. Strongly interacting photons in a nonlinear cavity. *Phys. Rev. Lett.*, 79(8):1467–1470, Aug 1997.
- [15] S. E. Harris, J. E. Field, and A. Imamoğlu. Nonlinear optical processes using electromagnetically induced transparency. *Phys. Rev. Lett.*, 64(10):1107–1110, Mar 1990.
- [16] S. E. Harris. Electromagnetically induced transparency. *Phys. Today*, 50:36, 1997.
- [17] A. V. Akimov, A. Mukherjee, C. L. Yu, D. E. Chang, A. S. Zibrov, P. R. Hemmer, H. Park, and M. D. Lukin. Generation of single optical plasmons in metallic nanowires coupled to quantum dots. *Nature*, 450:402, 2007.
- [18] H. J. Kimble. The quantum internet. *Nature*, 453:1023, 2008.
- [19] L.-M. Duan and C. Monroe. Colloquium: Quantum networks with trapped ions. *Rev. Mod. Phys.*, 82(2):1209–1224, Apr 2010.
- [20] Iacopo Carusotto and Cristiano Ciuti. Quantum fluids of light. *Rev. Mod. Phys.*, 85:299–366, Feb 2013.
- [21] A.D. Greentree, C. Tahan, J. H. Cole, and L.C.L. Hollenberg. Quantum phase transitions of light. *Nature Phys.*, 2:856–861, 2006.
- [22] M.J. Hartmann, F.G.S.L. Brandao, and M.B. Plenio. Strongly interacting polaritons in coupled arrays of cavities. *Nature Phys.*, 2:849–855, 2006.
- [23] Davide Rossini and Rosario Fazio. Mott-insulating and glassy phases of polaritons in 1d arrays of coupled cavities. *Phys. Rev. Lett.*, 99(18):186401, Oct 2007.
- [24] M.J. Hartmann, F.G.S.L. Brandão, and M.B. Plenio. Quantum many-body phenomena in coupled cavity arrays. *Laser Photon. Rev.*, 2:527–556, 2008.
- [25] D. E. Chang, V. Gritsev, G. Morigi, V. Vuletić, M. D. Lukin, and E. A. Demler. Crystallization of strongly interacting photons in a nonlinear optical fibre. *Nature Phys.*, 4:884, 2008.

- [26] S. Schmidt and G. Blatter. Strong coupling theory for the Jaynes-Cummings-Hubbard model. *Phys. Rev. Lett.*, 103(8):086403, Aug 2009.
- [27] I. Carusotto, D. Gerace, H. E. Tureci, S. De Liberato, C. Ciuti, and A. Imamoğlu. Fermionized photons in an array of driven dissipative nonlinear cavities. *Phys. Rev. Lett.*, 103(3):033601, Jul 2009.
- [28] Jens Koch and Karyn Le Hur. Superfluid–Mott-insulator transition of light in the Jaynes-Cummings lattice. *Phys. Rev. A*, 80:023811, Aug 2009.
- [29] S. Schmidt and G. Blatter. Excitations of strongly correlated lattice polaritons. *Phys. Rev. Lett.*, 104(21):216402, May 2010.
- [30] Dimitris G. Angelakis, Mingxia Huo, Elica Kyoseva, and Leong Chuan Kwek. Luttinger liquid of photons and spin-charge separation in hollow-core fibers. *Phys. Rev. Lett.*, 106:153601, Apr 2011.
- [31] Philippe Grangier, Daniel F. Walls, and Klaus M. Gheri. Comment on “Strongly interacting photons in a nonlinear cavity”. *Phys. Rev. Lett.*, 81(13):2833, Sep 1998.
- [32] A. Imamoğlu, H. Schmidt, G. Woods, and M. Deutsch. Erratum: Strongly interacting photons in a nonlinear cavity [Phys. Rev. Lett. 79, 1467 (1997)]. *Phys. Rev. Lett.*, 81(13):2836, Sep 1998.
- [33] K. M. Birnbaum, A. Boca, R. Miller, A. D. Boozer, T. E. Northup, and H. J. Kimble. Photon blockade in an optical cavity with one trapped atom. *Nature*, 436:87–90, 2005.
- [34] Martin Mücke, Eden Figueroa, Joerg Bochmann, Carolin Hahn, Karim Murr, Stephan Ritter, Celso J. Villas-Boas, and Gerhard Rempe. Electromagnetically induced transparency with single atoms in a cavity. *Nature*, 465:755, 2010.
- [35] Haruka Tanji-Suzuki, Wenlan Chen, Renate Landig, Jonathan Simon, and Vladan Vuletić. Vacuum-induced transparency. *Science*, 333(6047):1266, 2011.
- [36] C. Lang, D. Bozyigit, C. Eichler, L. Steffen, J. M. Fink, A. A. Abdumalikov, M. Baur, S. Filipp, M. P. da Silva, A. Blais, and A. Wallraff. Observation of resonant photon blockade at microwave frequencies using correlation function measurements. *Phys. Rev. Lett.*, 106:243601, Jun 2011.
- [37] A. D. Boozer, A. Boca, R. Miller, T. E. Northup, and H. J. Kimble. Reversible state transfer between light and a single trapped atom. *Phys. Rev. Lett.*, 98(19):193601, May 2007.

- [38] Max Hofheinz, E. M. Weig, M. Ansmann, Radoslaw C. Bialczak, Erik Lucero, M. Neeley, A. D. O'Connell, H. Wang, John M. Martinis, and A. N. Cleland. Generation of Fock states in a superconducting quantum circuit. *Nature*, 454:310–314, 2008.
- [39] Max Hofheinz, H. Wang, M. Ansmann, Radoslaw C. Bialczak, Erik Lucero, M. Neeley, A. D. O'Connell, D. Sank, J. Wenner, John M. Martinis, and A. N. Cleland. Synthesizing arbitrary quantum states in a superconducting resonator. *Nature*, 459:546, 2009.
- [40] A. A. Abdumalikov, O. Astafiev, A. M. Zagoskin, Yu. A. Pashkin, Y. Nakamura, and J. S. Tsai. Electromagnetically induced transparency on a single artificial atom. *Phys. Rev. Lett.*, 104:193601, May 2010.
- [41] M. Bajcsy, S. Hofferberth, V. Balic, T. Peyronel, M. Hafezi, A. S. Zibrov, V. Vuletic, and M. D. Lukin. Efficient all-optical switching using slow light within a hollow fiber. *Phys. Rev. Lett.*, 102(20):203902, May 2009.
- [42] T. M. Babinec, Birgit J. M. Hausmann, Mughees Khan, Yinan Zhang, Jeronimo R. Maze, Philip R. Hemmer, and Marko Lončar. A diamond nanowire single-photon source. *Nature Nanotech.*, 5(1038):195, 2010.
- [43] Julien Claudon, Joël Bleuse, Nitin Singh Malik, Maela Bazin, Perine Jaffrennou, Niels Gregersen, Christophe Sauvan, Philippe Lalanne, and Jean-Michel Gérard. A highly efficient single-photon source based on a quantum dot in a photonic nanowire. *Nat. Photon.*, 4(1038):174, 2010.
- [44] O. Astafiev, A. M. Zagoskin, A. A. Abdumalikov, Yu. A. Pashkin, T. Yamamoto, K. Inomata, Y. Nakamura, and J. S. Tsai. Resonance Fluorescence of a Single Artificial Atom. *Science*, 327(5967):840–843, 2010.
- [45] Joël Bleuse, Julien Claudon, Megan Creasey, Nitin. S. Malik, Jean-Michel Gérard, Ivan Maksymov, Jean-Paul Hugonin, and Philippe Lalanne. Inhibition, enhancement, and control of spontaneous emission in photonic nanowires. *Phys. Rev. Lett.*, 106:103601, Mar 2011.
- [46] Io-Chun Hoi, C. M. Wilson, Göran Johansson, Tauno Palomaki, Borja Peropadre, and Per Delsing. Demonstration of a single-photon router in the microwave regime. *Phys. Rev. Lett.*, 107:073601, Aug 2011.
- [47] A. Laucht, S. Pütz, T. Günthner, N. Hauke, R. Saive, S. Frédérick, M. Bichler, M.-C. Amann, A. W. Holleitner, M. Kaniber, and J. J. Finley. A waveguide-coupled on-chip single-photon source. *Phys. Rev. X*, 2:011014, Mar 2012.

- [48] Io-Chun Hoi, Tauno Palomaki, Joel Lindkvist, Göran Johansson, Per Delsing, and C. M. Wilson. Generation of nonclassical microwave states using an artificial atom in 1d open space. *Phys. Rev. Lett.*, 108:263601, Jun 2012.
- [49] T. Giamarchi. *Quantum Physics in One Dimension*. Oxford University Press, New York, 2003.
- [50] H. J. Carmichael. *An Open Systems Approach to Quantum Optics (Lecture Notes in Physics)*. Springer, Berlin, 1993.
- [51] A. Wallraff, D. I. Schuster, A. Blais, L. Frunzio, R.-S. Huang, J. Majer, S. Kumar, S. M. Girvin, and R. J. Schoelkopf. Strong coupling of a single photon to a superconducting qubit using circuit quantum electrodynamics. *Nature*, 431:162, 2004.
- [52] I. Chiorescu, P. Bertet, K. Semba, Y. Nakamura, C. J. P. M. Harmans, and J. E. Mooij. Coherent dynamics of a flux qubit coupled to a harmonic oscillator. *Nature*, 431:159, 2004.
- [53] M. Brune, F. Schmidt-Kaler, A. Maali, J. Dreyer, E. Hagley, J. M. Raimond, and S. Haroche. Quantum rabi oscillation: A direct test of field quantization in a cavity. *Phys. Rev. Lett.*, 76:1800–1803, Mar 1996.
- [54] A. Boca, R. Miller, K. M. Birnbaum, A. D. Boozer, J. McKeever, and H. J. Kimble. Observation of the vacuum rabi spectrum for one trapped atom. *Phys. Rev. Lett.*, 93:233603, Dec 2004.
- [55] K. Hennessy, A. Badolato, M. Winger, D. Gerace, M. Atatüre, S. Gulde, S. Falt, E. L. Hu, and A. Imamoglu. Quantum nature of a strongly coupled single quantum dot-cavity system. *Nature*, 445:896, 2007.
- [56] A. Goban, K. S. Choi, D. J. Alton, D. Ding, C. Lacroûte, M. Pototschnig, T. Thiele, N. P. Stern, and H. J. Kimble. Demonstration of a state-insensitive, compensated nanofiber trap. *Phys. Rev. Lett.*, 109:033603, Jul 2012.
- [57] C. Eichler, D. Bozyigit, C. Lang, L. Steffen, J. Fink, and A. Wallraff. Experimental state tomography of itinerant single microwave photons. *Phys. Rev. Lett.*, 106:220503, Jun 2011.
- [58] C. Eichler, C. Lang, J. M. Fink, J. Govenius, S. Filipp, and A. Wallraff. Observation of entanglement between itinerant microwave photons and a superconducting qubit. *Phys. Rev. Lett.*, 109:240501, Dec 2012.
- [59] R. Shankar. *Principles of Quantum Mechanics*. Springer, New York, NY, second edition, 2008.

- [60] Alberto Politi, Martin J. Cryan, John G. Rarity, Siyuan Yu, and Jeremy L. O'Brien. Silica-on-Silicon Waveguide Quantum Circuits. *Science*, 320(5876):646–649, 2008.
- [61] D. E. Chang, A. S. Sørensen, P. R. Hemmer, and M. D. Lukin. Quantum optics with surface plasmons. *Phys. Rev. Lett.*, 97(5):053002, Aug 2006.
- [62] Darrick E. Chang, Anders S. Sørensen, Eugene A. Demler, and Mikhail D. Lukin. A single-photon transistor using nanoscale surface plasmons. *Nature Phys.*, 3:807–812, 2007.
- [63] Jie-Qiao Liao, Jin-Feng Huang, Yu-Xi Liu, Le-Man Kuang, and C. P. Sun. Quantum switch for single-photon transport in a coupled superconducting transmission-line-resonator array. *Phys. Rev. A*, 80(1):014301, Jul 2009.
- [64] Lan Zhou, Z. R. Gong, Yu-Xi Liu, C. P. Sun, and Franco Nori. Controllable scattering of a single photon inside a one-dimensional resonator waveguide. *Phys. Rev. Lett.*, 101(10):100501, Sep 2008.
- [65] Lan Zhou, S. Yang, Yu-xi Liu, C. P. Sun, and Franco Nori. Quantum Zeno switch for single-photon coherent transport. *Phys. Rev. A*, 80(6):062109, Dec 2009.
- [66] D. Witthaut and A. S. Sørensen. Photon scattering by a three-level emitter in a one-dimensional waveguide. *New J. Phys.*, 12(4):043052, 2010.
- [67] Paolo Longo, Peter Schmitteckert, and Kurt Busch. Few-photon transport in low-dimensional systems: Interaction-induced radiation trapping. *Phys. Rev. Lett.*, 104(2):023602, Jan 2010.
- [68] Pavel Kolchin, Rupert F. Oulton, and Xiang Zhang. Nonlinear quantum optics in a waveguide: Distinct single photons strongly interacting at the single atom level. *Phys. Rev. Lett.*, 106(11):113601, Mar 2011.
- [69] Dibyendu Roy. Two-photon scattering by a driven three-level emitter in a one-dimensional waveguide and electromagnetically induced transparency. *Phys. Rev. Lett.*, 106(5):053601, Feb 2011.
- [70] Huaixiu Zheng, Daniel J. Gauthier, and Harold U. Baranger. Cavity-free photon blockade induced by many-body bound states. *Phys. Rev. Lett.*, 107:223601, Nov 2011.
- [71] O. V. Astafiev, A. A. Abdumalikov, A. M. Zagoskin, Yu. A. Pashkin, Y. Nakamura, and J. S. Tsai. Ultimate on-chip quantum amplifier. *Phys. Rev. Lett.*, 104:183603, May 2010.

- [72] Eden Rephaeli and Shanhui Fan. Stimulated emission from a single excited atom in a waveguide. *Phys. Rev. Lett.*, 108:143602, Apr 2012.
- [73] P. Longo, P. Schmitteckert, and K. Busch. Dynamics of photon transport through quantum impurities in dispersion-engineered one-dimensional systems. *J. Opt. A*, 11:114009, 2009.
- [74] Jung-Tsung Shen and Shanhui Fan. Strongly correlated two-photon transport in a one-dimensional waveguide coupled to a two-level system. *Phys. Rev. Lett.*, 98(15):153003, Apr 2007.
- [75] Jung-Tsung Shen and Shanhui Fan. Strongly correlated multiparticle transport in one dimension through a quantum impurity. *Phys. Rev. A*, 76(6):062709, Dec 2007.
- [76] V. I. Yudson. Dynamics of integrable quantum systems. *Sov. Phys. JETP*, 61:1043, 1985.
- [77] V. I. Yudson and P. Reineker. Multiphoton scattering in a one-dimensional waveguide with resonant atoms. *Phys. Rev. A*, 78:052713, Nov 2008.
- [78] Shanhui Fan, Sükrü Ekin Kocabas, and Jung-Tsung Shen. Input-output formalism for few-photon transport in one-dimensional nanophotonic waveguides coupled to a qubit. *Phys. Rev. A*, 82:063821, Dec 2010.
- [79] Ben Q. Baragiola, Robert L. Cook, Agata M. Brańczyk, and Joshua Combes.  $N$ -photon wave packets interacting with an arbitrary quantum system. *Phys. Rev. A*, 86:013811, Jul 2012.
- [80] Mikhail Pletyukhov and Vladimir Gritsev. Scattering of massless particles in one-dimensional chiral channel. *New J. Phys.*, 14:095028, 2012.
- [81] Mikhail Pletyukhov, Matous Ringel, and Vladimir Gritsev. Full counting statistics of photons interacting with emitter. arXiv:1302.2156, 2013.
- [82] P. Maunz, D. L. Moehring, S. Olmschenk, K. C. Younge, D. N. Matsukevich, and C. Monroe. Quantum interference of photon pairs from two remote trapped atomic ions. *Nature Phys.*, 3:538, 2007.
- [83] Akinori Nishino, Takashi Imamura, and Naomichi Hatano. Exact scattering eigenstates, many-body bound states, and nonequilibrium current in an open quantum dot system. *Phys. Rev. Lett.*, 102(14):146803, Apr 2009.
- [84] Takashi Imamura, Akinori Nishino, and Naomichi Hatano. Entanglement generation through an open quantum dot: Exact two-electron scattering state in the Anderson model. *Phys. Rev. B*, 80(24):245323, Dec 2009.

- [85] J. J. Sakurai. *Modern Quantum Mechanics*. Addison-Wesley, Reading, MA, 1994.
- [86] So-Young Baek and Yoon-Ho Kim. Spectral properties of entangled photon pairs generated via frequency-degenerate type-i spontaneous parametric down-conversion. *Phys. Rev. A*, 77:043807, Apr 2008.
- [87] Won-Young Hwang. Quantum key distribution with high loss: Toward global secure communication. *Phys. Rev. Lett.*, 91(5):057901, Aug 2003.
- [88] Hoi-Kwong Lo, Xiongfeng Ma, and Kai Chen. Decoy state quantum key distribution. *Phys. Rev. Lett.*, 94(23):230504, Jun 2005.
- [89] Xiang-Bin Wang. Beating the photon-number-splitting attack in practical quantum cryptography. *Phys. Rev. Lett.*, 94(23):230503, Jun 2005.
- [90] M. Curty, T. Moroder, X. Ma, and N. Lütkenhaus. Passive decoy state quantum key distribution with practical light sources. *Opt. Lett.*, 34:3238, 2009.
- [91] Travis S. Humble and Warren P. Grice. Spectral effects in quantum teleportation. *Phys. Rev. A*, 75:022307, Feb 2007.
- [92] Irfan Ali-Khan, Curtis J. Broadbent, and John C. Howell. Large-alphabet quantum key distribution using energy-time entangled bipartite states. *Phys. Rev. Lett.*, 98:060503, Feb 2007.
- [93] Huaixiu Zheng, Daniel J. Gauthier, and Harold U. Baranger. Waveguide QED: Many-body bound-state effects in coherent and Fock-state scattering from a two-level system. *Phys. Rev. A*, 82(6):063816, Dec 2010.
- [94] Takao Aoki, Barak Dayan, E. Wilcut, W. P. Bowen, A. S. Parkins, T. J. Kippenberg, K. J. Vahala, and H. J. Kimble. Observation of strong coupling between one atom and a monolithic microresonator. *Nature*, 443:671, 2006.
- [95] Barak Dayan, A. S. Parkins, Takao Aoki, E. P. Ostby, K. J. Vahala, and H. J. Kimble. A photon turnstile dynamically regulated by one atom. *Science*, 319(5866):1062, 2008.
- [96] R. Bianchetti, S. Filipp, M. Baur, J. M. Fink, C. Lang, L. Steffen, M. Boissonneault, A. Blais, and A. Wallraff. Control and tomography of a three level superconducting artificial atom. *Phys. Rev. Lett.*, 105:223601, Nov 2010.
- [97] J. B. Majer, F. G. Paauw, A. C. J. ter Haar, C. J. P. M. Harmans, and J. E. Mooij. Spectroscopy on two coupled superconducting flux qubits. *Phys. Rev. Lett.*, 94(9):090501, Mar 2005.

- [98] L. Slodička, G. Hétet, S. Gerber, M. Hennrich, and R. Blatt. Electromagnetically induced transparency from a single atom in free space. *Phys. Rev. Lett.*, 105:153604, Oct 2010.
- [99] Magnus Albert, Aurélien Dantan, and Michael Drewsen. Cavity electromagnetically induced transparency and all-optical switching using ion coulomb crystals. *Nat. Photon.*, 5(214):633, 2011.
- [100] Hong Chang, Haibin Wu, Changde Xie, and Hai Wang. Controlled shift of optical bistability hysteresis curve and storage of optical signals in a four-level atomic system. *Phys. Rev. Lett.*, 93:213901, Nov 2004.
- [101] M. Baur, S. Filipp, R. Bianchetti, J. M. Fink, M. Göppl, L. Steffen, P. J. Leek, A. Blais, and A. Wallraff. Measurement of Autler-Townes and Mollow transitions in a strongly driven superconducting qubit. *Phys. Rev. Lett.*, 102:243602, Jun 2009.
- [102] Mika A. Sillanpää, Jian Li, Katarina Cicak, Fabio Altomare, Jae I. Park, Raymond W. Simmonds, G. S. Paraoanu, and Pertti J. Hakonen. Autler-Townes effect in a superconducting three-level system. *Phys. Rev. Lett.*, 103:193601, Nov 2009.
- [103] William R. Kelly, Zachary Dutton, John Schlafer, Bhaskar Mookerji, Thomas A. Ohki, Jeffrey S. Kline, and David P. Pappas. Direct observation of coherent population trapping in a superconducting artificial atom. *Phys. Rev. Lett.*, 104:163601, Apr 2010.
- [104] Bixuan Fan, Anton F. Kockum, Joshua Combes, Göran Johansson, Io-chun Hoi, C. M. Wilson, Per Delsing, G. J. Milburn, and Thomas M. Stace. Breakdown of the cross-Kerr scheme for photon counting. *Phys. Rev. Lett.*, 110:053601, Jan 2013.
- [105] Andrei Faraon, Ilya Fushman, Dirk Englund, Nick Stoltz, Pierre Petroff, and Jelena Vučković. Coherent generation of non-classical light on a chip via photon-induced tunneling and blockade. *Nature Phys.*, 4(16):859, 2008.
- [106] Jie-Qiao Liao and C. K. Law. Correlated two-photon transport in a one-dimensional waveguide side-coupled to a nonlinear cavity. *Phys. Rev. A*, 82:053836, Nov 2010.
- [107] Danna Rosenberg, Jim W. Harrington, Patrick R. Rice, Philip A. Hiskett, Charles G. Peterson, Richard J. Hughes, Adriana E. Lita, Sae Woo Nam, and Jane E. Nordholt. Long-distance decoy-state quantum key distribution in optical fiber. *Phys. Rev. Lett.*, 98:010503, Jan 2007.

- [108] Nicolas Gisin and Rob Thew. Quantum communication. *Nat. Photon.*, 1:165, 2007.
- [109] Eden Rephaeli, S. E. Kocabas, and Shanhui Fan. Few-photon transport in a waveguide coupled to a pair of colocated two-level atoms. *Phys. Rev. A*, 84:063832, Dec 2011.
- [110] Dibyendu Roy. Correlated few-photon transport in one-dimensional waveguides: Linear and nonlinear dispersions. *Phys. Rev. A*, 83:043823, Apr 2011.
- [111] Huaixiu Zheng, Daniel J. Gauthier, and Harold U. Baranger. Strongly correlated photons generated by coupling a three- or four-level system to a waveguide. *Phys. Rev. A*, 85:043832, Apr 2012.
- [112] David Dzsotjan, Anders S. Sørensen, and Michael Fleischhauer. Quantum emitters coupled to surface plasmons of a nanowire: A Green's function approach. *Phys. Rev. B*, 82:075427, Aug 2010.
- [113] David Dzsotjan, Jürgen Kästel, and Michael Fleischhauer. Dipole-dipole shift of quantum emitters coupled to surface plasmons of a nanowire. *Phys. Rev. B*, 84:075419, Aug 2011.
- [114] A. Gonzalez-Tudela, D. Martin-Cano, E. Moreno, L. Martin-Moreno, C. Tejedor, and F. J. Garcia-Vidal. Entanglement of two qubits mediated by one-dimensional plasmonic waveguides. *Phys. Rev. Lett.*, 106:020501, Jan 2011.
- [115] Diego Martin-Cano, Alejandro Gonzalez-Tudela, L. Martin-Moreno, F. J. Garcia-Vidal, Carlos Tejedor, and Esteban Moreno. Dissipation-driven generation of two-qubit entanglement mediated by plasmonic waveguides. *Phys. Rev. B*, 84:235306, Dec 2011.
- [116] Juan Pablo Paz and Augusto J. Roncaglia. Dynamics of the entanglement between two oscillators in the same environment. *Phys. Rev. Lett.*, 100:220401, Jun 2008.
- [117] Thomas Zell, Friedemann Queisser, and Rochus Klesse. Distance dependence of entanglement generation via a bosonic heat bath. *Phys. Rev. Lett.*, 102:160501, Apr 2009.
- [118] Hua-Tang Tan, Wei-Min Zhang, and Gao-xiang Li. Entangling two distant nanocavities via a waveguide. *Phys. Rev. A*, 83:062310, Jun 2011.

- [119] A. Wolf, G. De Chiara, E. Kajari, E. Lutz, and G. Morigi. Entangling two distant nanocavities via a waveguide. *Europhys. Lett.*, 95:60008, Sept 2011.
- [120] J. Majer, J. M. Chow, J. M. Gambetta, Jens Koch, B. R. Johnson, J. A. Schreier, L. Frunzio, D. I. Schuster, A. A. Houck, A. Wallraff, A. Blais, M. H. Devoret, S. M. Girvin, and R. J. Schoelkopf. Coupling superconducting qubits via a cavity bus. *Nature*, 449:443, 2007.
- [121] Z. Ficek and R. Tanas. Entangled states and collective nonclassical effects in two-atom systems. *Phys. Rep.*, 372:369, 2002.
- [122] Sumanta Das, G. S. Agarwal, and Marlan O. Scully. Quantum interferences in cooperative dicke emission from spatial variation of the laser phase. *Phys. Rev. Lett.*, 101:153601, Oct 2008.
- [123] P. W. Milonni, D. F. V. James, and H. Fearn. Photodetection and causality in quantum optics. *Phys. Rev. A*, 52:1525–1537, Aug 1995.
- [124] L.-M. Duan and H. J. Kimble. Scalable photonic quantum computation through cavity-assisted interactions. *Phys. Rev. Lett.*, 92:127902, Mar 2004.
- [125] Abhishek Dhar, Diptiman Sen, and Dibyendu Roy. Scattering of electrons from an interacting region. *Phys. Rev. Lett.*, 101:066805, Aug 2008.
- [126] Z. Ficek and B. C. Sanders. Quantum beats in two-atom resonance fluorescence. *Phys. Rev. A*, 41:359–368, Jan 1990.
- [127] William K. Wootters. Entanglement of formation of an arbitrary state of two qubits. *Phys. Rev. Lett.*, 80:2245–2248, Mar 1998.
- [128] O. Benson. Assembly of hybrid photonic architectures from nanophotonic constituents. *Nature*, 480:193, 2011.
- [129] Tiecke Tobias, Jeff Thompson, Johannes Feist, Chun Yu, Alexey Akimov, Darrick Chang, Alexander Zibrov, Vladan Vuletic, Hongkun Park, and Mikhail Lukin. A nanoscale quantum interface for single atoms. Abstract APS 2012 March Meeting (2012).
- [130] R. F. Oulton, V. J. Sorger, D. A. Genov, D. F. P. Pile, and X. Zhang. A hybrid plasmonic waveguide for subwavelength confinement and long-range propagation. *Nat. Photon.*, 2:496, 2008.
- [131] Johannes Feist, Semion K. Saikin, M.T. Homer Reid, Alán Aspuru-Guzik, and Mikhail D. Lukin. Plasmonic nanotips for spectroscopy with nanometer-scale resolution. Abstract APS 2012 March Meeting (2012).

- [132] Chang-Ling Zou, Fang-Wen Sun, Chun-Hua Dong, Yun-Feng Xiao, Xi-Feng Ren, Xiang-Dong Chen Liu Lv, Jin-Ming Cui, Zheng-Fu Han, , and Guang-Can Guo. Movable fiber-integrated hybrid plasmonic waveguide on metal film. *IEEE Photon. Tech. Letts.*, 24:1041, 2012.
- [133] E. Vetsch, D. Reitz, G. Sagué, R. Schmidt, S. T. Dawkins, and A. Rauschenbeutel. Optical interface created by laser-cooled atoms trapped in the evanescent field surrounding an optical nanofiber. *Phys. Rev. Lett.*, 104(20):203603, May 2010.
- [134] Jung-Tsung Shen, M. L. Povinelli, Sunil Sandhu, and Shanhui Fan. Stopping single photons in one-dimensional circuit quantum electrodynamics systems. *Phys. Rev. B*, 75:035320, Jan 2007.
- [135] Martin V. Gustafsson, Paulo V. Santos, Goran Johansson, and Per Delsing. Local probing of propagating acoustic waves in a gigahertz echo chamber. *Nat. Phys.*, 8:338–343, 2012.
- [136] C. H. Bennett and G. Brassard. Proceedings of ieee international conference on computers, systems, and signal processing. pages 175–179, New York, 1984. IEEE.
- [137] Hoi-Kwong Lo, Marcos Curty, and Bing Qi. Measurement-device-independent quantum key distribution. *Phys. Rev. Lett.*, 108:130503, Mar 2012.
- [138] D. Gottesman, H.-K. Lo, Norbert Lütkenhaus, and John Preskill. Security of quantum key distribution with imperfect devices. *Quantum Inf. Comput.*, 4:325, 2004.
- [139] Gilles Brassard, Norbert Lütkenhaus, Tal Mor, and Barry C. Sanders. Limitations on practical quantum cryptography. *Phys. Rev. Lett.*, 85:1330–1333, Aug 2000.
- [140] Xiongfeng Ma, Bing Qi, Yi Zhao, and Hoi-Kwong Lo. Practical decoy state for quantum key distribution. *Phys. Rev. A*, 72:012326, Jul 2005.
- [141] G. Gobby, Z. L. Yuan, and A. J. Shields. Quantum key distribution over 122 km of standard telecom fiber. *Appl. Phys. Lett.*, 84:3762–3764, 2004.
- [142] Thomas H. Cormen, Charles E. Leiserson, Ronald L. Rivest, and Clifford Stein. *Introduction to Algorithms*. MIT Press and McGraw-Hill, New York, third edition, 2009.

- [143] Qin Wang, Wei Chen, Guilherme Xavier, Marcin Swillo, Tao Zhang, Sébastien Sauge, Maria Tengner, Zheng-Fu Han, Guang-Can Guo, and Anders Karlsson. Experimental decoy-state quantum key distribution with a sub-poissonian heralded single-photon source. *Phys. Rev. Lett.*, 100:090501, Mar 2008.
- [144] M. A. Nielsen and I. L. Chuang. *Quantum Computation and Quantum Information*. Cambridge University Express, Cambridge, 2000.
- [145] I. Buluta and F. Nori. Quantum simulators. *Science*, 326:108, 2009.
- [146] J. I. Cirac and P. Zoller. Goals and opportunities in quantum simulation. *Nat. Phys.*, 8:264, 2012.
- [147] T. D. Ladd, F. Jelezko, R. Laflamme, Y. Nakamura, C. Monroe, and J. L. O'Brien. Quantum computers. *Nature*, 464:45, 2010.
- [148] D. Petrosyan. Towards deterministic optical quantum computation with coherently driven atomic ensembles. *J. Opt. B*, 7:S141–S151, 2005.
- [149] C. Santori, D. Fattal, J. Vuckovic, G. Solomon, and Y. Yamamoto. Indistinguishable photons from a single-photon device. *Nature*, 419:594, 2002.
- [150] C. W. Chou, S. V. Polyakov, A. Kuzmich, and H. J. Kimble. Single-photon generation from stored excitation in an atomic ensemble. *Phys. Rev. Lett.*, 92:213601, May 2004.
- [151] Morgan P. Hedges, Jevon J. Longdell, Yongmin Li, and Matthew J. Sellars. Efficient quantum memory for light. *Nature*, 465:1052, 2010.
- [152] K. F. Reim, P. Michelberger, K. C. Lee, J. Nunn, N. K. Langford, and I. A. Walmsley. Single-photon-level quantum memory at room temperature. *Phys. Rev. Lett.*, 107:053603, Jul 2011.
- [153] E. Knill, R. Laflamme, and G. J. Milburn. A scheme for efficient quantum computation with linear optics. *Nature*, 401:46, 2001.
- [154] Kazuki Koshino, Satoshi Ishizaka, and Yasunobu Nakamura. Deterministic photon-photon  $\sqrt{\text{SWAP}}$  gate using a  $\lambda$  system. *Phys. Rev. A*, 82:010301, Jul 2010.
- [155] Alexey V. Gorshkov, Johannes Otterbach, Michael Fleischhauer, Thomas Pohl, and Mikhail D. Lukin. Photon-photon interactions via Rydberg blockade. *Phys. Rev. Lett.*, 107:133602, Sep 2011.

- [156] Thibault Peyronel, Ofer Firstenberg, Qi-Yu Liang, Sebastian Hofferberth, Alexey V. Gorshkov, Thomas Pohl, Mikhail D. Lukin, and Vladan Vuletic. Quantum nonlinear optics with single photons enabled by strongly interacting atoms. *Nature*, page 57, 2012.
- [157] F. Ciccarello, D. E. Browne, L. C. Kwek, H. Schomerus, M. Zarcone, and S. Bose. Quasideterministic realization of a universal quantum gate in a single scattering process. *Phys. Rev. A*, 85:050305(R), May 2012.
- [158] M. J. Madsen, D. L. Moehring, P. Maunz, R. N. Kohn, L.-M. Duan, and C. Monroe. Ultrafast coherent excitation of a trapped ion qubit for fast gates and photon frequency qubits. *Phys. Rev. Lett.*, 97:040505, Jul 2006.
- [159] D Bozyigit, C Lang, L Steffen, J M Fink, C Eichler, M Baur, R Bianchetti, P J Leek, S Filipp, A Wallraff, M P Da Silva, and A Blais. Correlation measurements of individual microwave photons emitted from a symmetric cavity. *Journal of Physics: Conference Series*, 264(1):012024, 2011.
- [160] U. Fano. Effects of configuration interaction on intensities and phase shifts. *Phys. Rev.*, 124:1866–1878, Dec 1961.
- [161] Andrey E. Miroshnichenko, Sergej Flach, and Yuri S. Kivshar. Fano resonances in nanoscale structures. *Rev. Mod. Phys.*, 82:2257–2298, Aug 2010.
- [162] Hanhee Paik, D. I. Schuster, Lev S. Bishop, G. Kirchmair, G. Catelani, A. P. Sears, B. R. Johnson, M. J. Reagor, L. Frunzio, L. I. Glazman, S. M. Girvin, M. H. Devoret, and R. J. Schoelkopf. Observation of high coherence in josephson junction qubits measured in a three-dimensional circuit QED architecture. *Phys. Rev. Lett.*, 107:240501, Dec 2011.
- [163] Chad Rigetti, Jay M. Gambetta, Stefano Poletto, B. L. T. Plourde, Jerry M. Chow, A. D. Córcoles, John A. Smolin, Seth T. Merkel, J. R. Rozen, George A. Keefe, Mary B. Rothwell, Mark B. Ketchen, and M. Steffen. Superconducting qubit in a waveguide cavity with a coherence time approaching 0.1 ms. *Phys. Rev. B*, 86:100506, Sep 2012.
- [164] J. Clarke and F. K. Wilhelm. Superconducting quantum bits. *Nature*, 453:1031, 2008.
- [165] T. Niemczyk, F. Deppe, H. Huebl, E. P. Menzel, F. Hocke, M. J. Schwarz, J. J. Garcia-Ripoll, D. Zueco, T. Hummer, E. Solano, A. Marx, and R. Gross. Circuit quantum electrodynamics in the ultrastrong-coupling regime. *Nat. Phys.*, 6:772, 2010.

- [166] D. Ballester, G. Romero, J. J. Garcia-Ripoll, F. Deppe, and E. Solano. Quantum simulation of the ultrastrong-coupling dynamics in circuit quantum electrodynamics. *Phys. Rev. X*, 2:021007, May 2012.
- [167] Karyn Le Hur. Kondo resonance of a microwave photon. *Phys. Rev. B*, 85:140506, Apr 2012.
- [168] Moshe Goldstein, Michel H. Devoret, Manuel Houzet, and Leonid I. Glazman. Inelastic microwave photon scattering off a quantum impurity in a Josephson-junction array. *Phys. Rev. Lett.*, 110:017002, Jan 2013.
- [169] K. Le Hur. *Chapter 9 "Spin-Boson Systems: Dissipation and Light Phenomena" in "Understanding Quantum Phase Transitions"*. Editor: Lincoln D. Carr, CRC Press, Boca Raton, FL, first edition, 2011.
- [170] Huaixiu Zheng, Daniel J. Gauthier, and Harold U. Baranger. Waveguide-QED-based photonic quantum computation. arXiv: 1211.1711, 2012.

# **Biography**

## **Huaixiu Zheng**

### **Personal**

- Born on January 21, 1985 in Bengbu, Anhui Province, China

### **Education**

- PhD in Physics (expected), Duke University, Durham, NC, 2008-2013
- M.A. in Physics, Duke University, Durham, NC, 2011
- M.S. in Electrical and Computer Engineering, University of Alberta, Edmonton, Alberta, Canada, 2006-2007
- B.S. in Physics, University of Science and Technology of China, Hefei, Anhui, China, 2002-2006

### **Awards**

- Chinese Government Award for Outstanding Self-Financed Students Abroad, China Scholarship Council, 2013
- John T. Chambers Scholars, Fitzpatrick Institute for Photonics, Duke University, 2011-2013
- GPNano-Fellowship, Duke University, 2008 & 2009

- Outstanding Undergraduate Research Project, University of Science and Technology of China, 2005
- Scholarship for Academic Excellence, University of Science and Technology of China, 2004 & 2006

## Papers in Preparation

- Huaixiu Zheng, Serge Florens, and Harold U. Baranger, "Non-Fermi Liquid Quantum Critical Point Probed by Resonant Tunneling with Dissipation", (2013).
- Huaixiu Zheng, Daniel J. Gauthier, and Harold U. Baranger, "Transport in a One-dimensional Waveguide Coupled to a Microtoroidal Resonator with a Trapped Atom", (2013).
- Dong E. Liu, Huaixiu Zheng, H.T. Mebrahtu, Gleb Finkelstein and Harold U. Baranger, "Tunable Quantum Phase transition in Dissipative Resonant Level", (2013).

## Papers Submitted

- Huaixiu Zheng, Daniel J. Gauthier, and Harold U. Baranger, "Waveguide-QED-Based Photonic Quantum Computation", submitted to Phys. Rev. Lett. (2013).
- H.T. Mebrahtu, I.V. Borzenets, H. Zheng, Yu. Bomze, A.I. Smirnov, S. Florens, H.U. Baranger, and G. Finkelstein, "Observation of Majorana-like Quantum Critical Behavior in a Resonant Level Coupled to a Dissipative Environment", submitted to Nature Physics (2013).

## Publications

1. Huaixiu Zheng, and Harold U. Baranger, "Persistent Quantum Beats and Long-Distance Entanglement from Waveguide-Mediated Interactions", **Phys. Rev. Lett.** 110, 113601 (2013).
2. Huaixiu Zheng, Daniel J. Gauthier, and Harold U. Baranger, "Decoy-State Quantum Key Distribution with Non-classical Light", **Opt. Lett.** 38, 622 (2013).
3. H.T. Mebrahtu, I.V. Borzenets, D.E. Liu, H. Zheng, Yu. Bomze, A.I. Smirnov, H.U. Baranger, and G. Finkelstein, "Quantum phase transition in a resonant level coupled to interacting leads", **Nature** 488, 61 (2012).
4. Huaixiu Zheng, Daniel J. Gauthier, and Harold U. Baranger, "Strongly-correlated photons generated by coupling a three- or four-level system to a waveguide", **Phys. Rev. A** 85, 043832 (2012).
5. Huaixiu Zheng, Daniel J. Gauthier, and Harold U. Baranger, "Cavity-Free Photon Blockade Induced by Many-Body Bound States", **Phys. Rev. Lett.** 107, 223601 (2011).
6. Huaixiu Zheng, Daniel J. Gauthier, and Harold U. Baranger, "Waveguide QED: Many-Body Bound State Effects in Coherent and Fock State Scattering from a Two-Level System", **Phys. Rev. A** 82, 063816 (2010).
7. Z. F. Wang, Huaixiu Zheng, Q. W. Shi, and Jie Chen, "Emerging Nanodevice Paradigm: Graphene-Based Electronics for Nanoscale Computing", **ACM Journal on Emerging Technologies in Computing Systems** 5, 3 (2009).
8. Huaixiu Zheng, and Walter Duley, "Field effects on the electronic and spin properties of undoped and doped graphene nanodots", **Phys. Rev. B** 78, 155118 (2008).
9. Huaixiu Zheng, and Walter Duley, "First-principles study of edge chemical modifications in graphene nanodots", **Phys. Rev. B** 78, 045421 (2008).

10. Z. F. Wang, Qunxiang Li, Q. W. Shi, Xiaoping Wang, J. G. Hou, Huaixiu Zheng, and Jie Chen, "Ballistic rectification in a Z-shaped graphene nanoribbon junction", **Appl. Phys. Lett.** 92, 133119 (2008).
11. Z. F. Wang, Q. W. Shi, Qunxiang Li, Xiaoping Wang, J. G. Hou, Huaixiu Zheng, Yao Yao, and Jie Chen, "Z-shaped Graphene Nanoribbon Quantum Dot Device", **Appl. Phys. Lett.** 91, 053109 (2007).
12. Huaixiu Zheng, Z. F. Wang, Tao Luo, Q. W. Shi and Jie Chen, "Analytical Study of Electronic Structure in Armchair Graphene Nanoribbons", **Phys. Rev. B** 75, 165414 (2007).
13. Z. F. Wang, Qunxiang Li, Huaixiu Zheng, Hao Ren, Haibin Su, Q. W. Shi, and Jie Chen, "Tuning electronic structures of the graphene nanoribbons through chemical edge modification: A theoretical study", **Phys. Rev. B** 75, 113406 (2007).
14. Huaixiu Zheng, Z.F. Wang, Qinwei Shi, Xiaoping Wang and Jie Chen, "Statistical model for analyzing the dephasing effect in a one-dimensional scattering chain", **Phys. Rev. B** 74,155323 (2006).